



HAL
open science

Elaboration and properties of nanostructured Layered Double Hydroxides derived from MOFs conversion

Mengwei Li

► **To cite this version:**

Mengwei Li. Elaboration and properties of nanostructured Layered Double Hydroxides derived from MOFs conversion. Material chemistry. Université Clermont Auvergne; Université de Wuhan (Chine), 2024. English. NNT : 2024UCFA0043 . tel-04646084

HAL Id: tel-04646084

<https://theses.hal.science/tel-04646084>

Submitted on 12 Jul 2024

HAL is a multi-disciplinary open access archive for the deposit and dissemination of scientific research documents, whether they are published or not. The documents may come from teaching and research institutions in France or abroad, or from public or private research centers.

L'archive ouverte pluridisciplinaire **HAL**, est destinée au dépôt et à la diffusion de documents scientifiques de niveau recherche, publiés ou non, émanant des établissements d'enseignement et de recherche français ou étrangers, des laboratoires publics ou privés.



École Doctorale des Sciences Fondamentales

THESE

Présentée par

Mengwei LI

Pour obtenir le grade de

Docteur d'Université

Spécialité : Chimie des Matériaux, Nanomatériaux et Procédés

Thèse en cotutelle avec l'université de Wuhan - Chine

**Elaboration and properties of nanostructured
Layered Double Hydroxides derived from
MOFs conversion**

PhD defence: 31 May 2024 in Wuhan in front of the examination committee comprised of :

M. MARCELLO BRIGANTE	Professeur, Université Clermont Auvergne, Clermont-Ferrand, France	Président
Mme MAGUY JABER	Professeure, Sorbonne University, Paris, France	Rapporteure
Mme YANRONG ZHANG	Professeure, Huazhong University of Science and Technology, Wuhan, China	Rapporteure
M. FENG WU	Professeur, Université Wuhan, China	Examineur
M. JINJUN Li	Professeur, Université Wuhan, China	Examineur
M. C. FORANO	Professeur Université Clermont Auvergne, Clermont-Ferrand, France	Directeur de thèse
Mme VANESSA PREVOT	Directrice de Recherche CNRS, ICCF, Clermont- Ferrand, France	Directrice de thèse
M. ZHIXIONG YOU	Professeur Université Wuhan , China	Directeur de thèse

To all that I love and who love me:

I never imagined that my childhood self, who wished to become a scientist for kidding, could actually take one step at a time until I was about to graduate with my PhD. It's like I never thought that "doing research" would be such a daunting task. Countless nights bursting into tears, countless times I wanted to give up, only to be transformed into motivation to do experiments over and over again. Thank you so much to my family, to my friends, and more importantly to my two mentors, Claude FORANO and Vanessa PREVOT for always giving me support. You are the ones who have revitalized me time and time again, and have made me stronger and stronger in spite of my failures.

In fact, I always think that I am the luckier one. Lucky enough to get a master's degree and a PhD from Wuhan University, and then to be a PhD student at UCA on a joint program. The year and a half I spent in France was the happiest and most fulfilling time of my studies. During this time, I met the best tutors in the world, my friends who always support me: Cai Minjuan, Zhang Xiaoyu, Cheng Peng. Of course, I also have to thank my mom, dad, boyfriend, who kept in touch with me every day despite the seven-hour time difference, and my grandmother, who went to heaven without waiting for me to return home.

Of course, everyone I met at UCA was very nice to me: Guo Yixuan who took great care of me since I first arrived in France ; handsome Prof. Marcello BRIGANTE with humor picked us up at the airport in an oversized car, pushing 6 suitcases by himself ; Prof. Gilles MAILHOT who was always there to warm me up, the beautiful and warm-hearted Alexandra, Julian who didn't communicate much with me, but was always there to help me with any problems that I encountered, the nice Ali TARHINI who always liked to imitate me, and Prof. Christine Taviot-Gueho and Prof. Fabrice LEROUX who greet each other warmly every time During the period of my stay at UCA I lamented countless times how fortunate I was to be able to meet such a lot of such nice people.

Last but certainly not least, thanks to my two best mentors in the whole world, no, the whole universe. I wonder if all the strange and unfortunate things that always happened to me during my PhD were because I overdrew all my luck to meet these two mentors. I had just arrived in France and had to be vaccinated and I didn't even know where the hospital was, Claude did this in half an hour and even when I realised I already had the vaccination certificate. And when I was in the lab and caused bad repercussions because of mishandling, the first thing Vanessa told me was that 'it's

normal to have accidents in experiments, we know you don't want to'. Most importantly, they were very attentive to my research topic. They have thought of many ways to help me solve the problems about my thesis. And even when I ask basic or "stupid" questions, they will patiently give me answers. The weekly group meeting was a stressful time, but it was also a "recharging station" for me to overcome one big mountain after another. And when it came to correcting my thesis, their seriousness even made me think, " How could I have such a perfect mentor?". I knew that my research and writing skills were far from being up to par. My two supervisors, however, reverse them word by word, even including punctuation and superscripts. In short, they are the perfect mentors in my mind.

I seem to forget to thank myself. Thanks to myself because I cried and worked hard at the same time without overcome the incontinence of tears. Thanks to myself because I'm getting stronger and stronger on the outside and on the inside. Thanking myself because I bring positive energy to those around me. Thanks to me, because I am.

2024.4.18

LuoJia Moutain

Abstract

Due to their flexible chemical composition, reversible intercalation reaction, and adaptable morphology, layered double hydroxides (LDHs) hold promising applications in catalysis, decontamination of polluted environmental media, and energy production. Additionally, microporous materials such as Metal Organic Frameworks (MOFs) constitute a class of precursors for the topotactic preparation of a wide range of inorganic materials due to their diverse chemical compositions and easily adjustable structures. This thesis focuses on the synthesis of LDHs derived from MOFs and their performance in environmental remediation. The main contents of the thesis are as follows:

(1) The MOF MIL-88A is synthesized using a novel method. Since the hydrothermal synthesis of MIL-88A requires over 6 h of reaction time, microwave-assisted precipitation, which is more efficient, is chosen to synthesize MIL-88A, and the optimal synthesis conditions are investigated. The results show that the microstructure of MIL-88A synthesized by the microwave method is more homogeneous, and the crystalline form is more stable.

(2) A new method is developed for the conversion of MOF as a precursor to new 3D LDH structures. Mesoporous Ni_xFe LDHs are prepared by converting MIL-88A (Fe), used here as a sacrificial "template" structure, by reacting nickel nitrate in a basic medium, with pH controlled by urea decomposition. The hydrolysis/nucleation/growth steps are localized on the surface of the MOF and lead to the intergrowth of Ni_xFe LDH nanoplates (LDH/88A), maintaining the initial 3D rod-like structure of MIL-88A. The reaction is performed in a microwave reactor, and its optimal conditions are studied.

(3) Other LDH/MOF conversion reactions have been explored to prepare new mesoporous 3D LDH structures with varied compositions and morphologies. The effects of ligands and metal cations have been investigated. Microwave syntheses of MOFs MIL-101 (Fe), analogous to MIL-88A (Fe) (fumarate ligand replaced by benzenetricarboxylate), and MIL-88 (Al), analogous to MIL-88 (Fe), have been optimized, and the conditions for their conversion into NiFe and NiAl LDHs studied. The reactivity of MIL-88A (Fe) with Co (II), Al (III), and Mg (II) salts has been tested with conversion results highly sensitive to the nature of the metal and medium conditions (pH).

(4) In order to develop new materials more effective for heavy metal adsorption,

the new 3D LDH structures have been modified by inserting phosphate anions, which are reactive towards heavy metals. The adsorption of heavy metals (Pb (II), Cd (II), Ni (II)) by $\text{Ni}_x/88\text{A-PO}_4$ ($x=3,5$) is studied and compared to the precursors $\text{Ni}_x\text{FeLDH}/88\text{A-Cl}$ ($x=3,5$), coprecipitated phases $\text{Ni}_x\text{FeLDH}/\text{COP-PO}_4$ ($x=2,3$), and MIL-88A (Fe). The results show that the $\text{Ni}_3\text{FeLDH}/88\text{A-PO}_4$ compound exhibits one of the highest Pb (II) adsorption capacities (538 mg/g) ever reported in the literature, higher than those of coprecipitated phases. Adsorption is compatible with the pseudo-second-order kinetic model and the Langmuir adsorption thermodynamic model. Structural analysis of residues after adsorption (XRD, FTIR, XPS) has revealed the nucleation and precipitation of $\text{Pb}(\text{OH})_2$ and $\text{Pb}_3(\text{PO}_4)_2$ phases on the LDH rod surface.

(5) $\text{Ni}_x\text{FeLDH}/88\text{A}$ and their calcined derivatives have demonstrated strong catalytic reactivity for the degradation of organic pollutants, particularly bisphenol A (BPA) activated by peroxydisulfate. Experimental conditions have been optimized to achieve the best efficiency. The mesoporous $\text{Ni}_x\text{Fe}/88\text{A-S}_2\text{O}_8^{2-}$ coupling promotes very rapid BPA degradation kinetics (a few minutes), more effective than coprecipitated analogues. These new catalysts are stable and recyclable.

Résumé

En raison de leur composition chimique flexible, de leur réaction d'intercalation réversible et de leur morphologie adaptable, les hydroxydes doubles lamellaires (LDH) présentent des applications prometteuses en matière de catalyse, de décontamination de milieux environnementaux pollués, ainsi que de production d'énergie. Par ailleurs, les matériaux microporeux de type MOFs (Metal Organic Framework) constituent une classe de précurseurs pour la préparation topotactique d'une large gamme de matériaux inorganiques en raison de leurs diverses compositions chimiques et de leurs structures facilement ajustables. Cette thèse se concentre sur la synthèse d'HDL dérivés de MOF et sur leurs performances en matière de remédiation environnementale. Les principaux contenus de la thèse sont les suivants:

(1) Le MOF MIL-88A est synthétisé par une nouvelle méthode. La synthèse hydrothermale du MIL-88A nécessitant plus de 6 heures de réaction, la précipitation assistée par micro-ondes, plus efficace, est choisie pour synthétiser le MIL-88A et les conditions optimales de synthèse sont étudiées. Les résultats montrent que la

microstructure du MIL-88A synthétisé par la méthode des micro-ondes est plus homogène et que la forme cristalline est plus stable.

- (2) Une nouvelle méthode est développée pour la conversion de MOF en tant que précurseur de nouvelles structures HDL 3D. Des HDL Ni_xFe à structure mésoporeuse sont préparés par conversion du MIL-88A(Fe), utilisé ici comme structure « template » sacrificielle, par réaction du nitrate de nickel en milieu basique, dont le pH est contrôlé par décomposition de la base retard urée. Les étapes d'hydrolyse/nucléation/croissance sont localisées à la surface du MOF et conduisent à l'intercroissance de nanoplaquettes d'HDL Ni_xFe (LDH/88A) maintenant la structure 3D initiale de type bâtonnet du MIL88A. La réaction est effectuée dans un réacteur à micro-ondes et ses conditions optimales sont étudiées.
- (3) D'autres réactions de conversion MOF/HDL ont été explorées afin de préparer de nouvelles structures HDL 3D mésoporeuses, de composition et morphologie variées. Les effets de ligands et de cations métalliques ont été regardés. Les synthèses par micro-ondes du MOF MIL-101 (Fe), analogue du MIL88A (Fe) (ligand fumarate remplacé par le benzenedicarboxylate) et du MIL-88 (Al), analogue du MIL-88 (Fe) ont été optimisées et les conditions de leur conversion en HDL NiFe et NiAl étudiées. La réactivité du MIL-88A (Fe) avec des sels de Co (II), d'Al (III) et de Mg (II) ont été testés avec des résultats de conversions très sensibles à la nature du métal et des conditions du milieu (pH).
- (4) Dans l'objectif d'élaborer de nouveaux matériaux plus efficace pour l'adsorption de métaux lourds, les nouvelles structures HDL 3D ont été modifiées par insertion d'anions phosphates, anions réactifs vis-à-vis de métaux lourds. L'adsorption des métaux lourds (Pb (II), Cd (II), Ni (II)) par $Ni_xFeLDH/88A-PO_4$ ($x=3,5$) est étudiée et comparée aux précurseurs $Ni_xFeLDH/88A-Cl$ ($x=3,5$), aux phases coprécipitées $Ni_xFeLDH/COP-PO_4$ ($x=2,3$) et au MIL-88A (Fe). Les résultats montrent que le composé $Ni_3FeLDH/88A-PO_4$ présente une des meilleures capacité d'adsorption de Pb (II) (538 mg/g) jamais reportée dans la littérature, plus élevée que celles des phases coprécipitées. L'adsorption est compatible avec le modèle cinétique de pseudo-seconde ordre et le modèle thermodynamique d'adsorption de Langmuir. L'analyse structurale des résidus après adsorption (DRX, FTIR, XPS) a mis en évidence la nucléation et précipitation de phases $Pb(OH)_2$ et $Pb_3(PO_4)_2$ à la surface de bâtonnet d'HDL.
- (5) Les matériaux HDL $Ni_xFe/88A$ et leur dérivés calcinés ont démontré de forte

réactivité catalytique pour la dégradation de polluants organiques et en particulier pour le bisphénol A (BPA) activée par le peroxydisulfate. Les conditions expérimentales ont été optimisées pour obtenir la meilleure efficacité. Le couplage $\text{Ni}_x\text{FeLDH}/88\text{A-S}_2\text{O}_8^{2-}$ mésoporeuse favorise des cinétiques de dégradation du BPA très rapide (quelques minutes), plus efficace que les analogues coprécipités. Ces nouveaux catalyseurs sont stables et recyclables.

Table of contents

Introduction.....	11
Chapter I Bibliography	15
I.1. Overview of layered double hydroxides (LDHs).....	16
I.1.1. Structure and composition of LDHs	16
I.1.2. Synthesis methods of LDHs.....	18
I.1.3 Properties of LDHs	22
I.2 Overview of Metal Organic Framework (MOF) materials	24
I.2.1 Structure, composition and morphology of MOFs	24
I.2.2 Synthesis of MOFs.....	32
I.3 Conversion of MOF to LDH and to heterostructure-based LDH.....	44
I.3.1 Alkaline hydrolysis	46
I.3.2 Pyrolysis with post-growth	47
I.3.3 Etching templates.....	48
I.4 Application of MOF-derived LDH in the remediation of aquatic environments	53
I.4.1 Modification of adsorption properties	53
I.4.2 Advanced oxidation processes	55
I.4.3 Capacitive deionization (CDI) and chemical sensors	56
Chapter II Synthesis and characterizations of MIL-88A and conversion into LDH/88A and LDO/88A	57
II.1. Introduction.....	58
II.2. Synthesis and characterizations of MIL-88A	60
II.2.1. Experimental section	60
II.2.2. Results and discussion	61
II.2.3. Conclusion	70
II.3. Conversion of MIL-88A to LDH/88A	71
II.3.1. Experimental section	71
II.3.2. Investigation of the protocole for LDH/88A formation	73
II.3.3. Characterization of LDH/88A	82
II.3.4. Conclusion	85
II.4. Synthesis and characterization of LDO/88A	86

II.4.1. Experimental section	86
II.4.2. Results and discussion	86
II.4.3. Conclusion	92
II.5. Conclusion	92
Chapter III Extension of MIL-88A (Fe) conversion into LDH/88A to other LDH/MOF systems.....	94
III.1. Introduction	95
III.2 Effects of metal ions	96
III.2.1 Behavior of metal ions as etching agents	96
III.2.2 Behavior of metal ions as MOF skeletons	106
III.3 Effects of organic ligand.....	112
III.3.1 Synthesis of MIL-101 (Fe-BDC) and its conversion to LDH/101...	113
III.3.2 Synthesis of Al-BDC and its conversion to NiAl-LDH/BDC.....	124
III.3.3 Conclusion.....	127
III.4 Conclusion	127
Chapter IV Synthesis of phosphate intercalated LDH/88A and its application: adsorption of lead ions in water.....	128
IV.1. Introduction.....	129
IV. 2. Materials and methods	131
IV. 2.1 Materials and characterization techniques	131
IV. 2.2 Synthesis method	131
IV. 3. Morphological and structural characterization	133
IV. 4 Pb ²⁺ adsorption properties of PO ₄ loaded LDH.....	139
IV. 4.1 Effect of pH.....	139
IV. 4.2 Kinetic study of Pb ²⁺ adsorption by LDH-PO ₄	142
IV. 4.3 Adsorption isotherms of Pb ²⁺ adsorption by LDH-PO ₄	146
IV. 4.4 Selectivity towards Pb ²⁺ /Ni ²⁺ /Cd ²⁺ adsorption.....	149
IV. 4.5 Insight in the Pb ²⁺ adsorption mechanism	151
IV.5 Conclusion	158
Chapter V Catalytic reactivity of LDH/88A and LDO/88A for the degradation of organic pollutants.....	160
V.1 Introduction	161
V.2. Application of LDH/88A catalytic PS degradation of BPA	165
V.2.1 Effects of light	165

V.2.2. Effect of peroxodisulfate $S_2O_8^{2-}$ (PS) concentration	167
V.2.3. Effect of catalysis concentration	169
V.2.4. Comparison with Ni_3FeLDH/COP and MIL-88A.....	171
V.2.5. Kinetic study.....	173
V.2.6. recycle experiment	174
V.2.7. catalytic mechanism exploration	175
V.3. Catalytic reactivity of $Ni_3FeLDO/88A$ for the degradation of BPA and structural characterizations of LDH catalysts.....	177
V.3.1 Catalytic reactivity of $Ni_3FeLDO/88A$ for BPA degradation activated by PS	177
V.3.2 Characterization of $Ni_3FeLDO/88A$	179
V.4. Conclusion.....	182
VI. Conclusion and perspectives.....	184
Annexes.....	187
Reference	199

Introduction

The manufacture of functional materials has long been recognized as a central topic in the energy and environmental fields [1]. The composition, morphology and structure of materials give them a wide range of properties to meet the needs of the target application. In particular, metal-organic frameworks (MOFs), which have a periodic structure with organic groups and metal centers as bridges, are becoming an alternative to conventional materials due to their versatile superiority [2]. Fundamentally, the large surface area and complex pore pattern favor the contact of MOFs with substances in most systems. Task specificity can be achieved by their easily adjustable structure. Self-templating derivatization can partially inherit the properties of MOF precursors, while chemical/thermal treatments will give them more diverse properties. A great deal of effort has been invested in the construction of MOF-derived metal oxides, carbides, or their composites by thermal treatment. Ultimately, the fragile organic framework is changed into a more robust carbon matrix with greater resistance to chemicals, currents, acids and bases [3]. As catalysts for energy and environmental applications, they present great opportunities and many breakthroughs. However, some morphological and structural properties are lost as the framework shrinks during thermal conversion. In addition, there is a risk of aggregation of periodically dispersed metal nodes, which hinders the fabrication of atomically dispersed metal catalysts [4]. It has been found that MOFs template-grown metal hydroxides can be chemically regulated to relatively avoid damage similar to that during pyrolysis [5]. Well-defined MOF-derived layered double hydroxides can be generated from in situ converted metal nodes by judiciously choosing the reaction temperature, time, and synthesis conditions.

Layered double hydroxides (LDHs), are composed of layers of divalent and trivalent metal hydroxides as well as anions in the interlayer/inter-lamellar domains, represented as $M_{1-x}^{2+}[M_x^{3+}(\text{OH})_2(\text{A}^{n-})_{x/n}]^{x+} \cdot m\text{H}_2\text{O}$ [6]. LDH is also considered as an optional material in many fields due to its highly tunable compositional properties and easy-to-apply laminate structure [7]. The large specific surface area, highly exposed metal sites and surface functional groups allow LDH to excel in catalysis and adsorption [8]. The inner cavity of the hollow layered double hydroxide material derived from MOF not only increases the loading capacity of the active material and unclogs the diffusion pathway, but also provides a buffer space for the volume expansion of the

active material, which is conducive to the sustainable utilization of the active material, thus effectively improving the overall stability of the active material [9].

On the other hand, with the continuous advancement of industrialization, a large amount of industrial wastewater containing a variety of inorganic and organic compounds has been generated, which has caused increasingly serious pollution of surface water and groundwater, giving rise to serious environmental problems and widespread concern [10]. Although most of these pollutants are found in low concentrations in wastewater, most of these pollutants pose a threat to aquatic organisms and thus to human health due to their significant bioaccumulation, very persistent environmental properties, potential toxicity to humans, and ecological safety [11]. For example, bisphenol A (BPA), which is used in the manufacture of epoxy resins and plastics, is suspected to be an endocrine disruptor that adversely affects the human immune system and the mammary glands at concentrations below critically toxic levels [12]. Similarly, various heavy metals such as Ba (II), Zn (II), Hg (II), Co (II), Cr (III), Pb (II), Fe (III) and Cd (II) are usually toxic, non-degradable and can not polymerize efficiently into macromolecular units, thus exacerbating the removal problem [13]. Among these toxic heavy metals, lead (Pb (II)) wastes are of greatest concern. Pb (II) is a common highly toxic, non-biodegradable, environmentally persistent and chronic neurotoxin associated with many cardiovascular and renal problems that enters water systems from different industrial activities [14]. Therefore, it is urgent to deal with the above pollutants.

Therefore, in this thesis, novel mesoporous layered double hydroxide materials with three-dimensional assembly were prepared by microwave-assisted topologically oriented transformation of "metal-organic frameworks" (MOFs) structures (MIL-88A, MIL-101) and the synthesis method was optimized. The study focused on $Ni_xFe/88A$ materials obtained by transforming MIL-88A (Fe) by ureolysis with Ni^{2+} ionization in a controlled alkaline medium and their derived oxides, as well as the possibility to extend the chemical composition to other metal cations. The mesoporous three-dimensional rod-like structures formed by intergrowth of $Ni_xFe/88A-X$ ($X = NO^-, Cl^-, PO_4^{3-}$) LDH nanoplates were obtained by ion-exchange and their ability to remove heavy metals was investigated.

In addition, the catalytic properties of these new Ni_xFe/88A-X materials and their calcined derivatives were investigated for the degradation of organic pollutants, in particular bisphenol A, by activated persulfate.

The present manuscript is organized as follows:

Chapter I is bibliography on MOFs and LDHs, which includes the structure, composition and properties of MOFs and LDHs. And the method of converting MOF to LDH and the application of MOF-derived LDH are elaborated.

Chapter II focuses on the synthesis of the materials: it includes a comparison of the synthesis of a typical iron-based MOF, MIL-88A, in different reactors, at different temperatures and times, and it explores the conditions for the conversion of MIL to LDH, and furthermore, the calcination of MIL-88A derived Ni₃Fe-LDH/88A to obtain Ni₃Fe-LDO/88A. The materials were characterized using IR spectroscopy, X-ray diffraction spectroscopy, BET and thermogravimetric etc. for characterization.

Chapter III explores the conditions under which MOF is converted to LDH. The roles of organic ligands, divalent metals, trivalent metals, MOF backbone metals, and etched metal cations are explored separately.

In Chapter IV, the heavy metal adsorbent Ni₃FeLDH/88A-PO₄ was prepared by inserting phosphate into the intercalation layer of Ni₃FeLDH/88A using ion-exchange. Not only the co-precipitated synthesized Ni₃FeLDO/COP-PO₄ was compared for adsorption efficiency, but also the adsorbents with different nickel-iron ratios were compared. Further, selective adsorption and adsorption kinetics and thermodynamics were investigated.

Chapter V, on the other hand, focuses on the ability of Ni₃Fe LDH/88A and Ni₃Fe LDO/88A to degrade the organic pollutant BPA in water. Similarly, co-precipitation synthesized Ni₃FeLDH/COP and Ni₃FeLDO/COP were used for comparison, including an examination of the effect of light, the rate of catalytic degradation, and the ability to recycle.

Finally, the manuscript will provide a general summary and outlook of this thesis work.

Details of the experiments and publication of the results can be found in the Appendix.

Chapter I

Bibliography

I.1. Overview of layered double hydroxides (LDHs)

Hydrotalcite is a natural mineral with a layered structure, representative of a large family of isostructural compounds, also named layered double hydroxides (LDHs) [15]. From the discovery of hydrotalcite in natural clay minerals by the Swede Circa in 1842 [16] to the present day, research related to LDHs has a history of more than one hundred years. However, the chemical composition of $[\text{Mg}_6\text{Al}_2(\text{OH})_{16}\text{CO}_3 \cdot 4\text{H}_2\text{O}]$ was not reported until 73 years later [17]. LDHs were first prepared in 1942 by Feitknight et al. using the reaction of solutions of magnesium chloride, aluminium chloride, etc. with hydroxides [18]. After the discovery of the base catalytic reactivity of LDHs at the beginning of the 20th century, the structure of them was gradually explored. Between 1968 and 1969, Allmann [19] and Taylor [20], for the first time, solved the layered structure of LDHs (Hexagonal lattice with rhombohedral symmetry; space group R-3m) by means of X-ray diffraction techniques, and pointed out that metal ions were statistically located in the octahedral sites of the CdI_2 like hexagonal layer, the anions and structural water molecules sitting in the interlayer sites.

Since the end of the 20th century, due to the continuous progress of experimental characterization methods and analytical techniques, the scope of research on the structure, properties, and applications of LDHs has become more and more extensive, and the structures and properties of their layers and interlayer guests have been largely explored [15, 21, 22]. LDHs are not only found in nature but can be easily prepared with wide range of chemical composition and properties. Therefore, it shows important application values in the fields of catalysis [23], energy storage [24], supercapacity [25], adsorption of pollutants [26], biology/pharmaceuticals vectorization [27], and nanocomposite materials such as flame retardants [28].

I.1.1. Structure and composition of LDHs

LDHs are a class of two-dimensional layered anionic clay materials. Their structure derived from the brucite-like structure $\text{M}^{\text{II}}(\text{OH})_2$, which consists of stacked hexagonal layers made of edge-sharing $\text{Mg}(\text{OH})_6$ octahedra [6]. Except that in LDH, part of the M^{II} divalent metal cations are replaced by M^{III} trivalent metal cations giving

rise to positive layers $[M_{1-x}M_x(OH)_2]^{x+}$ whose charge are compensated by intercalated hydrated anionic species $(A^{n-})_{x/n} \cdot m H_2O$. The chemical composition of LDH can then be expressed as $[M_{1-x}M^{III}_x(OH)_2]^{x+}[(A^{n-})_{x/n} \cdot m H_2O]$ [15, 29, 30], where M^{II} is a divalent metal cation such as Mg^{2+} , Ca^{2+} , Mn^{2+} , Fe^{2+} , Co^{2+} , Ni^{2+} , Cu^{2+} , Zn^{2+} , and M^{III} is a trivalent metal cation such as Cr^{3+} , Fe^{3+} , Al^{3+} , Ga^{3+} , and A^{n-} is a guest anion such as F^- , Cl^- , Br^- , I^- , NO_3^- , CO_3^{2-} , other organic (carboxylates, sulfates, sulfonates, phosphates, phosphonates), oxometallates and anionic complexes [31]. The substitution rate of M^{III} ($x = M^{III}/(M^{II} + M^{III})$), x , may vary between 0.33 and 0.20, i.e., when the molar ratio ($R = M^{II}/M^{III} = (1-x)/x$) ranges from 2-4 [32]. Fig. I-1 shows the ideal layered structure of LDHs, the surface hydroxyl groups (OH) bound the M^{II} and M^{III} cations in a μ^3OH coordination mode, and the guest anions are uniformly arranged with water molecules in the interlayers domains [33-35].

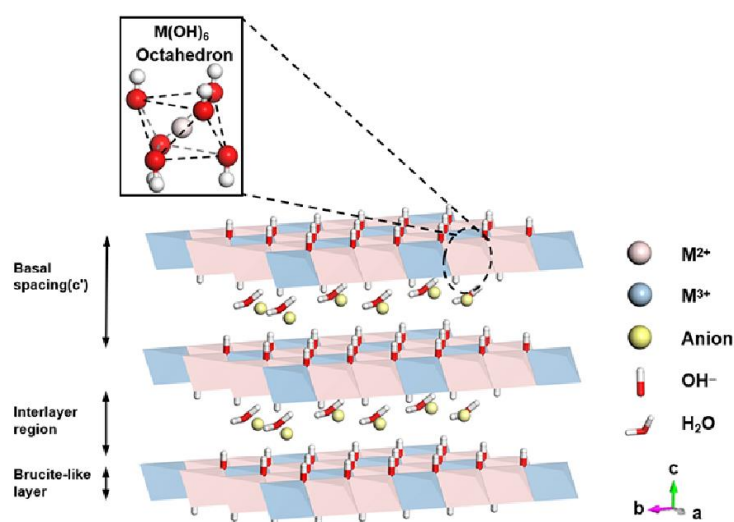


Fig. I-1 Schematic representation of an ideal structure for LDH [36].

It is worth noting here that as research continues, chemical composition of LDHs extended to more than two M^{II} or M^{III} cations in the layer. For example, there have been many studies of layered containing three or more metal ions introduced into LDHs [37-39], increasing then the versatility of their properties. There are a variety of weak interaction forces such as van der Waals forces, electrostatic attraction, and hydrogen bonding between the hydrotalcite host and guest, and the interlayer water molecules combine with the OH on the layered or the interlayer guests in the form of hydrogen bonding that insure a great cohesion of the layer stacking [6].

I.1.2. Synthesis techniques for LDHs

I.1.2.1. Co-precipitation method

Co-precipitation is the most common method for synthesizing LDHs. This method involves the reaction of acidic cations (M^{II} , M^{III}) with an alkaline solution at constant or increasing pH (eq. 1).



Fig. I-2 illustrates the experimental device for a co-precipitation at constant pH. By carefully regulating the degree of supersaturation of the solution, and then controlling the nucleation and crystal growth, it becomes possible to control the purity of the phase and the particle size and shape of the synthesized LDHs. Moreover, co-precipitation, allows to fine-tune the structure of the material by manipulating the M^{II}/M^{III} molar ratio, selecting the appropriate interlayer anion, adjusting the synthesis duration, maintaining appropriate temperature, and controlling the pH of the solution [40]. It is crucial to control the pH of the solution during co-precipitation. Insufficiently low pH levels impede the complete precipitation of all metal ions, whereas excessively high pH levels result in the solubilization of one or more metal ions.

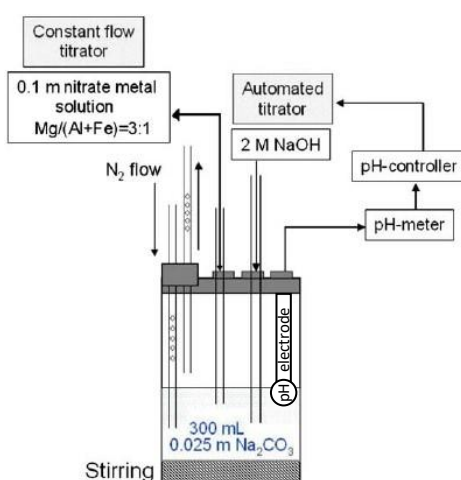


Fig. I-2 Scheme of the co-precipitation device used for LDH synthesis [41].

Co-precipitation synthesis is considered efficient for obtaining crystalline materials, mainly due to the relatively long synthesis duration (several days of addition and aging steps), the careful control of pH during synthesis, and the inclusion of supplementary treatments such as hydrothermal treatment [42]. However, it is worth noting that under typical conditions ($[\text{Mg}^{2+} + \text{Al}^{3+}] = 1\text{M}$, $\text{Mg}^{2+}/\text{Al}^{3+} = 2$, $[\text{OH}^-] = 2\text{M}$, addition time of 6 h, $\text{pH} = 10.0$, aging 24 h, $T = 25\text{ }^\circ\text{C}$), the resulting $\text{Mg}_2\text{Al-Cl}$ LDH particles have size in the range 300 to 500 nm, resulting in relatively small specific surface area values ranging from 30 to 70 m^2/g .

I.1.2.2. Microwave-assisted Co-precipitation method

Conventional methods of materials synthesis have changed dramatically with advances in technology and are rapidly being replaced by non-conventional synthesis methods. Among the non-conventional methods, the precipitation assisted by microwave irradiation has demonstrated increase in synthesis performances, increase in synthesis yield and reaction rates, gain of time, resulting in highly crystalline products of high purity [43]. Microwave methods offer several advantages, such as shorter reaction times and new physicochemical properties of the resulting materials. For example, microwave-assisted synthesis of Al-embedded clays has a higher surface area and shorter synthesis time than Al-inserted clays synthesized by conventional methods [44]. During microwave processing, microwave energy penetrates the material. Some of the energy is absorbed by the molecules and atoms and converted into heat by motion, which in turn raises the temperature of the material, the inner parts of the material being hotter than its surface, which dissipates more heat to making the surroundings. This property has the potential to heat large portions of the material uniformly. Using microwave heating does offer a number of advantages. These include rapid heating of the material without overheating the surface; removal of gases from porous materials without cracking; improved product quality and yield and synthesis of new materials and composites [45]. Crystallization is faster when LDH is synthesized using microwave irradiation. More precisely, it is applied to the aging of slurries obtained by the precipitation method [46].

Pokhriyal et al. found that irradiating a mixture of LiAlH_4 and the corresponding acid with microwaves for a few minutes rapidly produced a series of $\text{LiAl}_2(\text{OH})_6\text{X}_{0.5}\cdot n\text{H}_2\text{O}$ LDH compounds intercalated with the anions of aliphatic dicarboxylic acids (X: oxalate, malonate, succinate, glutarate, adipate, and sebacate). The microwave-assisted reaction of ethylene glycol with $[\text{LiAl}_2(\text{OH})_6]\text{OH}\cdot 2\text{H}_2\text{O}$ favour the intercalation of organic anions that are not easy to intercalated [47]. The specific operation is shown in the Fig. I-3.

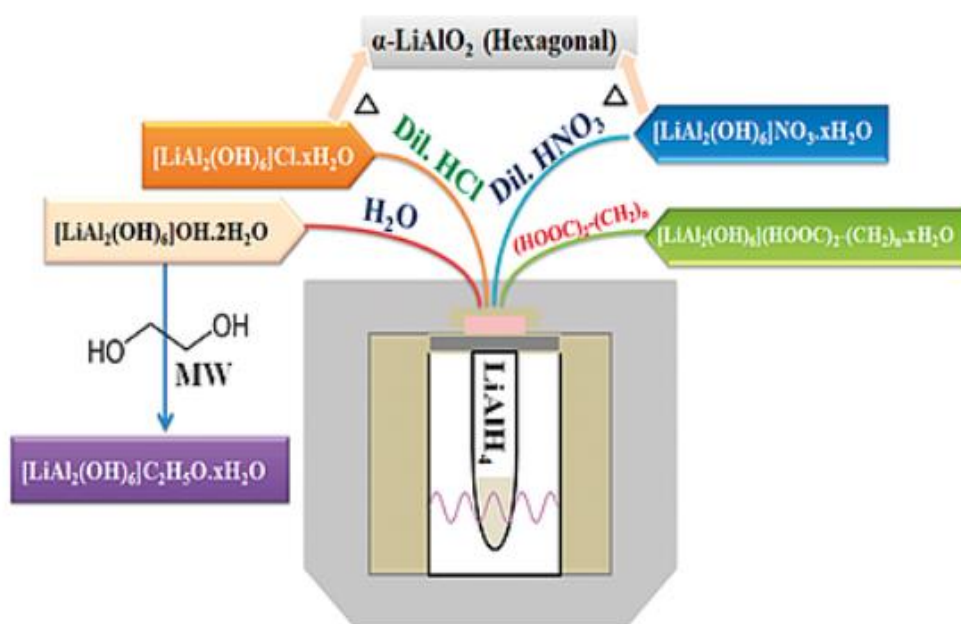


Fig. I-3 Scheme of LDH synthesis by microwave method [47].

Dileep Kumar Yadav et al. extended this method to the synthesis of Li-M-Al LDHs (M = Mg, Co, Ni, Cu, Zn, and Cd) containing three metals (Fig. I-4) [48]. Zhou et al. synthesized 3D novel flake-like flower morphology of NiCo-LDH by microwave heating and applied it to supercapacitors [49]. Leila Jafari Foruzin et al. provide a fast and simple method to improve the photoluminescence properties of lemon yellow/Zn-Al-LDH and lemon yellow/Mg-Al-LDH. The proposed hybrids were synthesized by inserting lemon yellow dye into Zn-Al-LDH and Mg-Al-LDH using a microwave-assisted method. The emission intensity was also improved due to its high crystallinity and uniform nanoplatelet size as compared to the pure dyes and similar hybrids (lemon yellow/Zn-Al-LDH-c and lemon yellow/Mg-Al-LDH-c) prepared using the co-precipitation method.

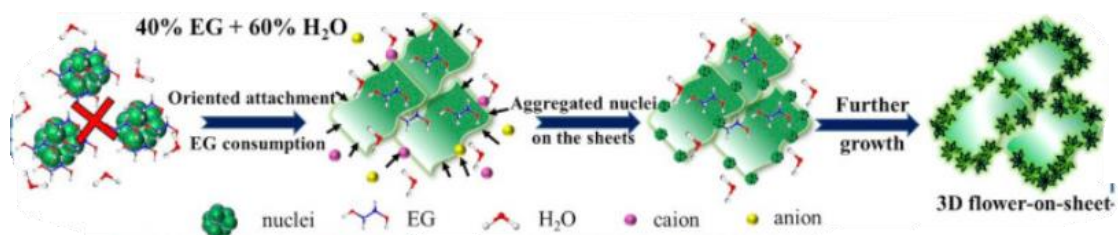


Fig. 1-4 Scheme of MW-assisted synthesis method for 3D petal-like shape LDH [48].

I.1.2.3 Urea hydrolysis

Urea is a weak Brønsted base, extremely soluble in water. It can be used as a precipitant instead of sodium hydroxide to raise the pH by its thermal decomposition. A slow decomposition starting at about 60 °C leads to a progressive increase of pH up to 10 [50]. Since urea decomposes slowly, it leads to a lower degree of supersaturation. Moreover, prolonged hydrolysis results in the formation of CO_3^{2-} anions in basic medium (eq.2). Thus, urea decomposition can effectively control pH and form monodisperse LDH materials with high crystallinity [51].



Nevertheless, the decomposition of urea results in the formation of CO_2 , which reacts with water to produce carbonates, serving as compensating anions displaying a strong affinity with the LDH layers [52]. In such cases, an additional acidic-assisted anion exchange may be necessary to replace carbonate anion, depending on the specific application being targeted [53]. The purity and crystallinity of LDH phases can be enhanced by adjusting the $\text{M}^{\text{II}}: \text{M}^{\text{III}}$ molar ratio, the concentration of urea, the temperature of decomposition, and the duration of aging [54]. Urea hydrolysis is a gradual process resulting in a limited degree of supersaturation during precipitation. This method offers the advantage of generating sizable and thin platelets with a more focused particle size distribution within a shorter aging period compared to co-precipitation [55]. Moreover, urea method is a low-cost method.

Combining thermal activation of urea decomposition and microwave irradiation increases further the precipitation efficiency and crystallinity of the as-prepared phases.

Ni-Al LDH have been synthesized by microwave-assisted urea decomposition, and pure hydroxalcite-type phase has been obtained in a very short period of time [56].

I.1.2.4 Hydrothermal post-synthesis treatment

The synthesis of LDH by co-precipitation, sol-gel method or urea hydrolysis can be optimized by a hydrothermal treatment to increase the crystallinity and the size of the microcrystals, as described previously [57]. The treatments are usually carried out under mild hydrothermal conditions up to 200 °C and autoclave pressure for durations ranging from few hours to few days. Fig. I-5 shows the hydrothermal synthesis process.

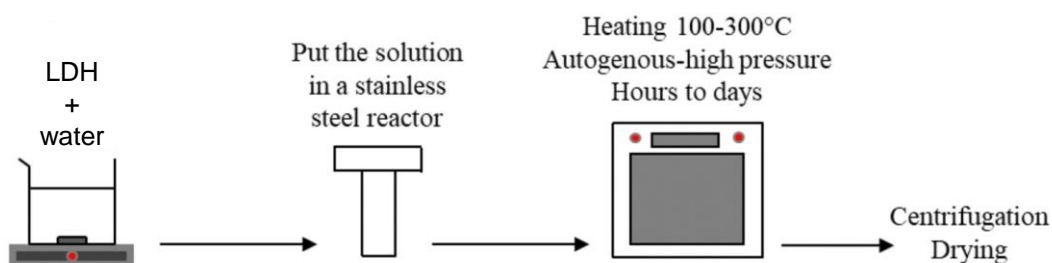


Fig. I-5 Scheme of the hydrothermal post-treatment method applied to LDH [57].

This method, generally performed in water, is typically done at moderate temperatures (30 - 300 °C) and steam pressure, with varying synthesis times ranging from a few hours to several days [58]. It involves a dissolution reprecipitation process. The advantage of using this synthesis process is the obtention of LDH with higher crystallinity, particle with microcrystalline size and high purity of the samples. Unfortunately, the longer synthesis time (from hours to days) is a disadvantage of the industrial implementation of the hydrothermal treatment.

I.1.3 Properties of LDHs

LDH is family of 2D materials with unique properties.

- (1) The compositional and structural versatility of LDHs is a key aspect worth highlighting. These materials exhibit a remarkable adaptability in their structure, characterized by the general formula $[M^{II}_{1-x}M^{III}_x(OH)_2]^{x+}[(A^{n-})_{x/n} \cdot mH_2O]$. This

formula allows for flexible adjustments in several parameters: the choice of metals within the layers, the ratio of these metals, and the type of anion occupying the interlayer spaces. Such adjustments can be tailored according to specific application requirements. Moreover, these variations profoundly impact the chemical and electronic properties of the layered structure, enhancing its utility across a wide range of contexts [59]. Thus, a wide variety of hydrotalcites with different properties can be prepared.

- (2) Exchangeability of interlayer anions. The LDH materials display high anion adsorption capacities with tunable values, from 257 to 358 cmol/kg for Mg_4Al-Cl and Mg_2Al-Cl respectively [60]. The interlayer anions can be replaced by other anions because the body lamellae of LDHs bind with weak interactions with the interlayer guest anions [61]. The interlayer anions of LDHs can be exchanged by a variety of anions, such as simple inorganic anions like CO_3^{2-} , SO_4^{2-} and other simple inorganic anions, organic anions such as $C_{18}H_{29}SO_3^-$ or $HOC_6H_4CO_2^-$, and metal complexes anions, etc [62]. By utilizing this feature of LDHs anion exchange, a variety of functional LDHs-based materials with anionic intercalation can be synthesized, and thus the prepared LDHs composites are also functional.
- (3) In addition to anion exchange properties, LDHs display adsorption properties, physisorption or chemisorption, through van der Waals or hydrogen bonding, for a large series of neutral or polar molecules. These adsorption properties depend on the surface charge of the platelets, which in turn depends on the M^{2+}/M^{3+} ratio and anion charge. The zeta potential (ζ) and the point of zero charge (PZC) are parameters that determine the adsorption properties. Any modification of the surface will result in a strong change of ζ , and PZC, e.g., for example after adsorption of lactate dehydrogenase (*ldh*), $Mg-Al-CO_3/ldh$, PZC can be as high as 12-12.5 [63]. LDH materials can also adsorb metal cations. As an example, with the intercalation of SO_4^{2-} and PO_4^{3-} anions, the adsorption capacity of LDHs for Cd^{2+} increased by an order of magnitude (up to 19.2 times) compare to the Cl^- precursor [64].

Topological transitions and structural memory effects. A topological transition is a reaction or transformation in which the product phase and the reactant phases exhibit one or more crystallographic invariance [65]. Some LDHs can undergo a topological

transformation under calcination-rehydration process, allowing the calcined LDH to reconstruct the original LDHs layered structure when exposed to air or contacted with aqueous solutions containing anions under certain conditions [66]. Zhang et al. [61] used a combination of theoretical and experimental simulations to model the topology of Mg₂Al-CO₃-LDH at different temperatures. They found that at 330 °C, the interlayer guest anions decompose in the interlayer of LDHs, but their layer structure remains basically unaffected by the decomposition while at 800 °C, the layered structure of LDHs undergoes a complete collapse and recrystallization into a mixture of M^{II}O and spinel M^{II}M^{III}₂O₄ oxides. Topological transformations of LDHs are important for the preparation of metal/metal oxide catalysts derived from LDHs as precursors, and can be used for the trapping of hazardous anions in wastewater as well as for the synthesis of other functional anion-inserted LDHs materials [67].

I.2 Overview of Metal Organic Framework (MOF) materials

I.2.1 Structure, composition and morphology of MOF

I.2.1.1 Definition and classification of MOF

According to the definition of Union of Pure and Applied Chemistry (IUPAC) A Metal-Organic Framework, abbreviated to MOF, is a coordination network with organic ligands containing potential voids [68]. MOFs consist of organic and inorganic components. They are synthesized from secondary building units (SBU), metal cations salts or clusters, and polydentate organic ligands (bridging ligands/joints) including carboxylic acids or anionic conjugate bases, such as organophosphorus compounds, sulfonates, and heterocyclic compounds, with coordination-type connections [69-71]. Their structures are flexible and can be tuned varying the nature of the metal cation and linkers and by post-synthesis modification (PSM) [72]. MOF constructions and applications have been pioneered and emphasized in the 1990s by the groups of Robson [73], Moore [74], Yaghi [75], Kitagawa [76], and Férey [77]. The general synthesis process is shown in the Fig. I-6 [78].

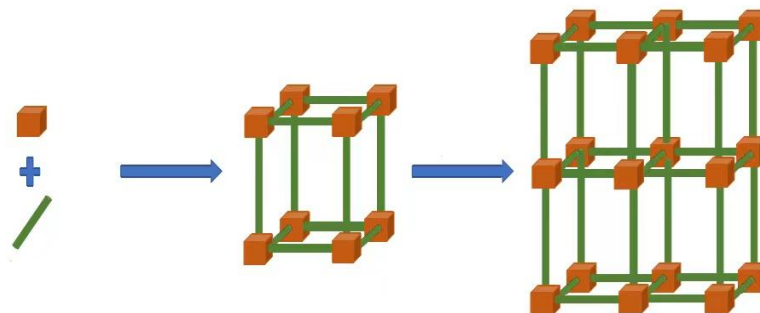


Fig. I-6 Schematic diagram of synthesis process for MOFs [78].

In 1995, Yaghi et al. [75] synthesized the first reticulated metal-organic skeleton materials (IRMOFs-MOF-5) and described the concept of MOFs, and the discovery of MOF-5 further proved that "the effective pore size of microporous molecular sieves can break 12 Å". In 1997, Kitagawa et al. [79] reported for the first time metal-organic framework materials for reversible gas adsorption and desorption. In 1999, Yaghi et al. [80] prepared the microporous structured metal-organic framework material $\text{OZn}_4(\text{R1-BDC})_3(\text{MOF-5})$. Based on the preparation of this compound, many porous coordination polymers with the same topology (IR-MOF-n) could be prepared by changing the type of organic ligand R groups (Br, NH_2 , C_2H_4 , C_4H_4 , OC_3H_7 and OC_5H_{11}). In addition, these MOFs exhibit good adsorption and thermal stability for gas storage applications. The above results lay a solid foundation for the theoretical study and the controlled preparation of metal-organic frameworks (MOFs).

Depending of the nature of both organic and inorganic components, MOFs can be further classified into different subgroups based on their constituent units [81].

- (i) Zeolitic Imidazolate Frameworks (ZIFs) are synthesized using various metal cations and imidazole derivatives. They are zeolite topological materials. ZIFs comprise ZIF-8, ZIF-90, ZIF-L, ZIF-71, ZIF-67, ZIF-7, etc. [82].
- (ii) Porous coordination networks (PCNs) are stereo-octahedron materials, and they have a hole–cage–hole topology with a 3D structure. Some of the PCNs are PCN-333, PCN-224, PCN-222, and PCN-57 [81].
- (iii) Materials Institute Lavoisier (MILs) MOFs are synthesized using various elements that have valence electrons and an organic compound containing two carboxylic functional groups and developed by G. Férey's group. The pore size

arrangement of MIL could be converted freely under outward incitement. MIL MOF family contains MIL-101, MIL-100, MIL-53, MIL-88, MIL-125, etc. [81].

(iv) A University of Oslo (UiO) MOF based on dicarboxylic acid as the PBU and $Zr_6(\mu^3-O)_4(\mu^3-OH)$ as the SBU was first synthesized by Lillerud and co-workers [81].

I.2.1.2 Structure and composition of MOF

MOFs are specialized frameworks of porous crystalline materials with different sizes and topologies obtained based on the geometry of the metal ions and the binding mode of the bridging ligands [83]. Depending on the structural dimension, MOFs can be categorized into species with objects and species without objects (Fig. I-7). In a one-dimensional (1D) MOF, the ligand bonds are distributed across the polymer in one direction, while the possible voids are accommodated by small molecules. In 2D MOFs, single types of layers are stacked together by edge-to-edge or interleaved stacking, with weak interactions between layers. Modifications to the ligands that make up the layers allow control over the stacking method and the functionality within the channel. There are two possibilities for the accommodation of guest molecules in a two-dimensional structure:

- (i) the space between the layer grids;
- (ii) the space between the layers.

In 3D MOFs, the frameworks are highly porous and stable due to the distribution of coordination bonds in three directions. Three-dimensional columnar layers and lattices appear in most MOFs. The non-covalent nature of π - π stacking bonds and hydrogen bonds facilitates the connections between the building units (one-, two- and three-dimensional frameworks). The involvement of these interactions not only transforms the framework into an infinite high-dimensional network, but also controls its strength and orientation.

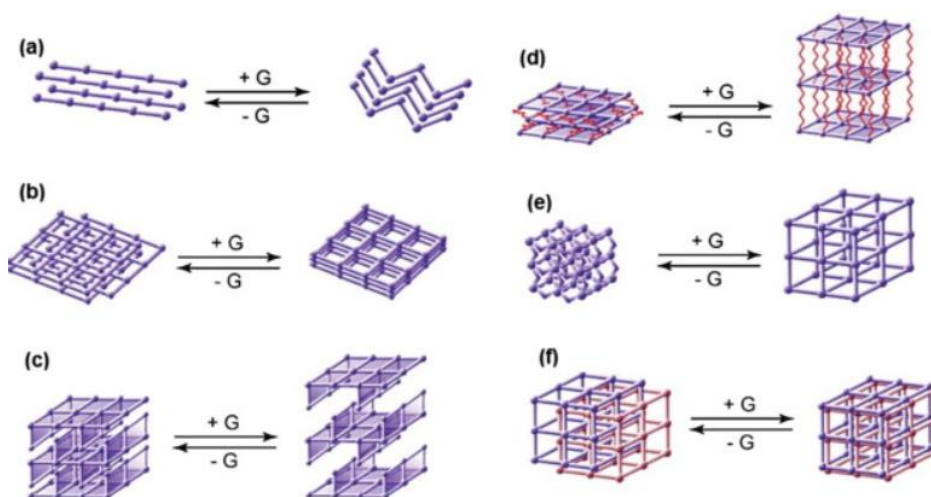


Fig. 1-7 Perspective view of dimensionality: (a) 1D chains, (b) 2D stacked layers, (c) 2D interdigitated layers, (d) 3D pillared layers, (e) 3D expanding and shrinking grids and (f) 3D interpenetrated grids, G = Guests [84].

MOFs structures contain nodes formed by clusters of inorganic units called PBUs (Primary Building Units) or clusters of metal cations called SBUs (Secondary Building Units) attached to organic polydentate ligands [85]. Due to the relatively strong ligand bonds between the metal and the ligand, well-defined porous crystal structures can be formed that remain stable even after removal of the solvent [69] (which is usually required during the synthesis phase). However, this is not always the case and many MOFs, especially those with high porosity, are very fragile and sensitive to how the solvent is removed. The most commonly used elements in the nodes are transition metals such as Zn, Cu, Fe, Cr, Co, Ni, V, Sc, and Y, but alkaline earth metals (e.g., Mg, Ca, Sr, Ba, Ra), base metals of the main group of the Periodic Table (e.g., Sn or Al), and/or rare earth metals (e.g., lanthanides) are also used [86]. Organic ligands (also known as linkers) are another essential component of the MOF structure. o-type (e.g., phosphonates, carboxylates, sulfonates) or n-type (e.g., thiazines, pyridines, imidazoles) donors are the most commonly used classes of linkers [87] (Fig. I-8). MOFs are constructed by linking metals or metal clusters (also known as secondary building units, SBUs) with organic linkers, which are mainly carboxylic acids or nitrogen-containing ligands [88]. Some representative SBUs and organic linkers are shown in Fig. I-9.

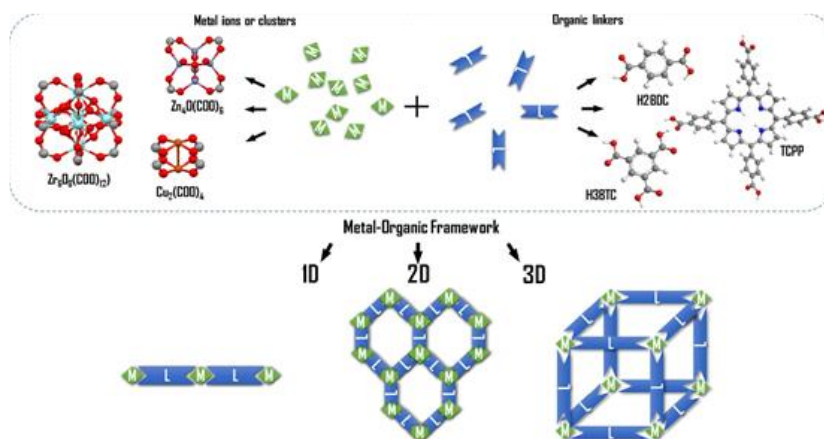


Fig. I-8 A generic scheme for the preparation of 1D, 2D and 3D MOF structures, with examples of metallic units called PBU (Primary Building Unit) (for example, Cu (II), Zn (II) and Zr (IV)) or clusters of metal cations named SBU (Secondary Built Unit)

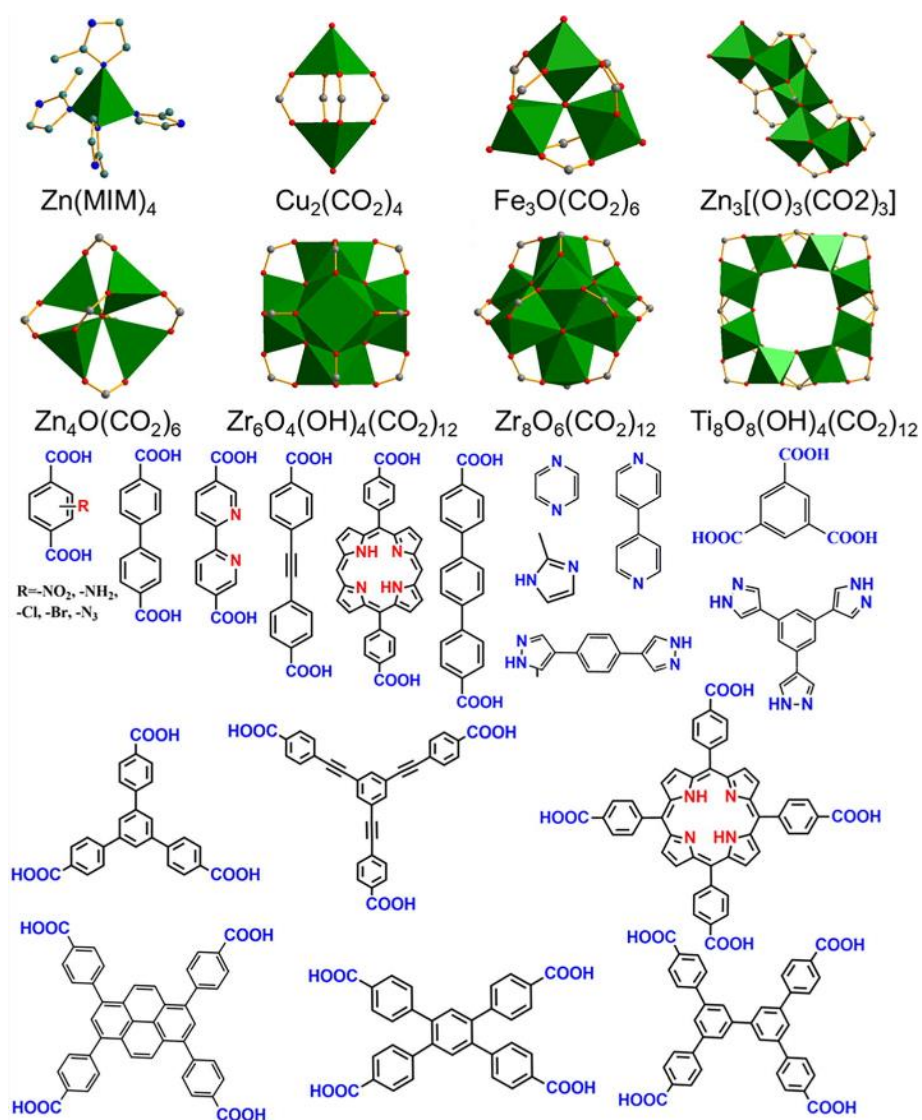


Fig. I-9 Some representative organic linkers for SBUs and MOFs.

MOFs can be tuned to some extent by judicious selection of SBUs and joints to give them the pore size, structure and function required for a particular application. As a representative example, Yaghi et al. demonstrated that by systematically elongating the ligand structure, an iso-reticulated series of MOF-74 structures (IRMOF-74-n) can be produced [89]. The defined structure of MOFs makes it possible to study the structure-property relationship, which is essential for the rational design of novel MOFs with desired functional applications.

I.2.1.3 Designable morphology of MOF

The anisotropy of MOFs allows for the controlled growth of specific crystal planes, which in turn allows for the control of MOF crystal size. To date, many structurally diverse MOFs have been described in the literature, including spheres, cubes, cuboids, cuboids, octahedrons, rods, filaments, sheets, and complex layered structures (e.g., flowers) (Fig. I-10).

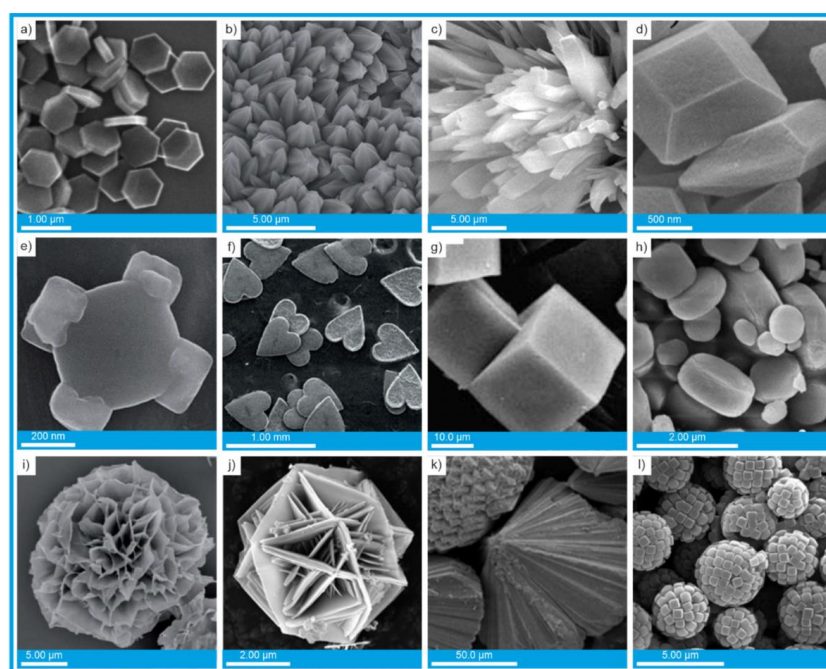


Fig. I-10 Various morphologies of MOF.

The use of monodentate additives modulates crystal growth by affecting the coordination equilibrium between metal ions and organic linkers (Fig. I-11). Modulating agents compete with multivalent linkers for metal coordination sites during

nucleation and crystal growth, thereby modulating the rate of framework extension and crystal growth [90]. Competitive coordination of modulating reagents can regulate (hinder) the rate of crystal growth, allowing more nuclei to form [91]. Additionally, the moderating agent slows down the precipitation of amorphous material, thereby increasing the crystallinity of the MOF [90], and physically prevents crystal aggregation, which can lead to anisotropic growth [90]. This approach allows control over the size (Fig. I-11a) and morphology (Fig. I-11b) of the resulting crystals. As a result, smaller and relatively uniform nanoparticles of different shapes can be formed. Typically, additives (e.g., monocarboxylic acids or salts) with the same chemical function as the linker are used to control the crystal size and morphology.

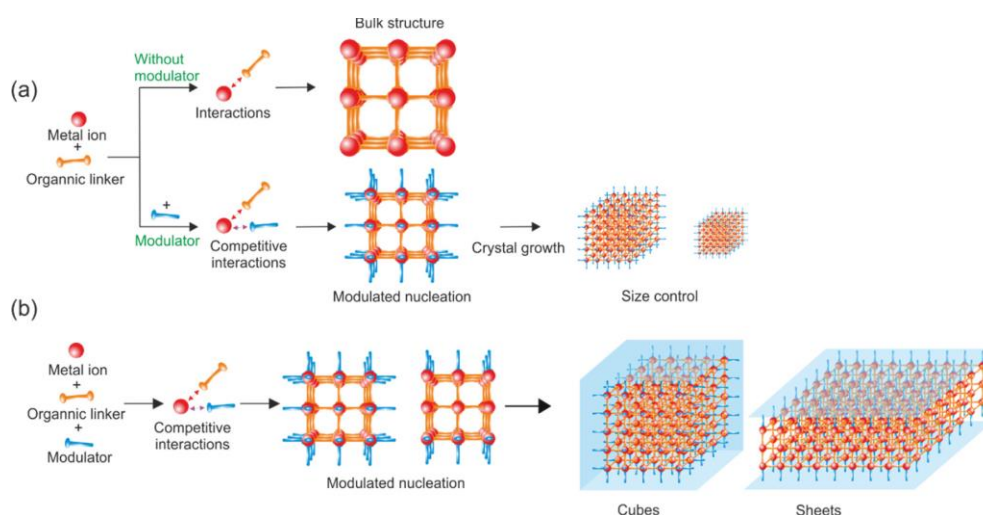


Fig. I-11. Schematic showing the coordination modulation method used to obtain metal-organic frameworks. (a) Control of MOF's size and (b) morphology is usually achieved by adding a reagent with the same chemical functionality as the linker [92].

Alkaline modifiers increase the pH of the reaction system, promote deprotonation of the linker, and provide more organic anions to coordinate the metal cations. These phenomena accelerate the rate of crystal nucleation (Fig. I-12). As a result, smaller structures (even nanocrystals) and sometimes altered morphology are possible due to the rapid decrease in supersaturation of the reaction system [93]. Nevertheless, a proper acid-base equilibrium is essential to regulate the nucleation rate and to obtain thermodynamically favorable MOF single crystals.

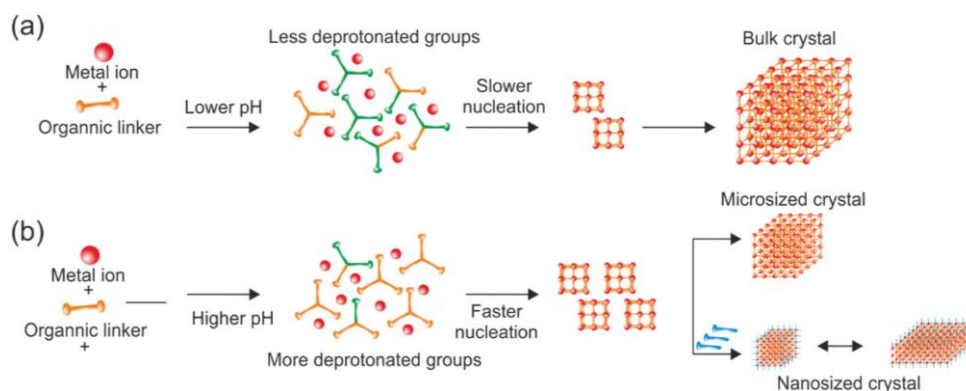


Fig. I-12 Protonation/deprotonation mechanism used to control morphology of metal-organic frameworks [92].

One particular additive used to modulate crystal morphology is surfactants. Adsorption of amphiphilic compounds on crystal surfaces plays a key role in changing crystal morphology and controlling particle size (Fig. I-13). Depending on the affinity (interaction energy) of the surfactant for a particular crystal surface, the adsorption of the additive is either strong or weak. This can lead to faster growth on one crystal surface and slower growth on the other, making it more difficult or easier for reactants to attach to the surface. Thus, the addition of surfactant affects the shape and size distribution of the product. In addition, amphiphilic compounds can aggregate in water and some other solvents to form nanostructured soft matrices.

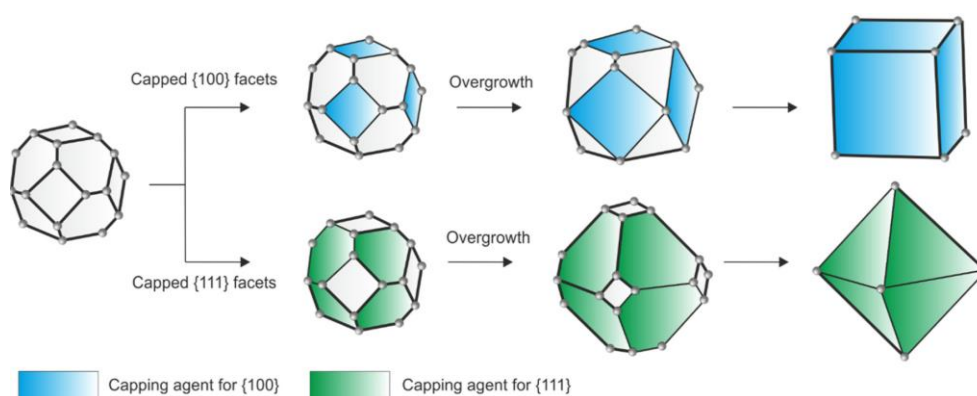


Fig. I-13 Morphology control of metal-organic frameworks by adsorption of surfactants on specific facets [92].

I.2.2 Synthesis of MOFs

I.2.2.1 Factors affecting the synthesis of MOFs

The synthesis of MOFs is affected by a variety of external factors such as the choice of organic ligands, metal ion salts, molar ratios, pH, solvents and temperature of the reaction medium [94]. Organic ligands can be classified into various types based on their coordination groups, including carboxylic acid-based linkers, nitrogen-containing heterocycles, phosphoryl and sulfonyl linkers, and cyano linkers. Carboxylic acid-based linkers are one of the various types of organic linkers, and they are often selected as multifunctional organic linkers because they have many coordination nodes that can act as hydrogen-bonding acceptors and donors for metal ions, thus allowing the assembly of MOFs structures with various structural topologies [95]. Heterocyclic linkers containing an N atom have a unique coordination pattern, which improves the structural control of the target compound [96]. In addition, positional isomerism of ligands with the same coordination group but located at different positions can also have a significant impact on the structure of MOFs. For example, the aromatic dicarboxylic acids H₂IPA and H₂TPA both have a tendency to bind and are involved in controlling the structural assembly of MOFs [97].

The choice of metal salts plays an important role in the synthesis of MOF structures. For instance, [Cu₃(BTC)₂] was prepared by using two different metal salts Cu(OAc)₂ and Cu(NO₃)₂ and H₃BTC as the organic linker. The result revealed that Cu(OAc)₂ was favourable for the preparation of [Cu₃(BTC)₂] with a high surface area [98]. In addition, the topology of MOFs can be predicted by tuning the coordination patterns of metal ions and organic ligands; moreover, the presence of numerous metal ions connected through various coordination ligands usually enhances the stability of MOFs. Metal ions are the construction nodes of MOFs and have a direct impact on the structure of MOFs through their coordination geometry.

The concentration (molar ratio) of precursors is also an important factor in the synthesis of MOFs. The topology of MOFs depends mainly on the ratio of metal ions to organic linkers [94]. Liu and co-workers explored the effect of the metal to linker molar ratio on the synthesized MOF structure by using CoCl₂ and btze [99]. The result

showed that the initial materials with a molar ratio of Co (II)/btze of 1: 1 or 1: 1.5 form 2D $[\text{Co}(\text{btze})_2(\text{SCN})_2]_n$ MOFs. When they used a molar ratio of 1: 2 or more btze linker, a 3D $[\text{Co}(\text{btze})_2(\text{SCN})_2]_n$ MOF structure resulted. Organic linkers can adopt different coordination modes in different pH ranges [100]. In addition, the degree of deprotonation of the linker increases with increasing pH. For example, by increasing the pH, Al^{3+} were coordinated with 4, 6 and 8 -COOH groups to produce MIL-121 (pH = 1.4), MIL-118 (pH = 2) and MIL-120 (pH = 12.2), respectively [101]. Spectroscopic data showed that the MOFs formed an interpenetrating network at higher pH values, whereas there was no interpenetration at lower pH values [102].

Solvents play an important role in the synthesis and morphology of MOFs. Solvents act as structure-directing agents for coordination through metal ions (Fig. I-14). Therefore, solvents with polarity and higher boiling points are widely used for MOF synthesis. The commonly used solvents are DEF, DMF, DMSO, DMA, acetone, alcohol, acetonitrile and so on [103]. The MOF preparation process is influenced by the reaction medium due to the solubility, solvent polarity and protosolvation behavior of the organic ligands. Under the same reaction conditions, different solvents produce different forms [104].

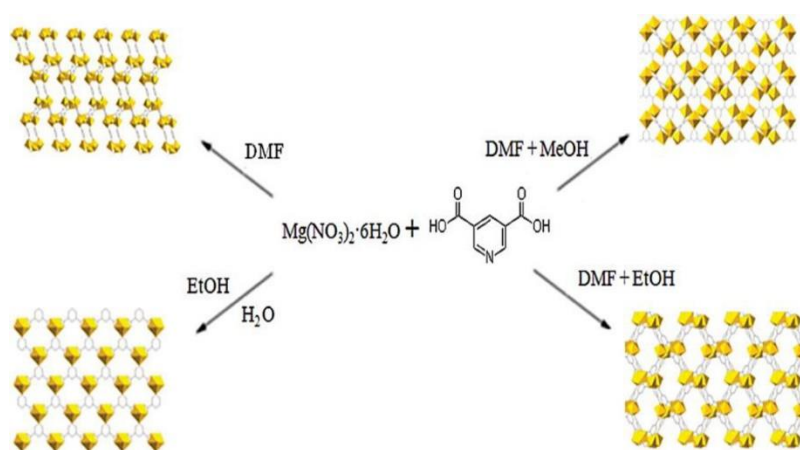


Fig. I-14 Influence of solvent systems on the morphology of the MOF [105].

Banerjee and co-workers reported Mg- and PDC-containing MOFs with different crystal structures prepared under the same conditions using different solvents [105] (DMF, H_2O , EtOH, and MeOH). They found that the dimension of the MOF network

depends on the solvent's ability to coordinate with the metal. Among them, H₂O is the most attractive to magnesium, while the other mixed solvents (EtOH: H₂O and DMF: MeOH) are unable to coordinate with the metal centers, suggesting that water as a solvent largely affects the formation of covalent bonds with metal ions.

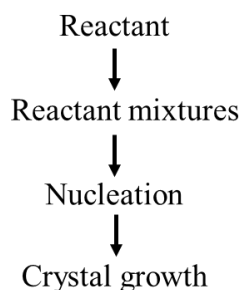
Temperature is another key factor affecting the properties of the synthesized MOFs. The material is highly crystalline at high temperatures due to the good solubility of the reactants and the production of large crystals with high superiority. The temperature of the reaction mixture is influenced by the rate of nucleation and crystal growth. As the reaction temperature changes, the morphology of the MOFs changes significantly, allowing it to be used in different applications [106]. Bernini and co-workers investigated the thermal stability of Ho-succinate MOFs prepared by hydrothermal method at both high and room temperatures, and the results showed that Ho-succinate MOFs prepared by hydrothermal method is more thermally stable than Ho-succinate MOFs prepared at room temperature [107].

I.2.2.2 Conditions of Synthesis of MOFs

The synthesis of MOFs is carried out in solvents at temperatures ranging from room temperature to approximately 250 °C. Energy is generally introduced using conventional electrical heating, through electric potentials, electromagnetic radiation, mechanical waves (ultrasound) or mechanical means. The energy source is closely related to the duration, pressure and energy per molecule introduced into the system, and each of these parameters can have a large impact on the products formed and their morphology. Different methods can produce compounds with different particle sizes and particle size distributions, as well as morphologies that may have an impact on material properties. However, many other synthesis methods and parameters must be considered, such as temperature, reaction time, pressure, pH and solvent. Many different synthetic methods, including slow diffusion, hydrothermal, electrochemical, mechanochemical, microwave-assisted, heating, and ultrasound can be used to produce MOFs based on the resulting structure and characterization.

1.2.2.2.1 Hydrothermal Synthesis

In hydrothermal methods [108], heterogeneous reactions are carried out under high temperature and pressure conditions in the presence of aqueous solvents and mineralising agents. Hydrothermal methods have traditionally been used for metal extraction and the generation of large crystals. In recent years, the advantages of hydrothermal technology in crystal engineering have been explored more. As far as MOFs are concerned, hydrothermal synthesis technology is respected for two reasons. The hydrothermal synthesis of metal-organic frameworks (MOFs) typically involves mixing solutions of metal ion salts and organic ligands in a solvent and maintaining the mixture at elevated temperatures (above 100 °C) for a specific period of time. The synthesis of MOFs involves the following steps: Firstly, solubility problems of heavy organic molecules can be minimised under experimental conditions. Secondly, the nucleation process can be initiated quickly to form rare complexes under the same experimental conditions [109, 110]. Under these conditions, the viscosity of the water decreases, favouring the mobile activity of the precursors. Under these conditions thermodynamically metastable phases of coordination networks or MOFs can be isolated. Crystal growth can be enhanced in a steel autoclave, which is placed in a programmable hot air oven and operates at temperatures below 300 °C with a retention time. The two ends of the vessel are kept at different temperatures, with the warmer end dissolving the components and the nucleus starting to grow at the cooler end [111]. The hydrothermal synthesis of metal-organic frameworks (MOFs) typically involves mixing solutions of metal ion salts and organic ligands in a solvent and maintaining the mixture at elevated temperatures (above 100 °C) for a specific period of time. The synthesis of MOFs involves the following steps:



The synthesis process of MOFs is carried out at high temperatures in order to obtain high crystal yields in an acceptable time. Variables in the synthesis process include temperature, pH and chemical composition of the reactants. To obtain nano-sized

particles, surfactants or molecular templates are often used. For example, ZIF-8 crystals can be turned into cubes in the presence of cetyltrimethylammonium bromide (CTAB) [112]. A series of iron-based MOFs, including MIL-53, MIL-88A, MIL-88Bt, MIL-100 and MIL-101-NH₂, have been synthesized by hydrothermal or solvothermal methods by P. Horcajada et al [113].

I.2.2.2.2 Microwave-Assisted Synthesis

Microwave-assisted synthesis relies on the interaction of electromagnetic waves with moving charges. These charges can be polar solvent molecules/ions in solution or electrons/ions in a solid. In a solid an electric current is formed and heating is due to the resistance of the solid. In a solution, polar molecules try to align themselves in the electromagnetic and oscillating fields so that the molecules permanently change direction. Therefore, using the appropriate frequency, collisions between molecules occur, resulting in an increase in the kinetic energy (i.e. temperature) of the system. Due to the direct interaction of the radiation with the solution/reactants, MW-assisted heating is a very energy-efficient heating method. As a result, high heating rates and uniform heating can be achieved throughout the sample. Care must be taken to select appropriate solvents and selective energy inputs, as the starting material may interact strongly with the MW radiation. Microwave ovens suitable for materials synthesis monitor temperature and pressure during the reaction, allowing more precise control of the reaction conditions. MW-assisted MOFs synthesis focuses on (1) accelerated crystallization, (2) formation of nanoscale products, but is also used to (3) improve product purity, and (4) selective synthesis of polycrystals.

A number of metal (III) carboxylate-based MOFs (M = Fe, Al, Cr, V, and Ce) were prepared by MW-assisted synthetic routes. The first MOFs synthesized by the MW method were Cr-MIL-100 [114]. The compound was synthesized in 4 h at 220 °C under MW irradiation in 44% yield, which is comparable to the yield of conventional heating synthesis. Similar iron compounds were prepared at 200 °C in 30 min. A systematic study showed the influence of composition and process parameters on the formation of nanoscale Fe-MIL-88A, where only MW-assisted hydrothermal synthesis ensured rapid synthesis of small (<100 nm), monodispersed nanoparticles in high yields [115]. In situ and time-resolved in situ crystallization studies were carried out for Fe-MIL-53 [116] and CAU-1-(OH)₂ [117], respectively. In both cases, MW irradiation

resulted in a faster reaction rate compared to conventional heating. There are few reports on the molecular aqueous solution-assisted synthesis of azide resin-based MOFs. Dodecahedral shaped imidazolium salt-based ZIF-8 crystals (~20 µm) were synthesized at 140 °C in 4 h [118]. The ZIF-8 crystals obtained by MW irradiation showed a larger specific surface area compared to the material synthesized under CE heating conditions. Thin films of ZIF-7 and -8 were also prepared by using MW radiation. In a report on ZIF-8, a dense, crack-free film was deposited on bare titanium by direct growth [119].

I.2.2.2.3 Electrochemical method

Instead of using metal salt solution, electrochemical synthesis involves the continuous introduction of metal ions into the reaction medium by anodic dissolution, which contains dissolved linker molecules and conductive salts. The use of a proton solvent avoids metal deposition on the cathode, but H₂ is produced in the process. Another approach is to use preferentially reducing compounds such as acrylonitrile, acrylates or maleates [120]. It is possible to prepare products containing small amounts of MOFs and obtain quantitative yields in a short time (10-16 min) [121]. In addition, water is an unifacial product produced from metal oxides and is used as a substitute for metal salts in some cases. On the other hand, the low solubility of metal oxides leads to their rare use in solvent-based reactions. The use of organic reactants with low melting points and hydrated metal salts, especially those containing essential anions, appears to be useful.

I.2.2.2.4 Sonochemistry method

Sonochemistry involves chemical reactions that occur using high-energy ultrasound waves on reaction mixtures. Chemical reactions in homogeneous liquids may occur in cavities (harsh conditions), at interfaces (intermediate pressures and temperatures), or in bulk media where there are strong shear forces. Under harsh conditions and strong shear, free radicals with additional reactions, bond breaking, and molecular buildup in excited mode may occur. Synthesis of organic and nanomaterials is carried out through a wide range of applications of sonochemistry. In the synthesis of MOFs, the main goal of sonochemical synthesis is to design a method that is fast, environmentally friendly, energy efficient, easy to use and can be applied at ambient

temperatures [122]. Some MOF synthesis methods as well as parameters are shown in Table. I-1.

Table. I-1. Representative MOF synthesis studies

Method	Sample	Metal	Ligand	Synthesis conditions		Comments	Ref
				Solvent	Condition		
CS	MOF-5	Zn(NO ₃) ₂ ·4H ₂ O	H ₂ BDC	DMF /chlorobenzene	120 °C, 24 h	Isorecticular MOF (IRMOF-n) synthesis, methane storage (25 °C,40 bar).	[123]
	UiO-66	ZrCl ₄	H ₂ BDC	DMF	120 °C, 24 h	H ₂ (-196 °C,1 bar) and CO ₂ (0 °C,1 bar) adsorption.	[124]
	Cr-MIL-101	Cr(NO ₃) ₃ ·9H ₂ O	H ₂ BDC	H ₂ O (add 1 M HF aq.)	220 °C, 8 h	Structure analysis.	[111]
	IRMOF-3	Zn(NO ₃) ₂ ·4H ₂ O	H ₂ BDC-NH ₂	DEF	85 °C, 96 h	CO ₂ adsorption (25 °C, 1-40 bar).	[125]
	Al-MIL-53-NH ₂	Al(NO ₃) ₃ ·9H ₂ O	H ₂ BDC-NH ₂	DMF	130 °C, 5 days	CO ₂ pressure swing adsorption (50°C, 20 bar).	[126]
	HKUST-1	Cu(NO ₃) ₂ ·3H ₂ O	H ₃ BTC	H ₂ O/EtOH	180 °C,12 h	Structure analysis.	[127]
	Fe-MIL-100	Metallic iron (Fe ⁰)	H ₃ BTC	H ₂ O (add HF + HNO ₃ , aq.)	150 °C, 6 days (pH<1)	Friedel-Crafts benzylation.	[128]
	ZIF-8	Zn(NO ₃) ₂ ·4H ₂ O	HMelm	DMF	85 °C, 72 h	High-throughput synthesis.	[129]
MW	MOF-5	Zn(NO ₃) ₂ ·4H ₂ O	H ₂ BDC	NMP	800 W,105 °C, 30 min	CO ₂ adsorption (25 °C,1-40 bar).	[130]
	Cr-MIL-101	Cr(NO ₃) ₃ ·9H ₂ O	H ₂ BDC	H ₂ O/EtOH	600 W, 210 °C, 40 min	Benzene sorption (30°C,1 bar).	[131]
	Fe-MIL-53	FeCl ₃ ·6H ₂ O	H ₂ BDC	DMF	300 W, 150 °C, 10 min	Synthesis study.	[132]

	Fe-MIL-101-NH ₂	FeCl ₃ ·6H ₂ O	H ₂ BDC-NH ₂	DMF	150 °C ,15 min	Br-BODIPY sorption (room temperature, 2 days).	[133]
	IRMOF-3	Zn(NO ₃) ₂ ·6H ₂ O	H ₂ BDC-NH ₂	DEF/EtOH	150 W,35 s	Synthesis study.	[134]
	Co-MOF-74	Co(NO ₃) ₂ ·6H ₂ O	H ₄ DHBDC	DMF: EtOH: H ₂ O=1: 1: 1	180 W,130 °C,60 min	CO ₂ and H ₂ O adsorption (25 °C, 1 bar), CO ₂ cycloaddition reaction	[135]
	HKUST-1	Cu(NO ₃) ₂ ·3H ₂ O	H ₂ BDC	EtOH	300 W, 140 °C,1 h	Synthesis study.	[136]
	Cr-MIL-100	C ₃ H ₉ CrO ₉ S ₃	H ₂ BDC	H ₂ O (HF aq. addition)	220 °C, 4 h	Synthesis study.	[114]
	ZIF-8	Zn(NO ₃) ₂ ·6H ₂ O	HMelm	DMF	140 °C, 3 h	Synthesis study.	[137]
SC	MOF-5	Zn(NO ₃) ₂ ·6H ₂ O	H ₂ BDC	NMP	60 W, 30 min	CO ₂ adsorption (25 °C,1-40 bar).	[138]
	Mg-MOF-74	Mg(NO ₃) ₂ ·6H ₂ O	H ₄ DHBDC	DMF: EtOH: H ₂ O=15:1: 1 (add TEA)	500 W,1 h	CO ₂ and H ₂ O adsorption (25 °C, 1 bar), CO ₂ cycloaddition reaction	[139]
	HKUST-1	Cu(OAc) ₂ ·2H ₂ O	H ₃ BTC	DMF:EtOH:H ₂ O=3: 1: 2	150 W,1 h	Synthesis study.	[140]
	PCN-6, PCN-6'	Zn(NO ₃) ₂ ·4H ₂ O	H ₃ BPTC	DEF	PCN-6; 300 W, 1 h; PCN-6'; 150 W, 1 h	Interpenetration controlled MOF synthesis, CO ₂ adsorption (25 °C, 1-30 bar).	[141]
	ZIF-8	Zn(NO ₃) ₂ ·6H ₂ O	HMelm	DMF (add TEA+NaOH aq.)	300 W, 1 h	Scale-up synthesis study, Knoevenagel condensation reaction	[142]
EC	Al-MIL-53	Al(NO ₃) ₃ ·9H ₂ O	H ₂ BDC	H ₂ O:DMF=90:10	Electrolyte : KCl, 90 °C, 10 mA	CO ₂ adsorption (25 °C,30 bar)	[143]
	Al-MIL-53-NH ₂	Al(NO ₃) ₃ ·9H ₂ O	H ₂ BDC-NH ₂	H ₂ O:DMF=90:10	Electrolyte : KCl, 90 °C, 10 mA	Synthesis study, CO ₂ adsorption (25 °C, 30 bar)	[143]

	HKUST-1	Copper plate	H ₃ BTC	MeOH	12-19 V, 1.3 A, 150 min	THT removal (25 °C, 1 bar), H ₂ storage (-196 °C, 40 bar), Kr/Xe separation (55 °C, 40 bar)	[144]
	Al-MIL-100	Al(NO ₃) ₃ ·9H ₂ O	H ₃ BTC	H ₂ O/EtOH=25: 75	Electrolyte: KCl, 60 °C, 50 mA	Synthesis study.	[143]
	ZIF-8	Zn(NO ₃) ₂ ·6H ₂ O	HMeIm	DMF	Electrolyte: MTBS, 25 °C, 50 mA	Synthesis study.	[143]
MC	HKUST-1	Cu(OAc) ₂ ·H ₂ O	H ₃ BTC	No solvent/MeOH	25 Hz, 15 min	Liquid-assisted grinding.	[145]
	ZIF-8	ZnO	HMeIm	DMF	5-60 min, 30 Hz	Synthesis study.	[146]
	ZIF-4	ZnO	HIm	DMF	5-60 min, 30 Hz	Synthesis study.	[146]

CS = conventional solvothermal heating, MW = microwave-assisted, SC = sonochemical, EC = electrochemical, MC = mechanochemical synthesis
H₂BDC = 1,4-benzenedicarboxylic acid, H₂BDC-NH₂ = 2-amino-1,4-benzenedicarboxylic acid, H₃BTC = 1,3,5-benzenetricarboxylic acid,
HMeIm = 2methyl imidazole, H₄DHBDC = 2,5dihydroxy-1,4-benzenedicarboxylic acid, H₃BPDC = 4,4'-biphenyldicarboxylic acid, HIm = imidazole
DMF = N, N-dimethylformamide, DEF = N,N-diethylformamide, NMP = N-methyl-2-pyrrolidone,
HF = hydrofluoric acid, MeOH = methanol, EtOH = ethanol, TEA = triethylamine, MTBS = tributylmethylammonium methyl sulfate,
Br-BODIPY = 1,3,5,7-tetramethyl-4,4-difluoro-8-bromomethyl-4-bora-3a,4a-diaza-s-indacene (optical imaging contrast agent),
THT = tetrahydrothiophene (sulfur odorant components).

I.2.2.3 Stability of MOFs

MOFs usually have weak stability, such as poor water stability, acid-base stability, thermal stability, and mechanical stability. However, the stability of MOFs is crucial for various practical applications. The degradation of MOFs in water vapor or liquid water can be observed as a series of substitution reactions in which the metal-ligand linker is replaced by water or hydroxide. Therefore, a direct way to improve the stability of MOFs is to increase the strength of the coordination bond between the SBU and the organic linker. Up to now, some water-stable MOFs that have been extensively studied include the chromium-based MIL-101 series [111], zeolitic imidazolate frameworks (ZIFs) [147] or metal azolate frameworks (MAFs), the zirconium-based carboxylates [148], the aluminum-based carboxylates [149], the pyrazole-based MOFs [150] and others. Zhang et al. greatly improved the moisture/water stability of hydrophilic MOFs by decorating the surface of hydrophobic and permeable polydimethylsiloxane (PDMS) thin layers by vapor deposition. The surface modification hardly changed the surface area of the original MOFs [151]. In addition, there are many other ways to change the thermodynamic stabilization factor of the framework. For example, Zhu et al. found that heterometallic MOFs have excellent water stability after doping metal ions (Cu^{2+} , Cd^{2+} , or Fe^{2+}) in STU-1A gyrolite MOFs [152].

Building stable MOFs with good acid/base stability is more challenging than water/wet stability. According to the hard/soft acid/base (HSAB) principle, the interactions between hard Lewis acids and bases or soft Lewis acids and bases are much stronger than those between hard acids and soft bases or soft acids and hard bases [153]. A common design strategy is to combine high oxidation state metal ions (hard acids) with carboxylic acid ligands (hard bases) to produce strong bonds resistant to chemical attack. Among them, zirconium-based MOFs are of particular interest due to their rich structural types, excellent stability, and diverse properties and functions [154]. For example, Feng et al. used Fe-TCPP (TCPP = tetrakis (4-carboxyphenyl) porphyrin) as the heme-like ligand and Zr_6 clusters as the nodes to obtain a highly stabilized mesoporous MOF, PCN-222 (Fe), which could remain stable in 8 M HCl for 24 h [155].

I.2.2.4 Functional sites of MOFs

Functional sites of MOF materials can be generated from the pore surface (Fig. I-15). For example, functional groups such as pyridine groups and amines capable of recognizing specific small molecules can be doped directly into organic linkers. Recently developed multivariate MOFs can easily introduce multiple functional sites into the pore surface. Post-synthetic modifications of SBUs or organic linkers may introduce functional groups that are incompatible with MOF synthesis. Metal ions/clusters and organic ligands of MOFs with different electronic, magnetic and optical properties can be carefully tuned to match specific applications. In addition, the pore space of MOFs can be equipped with a variety of functional guests to realize multiple functions. The pore sizes of MOFs range from micropores to macropores and can accommodate a wide variety of substances such as individual metal atoms, nanoparticles, metal complexes, organic dyes, polymetallic oxides, polymers, and small enzymes [156].

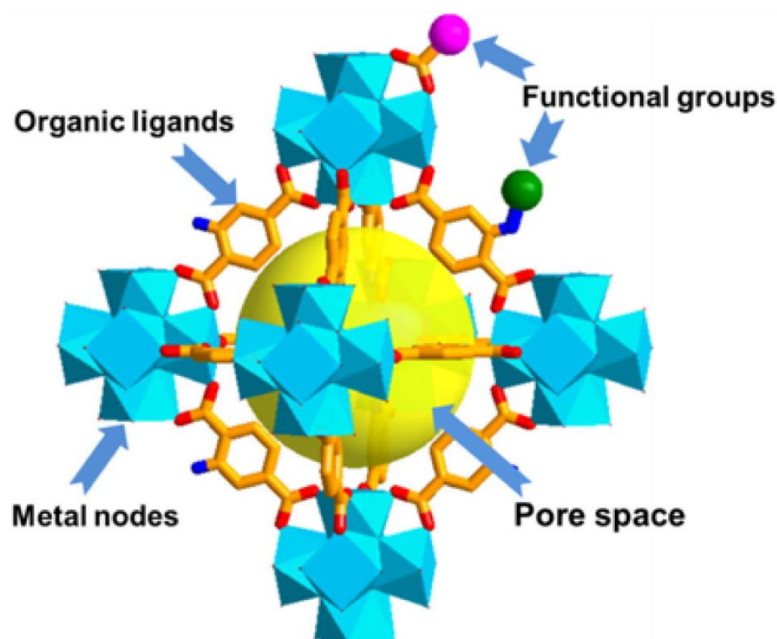


Fig. I-15 Illustration of the construction elements of a functional MOF.

I.3 Conversion of MOF to LDH and to heterostructure-based LDH

The construction of functional materials has long been recognized as a central topic of discussion in the fields of energy and the environment [1]. The composition, morphology and structure of materials endow them with a wide range of properties to fulfil the needs of target applications. In particular, metal-organic frameworks (MOFs) with periodic structures bridged by organic groups and metal centres are promising alternatives to conventional materials due to their multifunctionality [157]. By employing Metal-Organic Frameworks (MOFs) as either parent or sacrificial templates, self-templated derivatization can effectively harness and partially retain the unique properties of the MOF precursors. This approach not only preserves key characteristics but also introduces a wider range of variable properties through chemical and thermal treatments [158]. However, some morphological and structural properties of MOF-derived metal oxides, carbides, or their composites constructed by thermal treatment are lost due to the contraction of the framework in thermal transformations. There is also a risk of aggregation of periodically dispersed metal atoms, which hinders the construction of atomically dispersed metal catalysts [159]. Needless to say, the lack of well-organized structures is a regrettable loss during uncontrolled derivation [5]. In contrast to thermal treatment, it was found that metal hydroxides grown on templates of MOFs can be chemically regulated to relatively avoid damage similar to that during pyrolysis. As an example, a typical iron-based MOF, MIL-88A, has been successfully converted to LDH and used for environmental remediation by many researchers (Table I-2).

By methods such as etching, the original MOFs are deconstructed, while the isolated metal and organic anions are involved in the growth process of LDHs. Taking three-dimensional (3D) MOFs as a template, the growth process of LDHs is more centered on the uniformly distributed metal sites, forming a uniformly extended two-dimensional (2D) layer [160]. Derivatives can be endowed with new properties in terms of composition and structure.

Table. I-2. LDH transformed by MIL-88A as a template

	MOF	LDH	Application	Ref.
1	MIL-88A	CoFe-LDH	HER	[161]
2	MIL-88A	Ni-Fe-Cu LDH	Biosensor	[162]
3	MIL-88A	S@Ni/Fe LDH	Lithium-sulfur batteries	[163]
4	MIL-88A	Ni-Fe-MoS _x LDH	Electrocatalyst	[164]
5	MIL-88A	S@Ce-Ni/Fe LDH	Lithium-sulfur batteries	[165]
6	MIL-88A	Fe-Ni ₃ Co ₂ LDH	Supercapacitor	[166]
7	MIL-88A	Co-Fe LDH	Electrocatalyst	[167]
8	MIL-88A	Ni-Fe-Ce-LDH	Water splitting	[168]
9	MIL-88A	MIL-88@CoNi-LDH	OER	[169]
10	MIL-88A	Fe-FA@Co(OH) ₂	Supercapacitor	[170]
11	MIL-88A	CuNiFe-LDH	OER	[171]
12	MIL-88A	FeSe ₂ @CoSe ₂ /FeSe ₂ yolk-shell polyhedron	Batteries	[172]
13	MIL-88A	Fe ₂ P-NiCoP	OER	[173]
14	MIL-88A	Co-Fe LDH@S	Lithium-sulfur batteries	[174]
15	MIL-88A	NiCoFe-HO@NiCo-LDH	OER	[175]
16	MIL-88A	MIL-88A@Ce-FeCo LDH	OER	[176]
17	MIL-88A	MIL-88A/Ni(OH) ₂	OER	[177]
18	MIL-88A	CoFeS@rGO	Sodium Storage	[178]

Multiple aspects of catalytic performance can be directly improved by exposing more active metal sites in the layers and better mass diffusion through layered channels. In addition, fragile organic frameworks are transformed into more stable inorganic hydroxide structures. More importantly, the partial or complete conversion of MOFs to LDHs is equivalent to the creation of hollow structures, which provide unique cavities for reactions such as energy conversion and pollutant removal. Thus, the strengths of

the two are tightly integrated in the conversion process while overcoming each other's weaknesses. Common transformation strategies for the conversion of MOFs to LDHs, including alkaline hydrolysis, etching templates, and post-growth pyrolysis (Fig. I-16). The conversion of MOFs to LDHs in this form is simple and natural, and the resulting LDHs have more specific structural/compositional properties.

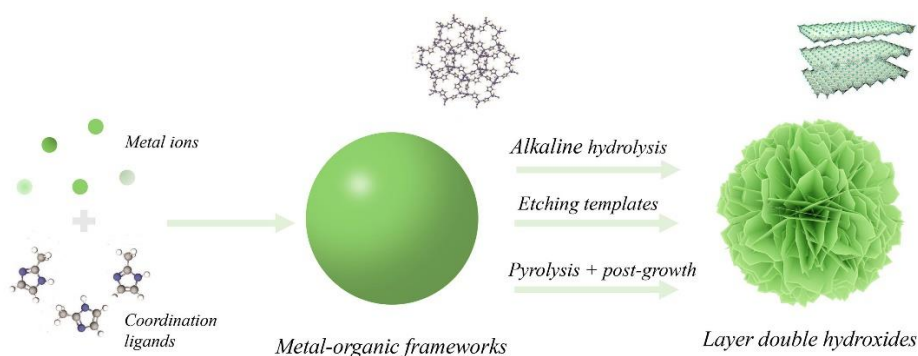


Fig. I-16 Schematic view of MOFs as templates for LDHs generation [179].

I.3.1 Alkaline hydrolysis

Since metal nodes in MOFs are usually complexed with negatively charged organic ligands, the generation of metal hydroxides by OH^- substitution is probably the most readily conceivable route and has been shown to be feasible [177]. Pretreatment and immobilization of MOFs with stable ligands can avoid the loss of metal ions and complete destruction of the framework during alkaline hydrolysis. Therefore, it is crucial to find or obtain relatively "robust" MOFs. In 2019, the role of $\mu^3\text{-OH}$ in MOFs named $\text{Ni}_3[(\text{OH})(\text{Ina})_3(\text{BDC})_{1.5}]$ was revealed by the introduction of ^{18}O -labeled MOFs by synthesis and alkaline hydrolysis (shown in Fig. I-17 [180]). Scanning electron microscopy images (Fig. I-17 b, c) show that hydroxyl substitution indeed occurs and the surface of the MOFs is covered with a lamellar structure. However, the $\mu^3\text{-OH}$ used to construct the MOFs was not completely substituted, retaining 28% and 32%, respectively. The study indicates that the pre-constructed stabilizing groups within the MOFs exhibit a certain level of resilience against internal Ni^{2+} leaching and the complete disruption of the framework. In fact, they further observed that the series of

MOFs without $\mu^3\text{-OH}$ showed morphological loss under alkaline conditions, which proved its importance.

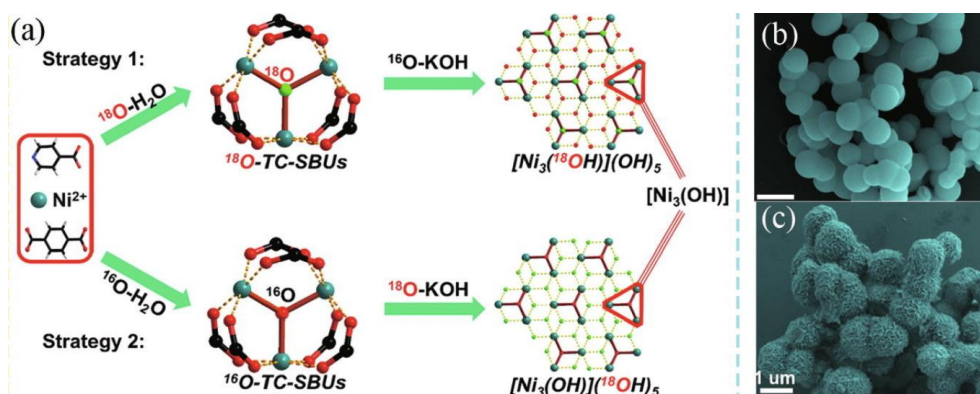


Fig. I-17 (a) Two ways to monitor the $\mu^3\text{-OH}$ groups by an isotopic tracing experiment; (b) SEM image of the Ni/Co-MOF-7:3 precursor; (c) SEM image of the Ni/Co-LDH-7:3 [180].

Conversion of MOFs to LDHs using alkaline hydrolysis has been rarely investigated, and such in situ conversion can bring many benefits: (i) well-dispersed metal sites in MOFs are the nucleation sites of LDHs, which avoids self-stacking; (ii) a larger specific surface area supports and exposes a larger number of active sites; (iii) a well-preserved porous structure provides channels for molecular diffusion, which increases the accessibility of LDHs; (iv) organic ligands isolated from frameworks by OH^- substitution can be recycled economically, which is beneficial for large-scale industrial production. However, the controlled growth of LDHs is difficult to realize due to its not yet fully defined mechanism. On the other hand, the unavoidable dilemma of the alkaline hydrolysis method is the necessity of selecting bimetallic MOF as a precursor, which is a demanding and complicated prerequisite.

I.3.2 Pyrolysis with post-growth

Compared to the direct conversion of MOFs, the pretreatment process of pyrolysis can confer higher chemical and thermal stability to the internal structure due to the replacement of the relatively fragile organic framework with an inactive carbon-based structure [181]. Chen and co-workers [182] added polyvinyl pyrrolidone to a mixture

of $\text{Ni}(\text{NO}_3)_2 \cdot 6\text{H}_2\text{O}$ and $\text{Fe}(\text{NO}_3)_3 \cdot 9\text{H}_2\text{O}$ solutions to promote chemical deposition of NiFe-LDHs on the surface of the ZIF-L derived Co-NC (Fig. I-18a). Ao et al. [183] employed Co-MOF/CC-derived CoS NRs/CC as precursors and adopted the electrodeposition method to load Co^{2+} and Ni^{2+} to generate CoNi-LDH (Fig. I-18 b). Zhang et al. [184] controlled the production of surface-covered LDHs by the addition of $\text{NH}_3 \cdot \text{H}_2\text{O}$ (Fig. I-18 c). Unfortunately, as seen in the above studies, the process of material synthesis is somewhat complex and energy intensive. Simpler and more controllable pyrolytic template generation is necessary but still challenging.

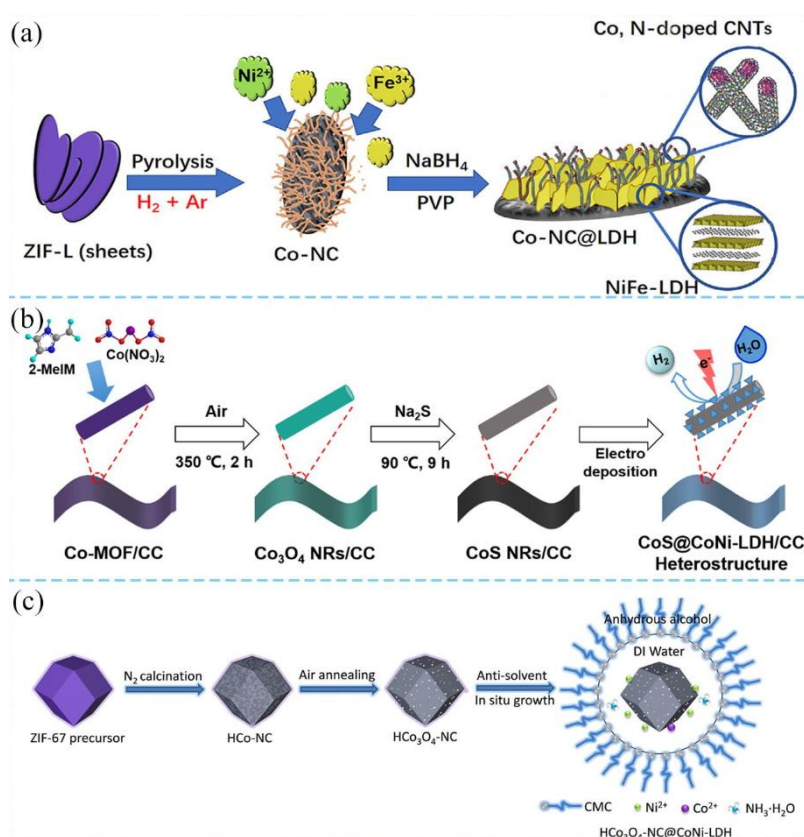


Fig. I-18 (a) Schematic illustration of the preparation process of Co-NC@LDH [182]; (b) Schematic of Synthesizing Heterostructural CoS@CoNi-LDH/CC [183]; (c) Schematic illustration of the in situ antisolvent method for the preparation of hydrangea-like $\text{HCo}_3\text{O}_4\text{-NC@CoNi-LDH}$ composites [184].

I.3.3 Etching templates

Etching has been recognized as an effective method to customize MOFs with different pore structures and rich functionalities [185]. Removal of linkers or clusters

of metal ions by chemical etching makes the MOF more defective, resulting in additional beneficial features [186]. Jiang et al. [187] realized the conversion of MOFs to LDHs by etching with an ethanol solution of metal nitrate. They suggested that the hydrolysis of metal nitrate is the main mechanism leading to the conversion. The protons generated by hydrolysis can etch the ZIF-67 template and release Co^{2+} at the same time. The free Co^{2+} can then combine with hydrolyzed metal ions, such as Mg^{2+} and Ni^{2+} , to form LDHs by co-precipitation. Ultimately, the higher hydrolysis rate of nickel nitrate produced more nucleation sites, leading to denser LDHs nanosheets (Fig. I-19 a). However, also in their study, both high valence and high concentration of metal ions led to the rapid dissolution of ZIF-67, resulting in undesired structures. The (003), (006), (012), and (110) reflections of a typical LDH material are clearly observed in the XRD spectra of the three samples (Fig. I-20 a), indicating that the samples have the same layered LDH structure. The different effective ionic radii of the divalent metals (Mg^{2+} , Ni^{2+} , Co^{2+}) lead to the different positions of the (110) reflection for each sample. The hierarchical structure of the Ni-Co LDH nanocage consisting of thin nanosheets yields a high Brunauer-Emmett-Teller (BET) surface area of about $196 \text{ m}^2/\text{g}$ (Fig. I-20 b), which may enhance its electrochemical properties.

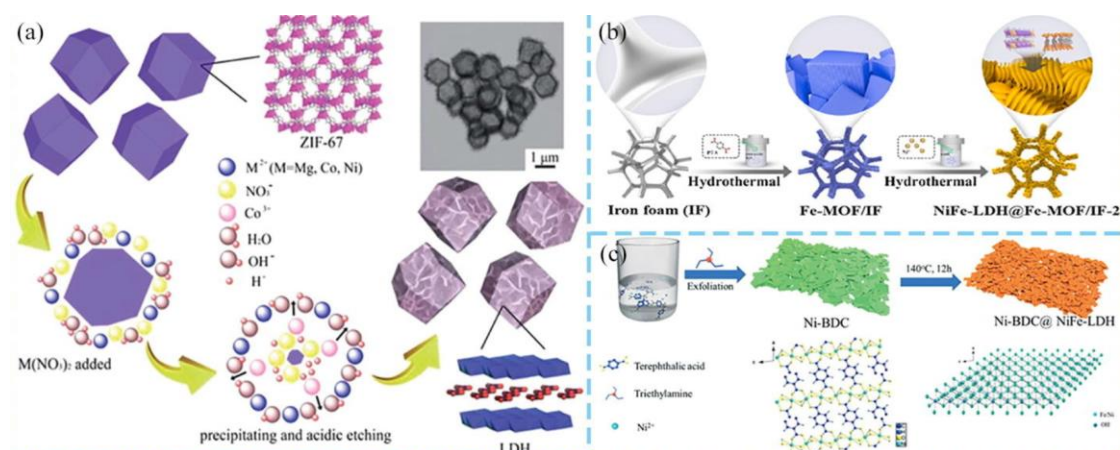


Fig. I-19 (a) The formation illustration of LDH nanocages by simultaneous precipitation and acidic etching. The TEM image in the upper right corner shows the as-prepared Mg–Co LDH nanocages [187]. (b) Schematic illustration of the formation process of NiFe-LDH@Fe-MOF/IF-2 [188]. (c) A schematic diagram of the preparation process for Ni-BDC@NiFe-LDH [189].

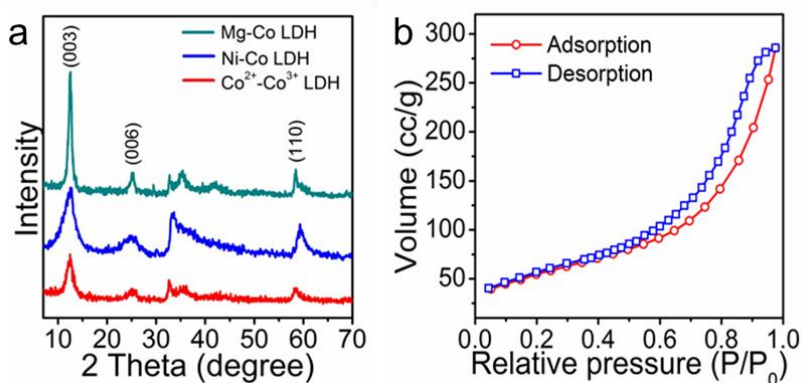


Fig. I-20 XRD patterns of the as-prepared LDH nanocages[187].

Similarly, the effects of etching metal salt concentration and etching time were observed in the Fe-MOFs to NiFe-LDHs transformation (Fig. I-19 b) [188]. With the gradual introduction of Ni^{2+} , the tightly stacked Fe-MOF sheets were separated and dispersed to generate layered LDH. The high concentration of Ni^{2+} induces the overgrowth of LDH, which results in agglomeration and leads to a decrease in surface area. Dong et al. [189] prepared the Ni-BDC@NiFe-LDH by dissolving NaOH and Na_2CO_3 into the solution of Ni-BDC and $\text{Fe}(\text{NO}_3)_3$ to control pH equal to 10 (Fig. I-19 c). The stage that MOFs and LDHs both existed was achieved. Besides, the free CO_3^{2-} could insert into the interlayers of LDHs to better construct their sheet-like structure. As the metal ions precipitate out of the framework to the outside, most of the similar transformations are formed on the surface of the MOFs, like the outer shell of the LDHs [190]. High etching leads to a hollow structure with complete structural evacuation of MOFs, whereas insufficient etching relatively retains MOFs to produce a core-shell structure [191]. Wang et al. [192] chose ZIF-8 nanocubes as precursors to explore the growth mechanism of LDHs. In the first stage, the (100) face of ZIF-8 was initially etched, and then a gap appeared between the newly generated shell of LDHs and the contracted ZIF-8 nanocubes. Eventually the LDHs nanocage was fully grown and the remaining ZIF-8 was completely etched away (Fig. I-21 a). Furthermore, the next study of the reaction conditions showed that high concentrations of $\text{Co}(\text{NO}_3)_2$ or high levels of water lead to failure of the LDHs shell growth, as the fast diffusion rate prevents the LDHs from precipitating on the surface. To generate homogeneous mixed core-shell or hollow structures, solvents such as low concentrations of metal nitrates or ethanol are required as buffer protection. Their work provides insight into the mechanism of the etching template method, and Fig. I-21b shows the gradual growth of shell-in-shell

LDH nanocages under the same mechanism [191, 193]. The etching proceeds from the outside in to grow LDH on the surface of pristine MOFs.

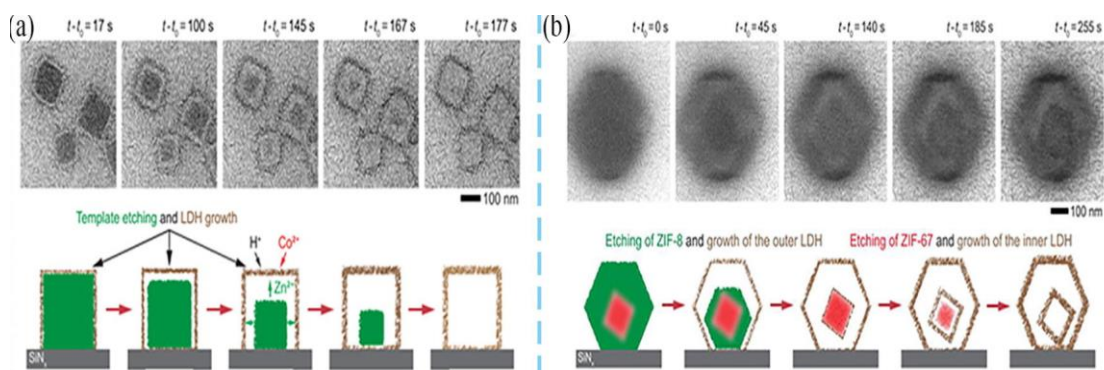


Fig. I-21 (a) The conversion of ZIF-8 nanocubes into LDH nanocages in a $\text{Co}(\text{NO}_3)_2$ solution; (b) The conversion process of core – shell ZIF nanoparticles into shell-in-shell LDH nanocages in a $\text{Co}(\text{NO}_3)_2$ solution [192].

Fig. I-22 shows the changes in the crystal structure of HIH-LDH-2 during each preparation step. In the XRD spectra of HIH-LDH-2, the ZIF-67 diffraction peaks of HCS@ZIF-67-2 disappeared, and new peaks appeared around $2\theta = 11.4^\circ, 22.7^\circ, 34.0^\circ,$ and 60.4° , which were related to the (003), (006), (009), and (110) diffraction of the LDH structure, respectively. In addition to the LDH diffraction peaks, the (002) carbon peak of HCS was also detected in the HIH-LDH-2 spectrum. This result suggests that the ZIF-67s of HCS@ZIF-67-2 were completely converted to nickel-cobalt LDH during the transformation process and retained the HCS crystal structure.

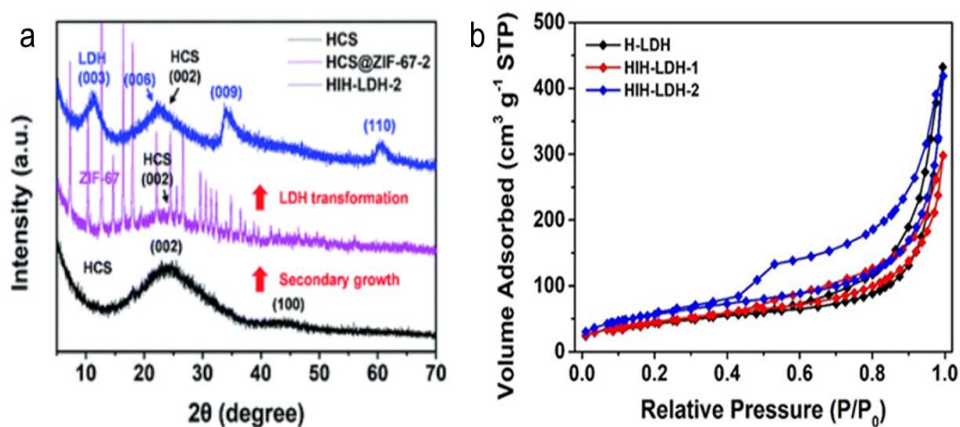


Fig. I-22 (a) XRD patterns and (b) Nitrogen adsorption/desorption plots of HCS, HCS@ZIF-67-2, and HIH-LDH-2.

Since the introduction of this etching template method, many MOFs have been used to synthesize LDHs, as shown in Table. I-3. Thus, their study has several advantages that contribute to the construction of LDHs. First, it is essential to intercalate the interlayers of LDHs with anionic groups, where negatively charged organic ligands and NO_3^- from nitrate can be naturally inserted into the interlayers during the transformation process [194]. The pH can then be adjusted by mixing other alkaline hydrolysis salts into the solution to simply promote the generation of LDHs, as well as interlayer anion supplementation [195]. In addition, the detached organic ligands can be recovered and reused, thus avoiding the waste of expensive organic ligands [196]. Various MOF composites are good precursors. The selection of them as precursors allows the construction of LDH composites, which proves the applicability of the method. More composite units are more adaptable to metal ion solutions than other methods. Therefore, more efforts can be made in applying this method to synthesize LDH with complex structures [197].

Table. I-3. A series of MOF-derived LDHs prepared by etching templates method.

MOF precursors	Etchants	Solution	Impregnation time	Temperature	LDH derivatives	Ref.
ZIF-67	Ni(NO ₃) ₂ Mg(NO ₃) ₂ Co(NO ₃) ₂	Ethanol	1 h	Room temperature	NiCo-LDH, MgCo-LDH, CoCo-LDH	[187]
ZIF-8, ZIF-67@ZIF-8	Co(NO ₃) ₂	DI water: Ethanol 2:1	1,3,5,10 min	Room temperature	ZnCo-LDH	[192]
ZIF-67	Co(NO ₃) ₂	Ethanol	1 h	90°C	NiCo-LDH	[198]
Fe-MOF/(iron foam)IF	NiCl ₂	Ethanol	6 h	150°C	NiFe-LDH@Fe-MOF/IF	[188]
Mg-MOF-74	Mg(NO ₃) ₂	DI water	30 min	Room temperature	Mg-MOF-74@Mg ₂ Al-CO ₃ LDH	[199]
CC@ZIF-67	Ni(NO ₃) ₂	Ethanol	1 h	25°C	CC@MOF-LDH	[200]
ZIF-67	Co(NO ₃) ₂	Ethanol	90 min	Room temperature	Co-LDH hollow dodecahedrons	[201]
Fe-MIL-88	Ni(CH ₃ COO) ₂	N,N-dimethyl formamide	4 h	85°C	NiFe-LDH	[202]

I.4 Application of MOF-derived LDH in the remediation of aquatic environments

During the transformation process, some properties of MOFs are naturally introduced into LDHs. As an example, the stability of the derived LDHs largely exceeds that of the MOF precursors due to the better tolerance of the inorganic hydroxides to oxidizing environments. In addition, the electron and ion transport efficiencies will be effectively improved due to the presence of a large number of coordinated unsaturated bimetals on the layers as well as the presence of free anions between the layers. Structurally, the surface-expanded layered LDHs have a larger specific surface area, which is favorable for the contact between the catalyst and the reaction medium. In addition, the structure of pristine MOFs provides more uniform and dispersed catalytic sites for LDHs. The three-dimensional MOF as a template avoids the problem of collapse of conventional pristine LDHs due to the interaction between different layers. The advantages of both are tightly combined. Therefore, as a transformation and combination between functional materials, synthetic LDHs have good performance in various fields. During the transition from MOFs to LDHs, effects such as ultrasonic or ethanol etching increase the roughness of the material, which means that larger surface areas and irregular pore sizes are created. At the same time, the structural and chemical stability of the formed LDHs in solution largely exceeds that of the MOFs, as the material in its inorganic state is more heat- and chemical-resistant. Therefore, this transformation can be an effective means to expand the application of MOFs in the field of environmental remediation.

I.4.1 Modification of adsorption properties

Adsorbents function by selectively separating contaminant molecules from solutes based on their mutual affinity. They are primarily classified into two categories: physical adsorption, which depends on van der Waals forces and electrostatic attraction, and chemical adsorption, which relies on chemical bonding. MOF-derived LDH demonstrates the potential to enhance both types of adsorption when compared to MOF precursors. Firstly, the resulting pore size is larger in LDHs derived from MOFs, providing contaminants with more exposure opportunities. This is due to the unique

structure of LDHs, where some metal cations within the constituent layers can serve as active sites, promoting chemisorption effects. Additionally, the property of interlayer anion exchange plays a significant role in the adsorption of anionic pollutants. As reported by Summaira et al [203], the negatively charged methyl orange (MO) and alizarin red S (ARS) ions were readily trapped by ZIF-67@LDH. The pore size of ZIF-67@LDH increased from 1.542 to 13.24 nm and the volume from $0.028 \text{ cm}^3 \cdot \text{g}^{-1}$ to $0.492 \text{ cm}^3 \cdot \text{g}^{-1}$, which is more convenient for mass transfer conditions compared to the micropore ZIF-67. ZIF-67@LDH has more convenient mass transfer conditions than microporous ZIF-67. As shown in Fig. I-23, the surface area and porosity changed significantly. In addition, the ZIF-67@LDH surface with positively charged sheets tends to trap anions MO and ARS through electrostatic and hydrogen bonding interactions. In addition, the surface of ZIF-67@LDH with positively charged sheets tends to adsorb anions MO and ARS through electrostatic interaction and hydrogen bonding. Normally, the adsorption capacity of cations decreases due to electrostatic repulsion, but some LDHs derived from MOFs are also able to adsorb cations very well due to their porous structure and -OH functional groups. Another pollutant of concern is heavy metals [204]. In general, the adsorption mechanisms of LDHs include isomorphic substitution, electrostatic interaction, complexation, and surface precipitation, which seems to apply to MOF-derived LDHs as well. The CoAl-LDH@Fe₂O₃/3DPCNF designed by Kim's group has the highest adsorption efficiency in various samples due to its superhydrophilicity and better morphological configuration. Furthermore, its superior performance remains unshaken regardless of variations in the degree of ionization or the phase of existence of Cr (VI) and Pb (II) at different pH values, as well as fluctuations in the Coulombic force acting on the adsorbent surface.

MOF-derived LDHs are competitive in the adsorption of organic pollutants and heavy metal ions due to the advantages of the homogeneous porous system of MOF and the affinity of LDHs for the reaction substrates. However, for the coexistence of MOF and LDH, the synergistic adsorption mechanism still needs to be further explored.

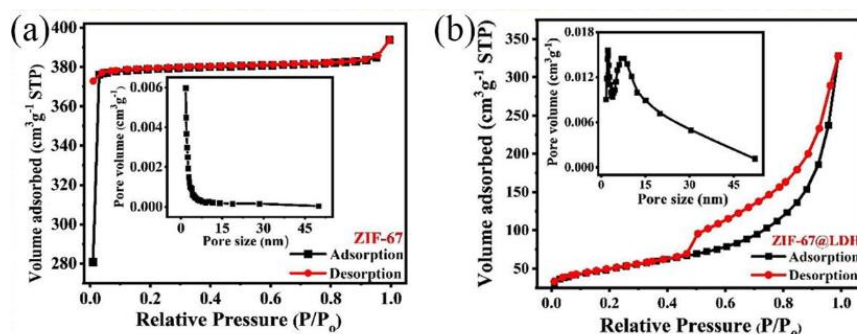


Fig. I-23 N₂ adsorption-desorption isotherms (a) ZIF-67, (b) ZIF-67@LDH.

I.4.2 Advanced oxidation processes

Recently, ZIF-67 was converted to Al-Co LDH by the etching template method by Cao et al [194]. They demonstrated a synergistic interaction between the low content of Co ions remaining in the etched Co-ZIF and the Al ions, which achieved excellent tetracycline (TC) degradation through activation of PMS. It is the low electronegativity of Al (1.6 eV) that promotes the release of more electrons from the electron-rich Co (11.9 eV) sites, resulting in the production of SO₄²⁻. The degradation mechanism is illustrated in Fig. I-24 a. Due to the increase in specific surface area and porosity, the accessibility of TC is improved, and the degradation rate constant is almost increased from 0.059 min⁻¹ to 0.98 min⁻¹, which is more than 16-fold (as shown in Fig. I-24 b). For the direction of advanced oxidative degradation of pollutants, MOF-derived LDHs still have a lot of application space. The good resistance of most MOF-derived LDHs to different experimental conditions makes MOF-derived LDHs an important candidate for practical wastewater treatment.

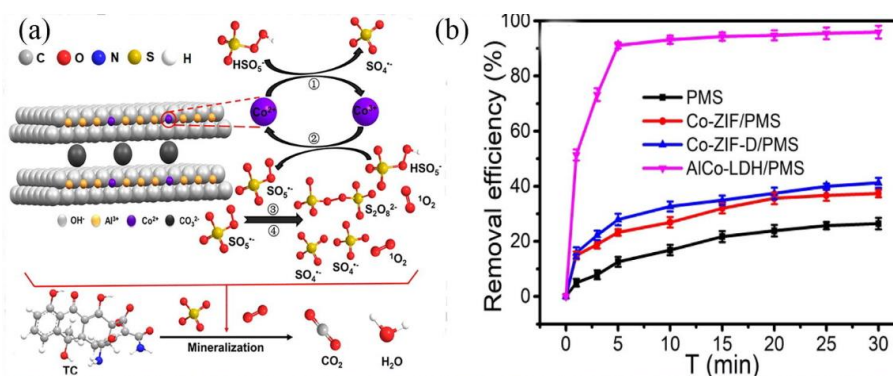


Fig. I-24 (a) Possible reaction mechanism of TC degradation by AlCo-LDH/PMS system; (b) Catalysis degradation of TC on different catalysts [194].

I.4.3 Capacitive deionization (CDI) and chemical sensors

Considerable progress has been made in the study of MOF derivatives in CDI [205]. Various types of MOF-derived carbon materials are considered as excellent electrodes due to their low mass transfer resistance, high specific capacitance and trap stability [206]. For wastewater treatment, plasma contaminants such as heavy metals, ionizable dyes and antibiotics, as well as potentially hazardous inorganic ions (F⁻, bromine-, phosphate) have been shown to be removed by CDI [207]. Compared to other nanomaterials, MOF-derived LDHs can enjoy the common redox mechanism of transition metals to catalyze reactions with the help of their specific structures. To date, a number of MOFs have been discovered and applied for chemical sensing, mainly by catalyzing chromogenic reactions or fluorescent properties. Yu and coworkers designed 2D layered MOFs to enable the detection of organic pesticides. By modifying the tetrapyrrolyl cup 4 aryl group, the MOFs exhibited a fluorescent reaction by binding to glyphosate, leading to selective and sensitive detection [208].

Chapter II

Synthesis and characterizations of MIL-88A and conversion into LDH/88A and LDO/88A

II.1. Introduction

Layered double hydroxides (LDHs) have a structure represented as $[M_{1-x}^{2+}M_x^{3+}(\text{OH})_2]^{x+}(\text{A}^{n-})_{x/n} \cdot m\text{H}_2\text{O}$, where M^{2+} and M^{3+} denote divalent and trivalent metal cations and A^{n-} denotes the interlayer anion, often abbreviated for simplicity as $M^{2+}M^{3+}$ LDH, $M^{2+}M^{3+}$ -A LDH or $M^{2+}_{(1-x)/x}M^{3+}$ -A LDH [209]. They have been widely employed as catalysts, catalyst precursors, or catalyst carriers in AOPs to remove organic pollutants in water because of their benefits due to its plentiful and tuneable active sites, strong thermal stability, and flexible ability for intercalated anions [210]. For example, Wu et al. [211] used the oxygen vacancy of FeCo-LDH to induce non-radical degradation of bisphenol A (BPA) in water. NiCo-LDHs prepared by Ramachandran et al. [212] through in situ etching of Ni-MOF templates catalyse fuel degradation by peroxydisulfate (PMS) through the generation of high-rate free radicals ($\text{SO}_4^{\cdot-}$ and HO^{\cdot}). However, the uncontrollability and complexity of conventional methods such as anion exchange, co-precipitation, solution mixing, and hydrothermal reactions make it difficult to prepare morphologically controllable, heterogeneous LDH catalysts. Morphologically controllable LDH materials, such as three-dimensional (3D) hollow structures, are ideal for improving performance. Hence, the utilization of 3D LDH is increasingly gaining popularity. Via fluoride ions as the functional template agent, a 3D flower-like CoAl-LDH was effectively made using a straightforward hydrothermal process [213]. The combination of fluoride ion functional templating agents with specific porous 3D flower-like nanostructures yields exceptional gas sensitivity. However, the choice of template remains limited by the composition or shape of the template. That is, the right template is the key to making 3D hollow structures with complex structures [214].

With high porosity, large specific surface area, customizable structure and customizable functionality, MOFs have great potential for many applications including sensing [215], gas storage [216], separation [217] and catalysis [218]. MOFs are porous hybridized inorganic-organic solids formed by the combination of metal clusters and organic ligands [219]. Due to the adjustable metal centers, large specific surface area and highly ordered structures, MOFs can be used as a self-sacrificial template and metal precursor to prepare a variety of new nanostructured materials [220]. Thus, leveraging

the original controllable skeleton, the drawback of MOFs, wherein most metal active sites are deeply embedded within the framework, can be ameliorated. This results in modified materials boasting complex structures characterized by porous walls and numerous cavities, facilitating the exposure of additional surface active sites to enhance reaction kinetics [221].

Among the iron-based MOFs materials, MIL-88A(Fe) represents a MOF constructed from hard acid Fe (III) and organic carboxylic acid ligands. The low toxicity and low cost of its organic ligand, fumaric acid, combined with its stability in water, make MIL-88A (Fe) an excellent template for modification [222]. However, conventional hydrothermal methods for synthesizing MIL-88A typically require more than 10 hours of heating [223, 224], or stirring the reaction at room temperature for 24 hours [225, 226]. In contrast, microwave heating, a more powerful alternative technology, is characterized by non-contact, reduced reaction times and lower energy consumption [227].

Therefore, the present study investigates in details the synthesis and modification of LDH, which strictly follows the concepts of simplicity, convenience, efficiency and environmental protection. Namely [228], A standard iron-based Metal-Organic Framework (MOF), such as MIL-88A, serves as the precursor in this process. Ni²⁺ are co-precipitated with iron on the MOF's surface under alkaline conditions, resulting in the transformation into regularly shaped Layered Double Hydroxides (LDHs). Both MOFs and LDHs were synthesized and converted by a highly efficient microwave method. We have successfully synthesized MIL-88A by microwave method and confirmed its structural and functional advantages over that by hydrothermal method. The in-situ growth of LDHs on MIL-88A was also performed under microwave conditions, and LDHs with regular structures, assembled in a 3D architecture, were successfully obtained.

II.2. Synthesis and characterizations of MIL-88A

II.2.1. Experimental section

II.2.1.1. Experimental material, instruments and procedure

All chemicals were of analytical reagent grade. $\text{Fe}(\text{NO}_3)_3 \cdot 9\text{H}_2\text{O}$ is purchased from sigma. Fumaric acid (FA) and $\text{Ni}(\text{NO}_3)_2 \cdot 6\text{H}_2\text{O}$ purchased from ACROS. Other chemicals used are of analytical reagent grade or the highest purity available.

Synthesis of MIL-88A by hydrothermal method (HT): 69.6 mg (0.6 mmol) fumaric acid was dissolved in 13 mL deionized water under sonication and 262.6 mg (0.65 mmol) $\text{Fe}(\text{NO}_3)_3 \cdot 6\text{H}_2\text{O}$ was dissolved 2 mL of deionized water by stirring at room temperature. The two solutions were mixed to form a clear yellow solution, which was transferred into Teflon stainless steel reactor in an oven heated to 110 °C for 6 h [229]. The product was separated by centrifugation and washed three times with ultrapure water and ethanol, respectively, before being dried in an oven at 60 °C overnight.

Synthesis of MIL-88A by microwave method (MW): 69.6 mg (0.6 mmol) fumaric acid ultrasonic was dissolved in 13mL deionized water and 262.6 mg (0.65 mmol) $\text{Fe}(\text{NO}_3)_3 \cdot 6\text{H}_2\text{O}$ was dissolved 2 mL of deionized water by stirring at room temperature. The clear yellow solution obtained by mixing the two solutions were submitted to microwave heating at different temperatures for different times [113]. The product was separated by centrifugation and washed three times with ultrapure water and ethanol, respectively, before being dried in an oven at 60 °C overnight.

II.2.1.2. Morphological and structural characterization

The morphology of materials was analysed using a Field Emission SEM (JEOL JSM-6700, Japan) and Transmission Electronic Microscopy (TEM) (JEOL JEM-2010, Japan). The powder X-ray diffraction (XRD) patterns of MIL-88A were obtained using an X-ray diffractometer Philips X'Pert pro diffractometer equipped with a X'celerator 1D detector (2.122° active length), using $\text{CuK}\alpha_1/\text{K}\alpha_2$ source in Bragg Brentano θ - θ geometry from 5 to 70° (2 θ) with a scan step of 0.016°. Absorption infrared (IR) spectra

of MIL-88A were measured by a Fourier-Transform Infrared spectrometer (Horiba FT-730, Japan) using the KBr pellet technique. Thermogravimetric (TG) curves were measured using a thermogravimetric analyser (ISI TGA i1000, USA) at a heating rate of 40 °C /min from 25 to 1000°C under air. The specific surface areas were measured using N₂ adsorption isotherm and an automatic surface analyser (ASAP 2020, Micromeritics, USA) by Brunauer- Emmett-Teller (BET) theory.

II.2.2. Results and discussion

II.2.2.1. Design of MIL-88A

The synthesis elaboration process and formula for MIL-88A, reported in the literature, are shown in Fig. II-1 a [230]. MIL-88A was synthesized by precipitating it from a solution containing iron nitrate and fumaric acid in deionized water, heated to 110 °C. Synthesized MIL-88A exhibits a three-dimensional (3D) structure consisting of an octahedral iron (III) trimer linked to six fumarate dianions. This structure divides a one-dimensional pore system and cage filled with solvent molecules along the c-axis [231]. Fig. II-1 b shows a single cell of MIL-88s with the chemical formula $[\text{Fe}_3\text{OX}(\text{OOC}-\text{CH}_2-\text{COO})_3(\text{H}_2\text{O})_x\text{X}]_n$ (X being a charge compensating anion) [232].

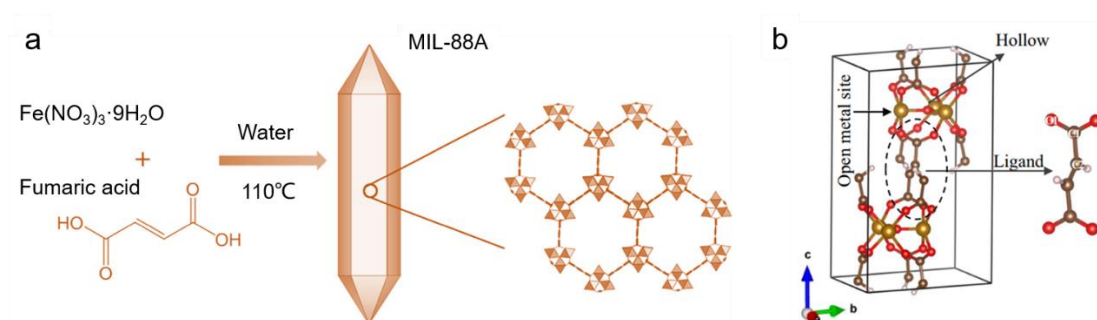


Fig.II-1 Schematic illustration of synthesis of MIL-88A [232].

II.2.2.2. Synthesis method

In order to investigate the effect of the thermal activation on the synthesis of MIL-

88A, two methods, hydrothermal and microwave were used to synthesize MIL-88A. The synthesis involved heating at 110 °C for 6 h using the hydrothermal method and for 30 min using the microwave method, respectively. The X-ray diffraction (XRD) patterns of MIL-88A synthesized by microwave and hydrothermal autoclave are shown in Fig. II-2. The XRD of MIL-88A synthesized by the two methods show narrow and well-defined reflections, indicating a typical feature of a MIL-88A(Fe) structure [233]. This highly crystalline structure is identical to that of the previously reported solvothermal synthesis [231, 234].

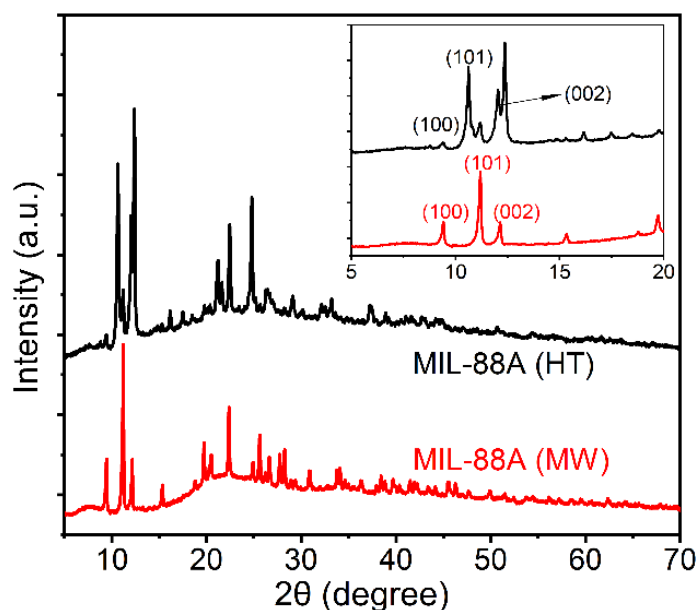


Fig. II-2 XRD patterns of MIL-88A (HT) and MIL-88A (MW).

Compared with MIL-88A (HT), the diffraction peaks (100), (101) and (002) of MIL-88A (MW) are shifted to the higher angles. Such differences could be attributed to modified cell parameters resulting from a variation in the structure and filling of micropores within the MOF [223]. And the difference in the XRD results of MIL-88A synthesized by the two methods are likely to be caused by the fact that the microwave-synthesized MIL-88A has smaller particles [223]. In terms of crystallinity, MIL-88A (MW) displays narrower peaks highlighting a higher crystallinity. This can be explained that, microwaves act as high-energy source that provide higher and homogeneous energy during synthesis. Because when the particles gain enough energy to maintain the coordination bond, a simple arrangement of molecules around the metal center will form a high crystallinity [235]. In microwave synthesis, the high dielectric absorption

of polar solvents leads to conversion into thermal energy, which heats the solution more efficiently and accelerates the dissolution of reactants [236]. This rapid localized superheating overcomes the energy barrier and causes the local concentration (hot spot) to exceed the supersaturation threshold, leading to rapid and uniform nucleation. Thus, microwave-assisted hydrothermal synthesis can be considered not only as a rapid method for preparing monodisperse nanoparticles, but also as a useful method for scaling up the reaction.

FTIR spectra of MIL-88A (Fig. II-3) show fundamental similarities. The $\nu_{as}(-\text{CO}_2^-)$ band vibration of the coordinated fumarate anionic ligands were observed at 1656 cm^{-1} . The $\nu_s(-\text{CO}_2^-)$ due to the symmetric vibration of the carboxyl group is visible at 1396 cm^{-1} . The short energy gap between the two vibrations $\Delta(\nu_{as}(-\text{CO}_2^-) - \nu_s(-\text{CO}_2^-)) = 260\text{ cm}^{-1}$ confirms the coordination of the fumarate anion to the Fe^{3+} cations. In addition, the Fe-O vibrations in the secondary building unit (SBU) or cluster unit of Fe-MIL-88A produced an absorption line at a wavelength of 670 cm^{-1} [237]. The bands at 1217 and 984 cm^{-1} are attributed to the stretching vibration of C-C and the bending vibration of C-H in trans-diene, respectively [238]. The Fe-O feature band is shown at 562 cm^{-1} , which indicates the binding of carboxyl ligands to metallic iron [239]. These bands indicate that MOFs have been successfully synthesized [234].

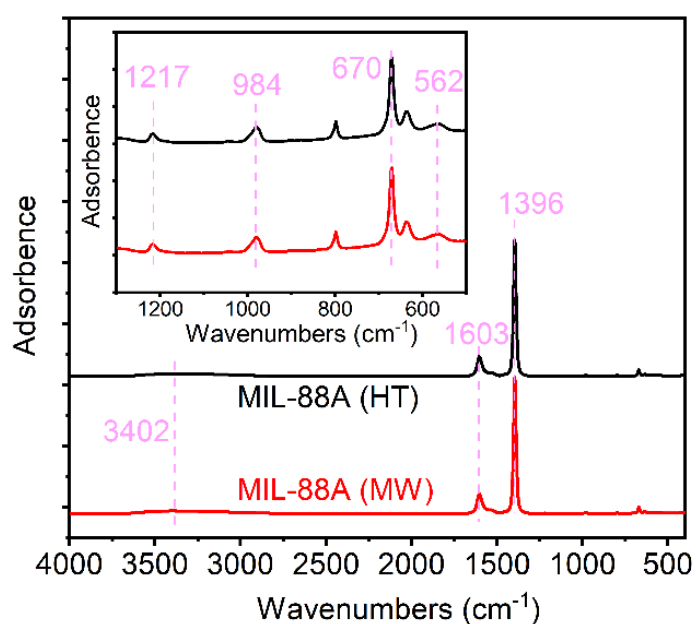


Fig. II-3 FTIR of MIL-88A (HT 110 °C-6 h) and MIL-88A (MW 110 °C-30 min).

Fig. II-4 shows electron microscopy images of MIL-88A (HT) and MIL-88A (MW) showing the well-defined morphology obtained. These materials exhibit a similar smooth rod-like structure with a tapered tip, which is a shape typical of MIL-88A [240]. However, the length of MIL-88A (HT) is about 3-5 microns and the width is about 600 nanometers, while the length and width of MIL-88A (MW) are 4 microns and 300 nm, respectively. In comparison, MIL-88A (MW) rods appear to be more thinner. Moreover, the surface of MIL-88A (HT) is clearly rough and angular, while that of MIL-88A (MW) is smoother. It is worth mentioning that the length of MIL-88A (HT) is not uniform, and the length of long MIL-88A (HT) rods can be even twice as long as the short ones, causing the rod-like structure to break. This is because, when the autoclave is placed in the oven, two different thermal zones are created consecutively: the growth zone (low-temperature zone) and the dissolution zone (high-temperature zone) [237]. The growth zone, located in the upper part of the vessel, where the material is less soluble, is more likely to produce longer rod-like structures, while the dissolution zone at the bottom of the vessel, where the material is more soluble, is more likely to produce shorter rod-like structures [237]. Since stirring operation was not possible in our reactor, the MIL-88A (HT) obtained had an inhomogeneous length.

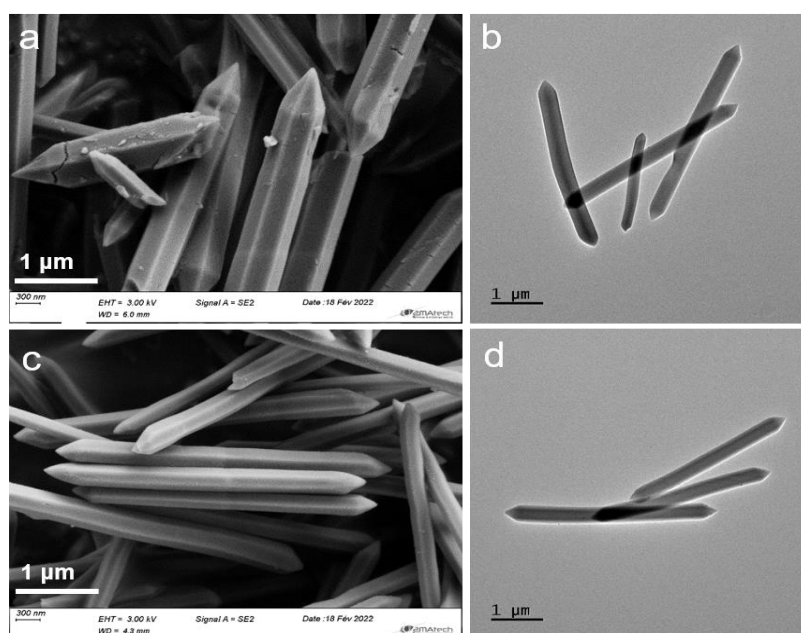


Fig. II-4 SEM and TEM images of MIL-88A (HT 110 °C-6 h) (a and b) and of MIL-88A (MW 110 °C-30 min) (c and d).

MIL-88A (MW), on the other hand, has uniform length and no fracture. This could be attributed to the microwave activation. Microwaves interact directly with the molecules in the reaction mixture, causing a rapid increase in temperature. This process does not rely on the thermal conductivity of the vessel materials, resulting in immediate localized superheating of any substance that responds to dipole rotation or ionic conduction, the primary mechanisms for transferring energy from microwaves to the heated substance. Considering that MIL-88A synthesized via both the hydrothermal and microwave methods possess the same functional group and crystal type, the microwave method demonstrates superior efficacy to form homogeneous well-defined particles. In microwave synthesis, the high dielectric absorption of polar solvents leads to thermal conversion of energy, which heats the solution more efficiently and accelerates the dissolution of reactants [236]. This rapid localized superheating overcomes the energy barrier and causes the local concentration (hot spot) to exceed the supersaturation threshold, leading to rapid and uniform nucleation. Thus microwave-assisted hydrothermal synthesis can be considered not only as a rapid method for preparing monodisperse nanoparticles but also as a useful method for scaling up the reaction [223].

II.2.2.3 Effect of MW irradiation time

In order to investigate the optimum time of irradiation for microwave synthesis of MIL-88A, temperature gradient and time gradient synthesis experiments were carried out. The time was increased from 1 to 60 min and the resulting solids were characterized. From Fig. II-5, the crystalline structure of MIL-88A (MW) begins to appear after (5 min of reaction), the intensity of the peaks increases gradually with reaction time in the range of 5 to 60 min. In particular, after 10 min of reaction, a clear (002) peak begins to appear at 12° . When the reaction time was extended to 60 min, the (002) peak began to weaken. Thus, the crystallinity of MIL-88A (MW) prepared for 20, 30 and 45 min reaction time was higher.

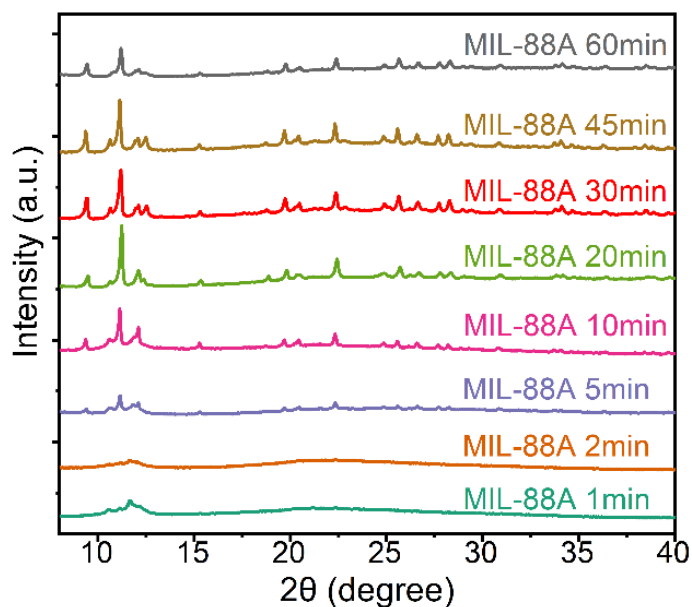


Fig. II-5 XRD results of synthetic MIL-88A (MW) at different times of irradiation.

The SEM results (Fig. II-6) also showed that the size of the rod structure of MIL-88A (MW) with a reaction time of 20 min was not uniform, suggesting that the lack of reaction time limits the growth of its microstructure, while the rod structure of MIL-88A (MW) with a reaction time of 40 min showed fractures. Therefore, 30 min is considered as the optimal reaction time.

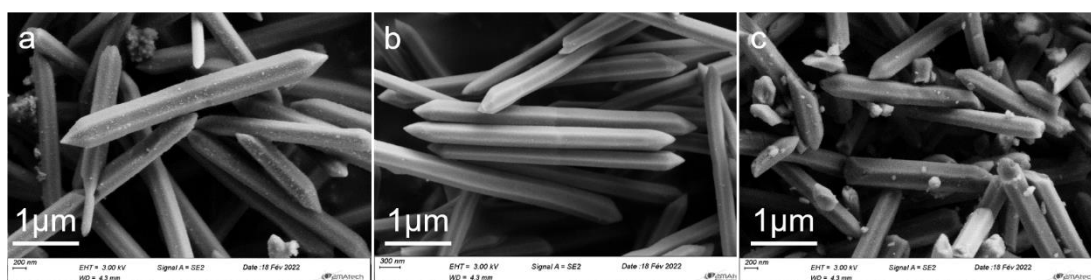


Fig. II-6 SEM of MIL-88A (MW) at different time of irradiation; (a) at 20 min, (b) at 30 min, (c) at 40 min.

II.2.2.4 Effect of temperature of MW irradiation

Both temperature and time greatly can affect the growth conditions and final particle size of the product. However, the effect of temperature is more important compared to reaction time [237]. Therefore, the effect of reaction temperature on the

synthesis of MIL-88A (MW) was explored. The experiments were reacted at 100, 110 and 120 °C for 30 min. The characterization results are shown by Fig. II-7. When the reaction temperature is 100 °C, no crystal structure is produced. At 110 °C, the structure of a typical MIL-88A (MW) is formed. However, when the temperature rises to 120 °C, the crystal structure is completely different from MIL-88A (MW) leading to the crystallization of Fe₂O₃. This is possible due to the temperature increase during the reaction and the subsequent production of metal oxides [241].

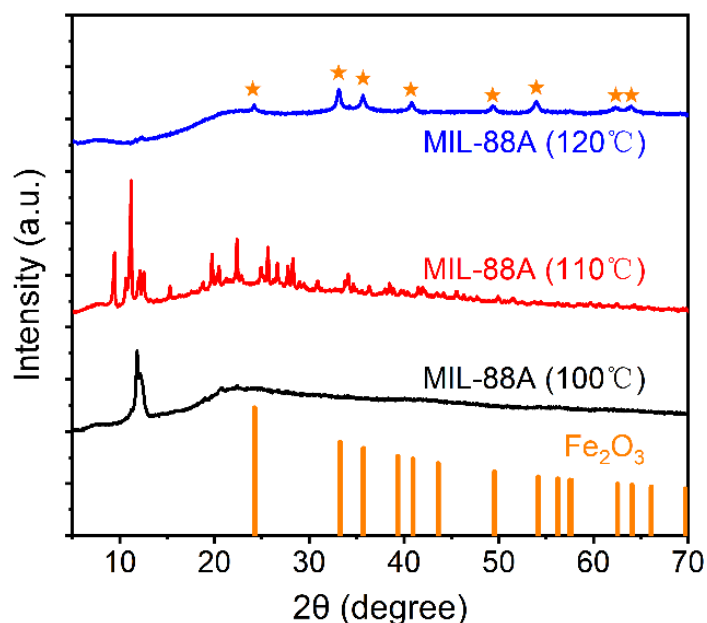


Fig. II-7 XRD result of MIL-88A synthesis using MW at different reaction temperature.

The results of FTIR spectra (Fig. II-8) show the ν_{as} and ν_s carboxylate characteristic bands of fumarate anion located at 1396 and 1603 cm^{-1} which are very sharp when the temperature are 100 and 110 °C, while the intensity of characteristic bands of C-C and C-O strongly decrease at 120 °C, which suggests that the structure of MIL-88A (MW) is disrupted by the high temperature. The absence of ν_3 intense stretching band of NO_3^- anion (1380 cm^{-1}) should indicate that the OH^- is the charge compensating anion. The Fe-O located at 565 cm^{-1} is not significantly displaced for the samples obtained at 100 °C and 110 °C, while an intense band at 470 cm^{-1} typical of the ionic bonding between Fe and O, Fe-O-Fe [242] is present for the sample prepared at 120 °C consistent with the Fe₂O₃ formation. Therefore, MIL-88A (MW) synthesized

at 110 °C for 30 min in a microwave reactor was chosen as the sacrificial template for the subsequent synthesis of LDH.

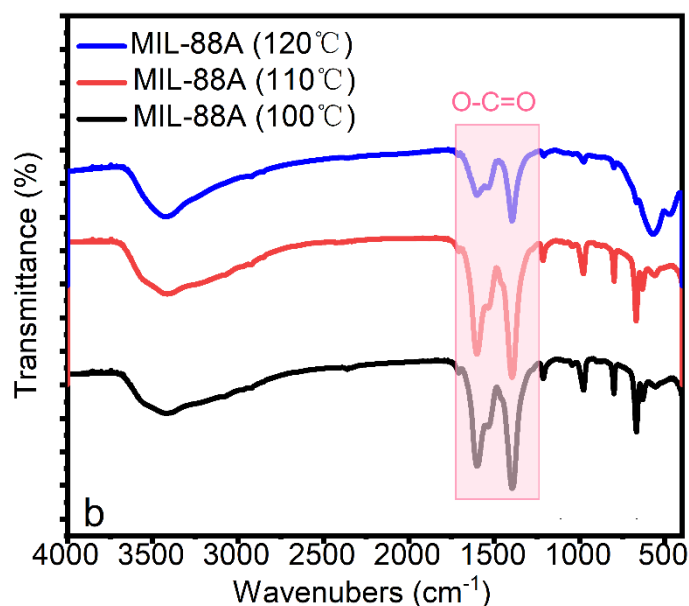
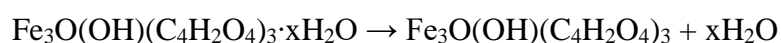


Fig. II-8 FTIR spectra of MIL-88A synthesised using MW at different reaction temperature.

II.2.2.5. Thermal behavior and porosity of MIL-88A (MW)

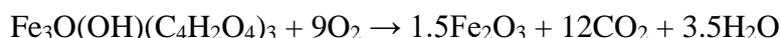
Thermogravimetric (TGA) provides a basis for further study of the thermal stability of MIL-88A. Fig.II-9 depicts the thermogravimetric stability of MIL-88A (MW) prepared under optimal conditions (30 min, 110 °C) and tested over a temperature range of 30-1000 °C. MIL-88A (MW) pyrolysis occurs in two main stages: the first stage of weight loss occurs below 150 °C as water molecules evacuate from the pores of the MIL-88A (MW) [243]. This process is endothermic and corresponds to the small endothermic (negative) peak on the DTA curve. The second stage of weight loss occurs between 150-292 °C and is primarily due to volatilization and degradation of unreacted organic solvents and organic ligands in the pores of the material and the decomposition of MIL-88A (MW), leading a solid residue corresponding to crystallized iron oxide Fe₂O₃ [244]. Based on the first weight loss, the number of water molecules per MIL-88A (MW) formulation unit can be calculated:



The solid residue is MIL-88A (MW) without moisture, and the experimental weight

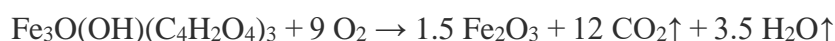
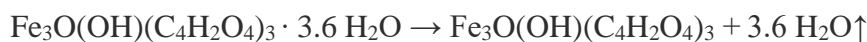
loss (WLexp) in this process corresponds to the evaporation of water. According to Fig. II-9 a, the WLexp is estimated to be 10.9%, and the calculation leads to $x = 3.6$.

The decomposition process of MIL-88A (MW) is as follows:



The theoretical value of WLth was calculated to be 56.0% through the decomposition process. The actual value of WLexp was calculated to be 55.6% based on the estimation of the TGA curve. The actual values of experimental weight loss obtained by thermogravimetric analysis agree with the formula of a MIL-88A(MW) $\text{Fe}_3\text{O}(\text{OH})(\text{C}_4\text{H}_2\text{O}_4)_3 \cdot 3.6\text{H}_2\text{O}$.

The loss of carbon and oxygen was calculated by the next two weight losses and the following results were obtained:



Therefore, the chemical formula of the MIL-88A (MW) is $\text{Fe}_3\text{O}(\text{OH})(\text{C}_4\text{H}_2\text{O}_4)_3 \cdot 3.6\text{H}_2\text{O}$.

The thermal stability of MIL-88A was followed from 30 to 1000 °C using in situ X-ray diffraction and the results are shown in Fig. II-9c. The characteristic peaks of MIL-88A (MW) were present up to 250 °C disappearing as the temperature increased, and finally transforming into Fe_2O_3 from 400 °C. The XRD of the MIL-88A (MW) is modified during the dehydration step with a shift of the peaks located at low angles attributed to a change of the MOF pore structure which has not been investigated in this work. These results are consistent with the TGA (Fig. II-9 b) which highlighted the degradation of organic ligands in MIL-88A (MW) between 250-300 °C, leading to the generation of metal oxides.

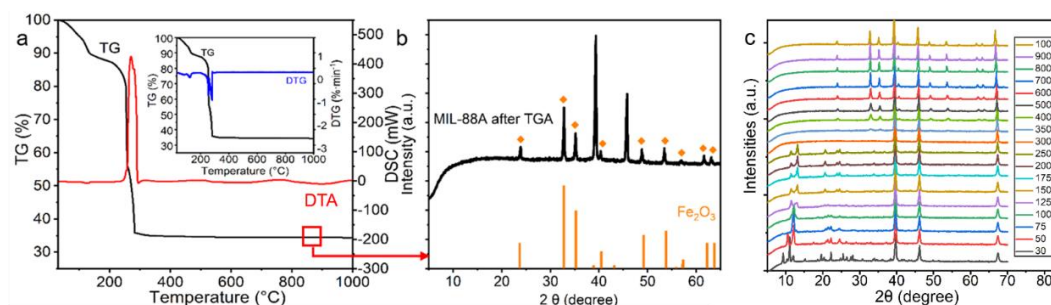


Fig. II-9 TGA/DTA of MIL-88A (MW) obtained at 110 °C for 30 min with DTG graph as insert (a) and (b) XRD pattern of MIL-88A (MW) residue after TGA, (c) In situ XRD results of MIL-88A (MW).

The porosity of the MIL-88A (MW) samples was investigated by nitrogen adsorption-desorption isotherm (Fig. II-10). The sample was degassed for 12 h at 150 °C under vacuum. The shape is of type II according to the International Union of Pure and Applied Chemistry (IUPAC) classification. This shape is typical of almost non porous materials. The specific surface area was calculated to be 18 m²/g based on the BET model with a pore diameter of about 3.1 nm. The measured porosity is notably lower than the expected value expected for microporous MIL-88A(MW). However, Wang et al. reported similar N₂ isotherm and specific surface area value for MIL-88A. This behaviour could be attributed to a collapse of the cage structure under dehydration blocking the pore accessibility.

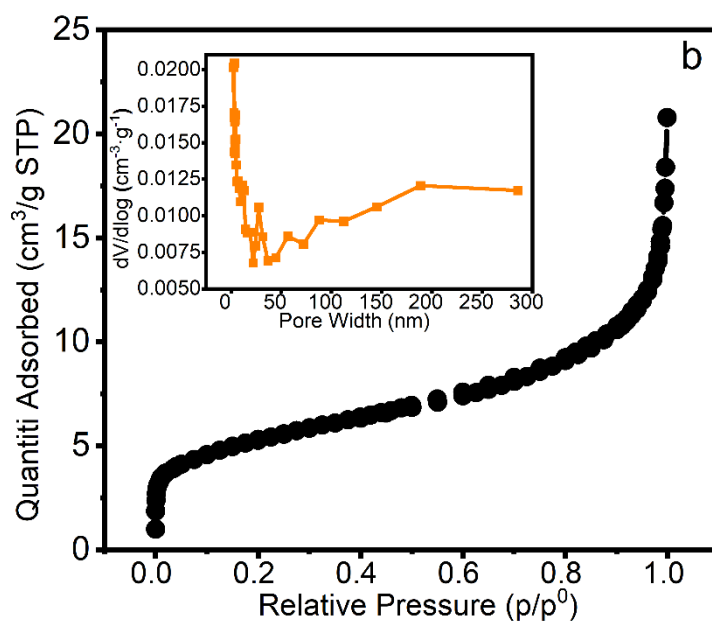


Fig. II-10 BET N₂ adsorption isotherm of MIL-88A (MW).

II.2.3. Conclusion

In this section, MIL-88A was successfully synthesized by both hydrothermal treatment and microwave activation. The MIL-88A (MW) synthesized using the microwave method exhibited the same characterization results as that synthesized using the hydrothermal method. Compared to the hydrothermal method, the microwave method consumes less energy, has a much shorter reaction time, and results in MIL-88A with a more uniform microstructure.

Optimal conditions for the MOF synthesis via the microwave method were also investigated showing that the optimized conditions are 110 °C for a 30 min reaction. MIL-88A (MW) generated under this condition exhibited a more homogeneous rod-like microstructure and increased stability. The structural formula of this MIL-88A was calculated as $\text{Fe}_3\text{O}(\text{OH})(\text{C}_4\text{H}_2\text{O}_4)_3 \cdot 3.6 \text{H}_2\text{O}$.

II.3. Conversion of MIL-88A to LDH/88A

II.3.1. Experimental section

II.3.1.1. Experimental material, instruments and procedure

II.3.1.1.1 Materials`

All chemicals were of analytical reagent grade. $\text{Ni}(\text{NO}_3)_2 \cdot 6\text{H}_2\text{O}$, NaOH and urea were purchased from sigma. Other chemicals applied are of analytical reagent grade or the highest purity available.

II.3.1.1.2 The conversion from MIL-88A (MW) to $\text{Ni}_x\text{FeLDH}/88\text{A}$

A mixture of MIL-88A, $\text{Ni}(\text{NO}_3)_2 \cdot 6\text{H}_2\text{O}$, and urea was stirred at room temperature, then sealed and heated using a microwave at various temperatures for different durations. The precipitate was subsequently washed three times with deionized water and ethanol, respectively [168].

Synthesis $\text{Ni}_x\text{FeLDH}/88\text{A}$ by two-step method: 50 mg of MIL-88A was dispersed in 4 mL of ethanol (solution A). 25 mg (0.08 mmol) 50 mg (0.17 mmol), 100 mg (0.34 mmol), 150 mg (0.52 mmol), 200 mg (0.69 mmol), 250 mg (0.86 mmol) of $\text{Ni}(\text{NO}_3)_2 \cdot 6\text{H}_2\text{O}$ and 100 mg (1.67 mmol) of urea were dissolved in 6 mL of deionized water (solution B) respectively. Solution A and solution B (solution C) were mixed with stirring at room temperature. Finally, solution C was sealed in a glass vial and reacted in a microwave heater at 110 °C for 1 h. The solution was washed with deionized water until there was no significant change in pH, then washed three times with ethanol and dried in a vacuum oven at 60 °C overnight. Finally $\text{Ni}_{0.5}\text{FeLDH}/88\text{A}$, $\text{Ni}_1\text{FeLDH}/88\text{A}$, $\text{Ni}_2\text{FeLDH}/88\text{A}$, $\text{Ni}_3\text{FeLDH}/88\text{A}$, $\text{Ni}_4\text{FeLDH}/88\text{A}$ and $\text{Ni}_5\text{FeLDH}/88\text{A}$ are obtained respectively [168].

II.3.1.1.3 Synthesis LDH/88A

Synthesis LDH/88A by single-pot method: 69.6 mg of fumaric acid and 288 mg of urea were dissolved in 15 mL of deionized water by stirring at room temperature. Sequentially, 567 mg of $\text{Ni}(\text{NO}_3)_2 \cdot 6 \text{H}_2\text{O}$ (1.95 mmol), 73.15 mg of $\text{Al}(\text{NO}_3)_3 \cdot 6 \text{H}_2\text{O}$ (Here, aluminium is present as a catalyst) (0.195 mmol) and 182.82 mg of $\text{Fe}(\text{NO}_3)_3 \cdot 9 \text{H}_2\text{O}$ (0.455 mmol) were added (the total molar value of nickel and iron is 0.65 mmol), and the mixed solution was transferred to a 20 mL Teflon-lined stainless steel autoclave, and the reaction was carried out at 110 °C for 6 h. After cooling, the solid was separated by centrifugation and evaporated with distilled water. After cooling, the solid was separated by centrifugation, washed with distilled water until there was no obvious change in pH, and then washed with ethanol for three times, and then dried in a vacuum oven at 60 °C overnight.

II.3.1.1.4 Synthesis $\text{Ni}_3\text{FeLDH/COP}$

Synthesis $\text{Ni}_3\text{FeLDH/COP}$ by coprecipitation method: 0.1 M ferric nitrate and 0.3 M nickel nitrate are dissolved in 100 mL of water (solution A). Separately 1 M sodium hydroxide and 0.05 M sodium hydroxide are dissolved in 50 ml of water (solution B). Solution A and solution B are slowly mixed under a nitrogen atmosphere with continuous stirring using a magnetic stirrer and maintaining a pH of 10.0. Stirring is continued overnight after full addition of the salt solution. The resulting mixture is then centrifuged and washed with ultrapure water until the pH remains unchanged and transferred to an oven at 40 °C for one day.

II.3.1.2. Morphological and structural characterization

The morphology of materials was analysed using a Field Emission SEM (JEOL JSM-6700, Japan) and Transmission Electronic Microscopy (TEM) (JEOL JEM-2010, Japan). Powder X-ray diffraction patterns were recorded with a Philips X'Pert automated X-ray diffractometer using $\text{CuK}\alpha$ radiation ($\lambda = 0.154051 \text{ nm}$), over the 2-70° (2 θ). FTIR spectra were recorded with a Nicolet 5,700 spectrometer from Thermo Electron Corporation using the KBr pellet technique. Thermogravimetric (TG) curve was measured using a thermogravimetric analyzer (ISI TGA i1000, USA) at a heating rate of 40 °C/min from 25 to 1000 °C in nitrogen. The specific surface areas were

measured using N₂ adsorption isotherm and an automatic surface analyzer (TriStar II 3020, Micromeritics, USA) by Brunauer-Emmett-Teller (BET) theory.

II.3.2. Investigation of the protocol for NiFe-LDH/88A formation

II.3.2.1. Synthesis methods

In this study, the conversion of MIL-88A into NiFe-LDH/88A (ratio of Ni to Fe was 3) was investigated using procedures previously reported in the literature, aiming to produce 3D hollow LDH nanostructures. Given [168] that the one-pot method has been reported to yield hollow LDH nanostructures for other compositions, we also tested its applicability to NiFe-LDH/88A [245]. The XRD results of the LDH synthesized by both the single-pot and two-step methods (Fig. II-11) show similar characteristics with the presence of the reflections expected for a typical hydroxide structure. The two intense reflection lines at 11.2° and 22.6° correspond to the harmonics (003) and (006), while the other belongs to the 0kl, and hkl reflections at 34.7°, 38.5°, 46.1° and 60.7° corresponding to the (012), (015), (018) and (110)/(113), respectively.

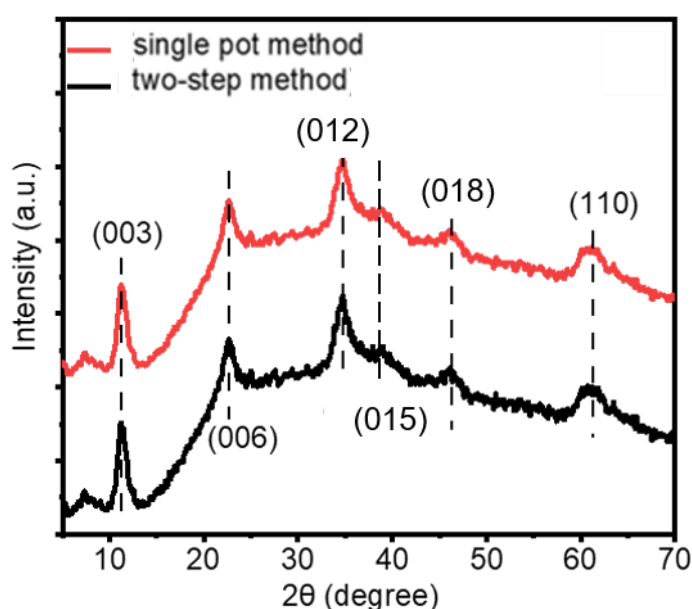


Fig. II-11 XRD results of Ni_xFe-LDH/88A (x = 3) derived from MIL-88A through different ways.

In the same way, the FTIR spectra show similar results for NiFe LDH/88A synthesized by both methods (Fig. II-12). The broad absorption band centered at 3430 cm^{-1} corresponds to the O-H stretching vibrations of the ligand hydroxide ions or entrapped/adsorbed water molecules, and the bands at 1568 and 1383 cm^{-1} are attributed to symmetric and asymmetric vibrations of the carboxyl groups attributed to fumarate coming from MOF. The shift of these vibration under MIL88A conversion (1656 cm^{-1} and 1393 cm^{-1}) towards values observed for carboxylates intercalated in LDH reveals a change in the bonding of the fumarate anions. The presence of these two intense bands, in absence of the carbonate or nitrate band observed usually at 1370 cm^{-1} supports the intercalation of fumarate in a lying position as observed for oxalate [246]. For both, Fe-O vibration is present at 661 and 671 cm^{-1} , for single pot and two step method. Note that the IR spectra of NiFe-LDH/88A synthesized by two-step method displays a Fe-O deformation band at 519 cm^{-1} , which is attributed to MIL-88A as a backbone.

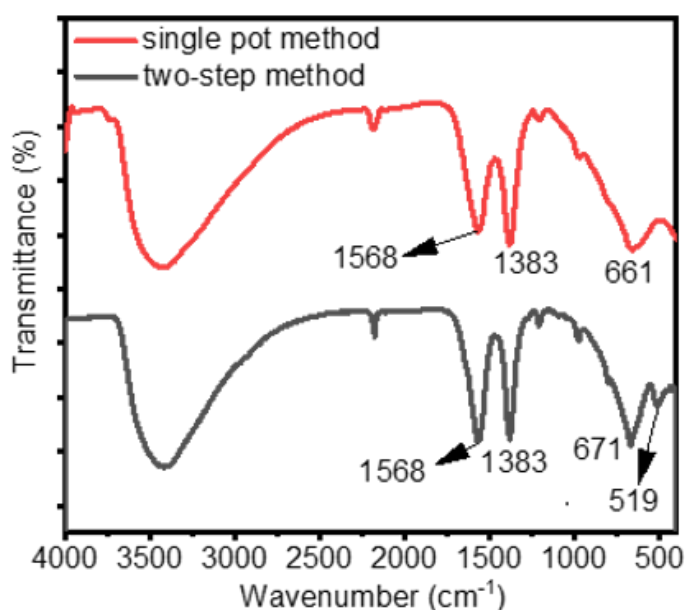


Fig. II-12 FTIR spectra of $\text{Ni}_x\text{Fe-LDH/88A}$ ($x = 3$) derived from MIL-88A through different ways.

Fig. II-13 show the TEM images of the single-pot method and the NiFe-LDH/88A derived from MIL-88A, respectively. The one-step generation displayed the rod-like structure of MIL-88A conjointly with an additional granular material on the surface. The rod structure as a skeleton is not well maintained. This may be due to the presence

of two successive reactions in the single-crucible method:

- 1) formation of MIL-88A and its conversion of NiFe-LDH/88A and
- 2) the direct coprecipitation of NiFe-LDH/88A phase.

During the reaction process, when the temperature reaches 110 °C, the two reactions are carried out at the same time, thus leading to the formation of two different morphologies. The reaction was carried out in a reactor with a long reaction time (6 h) and no stirring operation, which favours both the formation of MOF precipitate and its conversion into LDH, while simultaneously causing the precipitation of LDH on the side.

Fig. II-13 (c) and (d) show that the Ni₃Fe-LDH/88A synthesized by the two-step method maintains the rod-like structure of MIL-88A template intact. The petal-like structure of the surface is uniformly distributed on the surface of the rod structure. However, the shaded part in the middle suggests that the MOF conversion may not be fully completed at the surface, and a phase still remains in the inner part of the hollow structure. Obviously, the ultra-thin and uniform Ni₃Fe-LDH/88A arrays were produced on the surface of MIL-88A. These features suggest that MIL-88A plays a key role in providing iron, which is required for the growth of ordered NiFe-LDH/88A nanoplatelets.

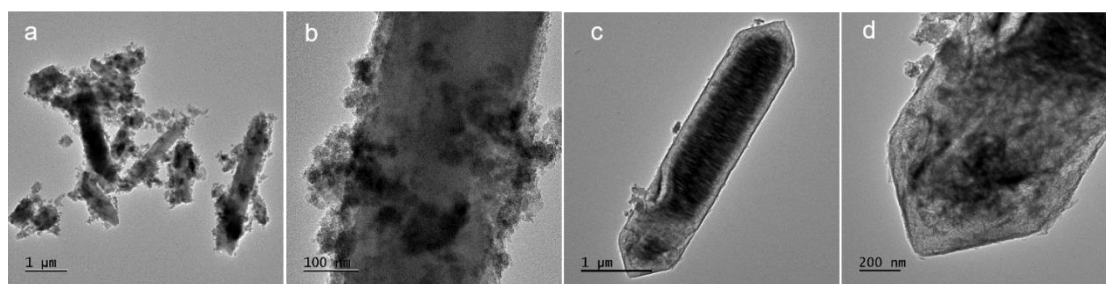


Fig. II-13 TEM images of NiFe LDH/88A synthesized by (a) (b) the one-pot method (HT 110 °C - 6 h), (c) (d) the two step method (MW 110 °C - 1 h).

MIL-88A participates in the reaction with its stable rod-like structure. In the microwave reactor, the glass tube can be heated uniformly and the reaction time is short, leading to a complete conversion process. In summary, the two-step method proves to be superior in converting pre-synthesized stable MIL-88A into NiFe-LDH/88A using microwaves. Not only was the reaction time significantly reduced, but the stability of

the NiFe-LDH/88A rod skeleton was also increased.

II.3.2.2. Influence of temperature and time of reaction in the two-step method

The NiFe-LDH/88A was prepared using the two-step method by varying the reaction temperature and reaction time, while other conditions (ion concentration, urea addition, etc.) were kept constant throughout the process.

The XRD patterns of NiFe-LDH/88A derived from MIL-88A (MW) under different microwave heating temperature and time conditions are shown in Fig. II-14. Except for the temperature of 90 °C at short time (30 °C and 60 °C), systematically the typical LDH reflections are present.

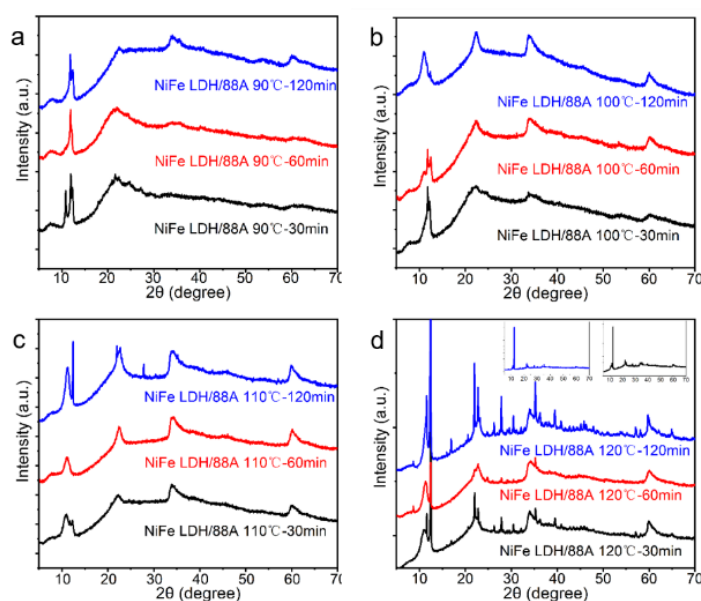


Fig. II-14 XRD patterns of NiFe-LDH/88A synthesized using two step method (a) at 90 °C, (b) at 100 °C, (c) at 110 °C, (d) at 120 °C with increasing time from 30 min to 60 min

The maintain of the MIL-88A structure is mainly followed by the maintain or not of the sharp reflection at 13.2° in 2θ. Clearly, the results indicate that:

- A low temperature (90 °C) leads only to a partial amorphization of the MOF, and does not allow an efficient NiFe LDH/88A coprecipitation. Low

temperature of 90 °C does not promote a full conversion of the MIL-88A and NiFe-LDH/88A crystallization especially at 30 min and 60 min.

- The intermediate temperatures (100 °C and 110 °C) and intermediate time (60 °C) are the most suitable to favor the formation of NiFe-LDH/88A as unique crystalline phase into the materials. When the temperature is 100 °C, there are obvious characteristic peaks of NiFe-LDH/88A, but the (101) plane belonging to MIL-88A can still be detected at 12.4 °.
- The use of a higher temperature of 120 °C obviously favors the stabilization of the MIL-88A, which is clearly shown after 60 min of reaction by the presence of its intense diffraction line.

In order to explore the optimal synthesis time of LDH, further exploration was carried out at 110 °C, and the results are shown in Fig. II-15. At time lower than 60 min MIL-88A is not fully converted while from 75 min, there are additional sharp peaks which gradually increase with time. Therefore, increasing the reaction temperature and time can promote the synthesis of LDH, but when the temperature and reaction time are too high, a side crystalline phase appears. Finally, it is noteworthy that optimized conditions are 110 °C and 60 min, leading to pure NiFe crystallized LDH without the characteristic peaks of MIL-88A.

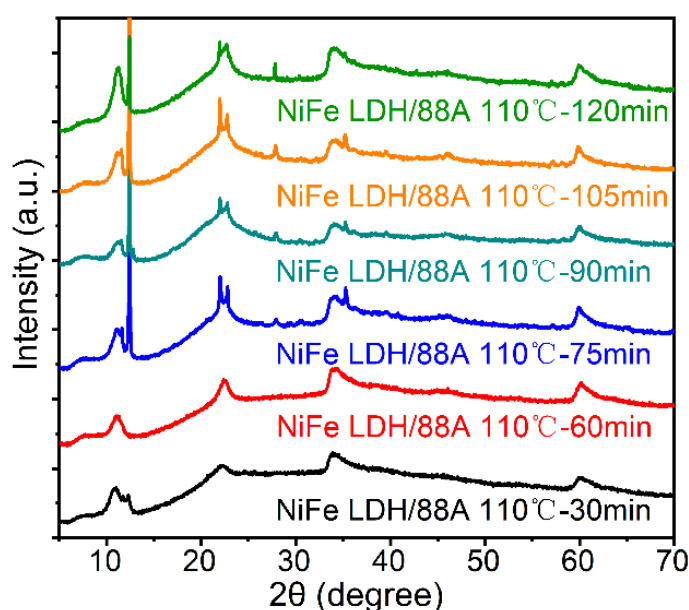


Fig. II-15 XRD results of LDH synthesized at different reaction temperatures of 110°C.

The ability of MOF to be converted into NiFe-LDH/88A can also be demonstrated in the SEM results Fig. II-16. By comparing, the morphology of the materials obtained after 30 min at different temperature, it is evident that a too low temperature leads to the maintain of MIL-88A pencil-like morphology conjointly with few ill-defined aggregates. When the reaction temperature was raised to 110 °C, the lamellar structure of LDH fully and uniformly covers the surface of the rod structure. After heating at 120 °C for 30 min, the rod-like structure of MIL-88A breaks up leading to large piece of particles on which can be seen many agglomerates.

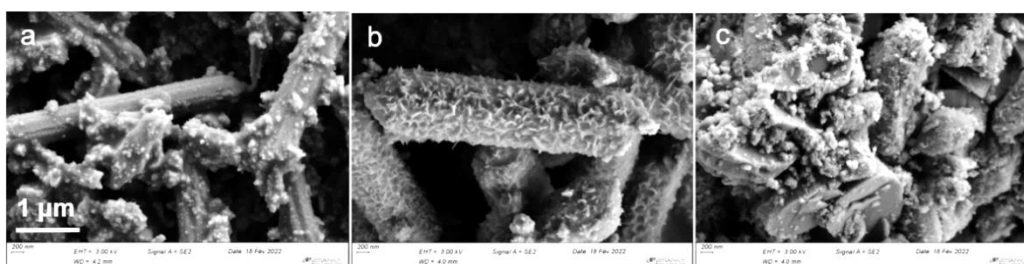


Fig. II-16 SEM images of NiFe-LDH/88A synthesised in two-step method in different conditions. (a) 90 °C for 30 min, (b) 110 °C for 30 min, (c) 120 °C for 30 min.

To further understand the effect of reaction time on the local geometry around Fe and Ni atoms, the Fourier transform (FT) and real components of extended X-ray absorption fine structure (EXAFS) spectra at the Fe K-edge and Ni K-edge were measured. MIL-88A and NiFe-LDH/COP were also analysed for comparison purpose, where NiFe-LDH/COP was synthesized by co-precipitation of LDH with a nickel-iron ratio of three. The two peaks observed in the FT spectra between 1-2 Å and 2-3.2 Å correspond to the first metal-oxide shell and second metal-metal shell, respectively, for the two edges. Fig. II-17 a presents FT and real-component spectra measured at the Fe K-edge. The first shell region between 1-2 Å and the second one between 2-3.2 Å show only a marginal variation in the FT peak position and real-component position. The results show that the length of Fe-O bond and Fe environment are not affected by the conversion time, the local Fe environment being stabilized after only 30 min. It is noteworthy that the environment of Fe in MIL-88A converted in NiFe-LDH/88A, and co-precipitated NiFe-LDH/COP is almost indistinguishable evidencing that the Fe atoms display the same local order in all the materials. From the Ni results (Fig. II-17

b), a net evolution is observed. As the reaction time increased:

- The peak between 1-2 Å for MIL-88A converted in LDH is almost unmodified but its intensity is lower than that observed for NiFe-LDH coprecipitated.
- The peaks at 2-3.2 Å increased progressively which could traduce the insertion of Ni into the Fe oxy hydroxide formed leading to LDH structure.
- The peak between 5-6 Å went from absent to present, evidencing a long-distance order as usually observed for LDH [247].

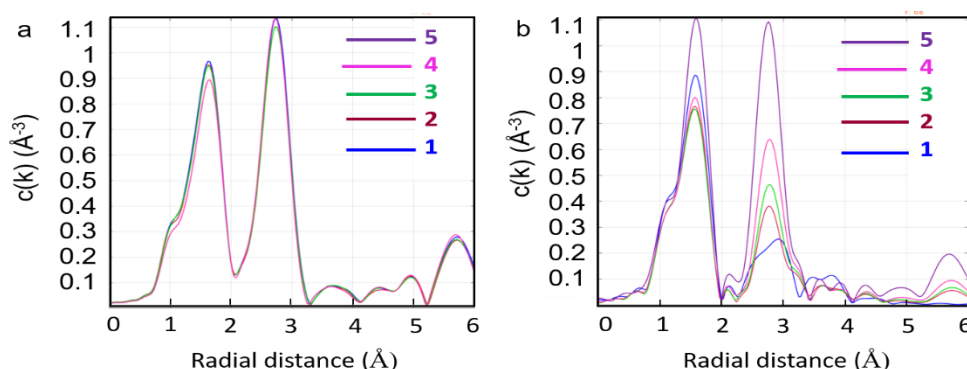


Fig. II-17 X-ray absorption fine structure of (a) Fe-Kedge; (b) Ni-Kedge; (1) MIL-88A, (2) NiFe LDH/88A 110 °C 30 min, (3) NiFe-LDH/88A 110 °C 60 min, (4) NiFe LDH/88A 110 °C 120 min (5) NiFe-LDH/COP.

II.3.2.3. Molar ratio of Ni/Fe

In order to determine the influence of molar ratio of Ni/Fe initially involved in the synthesis, NiFe-LDH/88A were synthesized using different molar ratios of Ni/Fe while keeping other conditions constant. The XRD patterns of the obtained samples with different Ni/Fe molar ratios are shown in Fig. II-18. Regardless of the Ni/Fe ratios used, XRD diagrams show that the crystalline structure of MIL-88A is no longer present and is replaced by diffraction peaks of the NiFe-LDH/88A structure even for very low ratios, which is unfavourable for the formation of a pure NiFe-LDH/88A structure, evidencing that NiFe-LDH/88A are the only crystalline phase present. Systematically, the diffraction peaks of 2θ at 11.6° , 22.6° , 34.2° and 60.2° can be observed which belong to the (003), (006), (012) and (110) reflections of NiFe-LDH/88A. According to XRD, the obvious NiFe-LDH/88A structure appears even when the nickel-iron ratio

is 0.5. Generally speaking, the larger the crystal size, the better the crystal state of the sample. However, in the XRD pattern, there is no significant variation in the width or intensity of the reflections, suggesting initially that similar LDH crystallinity is obtained for all ratios.

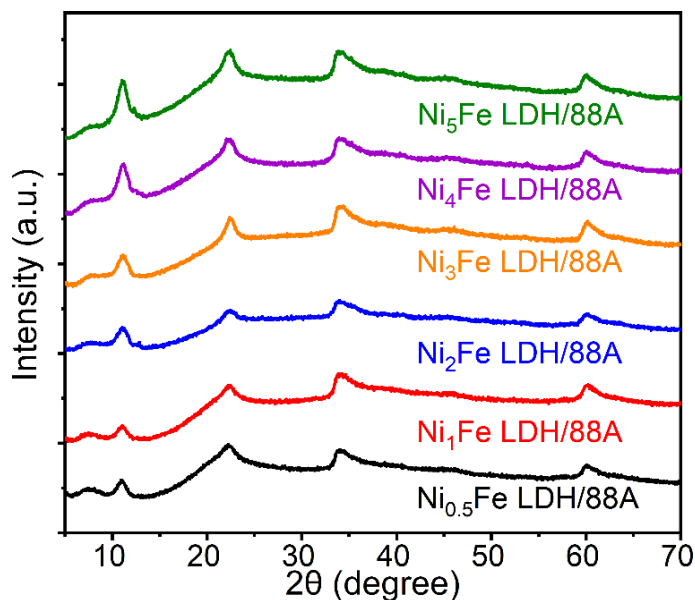


Fig. II-18 XRD results of NiFe-LDH/88A synthesized at different molar ratio of Ni/Fe.

The SEM images of the different materials (Fig. II-19) provide evidence contrary to the XRD and show the evolution of the morphology. Consistently, the pencil-like morphology of MIL-88A is observed even in the absence of the crystalline structure of the MOF. When Ni/Fe ratios are 0.5 and 1, a sheet structure forms on the surface of the rod structure, but does not completely cover it. When Ni/Fe increase to 2, in addition to the sheet, granular material appears and the surface becomes rough. When the Ni/Fe ratio increases to 3, the surface of pencil-like morphology is almost completely covered by petal-like material. When the ratio is 3, the distribution of petal-like material is the most uniform, with almost no presence granular material. At higher ratio (4 and 5) the covering of the surface appears to be denser, which seems to indicate that the increase of the Ni/Fe ratio favours the crystal growth of the NiFe LDH/88A platelets at the surface of the sacrificial MOF.

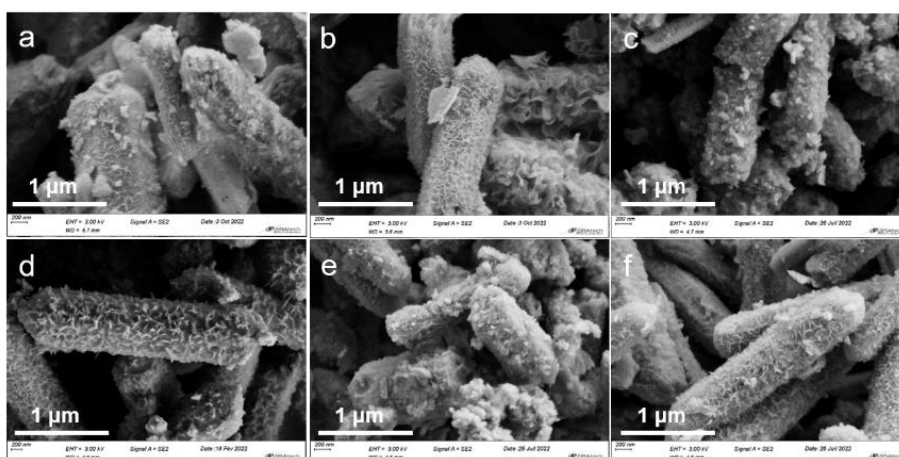


Fig. II-19 SEM results of NiFe-LDH/88A synthesized at different ratio of Ni/Fe. (a) 0.5, (b) 1, (c) 2, (d) 3, (e) 4, (f) 5.

EDS and ICP elemental analysis were performed on NiFe-LDH/88A with different Ni to Fe ratios, and the results obtained are shown in the Table. II-1. For both ICP and EDS analysis, the experimental Ni/Fe ratio for LDH/88A increases when nickel content increases, but remains always lower than the expected value for a total coprecipitation., For a Fe/Ni ratio of 3, the experimental Energy Dispersive X-ray Spectroscopy (EDS) ratio surprisingly deviates from the expected trend, showing a value close to the expected ratio. However, the Inductively Coupled Plasma (ICP) result aligns more coherently with the increasing trend. This EDS experiment should be reproduced.

In presence of an excess of nickel, some of the nickel diffuse into the interior of the LDH "shell" to react with the iron, leading in surface (EDS) to a lower value compared to ICP. In summary, the optimal conditions for the conversion of MIL-88A to NiFe-LDH/88A were as follows: MIL-88A is used as a precursor with a nickel-iron ratio of 3, mixed with urea and then heated to 110 °C in a microwave reactor for 60 min. In all instances, we observed that the obtained Ni/Fe ratios are lower than the expected value for a pure Layered Double Hydroxide (LDH) phase, where Ni/Fe should be greater than 2/1.

Table. II-1 Actual Fe/Ni ratio of LDH synthesized with different Fe/Ni ratios.

		Ni _{0.5} Fe	Ni ₁ Fe	Ni ₂ Fe	Ni ₃ Fe	Ni ₄ Fe	Ni ₅ Fe
Ni/Fe	EDS	1.16	1.27	1.28	2.88	1.35	1.55
	ICP	1.10	1.27	1.31	1.45	1.60	2.01

II.3.3. Characterization of LDH/88A

Ni₃FeLDH/88A was characterized and compared to, Ni₃FeLDH/COP, synthesized by conventional co-precipitation method. The XRD results of the two LDHs are shown in Fig. II-20. Peaks at 11.0°, 22.5°, 34.1° and 60.1° can be assigned to the (003), (006), (012) and (110) surfaces of hydrotalcite-like structures [248, 249]. The basal spacing values which corresponds to the $d_{003} = 7.95 \text{ \AA}$ is very close to the one of the co-precipitation synthesis of Ni₃FeLDH/COP., $d_{003} = 7.67 \text{ \AA}$. The XRD results of Ni₃FeLDH/88A exhibits typical LDH layered structural features with nearly identical layer spacing.

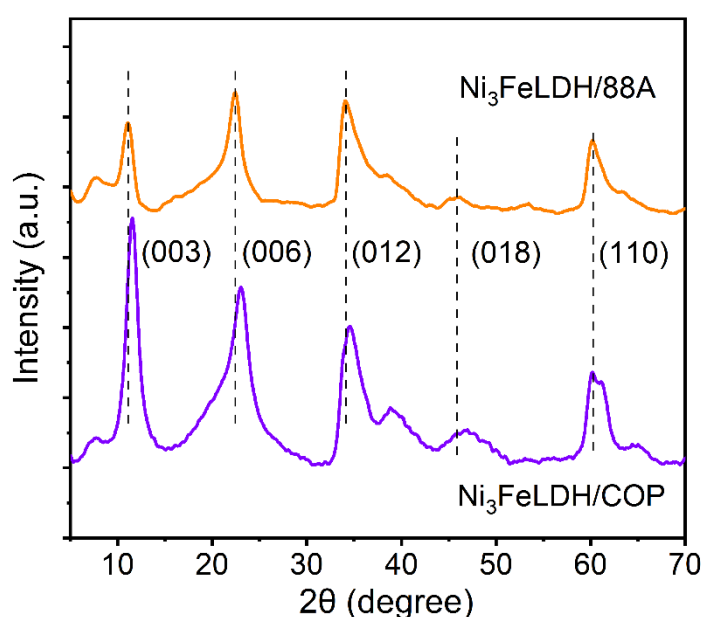


Fig. II-20 XRD results of Ni₃FeLDH/88A and Ni₃FeLDH/COP.

On the FTIR spectra of Ni₃FeLDH/88A (Fig. II-21), the broad band in the range of 3200-3700 cm⁻¹ corresponds to the O-H telescopic vibration of the metal hydroxide layer and interlayer water molecules. The strong broad band at 3429 cm⁻¹ was related to the stretching vibrations of the H-bond of the OH group (ν O-H) in the brucite-like layers[250, 251]. The stretching vibration (ν CO₂) symmetric and asymmetric of carboxylate in the interlayers appeared at 1567 cm⁻¹ and 1379 cm⁻¹ as reported earlier, indicating the presence of fumarate, which is unexpected in the Ni₃FeLDH/COP sample.

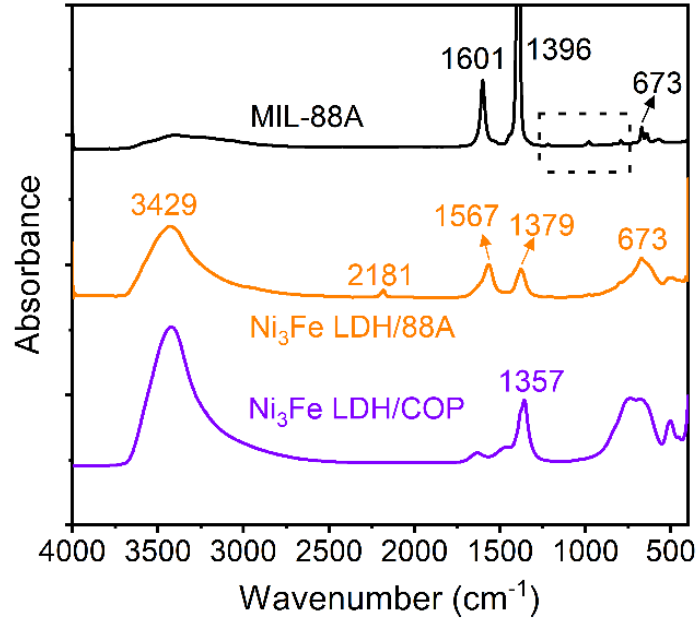


Fig. II-21 FTIR results of MIL-88A, Ni₃FeLDH/88A and Ni₃FeLDH/COP.

Fig. II-22 reveals the morphology of Ni₃FeLDH/88A. SEM image (Fig. II-22 a) clearly shows that Ni₃FeLDH/88A exhibits a uniform 3-dimensional layered nanocrystal morphology with an average length for the individual platelets of approximately 200 nm. Compared with MIL-88A, the length of the templated materials does not change significantly, and the smooth surface became a rough petal-like shell composed of nano-platelets growing perpendicularly to the surface of the template. In addition, these tiny Ni₃FeLDH/88A particles are crystallized, which are determined by strong polycrystalline rings in selected region electron diffraction (SAED) patterns collected from a single derived primary nanosheets. Interconnected Ni₃FeLDH/88A nanosheets are loosely stacked to form a highly porous structure. The Energy Dispersive Spectroscopy (EDS) image of Ni₃FeLDH/88A, showing even distribution of Fe, Ni, and O elements, is consistent with successful coating of LDH onto the MIL-88A template surface. The EDS element mapping image also confirms the different distributions of Ni, Fe and O in the nanostructure with Ni, Fe and O evenly distributed on interconnected LDH nanosheets.

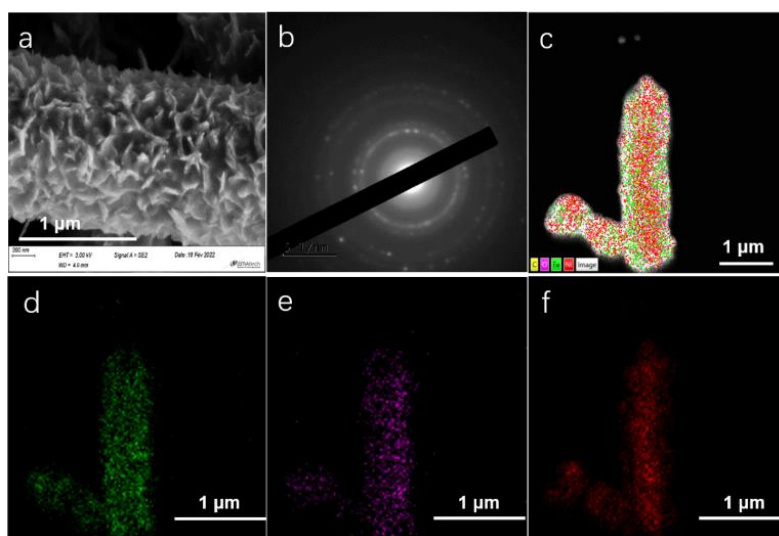


Fig. II-22 Morphology of $\text{Ni}_3\text{FeLDH}/88\text{A}$. (a) SEM; (b) SAED; (c) TEM EDS of $\text{Ni}_3\text{FeLDH}/88\text{A}$, distribution of the four elements of C, O, Fe and Ni; (d) Distribution of Fe; (e) Distribution of O; (f) Distribution of Ni.

Fig. II-23 a shows the Zeta potential results at increasing pH. MIL-88A and LDH exhibit very similar curves with a positive value of ζ at low pH that progressively decreases as the pH increases. The isoelectric point of $\text{Ni}_3\text{FeLDH}/88\text{A}$ is 10.3, which is not much different from the MIL-88A. The zeta potentials of MIL-88A, $\text{Ni}_3\text{FeLDH}/88\text{A}$ and $\text{Ni}_3\text{FeLDH}/\text{COP}$ at a pH of 7 are compared and the results shows that of MIL-88A and $\text{Ni}_3\text{FeLDH}/88\text{A}$ were much lower.

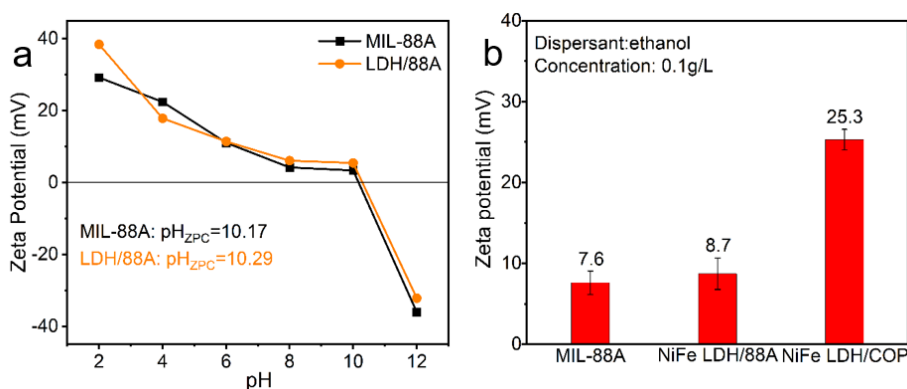


Fig. II-23 Zeta potentials (a) vs pH for MIL-88A and $\text{Ni}_3\text{FeLDH}/88\text{A}$ (b) of MIL-88A, $\text{Ni}_3\text{FeLDH}/88\text{A}$ and $\text{Ni}_3\text{FeLDH}/\text{COP}$ at pH 7.

Based on the classification of N₂ adsorption-desorption isotherms (Fig. II-24) according to IUPAC [252], the Ni₃Fe LDH/88A isotherm belongs to the type IV isotherm with H3-type hysteresis loop [253], which indicates that the sample has a mesoporous structure that is caused by particle aggregation [254]. Ni₃FeLDH/COP exhibits the same type of isotherm, characteristic of mesoporous solids with relatively small surfaces [25]. The main difference observed lies in the hysteresis, which does not exhibit the same shape, indicating a difference in pore geometry according to the synthetic procedure. Meanwhile, the BET specific surface area of Ni₃FeLDH/88A is 80.3 m²·g⁻¹, which is slightly larger than that of pure MIL-88A (50.3 m²·g⁻¹) and Ni₃FeLDH/COP (92.8 m²·g⁻¹) under the same conditions. This increase in BET specific surface area may be due to the organisation of graded LDH on the surface of MIL-88A [238, 255]. The average pore size of Ni₃FeLDH/88A is 3 nm, which is the same as the average pore size of Ni₃FeLDH/COP.

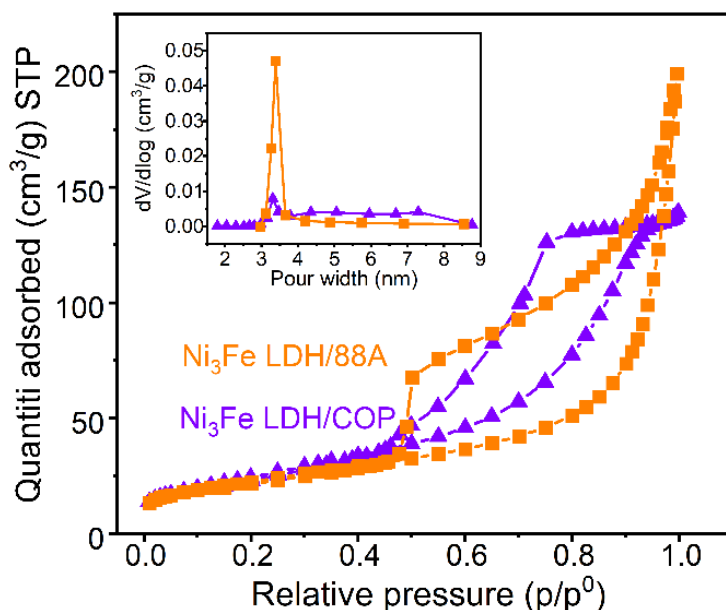


Fig. II-24 BET results of Ni₃FeLDH/88A and Ni₃FeLDH/COP.

II.3.4. Conclusion

In conclusion, MIL-88A was successfully synthesized as a precursor to Ni₃FeLDH/88A. The optimal conditions for the synthesis were defined as a nickel-iron ratio of 3 and heating at 110 °C for 60 min in a microwave reactor. The synthesized

Ni₃FeLDH/88A not only has the typical lamellar structure of LDH, but also can maintain the rod-like microstructure of MIL-88A. Iron and nickel are uniformly distributed on the surface of the rod-like structure. This Ni₃FeLDH/88A has a mesoporous structure with an isoelectric point of 10.3.

II.4. Synthesis and characterization of LDO/88A

II.4.1. Experimental section

Synthesis of Ni₃FeLDO/88A: Ni₃FeLDO/88A was obtained by calcination of Ni₃FeLDH/88A previously prepared, in a muffle furnace at 200, 300, and 400 °C for 2 h under air.

Synthesis of Ni₃FeLDO/COP: Ni₃FeLDH previously prepared by coprecipitation was calcined in a muffle furnace at 300 °C for 2 h under air to obtain Ni₃FeLDO/COP.

II.4.2. Results and discussion

In order to prepare NiFe based oxides and mixed oxides derived from LDH previously described, in a first attempt thermal analysis was performed.

The XRD results of Ni₃FeLDO/88A and Ni₃FeLDO/COP obtained by calcining at different temperatures were also recorded and are shown in Fig. II-25. After calcination of Ni₃FeLDH/88A at 200 °C which mainly correspond to the dehydrated materials, the XRD pattern exhibited mainly a shift of the (003) diffraction line to higher angles and the disappearance of the 006 reflection. This behaviour traduces a contraction of the interlayer space which could be due to a reorganization of the interlayer species after removal of the water molecules. Calcined at 200 °C, the resulting Ni₃FeLDO/88A-200 still retains the characteristic (012) and (110) peaks of LDH. Due to the collapse of the LDH structure, the characteristic peaks of LDH disappeared completely when the temperature was increased above 300 °C, in good agreement with the TGA curves (Fig. II-29). The characteristic diffraction peaks at 30.47 and 35.73 degrees are (220) and

(311) facets, respectively, which correspond to the spinel phase of NiFe_2O_4 (JCPDS Data Card No. 54-0964) [256]. Obvious peaks located at 37.23° , 43.32° , and 62.90° could be indexed to the (111), (200), and (220) planes of NiO (JCPDS 47-1049) [257]. When the calcination temperature was increased to 400°C , three additional peaks were attributed to Fe_2O_3 [258]. As a control, we calcined the co-precipitated LDH at 300°C to obtain $\text{Ni}_3\text{FeLDO/COP-300}$, whose XRD results are also consistent with those of NiO and NiFe_2O_4 materials, as expected for LDH decomposition. However, the additional crystallization of Fe_2O_3 is not observed for this latter, indicating that it could be due to an excess of Fe species into the starting materials due to an incomplete conversion of the template MOF in LDH.

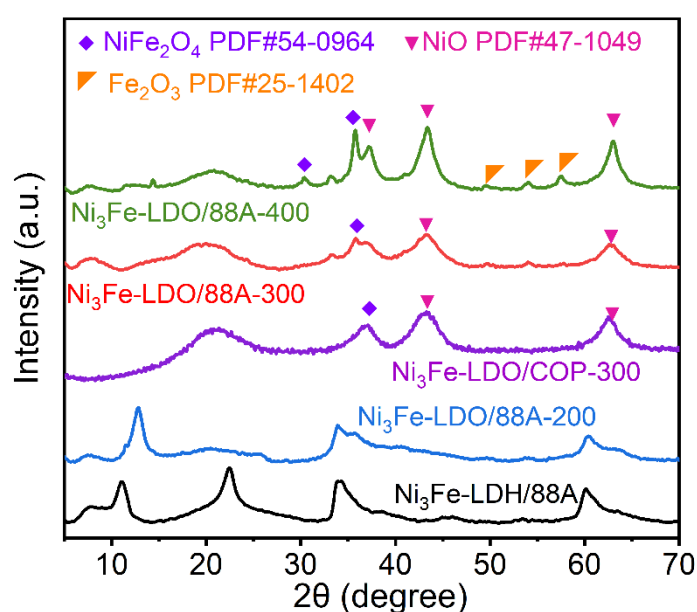


Fig. II-25 XRD of $\text{Ni}_3\text{FeLDH/88A}$, $\text{Ni}_3\text{FeLDO/88A}$ obtained after calcination at 200°C , 300°C and 400°C and $\text{Ni}_3\text{FeLDO/COP}$ obtained after calcination at 300°C .

Fig. II-26 shows the FTIR spectra of $\text{Ni}_3\text{FeLDO/88A}$ and $\text{Ni}_3\text{FeLDO/COP}$ samples calcined at different temperatures. The strong and broad adsorption band of $3350\text{-}3500\text{ cm}^{-1}$ is associated with O-H stretching vibrations generated by hydroxyl groups in the interlayer water molecules [259]. For $\text{Ni}_3\text{FeLDH/88A}$, the bands at 1567 and 1385 cm^{-1} arise from the vibration of the carboxyl group ($\text{O}=\text{C}-\text{O}$), which is attributed to the precursor of MIL-88A [260] as previously described. After thermal treatment at 200°C , the ν_{OH} significantly decreases in agreement with water removal and the carboxyl bands shift to lower wavenumber with a significant decrease of their

intensity which should be related to the contraction of the interlayer distance observed in the XRD pattern. At 300°C and above, the carboxylate bands disappear due to the removal of interlayer anions and dihydroxylation of the structure. The band at 1640 cm^{-1} is ascribed to the bending vibration of water [261]. The band between 500 and 680 cm^{-1} is attributed to metal-oxygen bonding, namely M-O. The band at about 672 cm^{-1} is attributed to Fe-O bonding [262]. The peaks at about 519 cm^{-1} is assigned to bonding between Ni and O [263]. The strength of M-O decreases with increasing calcination temperature and the spectra are modified in agreement with the oxides and mixed oxides formation. Meanwhile, $\text{Ni}_3\text{FeLDO}/88\text{A}-300$ and $\text{Ni}_3\text{FeLDO}/\text{COP}-300\text{A}$, which are calcined at 300 °C are compared, with mainly similar characteristic bands.

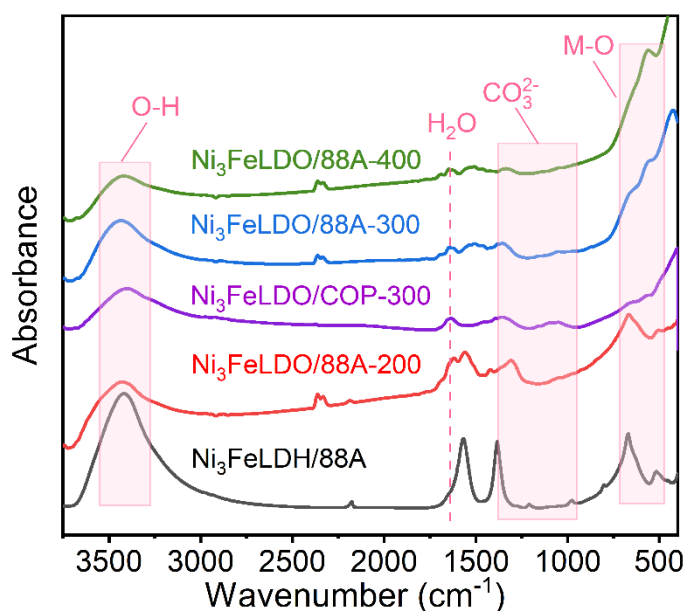


Fig. II-26 FTIR of $\text{Ni}_3\text{FeLDH}/88\text{A}$, $\text{Ni}_3\text{FeLDO}/88\text{A}$ obtained after calcination at 200 °C, 300 °C and 400 °C and $\text{Ni}_3\text{FeLDO}/\text{COP}$ obtained after calcination at 300 °C.

The morphological characteristics of the particles are shown on the SEM images in Fig. II-27. When the calcination temperature is below 300 °C, the lamellar structure on the surface of the rod structure can still be observed, which indicates that the decomposition doesn't lead to a morphological change. And when the temperature rises to 400 °C, a large number of granular structures appears, and this result is consistent with the XRD results and further crystallization of the oxide phases. The structure of $\text{Ni}_3\text{FeLDO}/\text{COP}-300$ is in the form of large irregular blocks with irregular surface distribution of lamellar structure, which is significantly different from that of

Ni₃FeLDO/88A-300, highlighting that the template synthesis allowed to prepare a 3D nanostructure which is maintained upon thermal treatment.

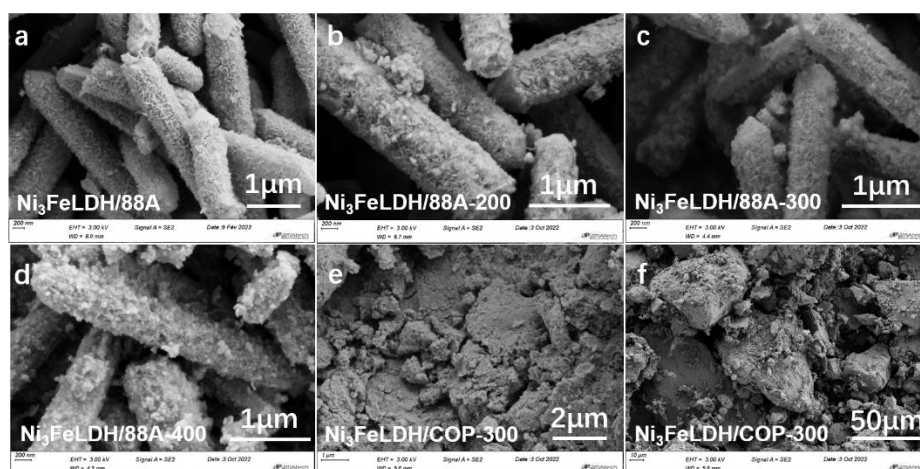


Fig. II-27 SEM results of (a) Ni₃FeLDH/88A, (b) Ni₃FeLDO/88A-200, (c) Ni₃FeLDO/88A-300, (d) (e) Ni₃FeLDO/COP-300.

The energy dispersive X-ray spectrum (EDS) in Fig. II-28 shows that the Ni₃FeLDO/88A-300 sample consists mainly as expected of O, Ni and Fe. The nickel-iron ratio after calcination is 1.9, which is slightly higher than the iron to nickel ratio of LDH before calcination (1.45 from ICP).

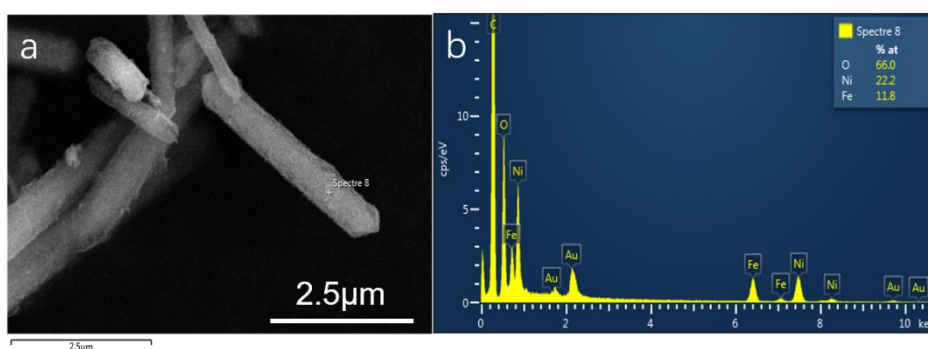


Fig. II-28 EDS (of SEM) results of Ni₃FeLDO/88A-300.

Fig. II-29 depict the thermograms of Ni₃FeLDH/88A and Ni₃FeLDH/COP, measured in air over a temperature range of 35-1000 °C. For both compounds, two main events are observed: a first between 25 °C and 250 °C (around 13% of weight loss) which corresponds to the removal of adsorbed and interlayer water and a second centered at 300 °C attributed to the de-hydroxylation and decomposition of the

interlayer anions. Surprisingly, for Ni₃FeLDH/88A the first event is continuous which could be due to the peculiar porosity of the phase obtained. The total weight losses for both are similar (less than 35%) even if it is slightly higher for Ni₃FeLDH/88A which could be due to the intercalation of fumarate in between the layer.

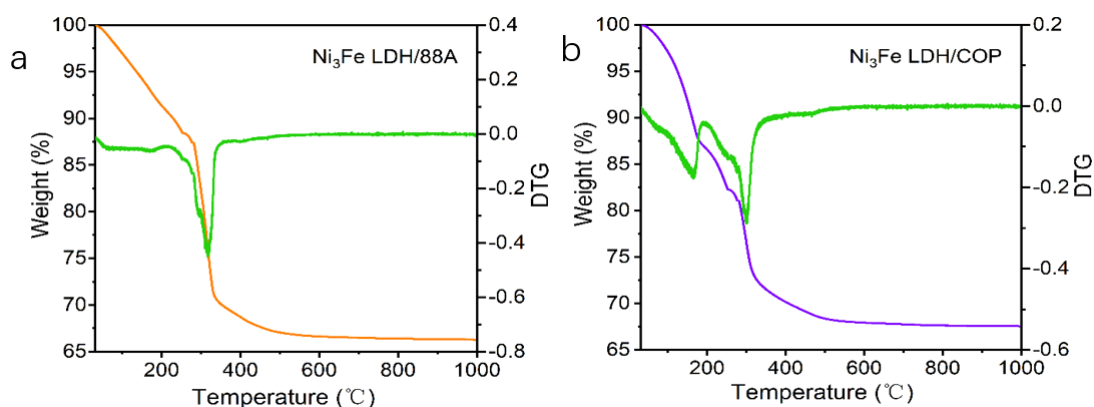


Fig. II-29 TGA and DTG curves of (a) Ni₃FeLDH/88A and (b) Ni₃FeLDH/COP.

Fig. II-30 shows the nitrogen isotherm measured for Ni₃FeLDH/88A and Ni₃FeLDO/88A samples calcined at different temperatures. The isotherms of both Ni₃FeLDH/88A and Ni₃FeLDO/88A are of type IV with H3 hysteresis loops, which is characteristic of mesoporous materials [264]. Further observations revealed that the hysteresis loop characteristics of Ni₃FeLDO/88A began to differ as the calcination temperature increased. This characteristic suggests a modification of the pore structure upon calcination.

For Ni₃FeLDH/88A and Ni₃FeLDO/88A submitted to calcination temperatures of 200 and 300 °C, hysteresis loops at relative pressures ranging from 0.45 to 1 indicate the presence of mesoporous structures in lamellar rods and slit-like pores due to aggregation of nanosheets. At a calcination temperature of 400 °C, the hysteresis loop of Ni₃FeLDO/88A-400 occurs at a relative pressure range of 0.8-1, which indicates the presence of large mesopores and macropores. Consistent with this, the specific surface area of Ni₃FeLDO/88A increases with increasing calcination temperature. This can be attributed to the loss of interlayer water during heat treatment and the formation of porous ill-crystallized derived oxide phases.

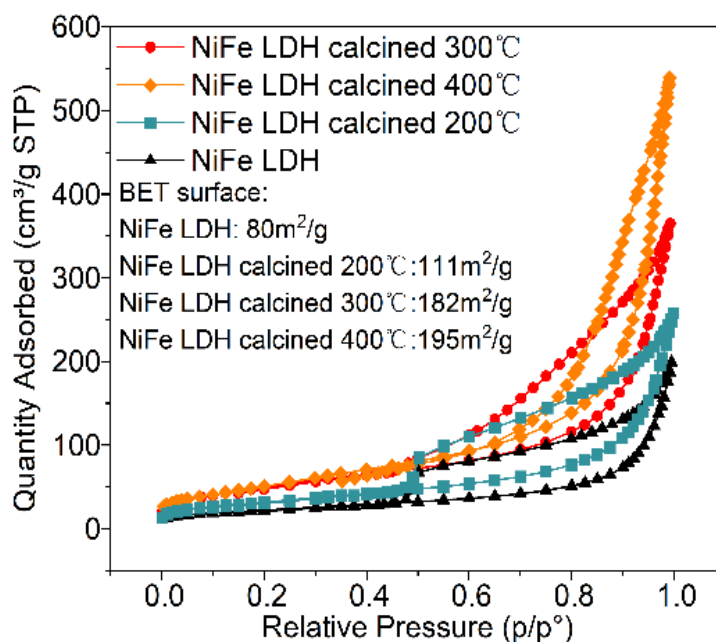


Fig. II-30 BET of Ni₃FeLDH/88A and Ni₃FeLDO/88A obtained by calcination at different temperature.

XPS is used to obtain chemical and elemental binding information (Fig. II-31). For the Fe 2p spectra of Ni₃FeLDO/88A-300, the peaks at 710.47 (Fe 2p_{3/2}) and 723.58 eV (Fe 2p_{1/2}) are considered to be the peaks of Fe³⁺, as evidenced by the satellite peaks of Fe³⁺ at 719.59 and 733.14 eV [265, 266]. The high-resolution spectra of Ni 2p in Ni₃FeLDO/88A-300 show that the peaks centered at 855.49 and 872.94 eV can be attributed to Ni²⁺ while the peaks located at 861.59 and 879.33 eV [267], respectively, are its satellite peaks. The O 1s spectrum of Ni₃FeLDO/88A-300 can be decomposed into two peaks at 529.89 and 531.44 eV, where the peak at 531.44 eV is generated by surface hydroxyl oxygen [268]. The peak at 529.89 eV corresponds to metal-oxygen bonds in metal oxides, i.e., iron-oxygen and nickel-oxygen bonds [269]. The XPS analysis results agree with the EDS and XRD analyses. This proves the presence of mixed oxides in Ni₃FeLDO/88A-300 samples.

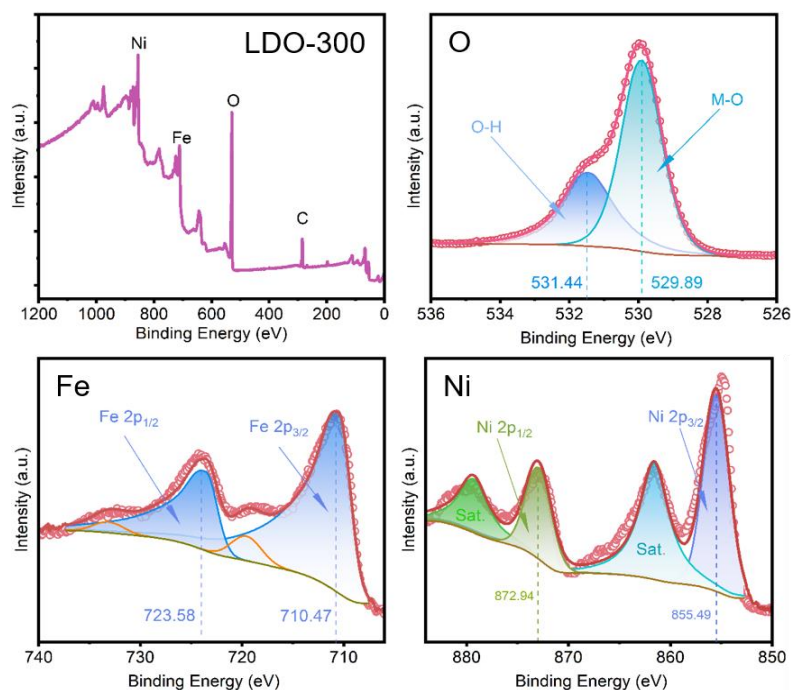


Fig. II-31 XPS of Ni₃FeLDO/88A-300.

II.4.3. Conclusion

Calcination of Ni₃FeLDH/88A at different temperatures ranging from 200 °C to 400 °C yielded to Ni₃FeLDO/88A, and interestingly calcination did not affect its rod-like microstructure. The calcined products were identified as nickel-iron mixed oxides. This is consistent with the calcined product Ni₃FeLDO/COP obtained from co-precipitated Ni₃FeLDH/COP. As usually observed upon LDH calcination, the surface area increases with increasing calcination temperature. Specifically, the specific surface area of Ni₃FeLDH/88A was 80.3 m²·g⁻¹, and the specific surface area of the Ni₃FeLDO/88A was 111 m²·g⁻¹ (at 200 °C), 182 m²·g⁻¹ (at 300 °C) and 195 m²·g⁻¹ (at 400 °C) as the calcination temperature increased.

II.5. Conclusion

The iron-based MOF MIL-88A was successfully synthesized by hydrothermal treatment and microwave thermal activation. This latter h greatly saves the reaction time compared with the traditional hydrothermal method and yields MIL-88A with a more homogeneous peritectic structure. The optimum conditions for the synthesis of

MIL-88A were deeply investigated, allowing to define as optimal conditions a synthesis at 110 °C for 30 min. The generated MIL-88A displays similar characteristics as described in the literature. Its molecular formula was calculated using thermogravimetry as $\text{Fe}_3\text{O}(\text{OH})(\text{C}_4\text{H}_2\text{O}_4)_3 \cdot 3.6 \text{H}_2\text{O}$.

The synthesized MIL-88A was used as an efficient precursor and was subsequently converted into $\text{Ni}_3\text{FeLDH}/88\text{A}$ by microwave method. In this case, the optimum synthesis conditions were as follows, nickel-iron ratio of 3 and reaction at 110 °C for 60 min. Typical lamellar structure of $\text{Ni}_3\text{FeLDH}/88\text{A}$ was uniformly distributed on the surface of the rod structure to form a hollow nanostructure. It has the typical crystalline structure of LDH.

$\text{Ni}_3\text{FeLDH}/88\text{A}$ was calcined in air at 200, 300 and 400 °C to obtain $\text{Ni}_3\text{FeLDO}/88\text{A}-200$, $\text{Ni}_3\text{FeLDO}/88\text{A}-300$ and $\text{Ni}_3\text{FeLDO}/88\text{A}-400$ respectively. The surface area increased with the increase in calcination temperature. And, its regular nanostructure remained mainly unchanged. This method based on MOF conversion allowed in an easy and fast process to produce both LDH and derived mixed oxides displaying a 3D nanostructured morphology.

Chapter III

**Extension of MIL-88A(Fe)
conversion into NiFe-LDH to
other LDH/MOF systems**

III.1. Introduction

Metal-organic frameworks (MOFs) are a class of porous materials with tunable pore sizes and large surface areas that have been used as versatile sacrificial templates for the preparation of a variety of materials (e.g., metal oxides, metal sulfides, and carbons) through altered synthesis schemes [270]. By replacing the organic ligand in MOF with -OH, and combining the MOF-M (II) or MOF-M (III) with a second metal cations, respectively M (III) and M (II), the resulting 3-Dimensional hollow layered double hydroxide may form keeping the original template structure of the MOF, enhancing its surface area and porosity and adsorption or catalytic properties compared to analogous LDH prepared by direct coprecipitation [271]. There have been many articles on the successful conversion of MOF into LDH [179] [192] and its application in adsorption [203], supercapacitor [272], advanced oxidation [194], as presented and discussed in chapter I. In Chapter II, NiFe-LDH/88A was successfully synthesized using a typical iron-based MOF, MIL-88A(Fe), as a precursor, which has the typical structure and characterization results of LDH with the regular structure and higher chemical activity of MIL-88A.

However, there are still some challenges and problems in constructing new MOF-derived LDH, including which MOFs can realize the conversion to LDH, how to precisely control the growth of LDH on MOF substrates, and how to improve the synergistic interaction between bimetallic active sites to further enhance their catalytic/energy storage/adsorption properties. And the key to solve these problems lies in figuring out the conditions and mechanism of LDH conversion by MOF. Therefore, the aim of this chapter is to investigate the conditions for the conversion various MOF into LDH and to make a preliminary investigation of the mechanism.

The MOF conversion reaction involves two primary types of reactive substances: the metal ions, which serve as the backbone for MOFs and also act as etching agents during the conversion process, and the organic ligands, which ensure the stability of MOFs and can also contribute to stabilizing LDH during its intercalation. The main focus of this chapter is therefore to explore the role as etching metals (divalent and trivalent metals) and MOF backbone metals (trivalent metals) as well as organic ligands. In addition, adjustment of other synthesis parameters, including metal

concentration, time, temperature is also explored [180].

III.2 Effects of metal ions

III.2.1 Behavior of metal ions as etching agents

To examine the influence of etching divalent metals on the conversion of MOF into LDH, MIL-88A, successfully synthesized in Chapter II, and stable in water, was selected as the precursor. In this study, magnesium and cobalt were employed instead of nickel for the conversion process. The effects of temperature, time, and other pertinent parameters on the conversion process were investigated.

III.2.1.1 Conversion of MIL-88A to MgFe-LDH

III.2.2.1.1 Synthesis temperature

Convert MIL-88A to MgFe-LDH: Similar to the conversion to NiFe-LDH/88A, nickel was replaced with magnesium under the same conditions, specifically: 50 mg MIL-88A was dispersed in 4 mL of ethanol (solution A), 0.6 mmol (132 mg) of $\text{Mg}(\text{NO}_3)_2 \cdot 6 \text{H}_2\text{O}$ and 100 mg of urea were (1.67 mmol) dissolved in 6 mL of deionized water (solution B). Then, solution A and solution B were mixed via stirring at room temperature (solution C). At last, the solution C was heated at different temperatures for different times by microwave without stirring [164].

The composition and crystal types of MgFe-LDH synthesized at different temperatures were studied using X-ray diffraction. Unlike NiFe LDH/88A with typical LDH diffraction peaks, the conversion reaction involving magnesium did not produce MgFe-LDH. The characteristic peaks of iron oxide, $\alpha\text{-Fe}_2\text{O}_3$ [273], appeared for temperatures $\geq 90^\circ\text{C}$ (Fig. III-1 a). The FTIR spectra are shown in Fig. III-1 b. Beside the infrared feature of the MIL-88A(Fe) that remains up to 100°C (presence of $\nu_{\text{as}}(\text{CO}_2^-)$ at 1600 cm^{-1} , and $\nu_{\text{as}}(\text{CO}_2^-)$ at 1395 cm^{-1} of Fe-Fumarate) and the Fe-O stretching band pointed at 576 cm^{-1} is growing under temperature increase. From XRD and FTIR results it can be concluding that MgFe-LDH was not successfully

synthesized.

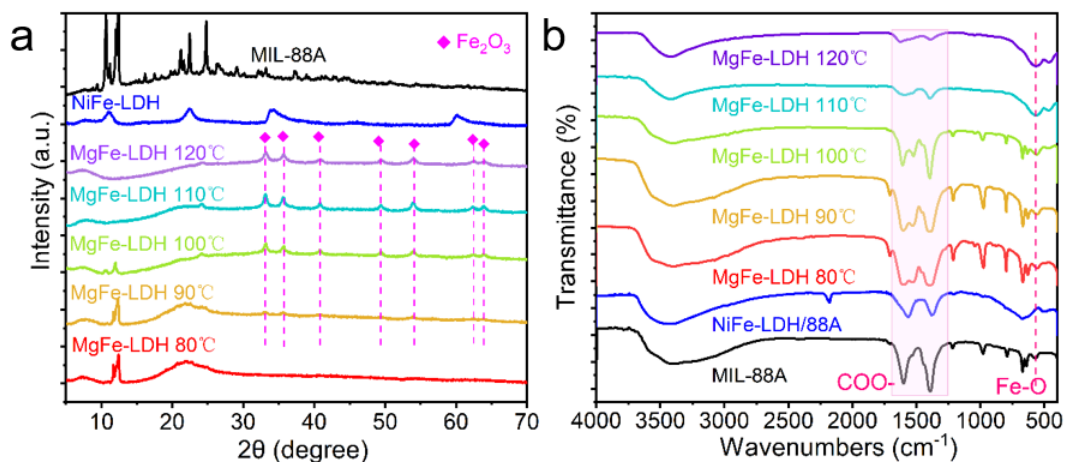


Fig. III-1 (a) XRD patterns and (b) FTIR spectra of MgFe-LDH converted from MIL-88A at different temperatures for 30 min by microwave irradiation.

III.2.2.1.2 Time of MW irradiation

The synthesis of MgFe-LDH was further explored for 30 min and 60 min reaction times at 90, 100, 110 and 120 °C (Fig. III-2). Although the reaction time was changed, the XRD patterns of the resulting materials were still not MgFe-LDH but iron oxide [274]. This is another proof of the failure of the conversion of MIL-88A to MgFe-LDH.

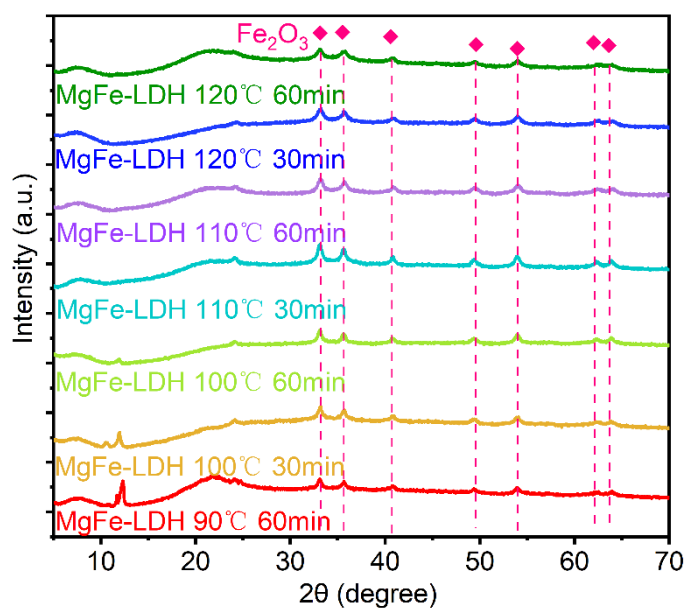


Fig. III-2 XRD patterns of MgFe-LDH derived from MIL-88A at different temperatures and different reaction times.

III.2.2.1.3 Addition of urea

The negative results previously obtained were probably caused by the fact that magnesium hydroxide precipitate in more basic conditions than iron hydroxide which reacts faster in urea solution and precipitate readily, so the conversion of MIL-88A to MgFe-LDH was explored by changing the urea concentration in order to increase the pH of the reaction (Table. III-1). Other conditions being equal, the amount of urea was varied and the pH values of the liquids were recorded before and after the reaction, which was carried out in a microwave reactor at 110 °C for 30 min.

Table. III-1 Urea amount and pH before and after conversion of MIL-88A to MgFe-LDH.

	Urea (mg)	pH _{in}	pH _{fin}
MgFe-LDH	50	4.43	4.04
MgFe-LDH	75	4.70	4.40
MgFe-LDH	100	4.36	5.87
MgFe-LDH	125	4.63	8.03
NiFe-LDH/88A	100	4.41	5.86

pH_{in}: initial pH, pH_{fin}: final pH after reaction pH

Before heating, there was no major difference in the pH of the liquids. After heating, the pH difference is considerable, which is mainly due to the fact that heating makes the hydrolysis process of urea accelerated. Carbonate is released thus increasing the pH [275]. In contrast to NiFe-LDH, the pH before and after the reaction was almost unchanged when the dosage of urea was 100 mg in both cases, indicating that the failure of MgFe-LDH should have little to do with pH.

The conclusions are further corroborated by XRD results (Fig. III-3). These findings reveal that varying the amount of urea still results in the formation of iron oxide, indicating that the quantity of urea added has minimal impact on the synthesis of MgFe-LDH. Even with 125 mg of urea, resulting in a final pH of 8.0 conducive to the precipitation of magnesium hydroxide, the irreversible formation of Fe₂O₃ hampers the conversion into MgFe-LDH. Obviously, Ni²⁺ ions participate in the earlier stage of

the mechanism of conversion to prevent the formation of Fe_2O_3 , what Mg^{2+} does not work.

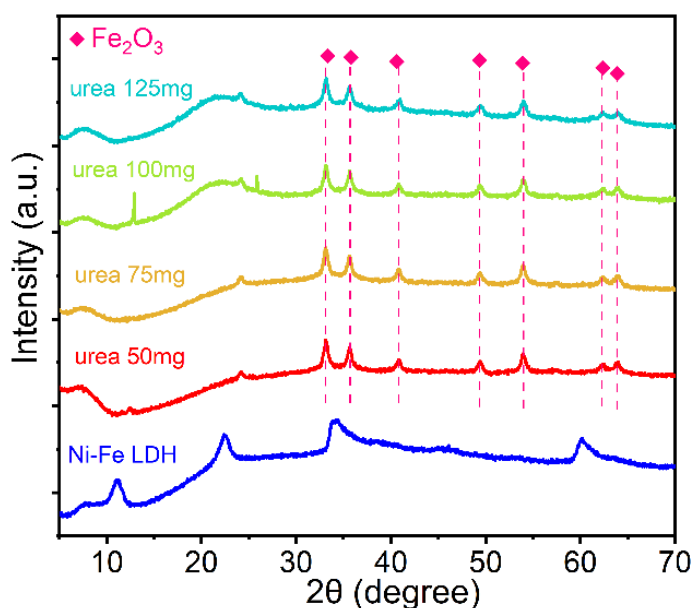


Fig. III-3 XRD results of MgFe-LDH converted from MIL-88A at different urea amounts, at 110 °C for 30 min.

III.2.2.1.4 Ratio of Ni and Mg

Further, since Ni^{2+} can successfully synthesize NiFe-LDH/88A, Mg^{2+} and Ni^{2+} were combined to jointly participate in the etching process with a view to doping magnesium in the etching of nickel. Therefore, etchants with different nickel-to-magnesium ratios were designed to convert MIL-88A into $\text{Ni}_{1-x}\text{Mg}_x\text{Fe-LDH/88A}$ materials, adjusting the molar ratio of nickel and magnesium while maintaining the total molar amount of nickel and magnesium at twice that of iron. All other conditions remained constant, and the reaction was conducted in a microwave oven at 110 °C for 30 min.

When the magnesium content is high ($\text{Ni/Mg} < 4/6$), iron oxide emerges as the primary crystallized phase in the XRD pattern (Fig. III-4a) [274]. In these chemical compositions, the predominant presence of Mg^{2+} inhibits the conversion of MIL-88A (Fe) into NiFe-LDH. Conversely, when the proportion of nickel reaches or exceeds 50%, the characteristic peak of NiFe-LDH becomes apparent [276]. This observation is further supported by the FTIR (Fig. III-4 b) results, where the characteristic peaks of

fumaric acid at $750\text{-}1200\text{ cm}^{-1}$ [277] diminish with increasing nickel content. This indicates that magnesium not only fails to participate in the conversion of MIL-88A to MgFe-LDH/88A but also impedes the etching process of nickel.

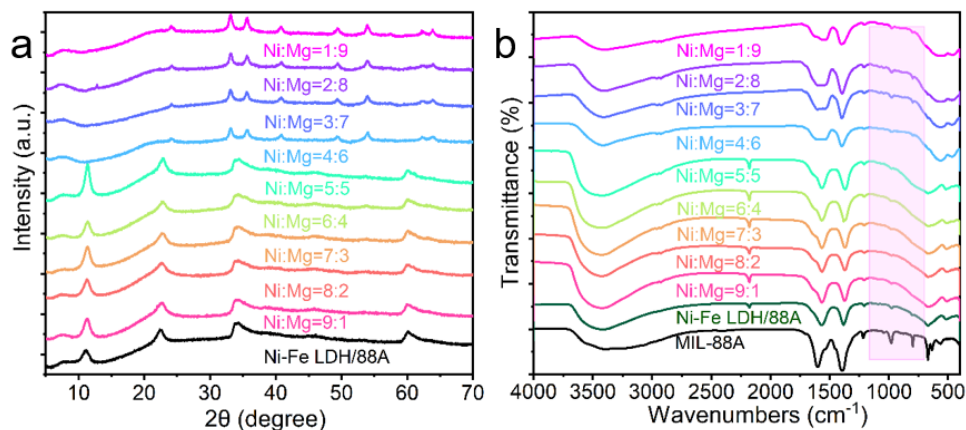


Fig. III-4. (a) XRD patterns and (b) FTIR spectra of LDH derived from MIL-88A with different Ni-Mg ratios as etching agents.

SEM analysis of the solids after conversion (Fig. III-5) show that the typical lamellar structure of LDH does not appear when the nickel content is insufficient. With the increase of nickel content, the more uniformly the petal-like structure is distributed on the surface of the rod structure. However, the EDS results indicated that no magnesium was detected regardless of the increase or decrease in the nickel-magnesium ratio, which means that magnesium was not involved in the etching process. While magnesium plays an interfering role in the etching process of nickel.

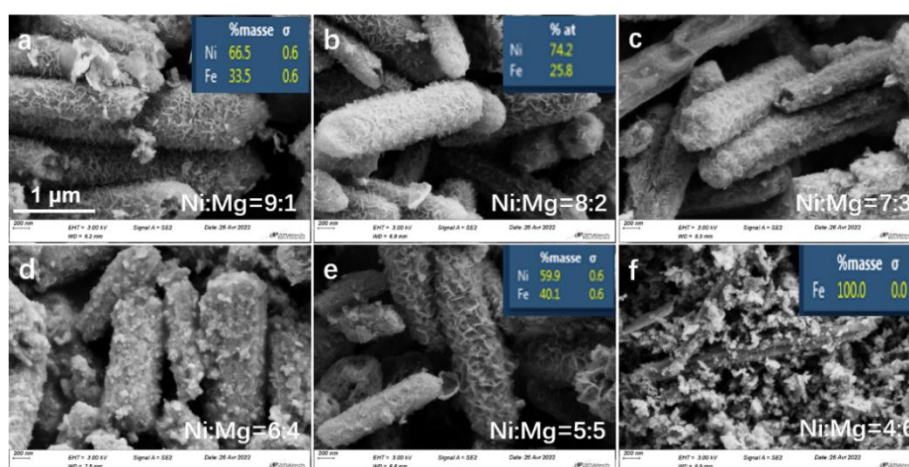


Fig. III-5 SEM images and EDS results of LDH converted from MIL-88A with different Ni-Mg ratios as etching agents.

During the nickel ion etching process of MIL-88A, the protons generated by nickel hydrolysis react with the organic ligands on the MIL-88A surface, leading to the gradual release of iron ions. Concurrently, $\text{Ni}(\text{OH})_2$ gradually forms LDH on the MIL-88A surface. However, when magnesium, possessing a smaller atomic radius, lower charge density, and weaker hydration capacity, replaces nickel, the hydrolysis rate decreases. Consequently, iron ions are released as protons from magnesium hydrolysis etch the organic ligands of MIL-88A. As iron exhibits a higher affinity for hydroxide compared to magnesium, primarily generated through the slow hydrolysis of urea, iron preferentially binds to hydroxide, ultimately resulting in the formation of iron oxide.

Therefore, the etched metal ions in alkaline solutions must possess properties ensuring that the hydrolysis rate is not excessively slow and facilitate easier binding with hydroxide ions to produce metal hydroxides compared to the MOF backbone metal ions.

Factors influencing hydrolysis rate include larger ionic radii, higher charge densities, greater hydration capacity, and higher valence states. Characteristics indicating a higher hydroxide affinity include higher charge densities, larger atomic radii, and higher valence states compared to the MOF backbone metal.

III.2.1.2 Conversion of MIL-88A to CoFe-LDH

To confirm the hypothesis that etching metals significantly influence hydroxide affinity and hydrolysis compared to skeletal iron ions during the MOF to LDH conversion, cobalt, which exhibits intermediate hydrolysis properties between nickel and magnesium, was selected for synthesizing CoFe-LDH/MOF. Building upon the unsuccessful synthesis of MgFe-LDH, nickel and cobalt were chosen at various molar ratios to participate as etching metals in the conversion of MIL-88A to CoNiFe-LDH.

Convert MIL-88A to CoNiFeLDH: 50 mg MIL-88A was dispersed in 4 mL of ethanol (solution A). different ratio of $\text{Co}(\text{NO}_3)_2 \cdot 6 \text{H}_2\text{O}$ and $\text{Ni}(\text{NO}_3)_2 \cdot 6 \text{H}_2\text{O}$ and 100 mg (1.67 mmol) of urea were dissolved in 6 mL of deionized water (solution B). The total molar amount of cobalt and nickel to the molar ratio of iron is 3. Solution A

and solution B were mixed via stirring at room temperature (solution C). At last, the solution C was heated at 100°C for 60 min by microwave without stirring [164].

Similar to the results observed for magnesium, characteristic LDH peaks were discernible at low cobalt content (Ni:Co = 9/1), while noise peaks emerged in the XRD results with increasing cobalt dosing (Fig. III-6 a). The diffraction peaks at 11.2°, 22.6°, and 34.5° correspond to the crystal planes of CoNiFe-LDH material, specifically (003), (006), and (015), respectively (PDF Card No. 40-0216) [278].

The FTIR spectra are shown in Fig. III-6 b. The broad absorption band at 3450 cm^{-1} is the stretching vibration of -OH, the absorption bands at 1383 and 1602 cm^{-1} are the vibration of carboxyl group, and the small bands at low frequency below 1000 cm^{-1} , which are part of the vibration and stretching of metal and oxygen lattices in the hydroxalate-like lattice, proved the successful preparation of CoNiFe-LDH/88A [279].

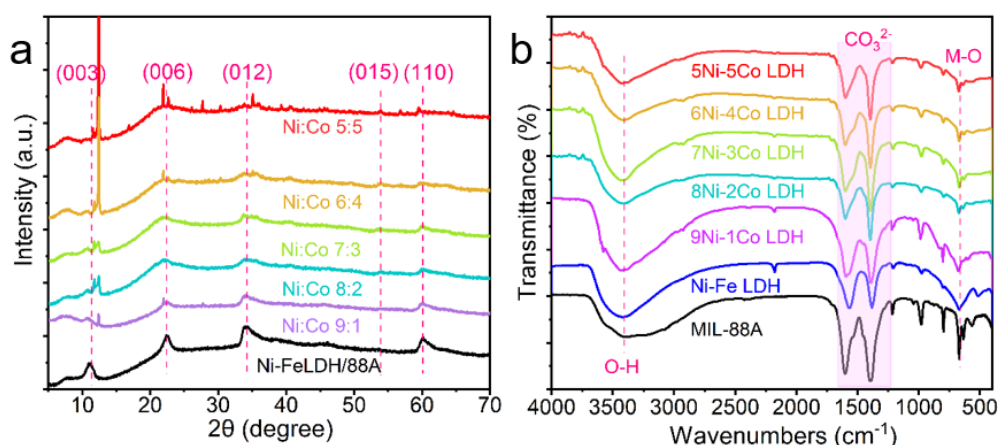


Fig. III-6 (a). XRD patterns and (b) FTIR spectra of MIL-88A converted to CoNiFe-LDH at different Ni/Co ratios.

Scanning electron microscopy (SEM) and energy dispersive X-ray spectroscopy (EDS) tests were conducted on CoNiFe-LDH with a nickel to cobalt ratio of 9:1 (Fig. III-7). SEM images revealed a rod-like structure, distinct from the smooth surface of MIL-88A, indicating coverage by a different structure (Fig. III-7 a). Further confirmation through TEM illustrated the transformation of MIL-88A into a homogeneous semi-transparent structure, confirming the successful conversion into CoNiFe-LDH. EDS analysis indicated cobalt's involvement in the conversion reaction,

with a Ni:Co ratio of 13:1, relatively close to the initial ratio. This suggests that unlike magnesium, which does not participate in the MOF to LDH conversion, cobalt can engage in the transformation to CoNiFe-LDH, albeit in collaboration with nickel and within a specific dosage range. Nickel and cobalt undergo hydrolysis in an alkaline solution, gradually etching MIL-88A and releasing iron, nickel, and cobalt into solution, ultimately forming CoNiFe-LDH.

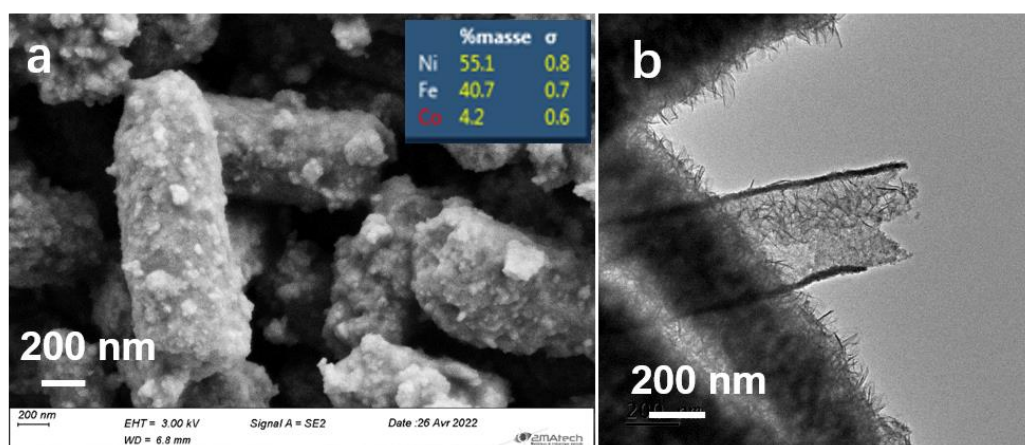


Fig. III-7 (a) SEM and (b) TEM images of CoNiFe-LDH at a cobalt-nickel ratio of 1:9.

III.2.1.3 Conversion of MIL-88A to NiAlFe-LDH

Aluminum, being a trivalent amphoteric metal, is prone to hydrolysis reactions in water, and aluminum ions readily combine with hydroxides to form hydroxides in alkaline solutions at low concentrations. Therefore, aluminum was selected to investigate whether trivalent metals can participate in the conversion of MOF to LDH as etching metals.

Convert MIL-88A to NiAlFe-LDH: 50 mg MIL-88A (Fe) dispersed in 4 mL EtOH (solution A), and 100 mg (1.67 mmol) of urea and different ratio of Ni/Al of nitrate salts dissolved in 6 ml H₂O (solution B), the ratio of total amount of Ni/Al and Fe is 3. Solution A and B are mixed and heated 110 °C for 60 min.

The XRD patterns of NiAlFe-LDH were recorded (Fig. III-8 a). Characteristic diffraction peaks of (003), (006), (012), (015), (018) and (110) planes can be found,

which match the hexagonal phase of the standard NiAl-LDH (JCPDS No. 15-0087) [280], suggesting that the LDH crystalline phase can be successfully formed in the reaction.

The infrared results are shown in the Fig. III-8 b, with broad and strong bands, ranging from 3350-3450 cm^{-1} spectra matching the stretching vibrational modes of the hydroxyl groups in the ortho-octahedral sheets of the LDH layer [281]. The presence of symmetric and asymmetric stretching modes of the carboxyl group at 1350 and 1570 cm^{-1} confirms the structural significance of the fumarate ligand in the formation of the LDH phase [282]. The vibrational bands observed in the low-frequency region of 500-1000 cm^{-1} are attributed to metal-hydroxyl (M-O) or metal-oxygen-metal (M-O-M) vibrations [283].

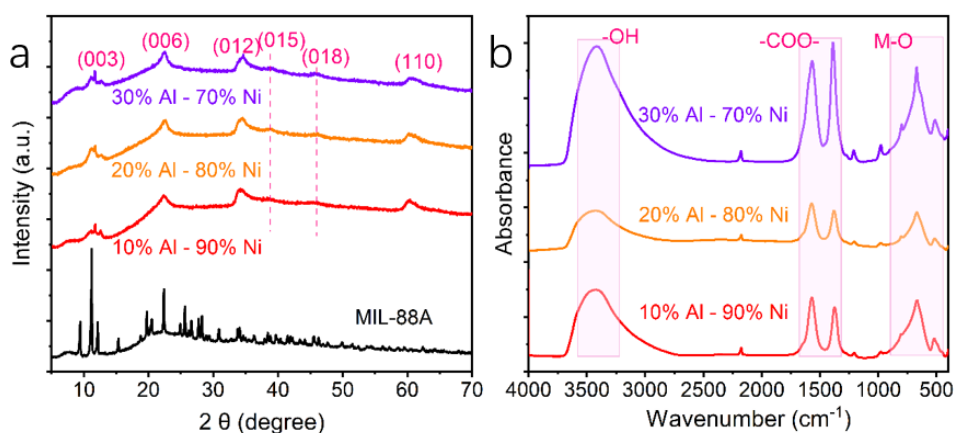


Fig. III-8 (a) XRD patterns and (b) FTIR spectra of LDH converted by MOF under different ratios of Ni and Al as etching metals.

The SEM analysis (Fig. III-9) revealed two distinct structures on the surface of MIL-88A, a larger petal-like structure and a smaller lamellar structure. EDS analysis of the petal-like structure indicated an elemental composition of Fe: Ni: Al of 3.25: 1.1: 1. This suggests that aluminum can indeed participate in the conversion of MIL-88A to LDH, albeit resulting in a microstructure different from that formed with nickel alone.

Aluminum hydrolyzes more rapidly than nickel in water, releasing a substantial number of protons during the process. These protons subsequently etch MIL-88A, leading to the release of iron ions. Concurrently, the presence of a significant quantity

of nickel ions in solution, which have a higher propensity for producing hydroxides compared to aluminum, may preferentially lead to the formation of NiFe-LDH. Consequently, there exists a possibility that aluminum may contribute to the formation of another type of LDH, such as NiAlFe-LDH.

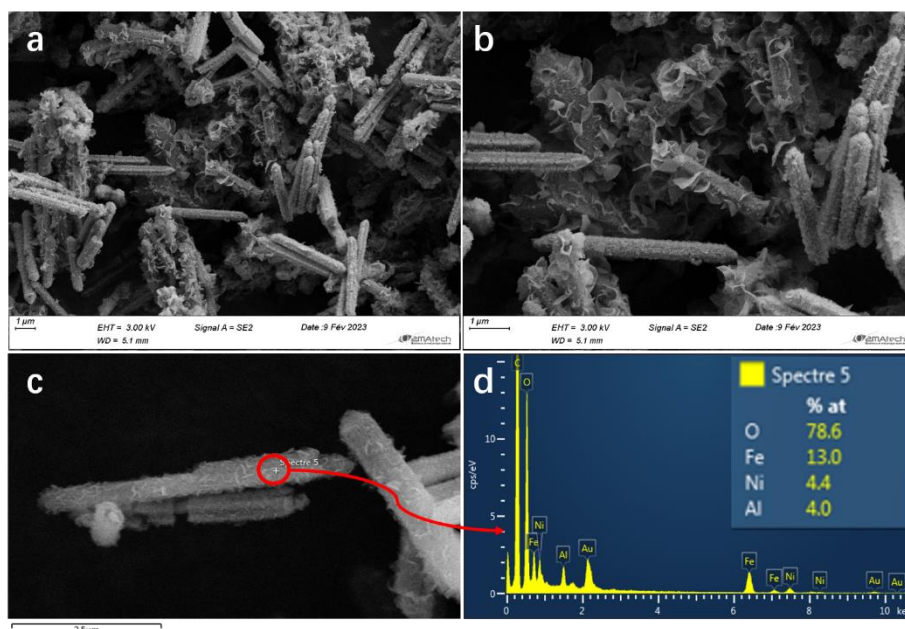


Fig. III-9 (a) (b) SEM and (c) (d) EDS images of LDH converted by MOF when the ratios of Ni and Al is 8:2.

III.2.1.4 Conclusion

The conditions for etching metals during the conversion of MOF to LDH were explored, choosing typical divalent metals, magnesium, cobalt with nickel already successfully involved in the conversion as well as the trivalent metal aluminum. The results showed that the rate of hydrolysis of metal ions is an important factor affecting the formation of LDH ; slower hydrolysis and the formation of oxides from the released iron and a large amount of hydroxide in the solution lead to the failure of LDH conversion. The affinity for hydroxide is another important factor in LDH formation compared to iron ions. With a lower affinity for hydroxide, hydroxide preferentially forms LDH with the released iron and nickel, while ions with a lower affinity are "discarded" in the process.

III.2.2 Behavior of metal ions as MOF skeletons

Metal ions serve a dual role: not only do they participate in the etching process and contribute to the formation of LDH [284], but they also serve as essential backbones for MOF materials, exhibiting morphologies other than the micro-rods displayed by MIL-88A (Fe) [285]. Hence, it is crucial to investigate the backbone metal for the conversion of MOF to LDH. Al^{3+} cations were selected to react with fumaric acid to synthesize an aluminum-based LDH, Al-FA [286], in acidic condition or Al-Fum in basic condition. Subsequently, these Al-FA and Al-Fum compounds were reacted with nickel ions under alkaline conditions to explore the possibility of their conversion into LDH.

III.2.2.1 Synthesis and characterization of Al-FA

Synthesis of Al-FA: 3.71 g $\text{Al}_2(\text{SO}_4)_3 \cdot 18 \text{H}_2\text{O}$ was added to 15.9 mL of water and heated to 60 °C for 5 min by microwave (solution A). 0.95 g NaOH and 1.29 g fumaric acid are dissolved in 19.1 mL water (solution B). Solution A is added into solution B and the mixture is heated in microwave at 60 °C for 10 min by stirring [287]. The product is collected by centrifuge and washed with water for 3 times.

The effect of two different heating times on the crystalline shape was examined, controlling the dissolution time of aluminum sulfate to 5, 20, and 40 min, and the MW irradiation time of the mixture to 10, 20, 40, and 60 min, respectively. The obtained powder X-ray diffraction (PXRD) patterns are shown in Fig. III-10. The diffraction patterns are generally similar to those of aluminum fumarate (Al-FA) and the reaction time has little effect on the crystalline shape [288]. This agrees well with the experimental XRD results of the literature [286], confirming the successful synthesis of these nanoparticles. The MOF structure was examined using FTIR analysis (Fig. III-11), revealing characteristic peaks associated with specific vibrational modes. Peaks at 500 cm^{-1} and in the range of $700\text{-}1200 \text{ cm}^{-1}$ correspond to vibrations of Al-O and O-Al-O within the lattice. Additionally, peaks observed at 1425 cm^{-1} and 1607 cm^{-1} represent the symmetric (vs) and asymmetric (vas) vibrational modes of the carboxylate group coordinated with aluminum, while the peak at 3440 cm^{-1} corresponds to the

stretching vibration of -OH groups [287].

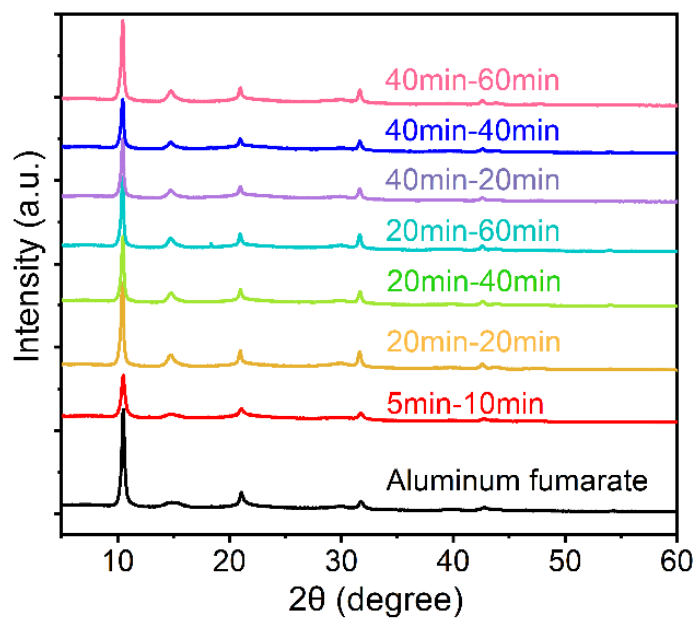


Fig. III-10 XRD patterns of Al-FA synthesized at different dissolution and reaction times.

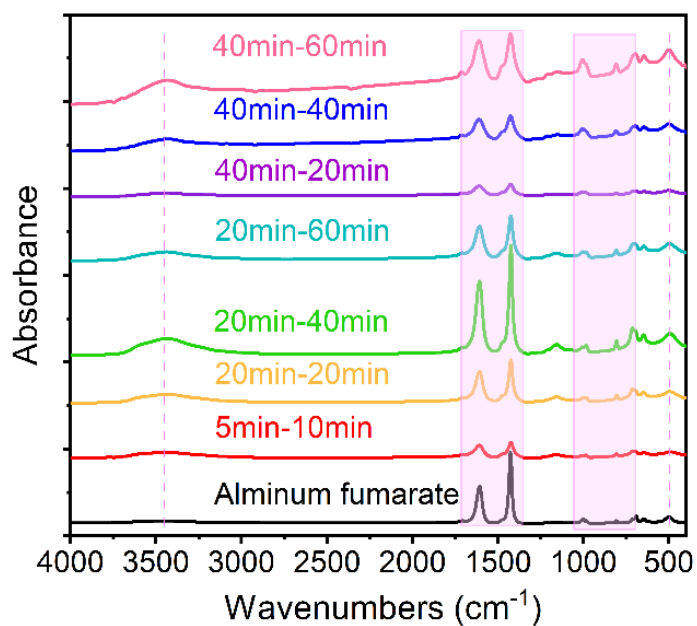


Fig. III-11 FTIR spectra of Al-FA synthesized at 110 °C for different reaction times.

By comparing the XRD and IR results, a reaction time of 20 min for dissolving aluminum sulfate followed by a 40-min reaction period was determined to be the optimal conditions.

Scanningelectron microscopy images (Fig. III-12 a) show that unlike MIL-88A and MIL-101, the aluminum-based MOF does not have a regular microstructure. Its structure is a stacking and agglomeration of rice-grain type elongated structures, so the surface of its agglomerated block microstructure is not smooth [289]. The rice-grain structure is small, with a length of about 70 nm, mean value. TEM results (Fig. III-12 b, c) show that the rice-grain structure is uniform in size and shape, and the large blocky structure is formed by its agglomeration.

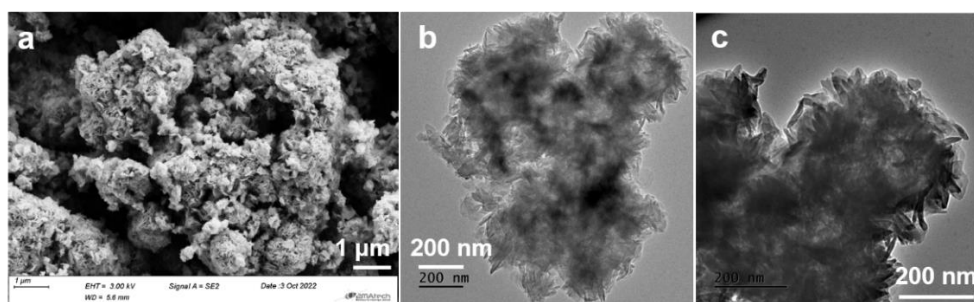


Fig. III-12 SEM (a) and TEM (b,c) results of Al-FA.

III.2.2.2 Convert Al-FA to NiAILDH/FA

The conversion of Al-Fu to NiAILDH/FA was investigated. The conversion was first explored as follows: 50 mg Al-FA was dispersed in 4mL of H₂O (solution A). 0.06 mmol (150 mg) Ni (NO₃)₂·6 H₂O and 100 mg of urea were dissolved in 6 mL of ethanol (solution B). Then, solution A and solution B were mixed via stirring at room temperature (solution C). At last, the solution C was heated at different 60 °C, 80 °C, 110 °C, 130 °C and 150 °C for 30 min by microwave without stirring.

The EDS results (Fig. III-13) show that Ni successfully diffuses into the MOF structure and the nickel-aluminum ratio is 2.5, which is consistent with the molar ratio of divalent and trivalent metals in LDH.

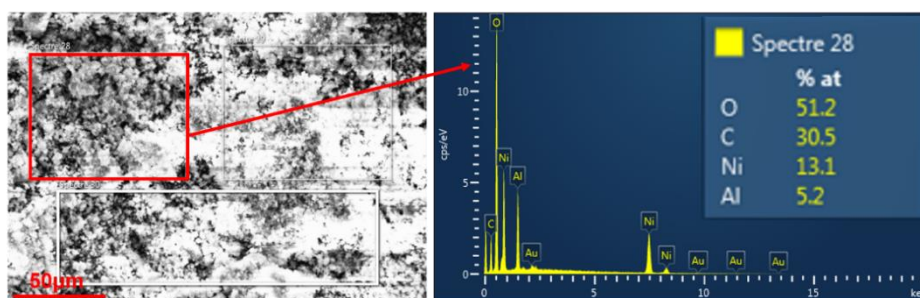


Fig. III-13 EDS of NiAlLDH/FA.

The XRD analysis (Fig. III-14) revealed that when the reaction temperature was below 110 °C, Al-FA retained its MOF structure, indicating its superior stability compared to MIL-88A and MIL-101 in alkaline solutions. However, at 110 °C, characteristic diffraction lines of LDH, such as (003), (006), (012), and (110), began to emerge [290]. As the temperature increased, the diffraction peaks became sharper and more symmetric, particularly at 180 °C. This enhancement suggests an improvement in the crystallinity and purity of LDH [280].

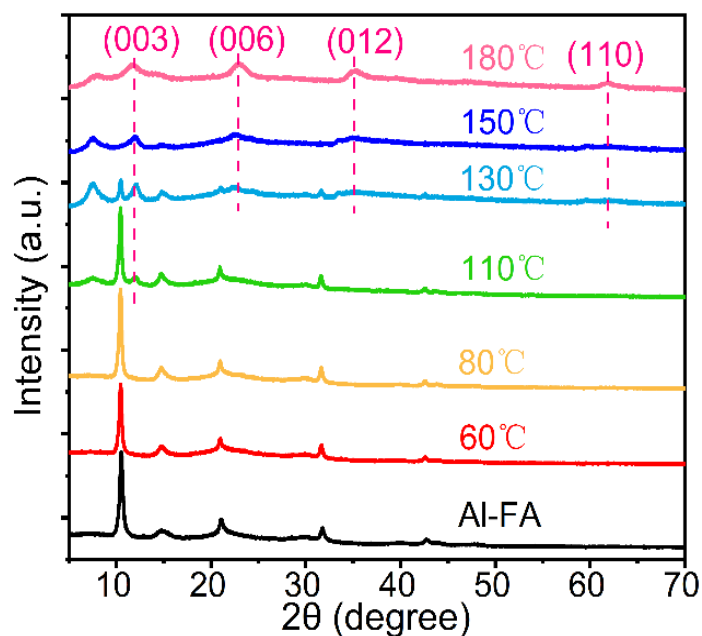


Fig. III-14 XRD patterns of NiAlLDH/FA converted from Al-FA at different temperatures.

XRD results were compared for reaction times of 30 and 60 min at temperatures of 150 °C and 180 °C (Fig. III-15), respectively. Interestingly, higher crystallinity was observed at 150 °C for 60 min, while at 180 °C, an increase in temperature resulted in

a weakening of the (003) surface. Consequently, the optimal synthesis conditions were determined to be 150 °C for 60 min, considering that the maximum temperature of the microwave heater does not exceed 200 °C. The presence of two sets of (003) and (006) diffraction lines accounts for the formation of mixed LDH, a NiAl carbonate phase and a NiAl fumarate phase.

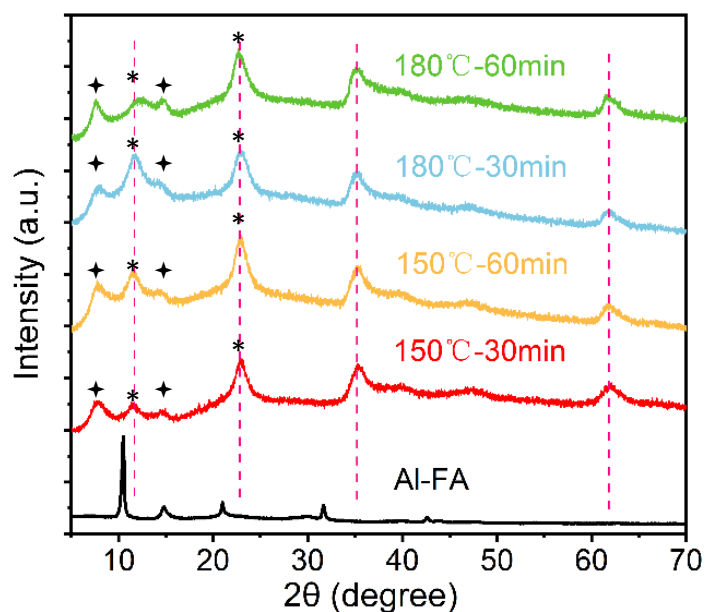


Fig. III-15 XRD results of NiAlLDH/FA converted from Al-FA at different time and temperatures. * NiAl-CO₃ and † NiAl-Fum.

The SEM images (Fig. III-16 a) of NiAlLDH/FA exhibit agglomerations, but unlike Al-FA, they are not composed of rice-like aggregates, but rather sand roses-like structures that grow more uniformly on the surface than Al-FA. TEM (Fig. III-16 b) shows more clearly the difference between NiAlLDH/FA and Al-FA.

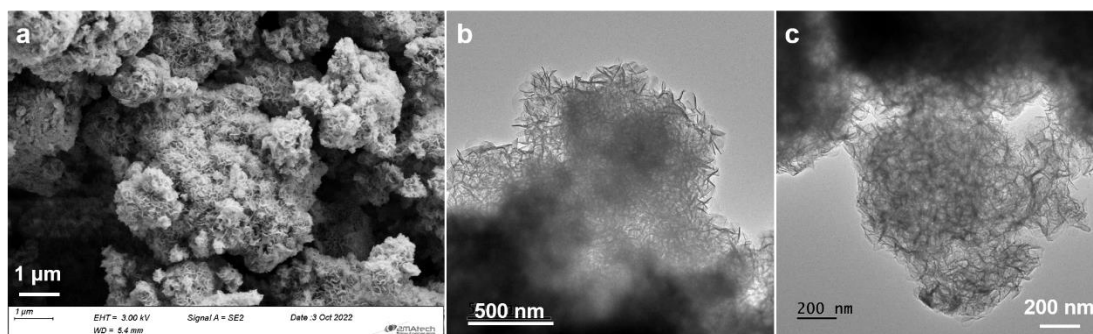


Fig. III-16 (a) SEM and (b) (c) TEM images of NiAlLDH/FA.

The thermal stability of NiAILDH/FA was analyzed by thermogravimetry. The TGA results (Fig. III-17) were characterized by two main mass loss regions. The mass loss between 25 and 219.8 °C indicates the loss of interlayer water and water molecules adsorbed on the surface. The second region of mass loss occurring between 220-379 °C is due to dehydroxylation of NiAILDH/FA and decomposition of interlayer ions, namely carbonate and fumarate [291]. The total mass loss is 35.5% by 800 °C.

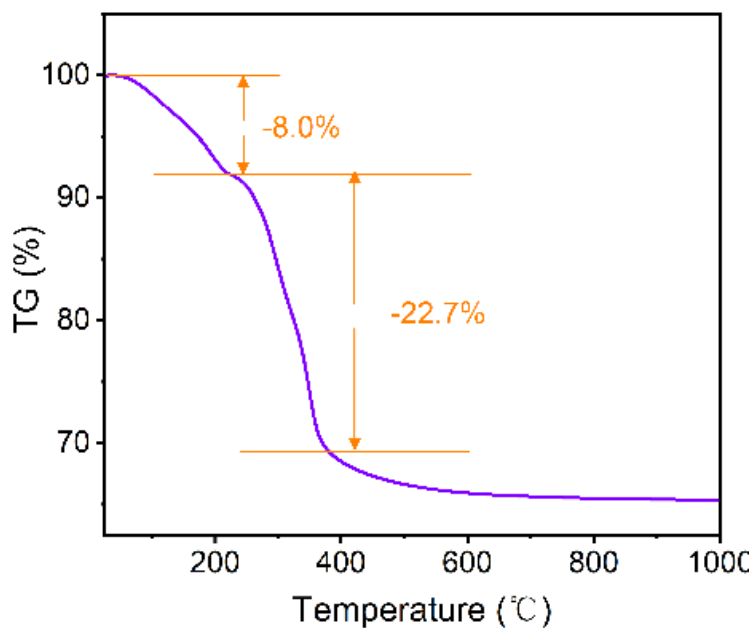


Fig. III-17. TGA of NiAILDH/FA.

The textural characteristics of the NiAILDH/FA samples were investigated through N₂ adsorption-desorption analysis (Fig. III-18). The isotherm of NiAILDH/FA is of type IV [292], which means, NiAILDH/FA is a mesoporous structure, and its pore size is 14.6 nm as calculated by BJH and the specific surface area is 110.6 m²/g. In the case of Al-FA, although it has a regular microstructure, its constituent "units" are so small that the NiAILDH/FA from which it is converted does not exhibit a regular microstructure similar to that of LDH/88A.

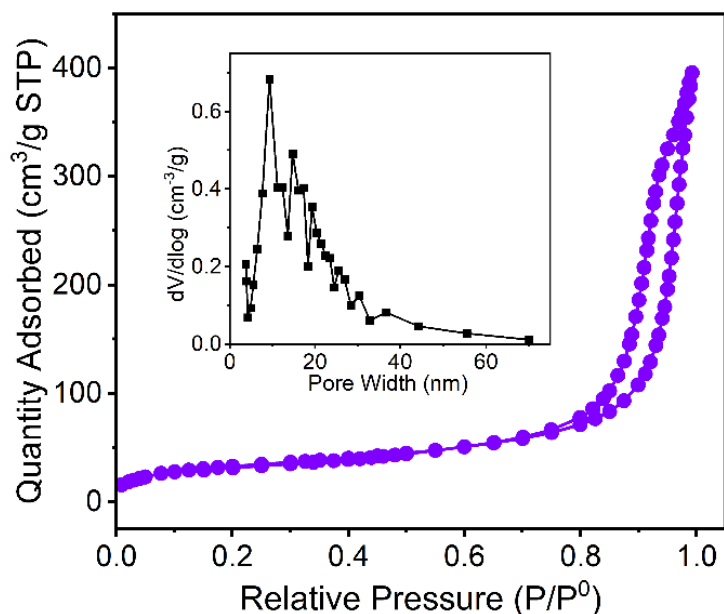


Fig. III-18 BET of NiAlLDH/FA.

III.2.2.3 Conclusion

Al^{3+} was combined with fumaric acid to synthesize an aluminum-fumaric MOF, Al-FA. Upon hydrolysis of nickel ions, the protons generated rapidly etched a large quantity of aluminum ions from Al-FA, while nickel ions facilitated LDH formation on the surface. Although successful conversion of MOF to NiAl-LDH was achieved, none of the resulting LDH exhibited a regular microstructure. Thus, to synthesize LDH with a regular microstructure from MOF, two conditions must be met regarding the MOF backbone metal: firstly, it should be capable of forming structures with organic ligands to create the MOF structure, and secondly, the microstructure "unit" of the MOF should not be excessively small.

III.3 Effects of organic ligand

In order to investigate the role of organic ligands, terephthalic acid (or benzene dicarboxylic acid, H_2BDC) was chosen to prepare MOF materials with iron and aluminum, respectively, and convert them to LDH. For iron and terephthalic acid synthesis is MIL-101 which has been heavily studied. For aluminum and terephthalic acid it is the synthesis of Al-BDC.

III.3.1 Synthesis of MIL-101 (Fe-BDC) and its conversion to LDH/101

III.3.1.1 Synthesis of MIL-101

Regarding the synthesis of MIL-101, several reaction conditions were explored, namely: method of synthesis, reaction temperature, reaction time etc.

III.3.1.1.1 Comparison of HT and MW synthesis method

Synthesis of MIL-101 by hydrothermal method: 2.48 mmol $\text{FeCl}_3 \cdot 6\text{H}_2\text{O}$ and 1.24 mmol H_2BDC were added into 20 mL DMF and mixture was stirred by magnetic stirrer until complete dissolution. The homogenous solution was then heated at 110 °C for 20 h in a Teflon reactor. The solid was recovered after washing several times with hot DMF (70 °C, 15 min). The purified light orange product (MIL-101 (HT)) was dried in oven at 60 °C overnight [293].

Synthesis of MIL-101 by Microwave method: 4.96 mmol (1.3406 g) $\text{FeCl}_3 \cdot 6\text{H}_2\text{O}$ and 2.48 mmol (0.412 g) H_2BDC were added in 40mL DMF, then stirred until completely dissolution, resulting in a bright yellow transparent solution. The solution was submitted to microwave irradiation at 110 °C for 30 min. The solid (MIL-101 (MW)) was washed twice with DMF and twice with ethanol and place overnight in a 60 °C oven.

The XRD diagrams (Fig. III-19) show that all the diffraction peaks of MIL-101 synthesized by microwave and hydrothermal methods have high intensity and sharp peaks. It indicates that the materials synthesized by the two methods are highly crystalline, and the characteristic diffraction peaks of the samples are consistent with the peak positions of the diffractogram reported in the literature for MIL-101(Fe) [294, 295] without the appearance of stray peaks, which indicates that MIL-101 was successfully synthesized by microwave and hydrothermal methods.

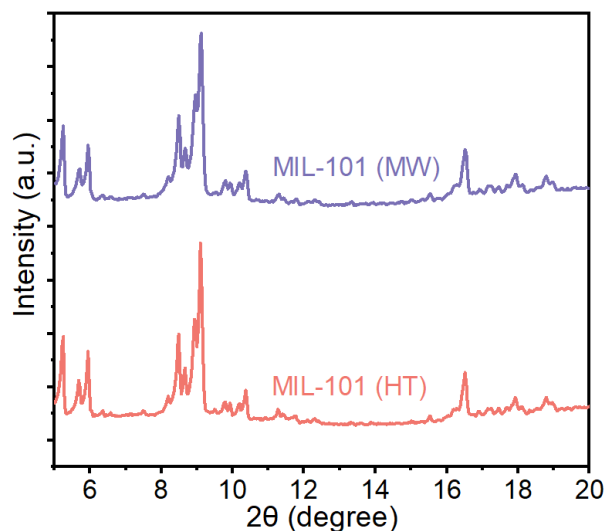


Fig. III-19 XRD results of MIL-101 synthesized by hydrothermal and microwave methods.

The FTIR (Fig. III-20) spectra of both samples exhibit vibration bands at 544, 747, 1392, 1590, and 1720 cm^{-1} , consistent with reported MIL-101 characteristics [296]. The band at 544 cm^{-1} corresponds to Fe-O vibration, while the band at 747 cm^{-1} indicates the bending vibration of C-H in benzene. Bands observed at 1392 and 1590 cm^{-1} denote symmetric and asymmetric vibrations of the carboxyl group, and the band at 1702 cm^{-1} is associated with C=O in the free carboxyl. These FTIR bands, corroborated by XRD analysis, confirm the successful synthesis of MIL-101 using both microwave and hydrothermal methods.

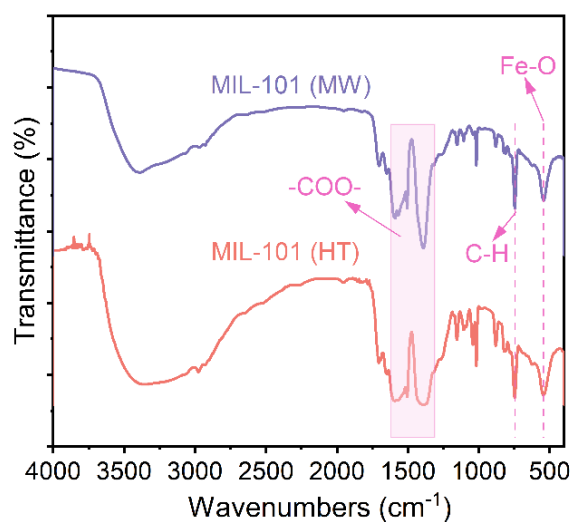


Fig. III-20 FTIR spectra of MIL-101 synthesized by hydrothermal and microwave methods.

The MIL-101 synthesized by both methods consisted of crystals with octahedral shape (Fig. III-21), as reported in previous studies [297]. However, MIL-101 (HT) has an octahedral edge of 1-2 μm and a concave surface, while MIL-101 (MW) crystals are shown to be not flat and has a diameter of less than 1 μm , which may be caused by the insufficient reaction temperature.

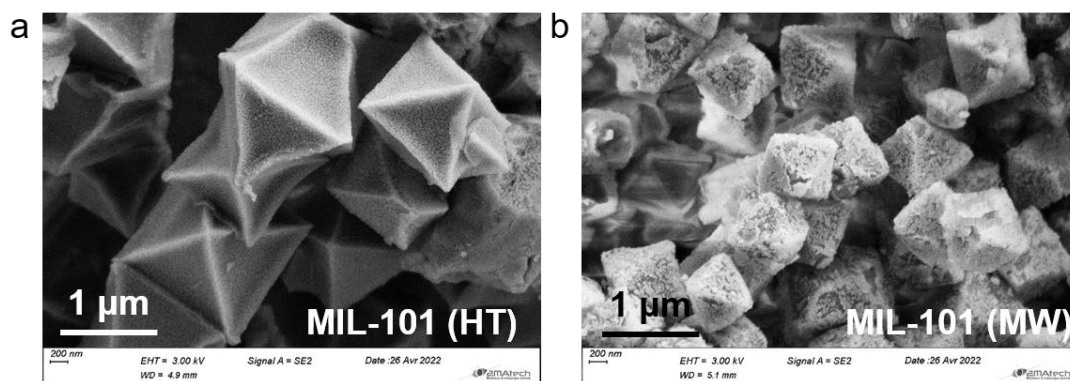


Fig. III-21 SEM images of MIL-101 synthesized by (a) hydrothermal and (b) microwave methods.

In view of the fact that both hydrothermal and microwave methods can successfully synthesize MIL-101, while the microwave method has a shorter synthesis time and lower energy, the microwave method was chosen as the synthesis method of MIL-101 precursor.

III.3.1.1.2 Effect of MW-assisted synthesis temperature

The bright yellow transparent solution (4.96 mmol $\text{FeCl}_3 \cdot 6\text{H}_2\text{O}$, 2.48 mmol H_2BDC , 20 mL DMF) was irradiated with microwave at temperature at 100, 110, 120, 130, 140 and 150 $^\circ\text{C}$ for 30 min. The precipitates were washed twice with DMF and twice with ethanol and dried overnight in a 60 $^\circ\text{C}$ oven.

The XRD analysis (Fig. III-22 a) of MIL-101(MW) synthesized at different temperatures reveals sharp and intense diffraction lines at temperatures exceeding 110 $^\circ\text{C}$. Furthermore, a better resolution of the peaks is observed at temperatures over 130 $^\circ\text{C}$. However, the FTIR spectra (Fig. III-22 b) show no significant differences, with distinct bands characteristic of Fe-O and terephthalic acid present across all samples.

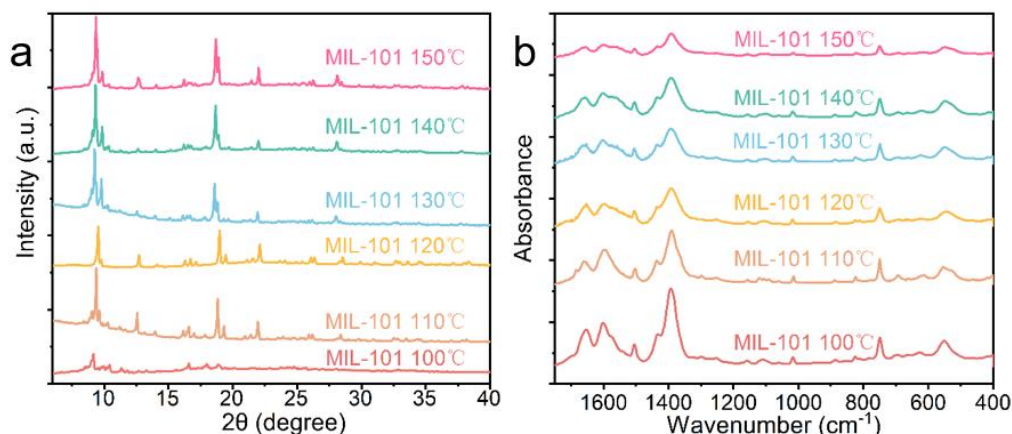


Fig. III-22 (a) XRD patterns and (b) FTIR spectra of MIL-101 synthesized by microwave method at different temperatures.

The morphologies of the as-prepared samples (Fig. III-23) are consistent with that reported in the literature [298]. At 100 °C, the microcrystals display heterogeneous shapes. However, at 120 °C, smoother surfaces and more uniform octahedra begin to appear. With further temperature increase, the size of the octahedra continues to grow, reaching its largest sizes with 5.14 μm in length and 4.14 μm in width at 150 °C. However, the structure becomes highly heterogeneous, with some octahedra several or even dozens of times larger than others. Therefore, 120 °C was determined to be the optimal temperature for microwave synthesis.

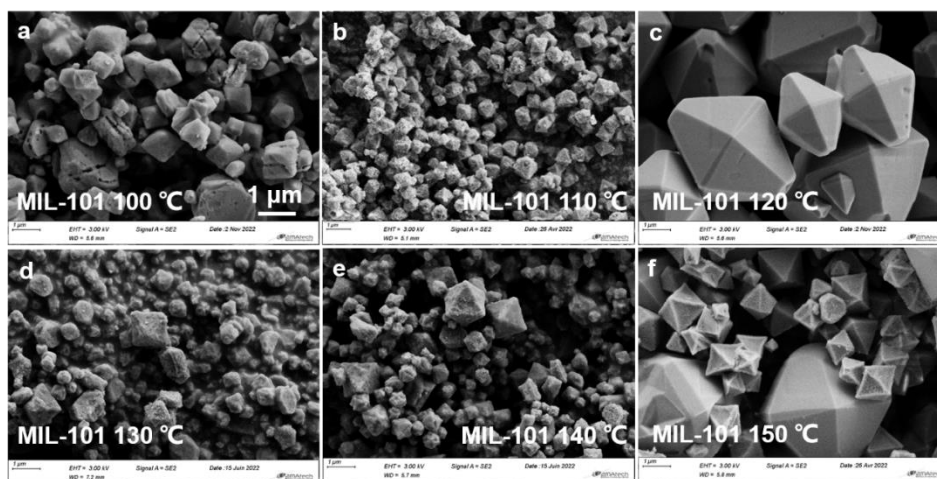


Fig. III-23 SEM results of MIL-101 synthesized by microwave method at different temperatures.

III.3.1.1.3 Effect of MW-assisted synthesis duration

In the second stage, the impact of microwave irradiation time was investigated. A yellow solution containing 4.96 mmol $\text{FeCl}_3 \cdot 6 \text{H}_2\text{O}$, 2.48 mmol H_2BDC , and 20 mL DMF was irradiated with microwaves at 120 °C for varying durations: 10, 20, 30, 40, 60, 80, and 100 min.

The XRD diagrams (Fig. III-24) demonstrate that the characteristic peaks of MIL-101 become gradually more pronounced from 10 min to 30 min, indicating the progressive stabilization of the crystalline form of MIL-101 with increasing irradiation time. After the reaction time exceeds 30 min, the XRD results remain almost unchanged, suggesting that the crystalline growth process has reached completion.

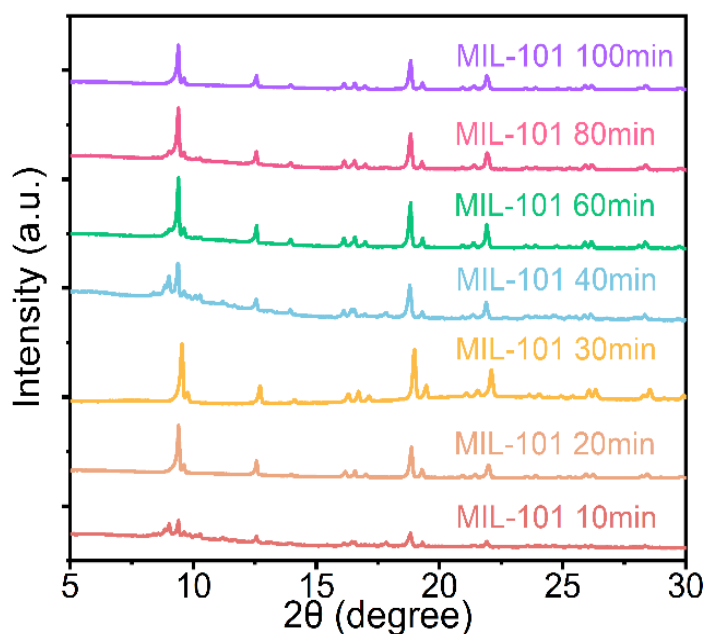


Fig. III-24 XRD results of MIL-101 synthesized by microwave method at different time.

SEM (Fig. III-25) images examination of MIL-101 samples subjected to reactions lasting 10 and 60 min corroborated the findings of XRD analysis. After 10 min of irradiation, the material displayed small discrete microcrystals taking shape, primarily manifesting as emerging octahedra, and predominantly ranged in size between 200 nm and 300 nm. Conversely, following a 60 min irradiation period, more regular structures were evident, appearing as either octahedra or truncated dodecahedra, albeit exhibiting highly heterogeneous sizes. This suggests that beyond the 30-minute mark, the

predominant reaction involves the growth of larger crystals from smaller ones. Thus, the optimal synthesis duration for MIL-101 is inferred to be 30 min.

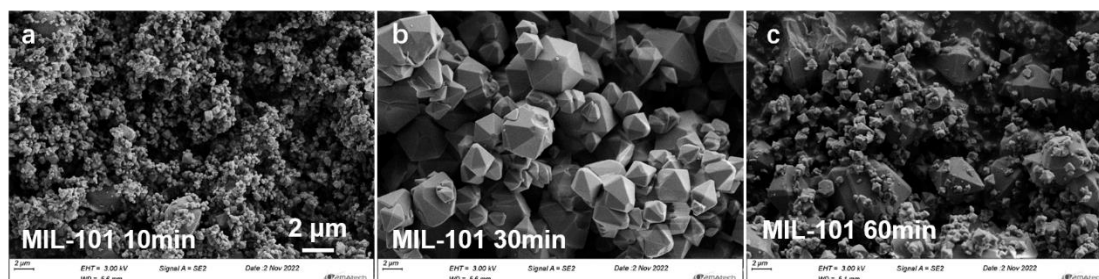


Fig. III-25 SEM results of MIL-101 synthesized by microwave method at different time.

III.3.1.1.4 Tuning the Fe to BDC ligand ratio

The effect of two Fe: H₂BDC molar ratio was investigated, Fe: H₂BDC 1: 1 [299] and 1: 2 [300] for 30 min of microwave irradiation at 120 °C.

The XRD results (Fig. III-26 a) showed that both ratios were able to produce the MIL-101 structure, however, the characteristic peaks were weaker when the dosage of iron was less, indicating a weaker crystalline structure. The IR results (Fig. III-26 b) also showed that the intensity of the carboxyl peak belonging to terephthalic acid was much weaker when H₂BDC was insufficient than when H₂BDC was sufficient.

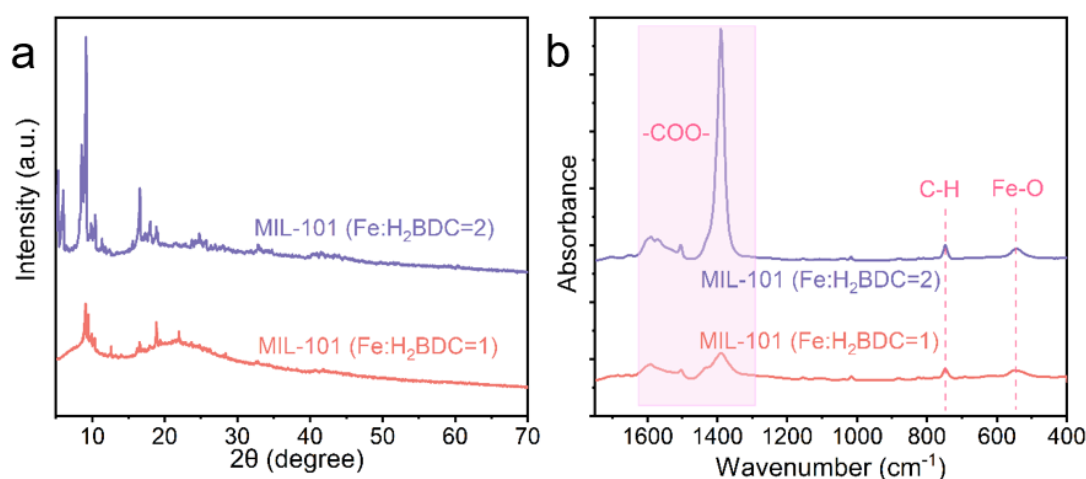


Fig. III-26 (a) XRD patterns and (b) FTIR spectra of MIL-101 synthesized by microwave method with different Fe:H₂BDC ratios.

The SEM results (Fig. III-27) bear this out. When there is insufficient iron, the microstructure of the sample has a large number of granular agglomerates in addition to the octahedra, which may be the remaining H₂BDC. whereas, when there is sufficient iron, a homogeneous octahedral and dodecahedral microstructure is generated.

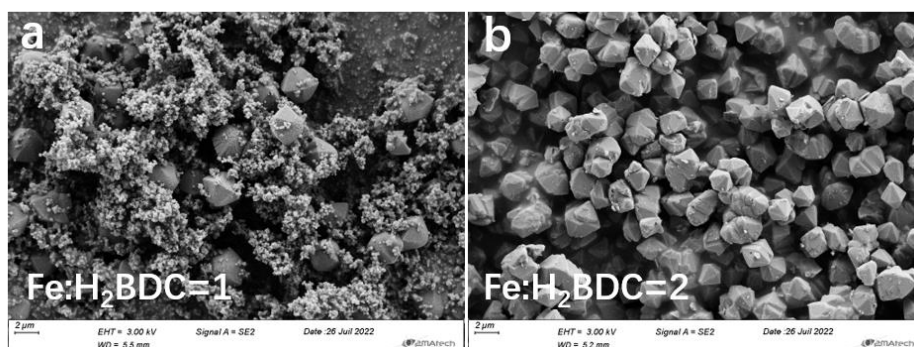


Fig. III-27 SEM images of MIL-101 synthesized by microwave method with different ratios of Fe and H₂BDC.

III.3.1.2 Characterization of MIL-101

Further characterization was performed on MIL-101 (Fe) prepared under optimized condition (30 min MW irradiation, 120 °C, Fe: H₂BDC = 2: 1). The TEM results (Fig. III-28) show that MIL-101 has a typical solid polyhedral structure, based on a mosaic of platelets crystals consistent with the SEM results and in agreement with previous reports. According to the IUPAC classification, the adsorption-desorption isotherm of MIL-101 belongs to the type IV isotherm. The porosity and surface properties of the MIL-101(Fe) material were calculated using the Barret-Joyner-Halenda (BJH) formula [301] and the Braunner-Emmett-Teller (BET) (Fig. III-29) formula [302], respectively. The specific surface area and pore size of MIL-101 were 94 m²/g and 18 cm³/g.

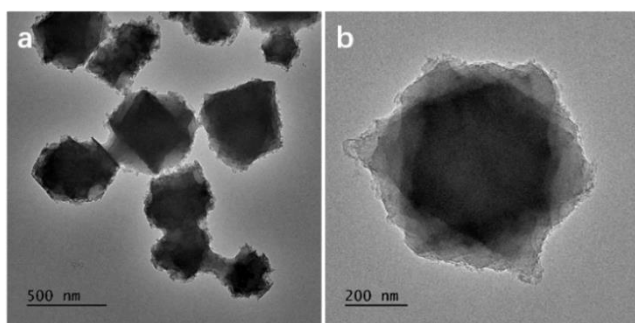


Fig. III-28 SEM of MIL-101.

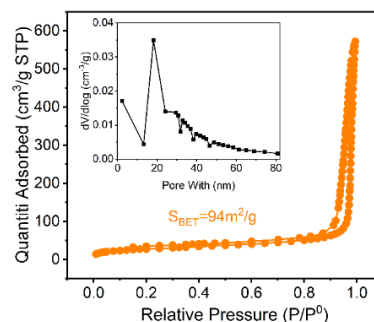


Fig. III-29 BET of MIL-101

Result of TGA (Fig. III-30) indicates that MIL-101 remains stable until 348 °C. The first weight loss (8.9%) that occurs between 25 and 348 °C is due to the evaporation of some solvent molecules and water. The second loss (61%) shown between 348 to 390 °C is due to the disintegration of part of the framework of MIL-101. The molecular formula of MIL-101, calculated by thermogravimetry, is $\text{Fe}_{2.6}\text{OCl}(\text{C}_8\text{H}_4\text{O}_4)_3 \cdot 3.8 \text{H}_2\text{O}$. The relative stability of the weight between 25 to 350 °C may be due to the high thermal stability of the carboxylate metal fragments [303].

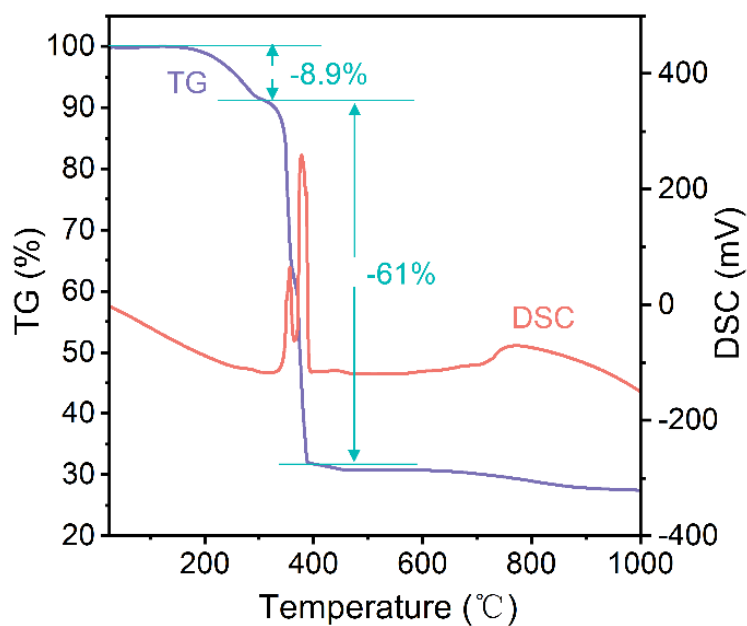


Fig. III-30 TGA of MIL-101.

III.3.1.3 Conversion of MIL-101 into LDH/101

III.3.1.3.1 Dosage of water

A similar approach as with MIL-88A was employed to investigate the transformation of MIL-101 into LDH/101 using nickel ion etching in a urea solution. However, MIL-101 is synthesized in an organic solvent (DMF), where it remains stable. When exposed to aqueous conditions, it becomes prone to hydrolysis [304], resulting in framework rupture. Conversely, the conversion process relies on urea hydrolysis [305], which necessitates water. Thus, the quantity of water added is crucial in the MIL-101 to LDH conversion. Various alcohol-water ratios were explored to study the conversion of MIL-101.

Based on the XRD and FTIR data (Fig. III-31), it appears evident that a layered phase emerges when the water content remains below 5% in ethanol. Notably, the MIL101 precursor persists under such conditions. However, with increased water content (25%, 50%, 75%, 100%), a distinct phase forms, characterized by terephthalate coordination to metal ions (Fe^{3+} , Ni^{2+}). A comparative analysis of the XRD patterns between NiFeLDH/88A and the layered phase (Fig. III-31 a) reveals a notable shift to lower 2 theta values in the (003), (012), and (110) peaks for the new phases. This deviation is inconsistent with the formation of a brucite-like M(II)(OH)_2 structure with M(III) isomorphic substitution but aligns more closely with the formation of $\alpha\text{-Ni(OH)}_2$ (JCPDS 14-0117), which exhibits a very similar structure to Ni-based LDH.

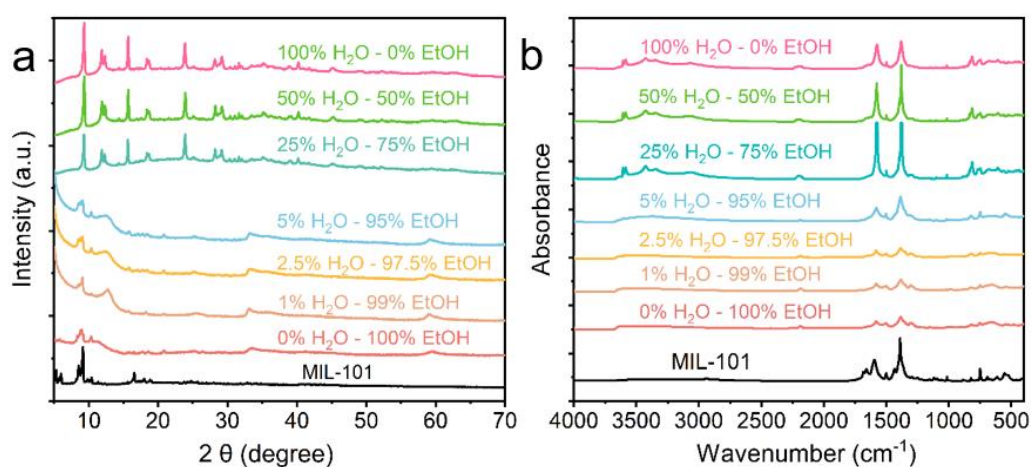


Fig. III-31 XRD and FTIR results of NiFeLDH/101 synthesized at different alcohol/water ratio.

EM images (Fig. III-32) revealed distinct outcomes based on the water content during the conversion process. In the absence of water, a flower-like structure formed, deviating from the regular morphology of the precursor. Conversely, when 1% water was introduced, the precursor's regular octahedral structure was maintained. However, with 5% water, the morphology was disrupted, giving rise to numerous lamellar structures. Additionally, particle attachment to these lamellar structures increased with higher water content. Notably, no typical LDH structure was observed, indicating a lack of LDH production. Consequently, 1% water was selected and further explored to improve the conversion reaction.

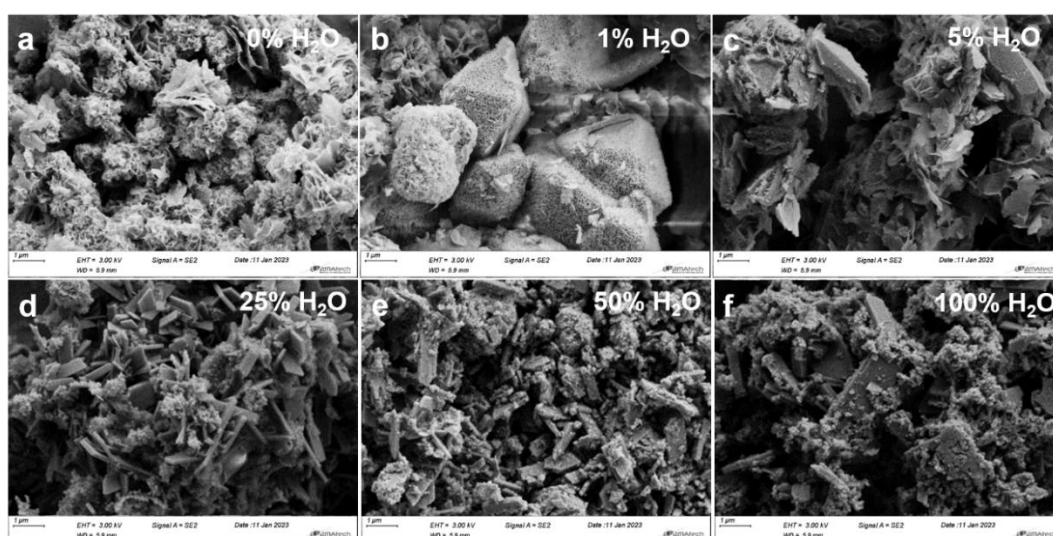


Fig. III-32 SEM images of NiFe-LDH/101 synthesized at different feed alcohol to water ratios.

TEM (Fig. III-33) is consistent with SEM. And TEM further illustrates that when there is no water involved in the conversion process, the product is a core-shell structure, and when there is too much water content, there is a lamellar structure appearing, and when it is in a pure water environment, lamellar structures are formed arising probably from the crystallization of a metal terephthalate salt that has not been identified so far.

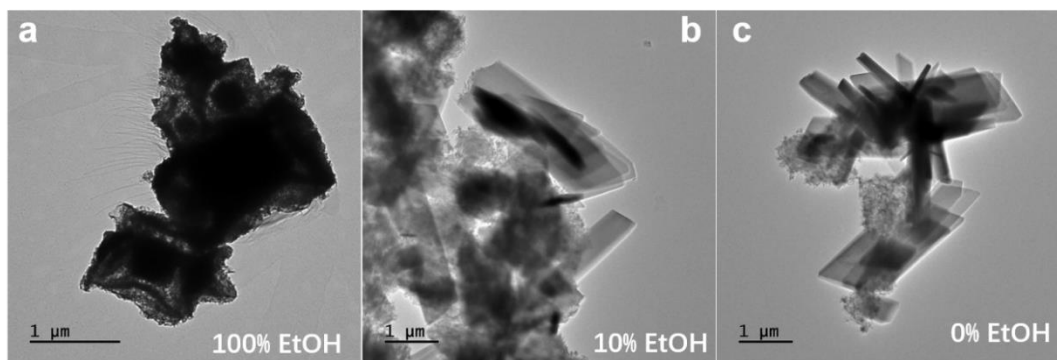


Fig. III-33 TEM images of NiFe-LDH/101 synthesized at different feed alcohol to water ratios.

III.3.1.3.2 Effect of reaction temperature and time for real MIL101 conversion

The effect of temperature and time on the transformation process was explored in order to obtain NiFe-LDH instead of α -Ni(OH)₂. Temperature and time of irradiation chosen were respectively 110, 120, 130, 140, 150 °C range 10, 30, 60 min. Unfortunately, whatever the conditions explored, the formation of NiFe-LDH was not evidenced but rather the growth of Ni(OH)₂ on the surface of MIL101 (Fig. III-34-35)

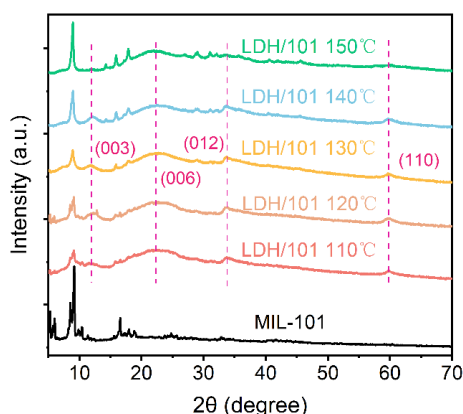


Fig. III-34 XRD patterns of LDH/101 converted from MIL-101 at different temperatures.

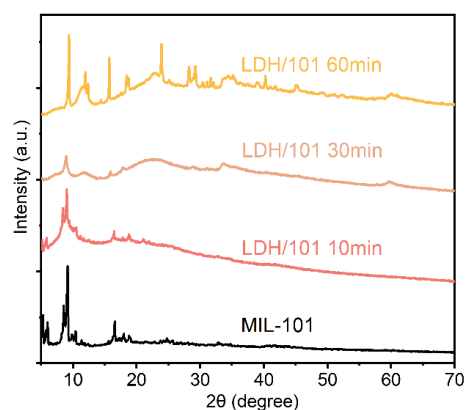


Fig. III-35 XRD patterns of LDH/101 at different reaction times.

SEM images (Fig. III-36) confirmed the XRD results. When the reaction temperature was insufficient, the MIL-101 precursor started to convert to LDH and could maintain a regular microstructure, but the conversion was but incomplete. When the temperature was too high, the structure of the MIL-101 precursor was disrupted and

a lamellar structure appeared, but the typical petal-like structure of LDH was still present, and on the other hand, its diameter was much smaller compared to the LDH synthesized at 130 °C. Therefore, 130 °C was chosen as the optimum conversion temperature.

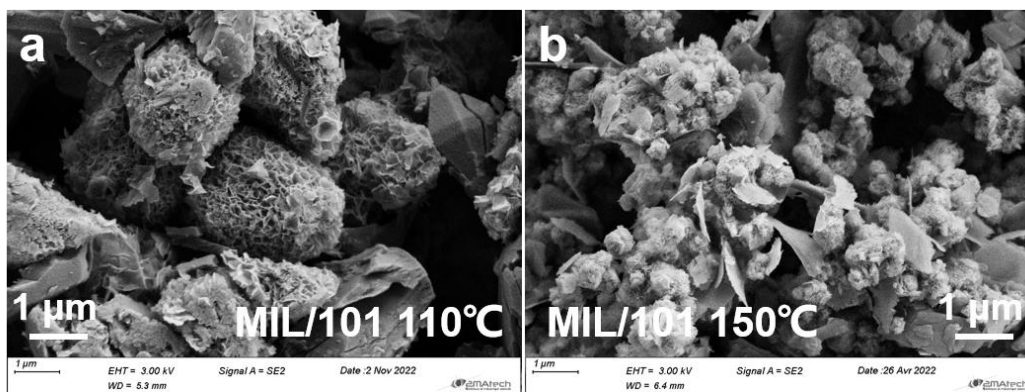


Fig. III-37 SEM images of LDH/101 converted from MIL-101 at different temperatures.

III.3.1.4 Conclusion

A metal-organic framework material MIL-101 synthesized from iron and terephthalic acid, which is different from MIL-88A of fumaric acid as organic ligand was successfully synthesized and its optimal synthesis conditions: 4.96 mmol of iron and 2.48 mmol of benzene dicarboxylic acid dispersed in 20 ml of DMF heated at 120 °C for 30 min in microwave were explored. This MIL-101 is an octahedral microstructure with a microporous structure.

This MIL-101 as precursor was unsuccessfully etched by nickel ions to form NiFe LDH. However, in alcohol-water solutions with water% < 5%, the formation of α -Ni(OH)₂ was observed.

III.3.2 Synthesis of Al-BDC and its conversion to NiAl-LDH/BDC

In the synthesis of metal-organic frameworks (MOFs), the combination of iron and fumaric acid yields MIL-88A, an iron-based MOF. To explore alternatives, aluminium,

was selected for the successful creation of an aluminium-based MOF, Al-FA, through reaction with fumaric acid. Additionally, the compatibility of terephthalic acid (BDC), known for its ability to produce MIL-101 with iron, with metals other than iron was investigated, with a focus on its potential conversion to layered double hydroxide (LDH). Consequently, the collaborative effect of aluminium and terephthalic acid, along with the subsequent conversion to LDH, was explored.

The synthesis of Al-BDC was conducted using aluminium chloride and terephthalic acid, following the method outlined by Wang [306]. Specifically, 3.1 mmol of $\text{AlCl}_3 \cdot 6\text{H}_2\text{O}$ was dissolved in 5 mL of water (solution A), while 3.1 mmol of H_2BDC was dissolved in 5 mL of DMF (solution B). Solutions A and B were thoroughly combined and subjected to microwave heating at 150 °C for 60 min. The resulting white solid was collected via centrifugation, washed three times with deionized water and ethanol, respectively, and subsequently dried in an oven at 60 °C.

The XRD results of the synthesized metal-organic ligand complex, which is, aluminum terephthalate is shown in Fig. III-38. The results are very different from Al-FA and even from the XRD results that have been for Al-BDC [307].

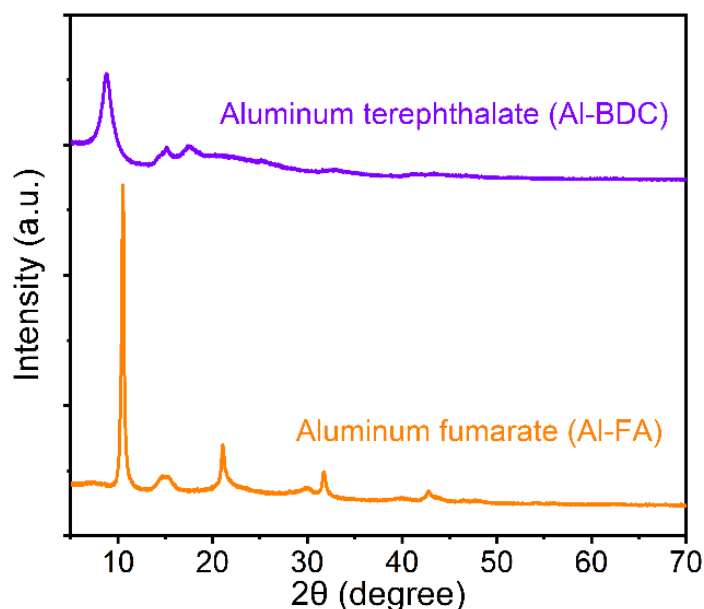


Fig. III-38 XRD patterns of Al-FA and Al-BDC.

SEM images (Fig. III-39) of Al-BDC show that its microstructure is aggregated regular spheres with a small diameter of less than 200 nm. The surface of the spherical structure is not smooth and is covered with granular material. This Al-BDC complex was probed by nickel ion etching for conversion to LDH.

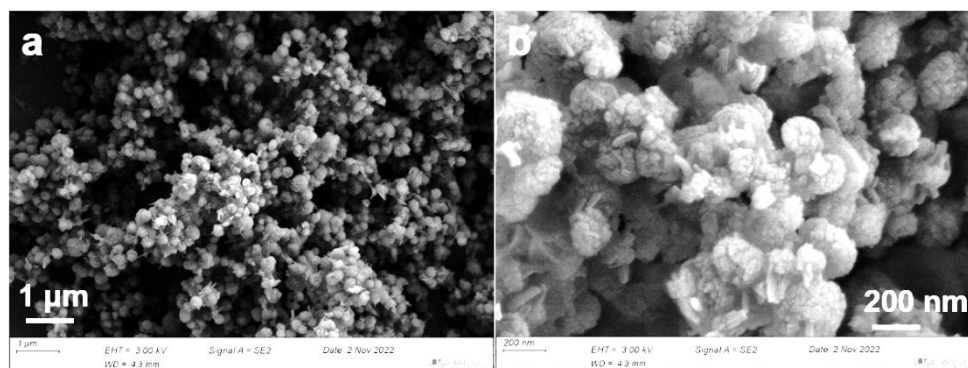


Fig. III-39 SEM images of Al-BDC.

After the conversion reaction, X-ray diffraction (XRD) (Fig. III-40 a) analysis revealed characteristic peaks corresponding to layered double hydroxide (LDH), specifically the (003), (006), (012), and (110) crystal planes, confirming the successful transformation. This observation was further corroborated by scanning electron microscopy (SEM) results, which depicted an abundance of flakes on the surface, indicative of the LDH structure. Notably, the originally observed spherical morphology of Al-BDC was disrupted during the conversion process.

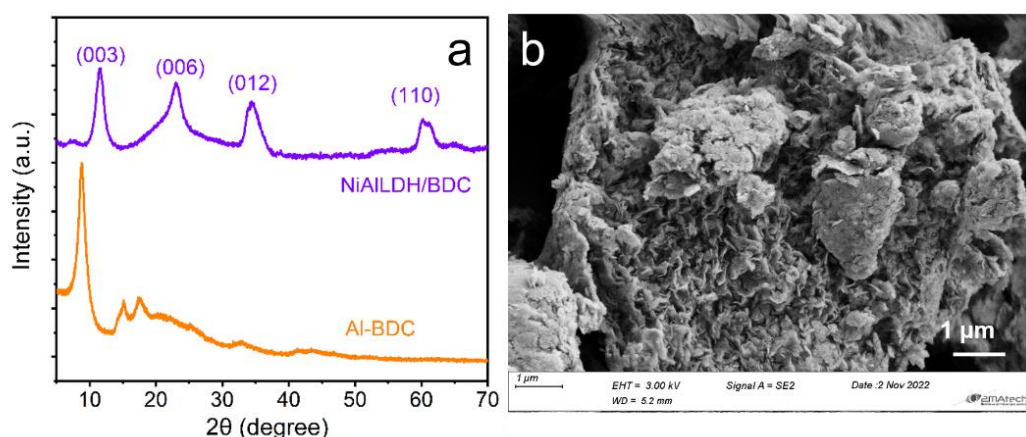


Fig. III-40 (a) XRD patterns and (b) SEM image of NiAlLDH/BDC.

Al-BDC synthesized from H₂BDC and aluminum displays small size particles and

when it is converted to LDH, the spherical microstructure is not maintained and the lamellar structure of LDH appears agglomerated.

III.3.3 Conclusion

This chapter explores the conditions under which organic ligands are used in the conversion of MOF to LDH. Iron-based MOFs and aluminum-based MOFs were successfully synthesized with terephthalic acid and iron and aluminum, respectively. During the conversion to LDH, the LDH/101 maintains its original ortho-octahedral structure due to the large diameter of the MIL-101 microstructure. On the contrary, Al-BDC, due to its small microstructure, the microstructure is destroyed and not maintained during the conversion process. Therefore, the organic ligands and metal ions only need to satisfy the conditions: to be able to synthesize stable MOF materials with large sizes.

III.4 Conclusion

This chapter explores the conditions of metal ions and organic ligands in the conversion of MOF to LDH, where metal ions are discussed in terms of their use as etchant and backbone.

For etching metal ions, they need to meet the following conditions: faster hydrolysis, able to release a large number of protons under alkaline conditions; stronger binding ability with hydroxide, able to form double hydroxide with nickel ions rapidly at the same time. For backbone ions and organic ligands, it is necessary to be able to synthesize micro-sized, stable MOF materials. For successful conversion of MOF to LDH, the above conditions must be met simultaneously.

Chapter IV

Synthesis of phosphate intercalated LDH/88A and its application: adsorption of lead ions in water

IV.1. Introduction

Water pollution caused by heavy metals (HMs) from human activities poses a serious contemporary challenge due to its profound toxicity to both terrestrial and aquatic ecosystems [308, 309]. Lead, as a prime example of a heavy metal, is exceptionally toxic, with acceptable upper limits for blood lead levels set at 10 $\mu\text{g/L}$ to prevent brain diseases and 3.5 $\mu\text{g/L}$ as the maximum acceptable limit in drinking water. Most contaminations originate from industrial processes, batteries, and paint. Effectively removing heavy metals has proven to be a daunting task for researchers. Various conventional techniques such as ion exchange [310], chemical precipitation [311], reverse osmosis [312], membrane filtration [313] and adsorption processes [314] are employed to treat wastewater containing heavy metals. However, chemical precipitation methods typically necessitate additional flocculation processes for assisted precipitation. Pollutants and heavy metals in wastewater form water-soluble complexes that do not directly react with chemical precipitation, potentially leading to secondary pollution, high energy costs, and other disadvantages [315]. Challenges such as the high cost of membrane preparation, susceptibility to clogging, poor strength, and potential consumption of membrane cleaning agents have constrained the advancement of membrane separation technology [316].

Although adsorption technology is considered one of the most cost-effective, easy-to-engineer, high-capacity, and high-volume technologies, designing a highly efficient, robust, selective, stable, and promising adsorbent for the adsorption process has always been a formidable challenge [317]. A plethora of inorganic and organic materials including zeolites, mesoporous silica, graphene oxide, multi-walled carbon nanotubes [318], activated carbon, metal-organic frameworks (MOFs), biomaterials, covalent organic frameworks, organic polymers and resins have been utilized to adsorb metal ions. However, such materials are also characterized by easy dispersion, difficulties in solid-liquid separation, and potential ecological safety hazards, significantly limiting their further development. Additionally, although natural adsorbents (including clays) boast cost-effectiveness, large specific surface areas, and excellent hydrophilicity and can serve as potent adsorbents, they suffer from weak selectivity and insufficient affinity in recognizing heavy metals.

Layered double hydroxides (LDHs) have garnered extensive attention from researchers due to their large theoretical specific surface area, interaction of surface positive metal ions with pollutants, high hydrophilicity, high interlayer negative charge density, low cost, and high efficiency [319]. LDHs are synthetic inorganic layered materials with the general chemical formula $[M(II)_{1-x}M(III)_x(OH)_2][X^{q-}_{x/q} \cdot nH_2O]$, composed of positively charged layers containing divalent M (II) and trivalent M (III) cations with exchangeable intercalated anions X^{q-} and water molecules. They are straightforward to prepare and cost-effective. While they have been extensively studied for their anion scavenging properties, they may also serve with their calcined derivatives (Layered Double Oxides, LDOs) as potentially effective cation adsorbents, capable of adsorbing heavy metal ions (HMs) through various mechanisms, either via surface precipitation or through complexation with molecular or macromolecular ligands modified LDHs [319-321]. However, the adsorption efficiency of LDHs for HMs may be limited by their poor surface and porosity properties or by their high tendency to aggregate due to their high surface charge density [192, 212, 322, 323]. The conversion of LDHs from MOFs has been utilized as an effective approach to enhancing the three-dimensional architecture of LDH platelets and subsequently their adsorption properties [324, 325]. Moreover, functionalization of LDH surface may be envisaged to enhance the adsorption selectivity for heavy metals [326]. Therefore, functional groups or structural components can be introduced into pristine LDHs via intercalation, surface modification, or loading to prepare functionalized LDHs [327]. Depending on the anion-exchangeability of LDHs, inorganic anions that can selectively react with heavy metals, such as sulphide, polysulfide, carbonate, sulphate, and phosphate, can be intercalated to improve the removal efficiency of HM pollutants [328].

Hence, the objective of the present study is to functionalize 3D Ni_xFe -LDH derived from MIL-88A conversion by HPO_4^{2-} phosphate anions capable of precipitating lead phosphate. Additionally, the removal efficiency of this new phosphorus-modified LDH material in aqueous solutions for lead ions is investigated. The adsorption kinetics and thermodynamics of this novel phosphorus-modified LDH material for lead ion adsorption are examined by fitting an existing kinetic model with kinetic and thermodynamic data. Furthermore, the adsorption mechanism is explored in depth.

IV. 2. Materials and methods

IV. 2.1 Materials and characterization techniques

All chemicals involved in this study are commercially available and used without additional purification. Ferric nitrate nonahydrate ($\text{Fe}(\text{NO}_3)_3 \cdot 9\text{H}_2\text{O}$), nickel nitrate hexahydrate ($\text{Ni}(\text{NO}_3)_2 \cdot 6\text{H}_2\text{O}$), urea ($\text{CO}(\text{NH}_2)_2$), fumaric acid ($\text{HOOC}-\text{CH}=\text{CH}-\text{COOH}$), sodium hydroxide (NaOH), nitric acid (HNO_3), sodium chloride (NaCl), dipotassium hydrogen phosphate (K_2HPO_4) all from Aladdin Scientific.

Powder X-ray diffraction (PXRD) analysis were performed with a PANalytical X'pert PRO diffractometer, equipped with a $\text{Cu K}\alpha$ ($\lambda = 1.5415 \text{ \AA}$) radiation source (45 kV and 40 mA). The samples were scanned for $2\theta = 5-70^\circ$ with a step size of 0.05° and a scan rate of 3 s per step. FTIR spectra were acquired with a Varion 7000 FTIR spectrometer using the KBr pellet technique. Spectra were recorded in transmittance mode from 4000 to 400 cm^{-1} using 64 scans at a 2 cm^{-1} resolution. Field-emission scanning electron microscopy (SEM, JEOL, JSM-6700F) with an energy dispersive X-ray spectrometer was used to characterize the morphology. The BET surface area of samples was determined by an ASAP 2020 surface analyzer. The surface compositions of the products were evaluated by X-ray photoelectron spectra (XPS, Thermo ESCALAB 250XI). The point of zero charge (pH-pzc) is measured by Zeta potential meter (Zetasizer nano from Malvern). pH was fixed using HNO_3 and NaOH 1 M, 0.1 M, and 0.01 M solutions. The content of lead ions in the solution before and after adsorption was analysed by inductively coupled plasma emission spectrometry (ICP-OES) (model Perkin-Elmer Optima 5300).

IV. 2.2 Synthesis method

Synthesis of $\text{Ni}_x\text{FeLDH}/\text{COP}-\text{NO}_3$ ($x=2, 3$): 50 mL of a mixed solution of 0.1 M $\text{Fe}(\text{NO}_3)_3 \cdot 9\text{H}_2\text{O}$ and 0.2 M $\text{Ni}(\text{NO}_3)_2 \cdot 6\text{H}_2\text{O}$, prepared in deionized water, is added dropwise to 100 mL of deionized water. Precipitation of Ni_2FeLDH is realized at a fixed pH of 10.0 by the simultaneous addition of a 0.5 M NaOH aqueous solution, under vigorous stirring, room temperature and N_2 atmosphere. After 6 h addition, the

suspension is aged at room temperature for 12 h. The product is collected by centrifugation and washed with water until the pH is unchanged. The Ni₂FeLDH/COP-NO₃ is then dried in an oven at 60 °C overnight [229]. Ni₃FeLDH/COP-NO₃ was prepared similarly by changing the nickel nitrate concentration to 0.3 M, the other conditions remaining unchanged.

Synthesis of Ni_xFeLDH/88A-NO₃ (x=3,5). Then, 50 mg of MIL-88A is dispersed in 4 mL of ethanol (solution A). 150 mg of Ni(NO₃)₃·6H₂O and 100 mg of urea are dissolved in 6 mL of deionized water (solution B). Then, solutions A and B are mixed and stirred at room temperature (solution C). Finally, solution C is placed in a microwave reactor and heated at 110 °C for 1 h. The product is washed three times with deionized water and ethanol by centrifugation and then dried at 60 °C overnight to obtain Ni₃FeLDH/88A-NO₃ [168]. The Ni₅FeLDH/88A-NO₃ can be obtained by changing the dosage of Ni(NO₃)₃·6H₂O to 250 mg, the other conditions remaining unchanged.

Synthesis of Ni_xFeLDH/COP-Cl (x=2,3) and Ni_xFeLDH/88A-Cl (x=3,5): 2.0 g of LDH (Ni₃FeLDH/88A-NO₃, Ni₅FeLDH/88A-NO₃, Ni₂FeLDH/COP-NO₃ and Ni₃FeLDH/COP-NO₃) are homogeneously dispersed in 100 mL of 0.05 M NaCl solution, at a pH adjusted to 7.0, stirred overnight in nitrogen atmosphere, centrifuged and separated, then washed with ultrapure water until the pH was unchanged, and dried into an oven at 60 °C for 24 h, leading to the as-prepared LDH-Cl.

Synthesis of Ni_xFeLDH/88A-PO₄ (x=3,5) and Ni_xFeLDH/COP-PO₄ (x=2,3): 1.7 g LDH-Cl (Ni₃FeLDH/88A-Cl, Ni₅FeLDH/88A-Cl, Ni₂FeLDH/COP-Cl, Ni₃FeLDH/COP-Cl) are homogeneously dispersed in 100 mL of 0.095 M of potassium dihydrogen phosphate (K₂HPO₄) solution, at a pH adjusted to 7.0, stirred overnight in a nitrogen atmosphere. The Ni₃FeLDH/88A-PO₄, Ni₅FeLDH/88A-PO₄, Ni₂FeLDH/COP-PO₄, Ni₃FeLDH/COP-PO₄ materials were recovered after centrifugation and separation, washing with deionized water until the pH is unchanged, and dried in an oven at 40 °C for 24 h. These phosphates loaded LDH sorbents will be abbreviated as LDH-PO₄ for simplifying.

IV. 3. Morphological and structural characterization

Different NiFe-LDH phases were prepared by either classic coprecipitation or MIL conversion and subsequently intercalated by both Cl^- and HPO_4^{2-} using anion exchange reaction to evaluate the influence of the LDH nanostructuration and chemical composition on Pb^{2+} adsorption.

The PXRD spectra of the four samples loaded with phosphate anions, exhibit the characteristic structural signature of the hexagonal (R-3 m) NiFe LDH phase (JCPDS Card 00-51-0462) [329]. The diffraction patterns reveal distinct (003), (006), (012), and (110) diffraction lines at approximately 11.3° (2θ), 23.5° (2θ), 34.0° (2θ), and 60.1° (2θ), respectively (Fig. IV-1). The mean basal spacings observed of approximately 7.70 Å highlight that phosphate anions are not located in the interlayer domains but are only exchanged at the LDH platelet surface. As reported by Sokol et al. [330], the intercalation of phosphate anions in LDH leads to basal spacing expansion between 10.0 Å and 10.8 Å.

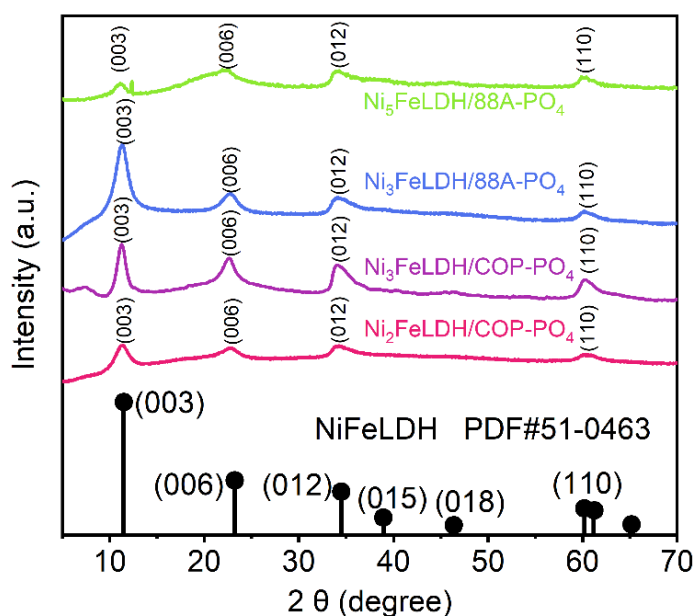


Fig. IV-1. XRD of $\text{Ni}_2\text{FeLDH}/\text{COP-PO}_4$, $\text{Ni}_3\text{FeLDH}/\text{COP-PO}_4$, $\text{Ni}_3\text{FeLDH}/88\text{A-PO}_4$ and $\text{Ni}_5\text{FeLDH}/88\text{A-PO}_4$.

Infrared spectroscopy (Fig. IV-2) further confirms the presence of phosphate in

the solids. The two symmetric and antisymmetric stretching bands ($\nu_1(\text{PO}_4)$ at 1095 cm^{-1} and $\nu_3(\text{PO}_4)$ at 1047 cm^{-1}) [331] are clearly observed, as well as the typical vibration bands of the $[\text{Ni}_{1-x}\text{Fe}_x(\text{OH})_2]^{x+}$ lattice ($\nu(\text{MO-H})$ and $\nu(\text{HO-H})$ at $3200\text{-}3600\text{ cm}^{-1}$, $\nu(\text{MO}_6)$ at 675 cm^{-1} , $\delta(\text{OMO})$ at 517 cm^{-1}) [332, 333], and the intercalated H_2O and CO_3^{2-} species ($\delta(\text{HOH})$ at 1630 cm^{-1} , $\nu_3(\text{CO}_3)$ at 1375 cm^{-1}) [334, 335]. As indicated by the presence of the typical doublet $\nu_{\text{as}}(-\text{CO}_2^-)$ (1569 cm^{-1}) and $\nu_{\text{s}}(-\text{CO}_2^-)$ (1375 cm^{-1}), some fumarate anions have not been fully removed during MIL-88A conversion.

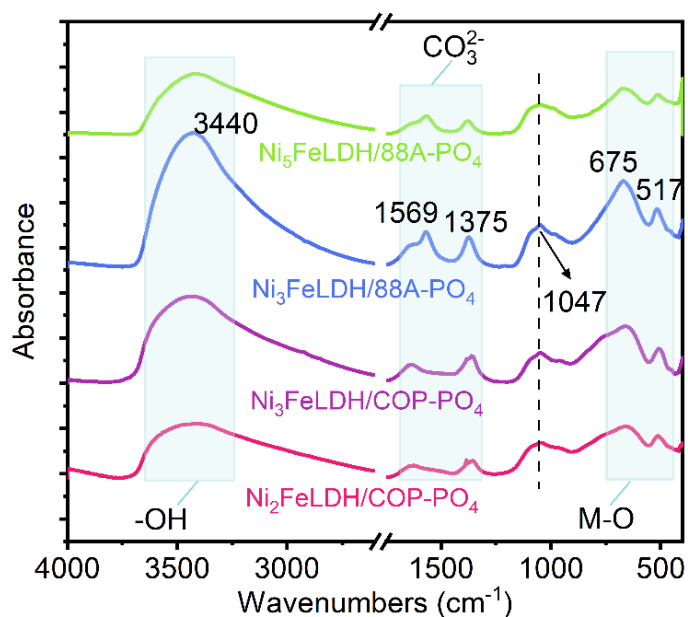


Fig. IV-2. FTIR of $\text{Ni}_2\text{FeLDH/COP-PO}_4$, $\text{Ni}_3\text{FeLDH/COP-PO}_4$, $\text{Ni}_3\text{FeLDH/88A-PO}_4$ and $\text{Ni}_5\text{FeLDH/88A-PO}_4$.

SEM mapping (see Fig. IV-3) shows a uniform distribution of the four elements (Ni, Fe, O, and P) into the particles. As shown in the SEM images (Fig. IV-4 a, b), direct synthesis by co-precipitation leads to the formation of highly aggregated platelets. Using MIL-88A microcrystals, which exhibit a typical hexagonal rod-like morphology with tip ends, as structural templates preserves the original rod-like structure (Fig. IV-4 c, d). The subsequent loading with phosphate anions in $\text{Ni}_x\text{FeLDH/88A-Cl}$ ($x=3, 5$) precursors does not alter the morphology. The rods of $\text{Ni}_3\text{FeLDH/88A-PO}_4$ and $\text{Ni}_5\text{FeLDH/88A-PO}_4$ have average sizes of $5\text{ }\mu\text{m}$ in length and $1.2\text{ }\mu\text{m}$ in width, comprising an intergrowth of hexagonal nanoplatelets smaller than 100 nm . These observations confirm that during the synthesis process, as MIL-88A dissolves, the shell of LDH gradually forms on the outer surface of the template [322].

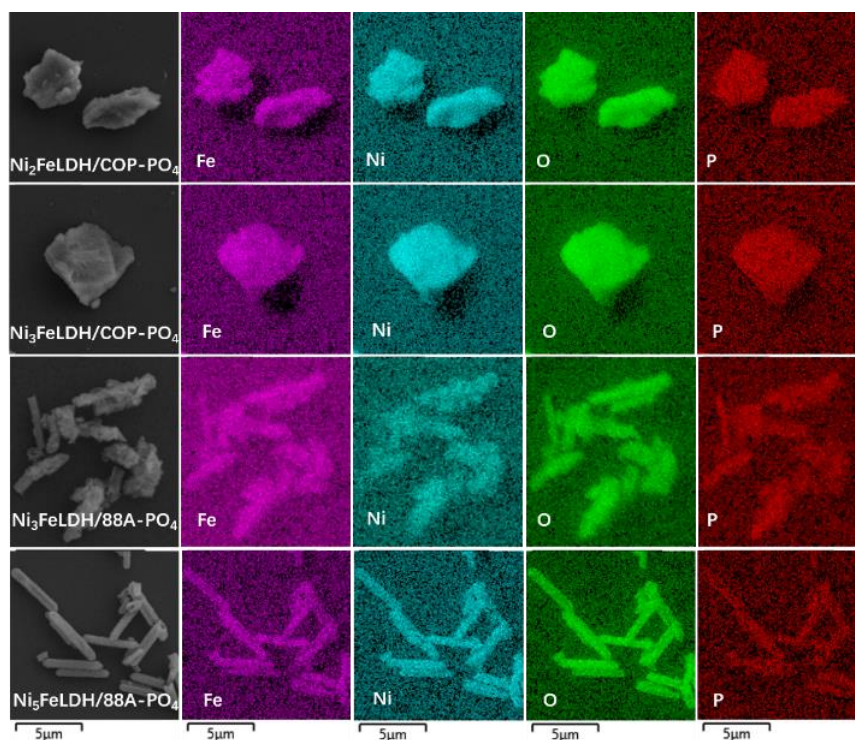


Fig. IV-3 SEM element mapping of $\text{Ni}_3\text{FeLDH}/88\text{A-PO}_4$, $\text{Ni}_5\text{FeLDH}/88\text{A-PO}_4$, $\text{Ni}_2\text{FeLDH}/\text{COP-PO}_4$ and $\text{Ni}_3\text{FeLDH}/\text{COP-PO}_4$.

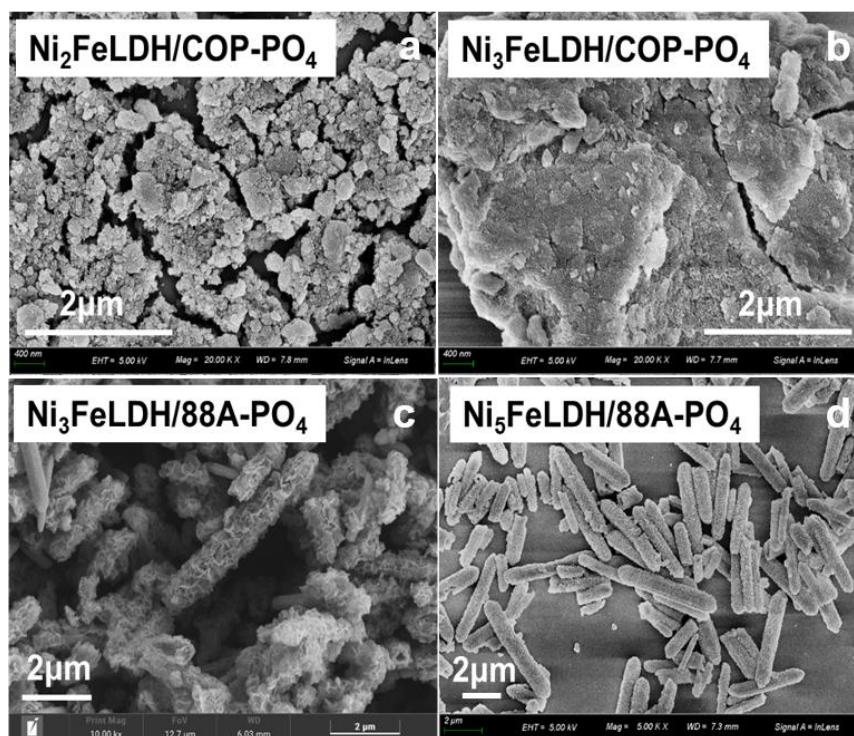


Fig. IV-4 (a) SEM of $\text{Ni}_2\text{FeLDH}/\text{COP-PO}_4$, (b) $\text{Ni}_3\text{FeLDH}/\text{COP-PO}_4$, (c) $\text{Ni}_3\text{FeLDH}/88\text{A-PO}_4$ and (d) $\text{Ni}_5\text{FeLDH}/88\text{A-PO}_4$.

The chemical composition of the four sorbents determined by ICP-OES (Table. IV-1) show that for the coprecipitated phases, the Ni/Fe values (1.89 and 3.31) closely match the expected ones (2.0 and 3.0) for a total coprecipitation. The presence of phosphorus is clearly detected in all adsorbents with a Fe/P atomic ratio slightly higher than require for a charge X^{q-}/M^{3+} compensation in pure LDH-phosphate structure ($Fe^{3+}/PO_4^{3-} = 3$). This is consistent with surface adsorption of phosphate rather than complete intercalation. $Ni_3FeLDH/88A-PO_4$ and $Ni_5FeLDH/88A-PO_4$ exhibit Ni/Fe below the solid solution limit Ni/Fe = 2.0 of the LDH structure and even below than that expected for x= 3 and 5. This excess of iron suggests that $Ni_3FeLDH/88A-PO_4$ and $Ni_5FeLDH/88A-PO_4$ contain iron phase impurities, formed under the uncompleted conversion of iron from MIL88A into LDH. This results in lower phosphate loading with Fe/P ratio values 5.91 and 6.05, for x = 3 and 5, respectively.

Table. IV-1 Atomic percentages and atomic ratio of elements from ICP-OES analysis.

ICP-OES analysis	Ni (At%)	Fe (At%)	P (At%)	Ni/Fe	Fe/P
$Ni_2FeLDH/COP-PO_4$	10.01	5.31	1.55	1.89	3.43
$Ni_3FeLDH/COP-PO_4$	16.89	5.1	1.52	3.31	3.36
$Ni_3FeLDH/88A-PO_4$	9.57	8.51	1.44	1.12	5.91
$Ni_5FeLDH/88A-PO_4$	12.81	6.71	1.11	1.91	6.05

N_2 adsorption experiments were conducted for the different samples to assess the impact of the topotactic conversion of MIL-88A into Ni_xFe LDH on their surface properties (Fig. IV-5). Initially, the isotherms of the $Ni_2FeLDH/COP-PO_4$ and $Ni_3FeLDH/COP-PO_4$ adsorbents, along with their chloride precursors, displayed type I isotherms, indicating low porous volumes and low specific surface areas ($< 32 \text{ m}^2/\text{g}$) (Table. IV-2). These characteristics are typical of non-porous solids [336]. Phosphate exchange did not alter the surface properties. In contrast, all samples derived from MIL-88A conversion exhibited type IV isotherms, accompanied by hysteresis loops associated with mesoporous structures. According to the International Union of Pure and Applied Chemistry (IUPAC) classification, this hysteresis ring is of the H3 type, indicating that the plate-like particles are clustered together to form slit-like pores [25]. Once again, phosphate loading preserved the porosity and surface properties.

Table. IV-2. Results of the parameters evaluated by the nitrogen adsorption assay (BET method) for LDH-PO₄ samples.

LDH samples	S _{BET} (m ² /g)	V _t (cm ³ /g)	LDH samples	S _{BET} (m ² /g)	V _t (cm ³ /g)
Ni ₃ FeLDH/88A	80	0.2983			
Ni ₃ FeLDH/88A-PO ₄	109	0.3385	Ni ₃ FeLDH/88A-Cl	120	0.3190
Ni ₅ FeLDH/88A-PO ₄	78	0.2858	Ni ₅ FeLDH/88A-Cl	63	0.1769
Ni ₂ FeLDH/COP-PO ₄	25	0.0314	Ni ₂ FeLDH/COP-Cl	32	0.0372
Ni ₃ FeLDH/COP-PO ₄	15	0.0195	Ni ₃ FeLDH/COP-Cl	12	0.0190

S_{BET}: area by BET method; V_t: total pore volume

The BET specific surface areas were 7 to 10 times higher than those of the coprecipitated phases (Table. IV-2), with values of 109 m²/g and 15 m²/g for Ni₃FeLDH/88A-PO₄ and Ni₃FeLDH/COP-PO₄, respectively, and 120 m²/g and 12 m²/g for Ni₃FeLDH/88A-Cl and Ni₃FeLDH/COP-Cl, respectively. Porous volumes were further increased by a factor of 17. This demonstrates the superiority of LDH converted from MOF material in terms of enhanced surface properties.

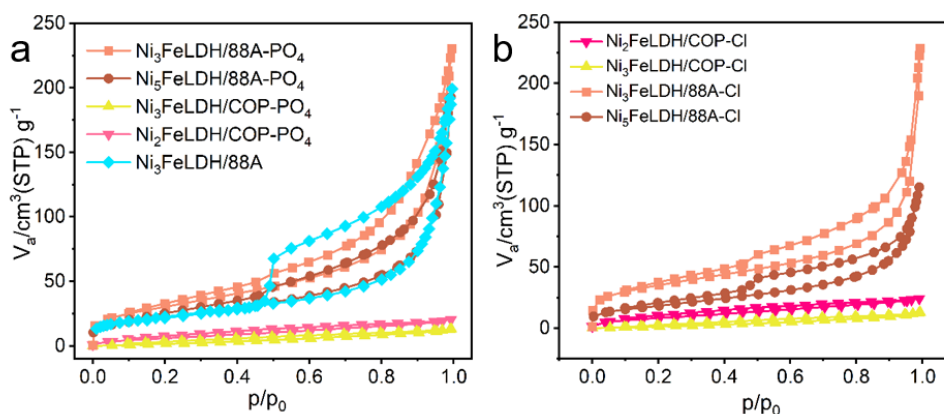


Fig. IV-5 BET analysis of a) Ni₂ or ₃FeLDH/COP-PO₄, Ni₃ or ₅ FeLDH/88A-PO₄ and b) Ni₂ or ₃FeLDH/COP-Cl, Ni₃ or ₅ FeLDH/88A-Cl.

The surface composition of the adsorbent underwent further investigation through X-ray photoelectron spectroscopy (XPS) analysis. The data were processed using a simple mathematical deconvolution of the XPS peaks (Fig. IV-6). The measured scanning spectra confirmed the presence of Ni, Fe, C, P, and O elements in the adsorbent. In the high-resolution XPS spectrum of Fe 2p, two peaks appeared at 711.5

and 725.2 eV, attributed to Fe³⁺ and corresponding to Fe 2p_{3/2} and Fe 2p_{1/2} energy bonds, respectively. Additionally, satellite peaks were observed at 710.5 and 730.2 eV [337, 338]. The Ni 2p spectra depicted distinct single peaks of Ni 2p_{1/2} and Ni 2p_{3/2} positioned at 873.5 and 856.1 eV, respectively, indicating the spin-orbit properties of Ni 2p in the four LDH-containing phosphorus adsorbents. The presence of Ni²⁺ in the four phosphorus-containing adsorbents was further verified by the correlation of two different peaks near 873.4 and 855.9 eV with the satellite peaks of Ni 2p [339, 340]. The high-energy peak located at 133.3 eV and 132.4 eV are close to the peak of the phosphor-like acid, which proves the formation of the P-O chemical bond [341], which indicates that the phosphate group was successfully loaded onto LDH.

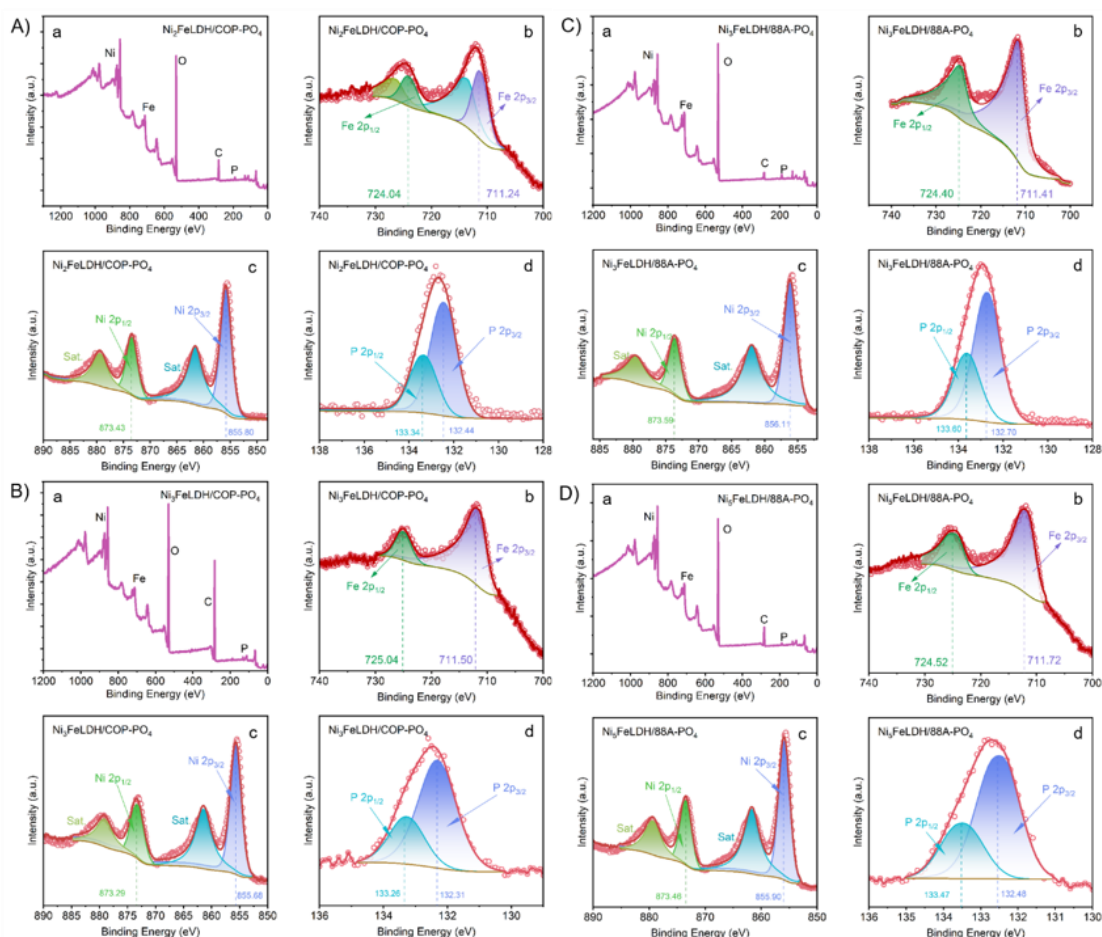


Fig. IV-6 XPS of (A) Ni₂FeLDH/COP-PO₄, (B) Ni₃FeLDH/COP-PO₄ (C) Ni₃FeLDH/88A-PO₄ and (D) Ni₅FeLDH/88A-PO₄.

IV. 4 Pb²⁺ adsorption properties of PO₄ loaded LDH

The adsorption processes typically entail intermolecular interactions between solute and solid phases. Interaction with surface anions, complexation, chelation, precipitation, and isomorphic substitutions are among the most commonly proposed mechanisms for the adsorption of metal ions onto the LDH surface [342]. These mechanisms are significantly influenced by factors such as pH, temperature, ionic strength, and adsorbent dose. Hence, it is crucial to ascertain the nature and mechanism of adsorption, as well as the stability of the adsorbent during the adsorption process.

IV. 4.1 Effect of pH

The effect of pH on the adsorption of heavy metals was carried out in 50 mL centrifuge tubes containing 10 mg of LDH-PO₄ and 500 ppm of lead ions; the solution in the centrifuge tubes is stirred at room temperature in a thermostatic shaker. The pH was adjusted to 4, 5, 6, 7, with HNO₃ or NaOH 1 M, 0.1 M, and 0.01 M solutions, and the Pb²⁺ concentrations were determined by ICP-OES analysis. The impact of pH on the adsorption of Pb²⁺ (500 ppm, 50 mL) by the LDH-PO₄ adsorbents (10 mg) is illustrated in Fig. IV-7 a-d. In this investigation, 100% removal corresponds to 2.5 g Pb²⁺ per g of sorbent. The pH of the solution plays a key role in phosphate adsorption [343]. The adsorption capacity of the four adsorbents for lead increased with pH within the range of pH 4-9, after which a plateau is reached. The co-precipitated adsorbents, Ni₂FeLDH/COP-PO₄ and Ni₃FeLDH/COP-PO₄, exhibited adsorption capacities of less than 80 mg. g⁻¹, with adsorption efficiencies of the co-precipitated LDH adsorbents, Ni₂FeLDH/COP-PO₄ and Ni₃FeLDH/COP-PO₄, were less than 20%, indicating extremely weak adsorption capacities for lead ions. In contrast, LDH adsorbents converted from MIL-88A exhibited higher adsorption capacities, particularly Ni₃FeLDH/88A-PO₄, which achieved 100% adsorption efficiency at pH 7 and beyond. As a comparison, chloride-containing LDH was evaluated for its ability to adsorb lead ions (Fig. IV-7 e-h). It was observed that the chloride-modified LDH demonstrated poor adsorption of Pb²⁺ ions. The adsorption efficiencies of co-precipitated Ni₂FeLDH/COP-Cl and Ni₃FeLDH/COP-Cl were less than 20%, while 3D structured Ni₃FeLDH/88A-Cl and Ni₅FeLDH/88A-Cl materials showed slightly better efficiencies but still

remained below 30%. Thus, the reactivity of PO₄ with lead appears to be an efficient pathway for Pb²⁺ removal.

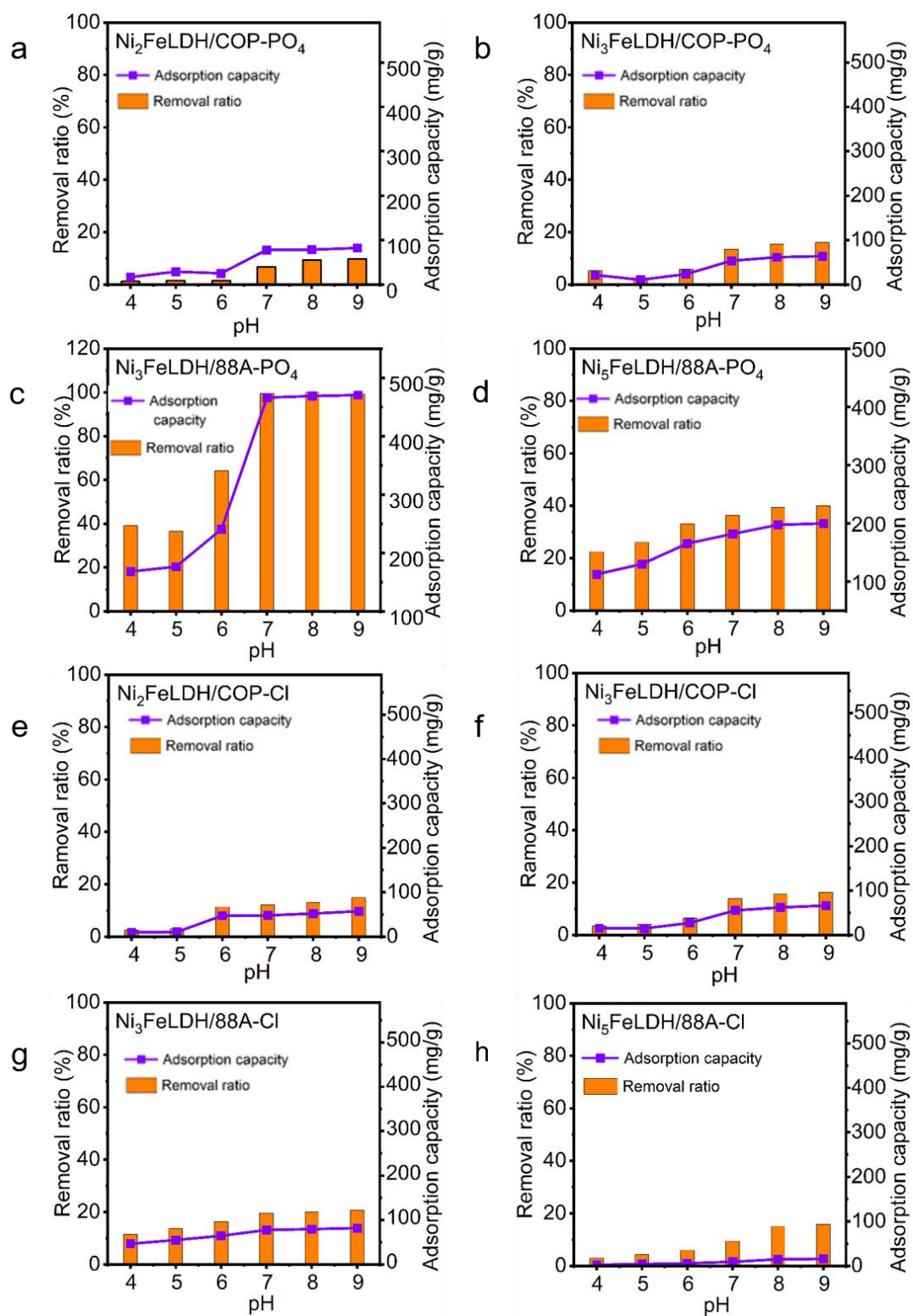


Fig. IV-7 Effect of pH on Pb²⁺ removal (500 ppm) by LDH adsorbents (10 mg) in aqueous solution (50 mL).

The variations in Pb^{2+} adsorption capacity of LDH- PO_4 and LDH-Cl with pH (Fig. IV-7) can be partly attributed to changes in surface charges, as pH conditions are known to impact the surface charges of metal oxides and hydroxides. The zeta potentials of LDH- PO_4 and LDH-Cl were measured across pH values ranging from 3.0 to 12.0 (Fig. IV-8), and the pH at the point of zero charge (pH@PZC) is reported in Table. IV-3. Except for the $\text{Ni}_2\text{FeLDH/COP-Cl}$ sample, all sorbents exhibited pH@PZC values lower than 5.7. This may explain the weakest adsorption capacities observed at $\text{pH} \leq 6.0$ (Fig. IV-7). Moreover, the pH@PZC of LDH- PO_4 was consistently lower than that of LDH-Cl. It is worth noting that the zeta potentials measured at pH 7.0 are much greater for LDH- PO_4 , favouring better adsorption of heavy metal cations.

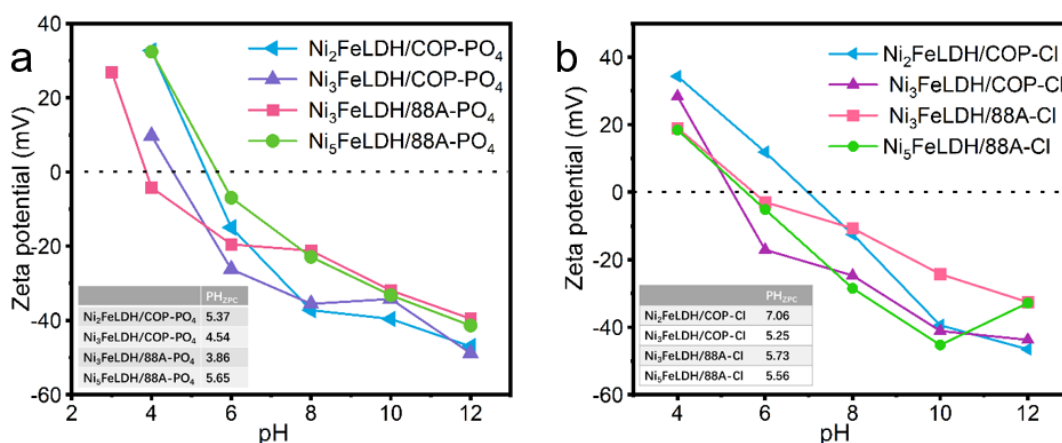


Fig. IV-8 Zeta potential of (a) LDH- PO_4 and (b) LDH-Cl materials.

Table. IV-3. pH_{PZC} values of LDH- PO_4 and LDH-Cl sorbents.

LDH- PO_4	pH_{PZC}	$\zeta_{\text{pH}7}$ (mV)	Adsorbents	pH_{PZC}	$\zeta_{\text{pH}7}$ (mV)
$\text{Ni}_2\text{FeLDH/COP-PO}_4$	5.4	-16	$\text{Ni}_2\text{FeLDH/COP-Cl}$	7.1	+10
$\text{Ni}_3\text{FeLDH/COP-PO}_4$	4.5	-30	$\text{Ni}_3\text{FeLDH/COP-Cl}$	5.2	-20
$\text{Ni}_3\text{FeLDH/88A-PO}_4$	3.9	-20	$\text{Ni}_3\text{FeLDH/88A-Cl}$	5.7	-7.5
$\text{Ni}_5\text{FeLDH/88A-PO}_4$	5.6	-7.5	$\text{Ni}_5\text{FeLDH/88A-Cl}$	5.6	-5

To gain further insight into the behaviour of lead and phosphate species in acidic and basic environments, the speciation of lead and phosphate in aqueous solution within

a pH range of 1.0-12.0 was simulated using the Medusa program (Fig. IV-9). The results indicate that as pH increases, the concentration of the Pb cationic species (Pb^{2+} , $\text{Pb}(\text{H}_2\text{PO}_4)^+$) decreases to zero up to pH 5.0, resulting in the disappearance of soluble Pb species above this value. Subsequently, from pH 5.0 to 12.0, theoretical thermodynamic computations predict the sequential formation of lead phosphate and lead hydroxide solid phases, $\text{Pb}(\text{HPO}_4)$, $\text{Pb}_3(\text{PO}_4)_2$, and $\text{Pb}(\text{OH})_2$, without consideration of the kinetics of formation. Clearly, the phosphate anions loaded in LDH facilitate the adsorption of Pb^{2+} through the possible precipitation of lead phosphate phases. Structural investigations were conducted on the solid residues after absorption and will be discussed in the next section. Based on these findings, a pH of 7.0 was selected as the conditions for the adsorption experiments, aligning with the commonly encountered pH of natural and waste waters.

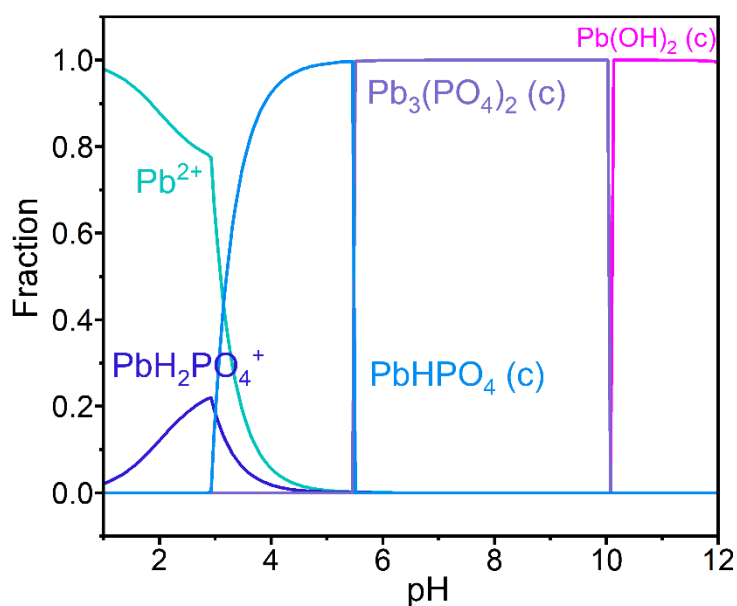


Fig. IV-9 pH-dependence of lead and phosphate speciation in aqueous solution.

IV. 4.2 Kinetic study of Pb^{2+} adsorption by LDH- PO_4

IV. 4.2.1 Experiment of kinetics

Exploration of kinetics is carried out at room temperature ($25 \pm 1^\circ\text{C}$) in well-sealed 50 mL centrifuge tubes containing 40 mL of 400 ppm lead ion solution and 10 mg of

LDH adsorbent. After addition of the adsorbent, the tubes are shaken in a thermostatic shaker at 120 revolutions per minute. The pH of the solution is adjusted at 7.0 ± 0.2 throughout the experiment by adding NaOH or HNO₃ solution. Adsorption experiments were stopped at different times ($t = 0, 5 \text{ min}, 10 \text{ min}, 20 \text{ min}, 30 \text{ min}, 60 \text{ min}, 120 \text{ min}, 180 \text{ min}, 240 \text{ min}, 300 \text{ min}, 360 \text{ min}, 480 \text{ min}, 600 \text{ min}$). At the end of the reaction, the liquid is separated by centrifugation at 10,000 rpm and analysed for adsorption efficiency. The residual lead ion concentration in the supernatant is determined by ICP-OES. Concentration of adsorbed Pb²⁺ was plotted versus time.

IV. 4.2.2 Models of kinetic experiment

Adsorption kinetic curves were fitted using the various mathematical models available, the pseudo-first-order model [344] (eq. 1), the pseudo-second-order model [345] (eq. 2), and the intraparticle diffusion model [346] (eq. 3) expressed as follows:

Pseudo-first-order model	Pseudo-second-order model	Intraparticle diffusion model
$\ln(q_e - q_t) = \ln q_e - k_1 t$ (eq. 1)	$\frac{t}{q_t} = \frac{1}{k_2 q_e^2} + \frac{t}{q_e}$ (eq. 2)	$q_t = k_i \cdot t^{0.5} + C$ (eq. 3)

where q_e (mg·g⁻¹) and q_t (mg/g) are the amounts of Pb²⁺ at equilibrium and at time t (h), respectively, and k_1 (h⁻¹) and k_2 (g mg⁻¹ h⁻¹) and are the rate constants of the pseudo-first-order and pseudo-second-order adsorption models, and k_i (mg g⁻¹ h^{0.5}) is the rate constant for intra-particle diffusion and C (mg/g) reflects the thickness of the boundary layer, respectively.

IV. 4.2.3 Results of kinetic study of Pb²⁺ adsorption by LDH-PO₄

From the kinetic plots of the LDH-PO₄ sample and the Ni₃FeLDH/88A reference material (Fig. IV-10 a), it is evident that 80% adsorption is achieved within one hour, and Pb²⁺ adsorption reaches equilibrium after 4 h of contact time. This period includes diffusion through the solution and solid, surface adsorption, and surface reaction processes. Further extension of time does not substantially affect the equilibrium phosphate concentration. All adsorbents exhibit a fast adsorption process in the initial

minutes, followed by a slow approach to adsorption equilibrium (plateau values). The initial rapid adsorption rate may be attributed not only to the presence of more active adsorption sites but also to the large concentration gradient of PO_4^{3-} between the lead ions and the adsorbent surface [347]. After two hours of reaction, the accumulation of Pb^{2+} on the active adsorbent sites results in a decrease in this gradient and a decline in the adsorption rate.

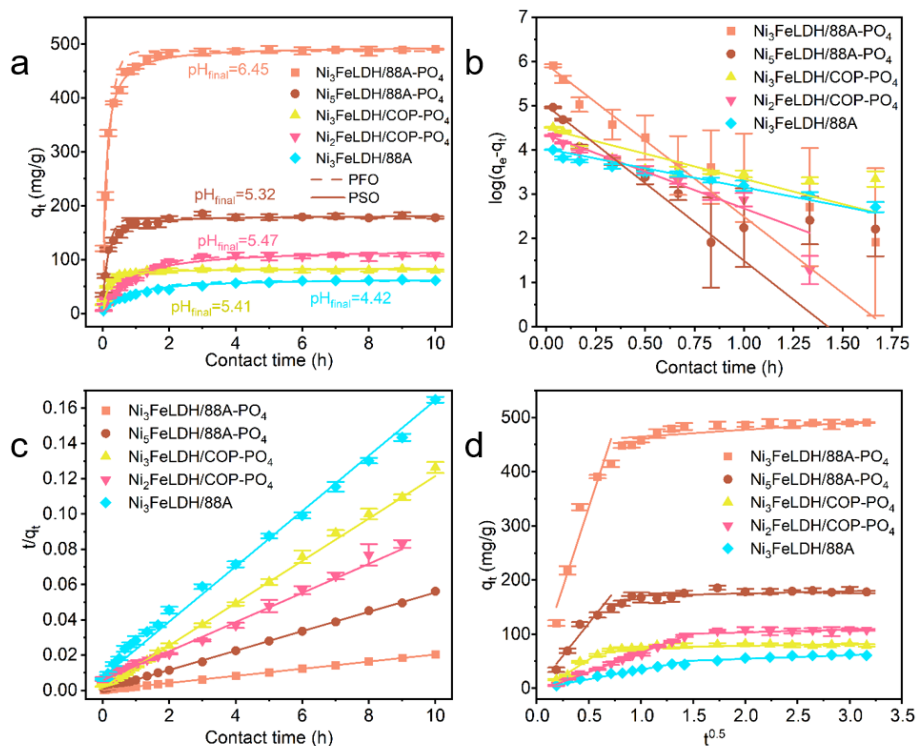


Fig. IV-10 Adsorption kinetics of $\text{Ni}_3\text{FeLDH}/88\text{A}$, $\text{Ni}_3\text{FeLDH}/88\text{A}-\text{PO}_4$, $\text{Ni}_5\text{FeLDH}/88\text{A}-\text{PO}_4$, $\text{Ni}_2\text{FeLDH}/\text{COP}-\text{PO}_4$ and $\text{Ni}_3\text{FeLDH}/\text{COP}-\text{PO}_4$. (a) adsorption kinetics, (b) PFO fitting, (c) PSO fitting, (d) intraparticle diffusion.

To investigate the adsorption mechanism and potential rate-control steps for lead removal, two common kinetic models, the pseudo-first-order (PFO) model [344], pseudo-second-order (PSO) model [345], as well as the intraparticle diffusion (IPD) model [346] were used to describe the adsorption process of Pb^{2+} ions on the adsorbents (Fig. IV-10 b, c, d).

Based on the comparison of correlation coefficients of the linear fits (Table. IV-4), it can be concluded that the pseudo-second-order model better describes the kinetic data of lead ion adsorption. This suggests that the adsorption process may be a

chemisorption process rather than a mass-transfer process in solution, since chemisorption assumes that the adsorption capacity of these adsorbents is controlled by the number of active sites on their surfaces [348].

Table. IV-4. Pseudo-first order and pseudo-second order kinetic parameters obtained by linear regression of kinetic plots for the LDH adsorbents.

LDH-PO ₄	Pseudo first-order kinetic			Pseudo second-order kinetic		
	q _e (mg/g)	k ₁ (h ⁻¹)	R ²	q _e (mg/g)	k ₂ (g mg ⁻¹ h ⁻¹)	R ²
Ni ₂ FeLDH/COP-PO ₄	88.48	1.139	0.9262	120.8	0.0122	0.9896
Ni ₃ FeLDH/COP-PO ₄	76.76	1.663	0.9780	83.40	0.095202	0.9989
Ni ₃ FeLDH/88A-PO ₄	387.8	3.449	0.9562	495.0	0.02270	0.9999
Ni ₅ FeLDH/88A-PO ₄	148.2	3.503	0.9151	181.8	0.05245	0.9996
Ni ₃ FeLDH/88A	56.06	0.865	0.9719	63.73	0.03243	0.9973

Fitting the adsorption process using the intraparticle diffusion model did not yield reliable results (Table. IV-5). Neither the correlation coefficients nor the values of adsorption capacities derived from the model fit to the experimental data were satisfactory. These results suggest that chemisorption or chemical bonding between lead ions and the active sites of the phosphoric adsorbent may be the main process of adsorption [349].

Table. IV-5. Parameters of intraparticle diffusion model of Ni₃FeLDH/88A, Ni₃FeLDH/88A-PO₄, Ni₅FeLDH/88A-PO₄, Ni₂FeLDH/COP-PO₄ and Ni₃FeLDH/COP-PO₄.

LDH-PO ₄	Phase 1			Phase 2		
	q _e (mg/g)	k ₁ (h ⁻¹)	R ²	q _e (mg/g)	k ₂ (g mg ⁻¹ h ⁻¹)	R ²
Ni ₂ FeLDH/COP-PO ₄	-7.227	122.6	0.9797	72.11	3.166	0.7774
Ni ₃ FeLDH/COP-PO ₄	-5.376	71.73	0.9981	-4.150	69.22	0.9960
Ni ₃ FeLDH/88A-PO ₄	42.13	591.7	0.9645	451.8	12.83	0.8713
Ni ₅ FeLDH/88A-PO ₄	1.296	241.1	0.9449	167.1	4.104	0.5284
Ni ₃ FeLDH/88A	0.7740	35.57	0.9913	41.04	6.860	0.8641

IV. 4.3 Adsorption isotherms of Pb²⁺ adsorption by LDH-PO₄

IV. 4.3.1 Experiment of adsorption isotherm

Adsorption isotherm were conducted in batch mode, by adding 10 mg (m) of LDH adsorbent and 40 mL (V) of different initial concentrations (C₀) of lead ion solution (0, 5 mg/L, 10 mg/L, 20 mg/L, 50 mg/L, 100 mg/L, 200 mg/L, 300 mg/L, 400 mg/L, 500 mg/L, 600 mg/L, 800 mg/L, 1000 mg/L) in a sealed 50 ml centrifuge tube at room temperature (25 ± 1 °C). After addition of the adsorbent, the centrifuge tubes are shaken at 120 revolutions per minute in a thermostatic shaker for 2 h (kinetic equilibrium time). Throughout the experiment, the pH of the solution is adjusted at 7.0 by addition of NaOH or HNO₃ solution. At the end of the reaction, the liquid is separated by centrifugation at 10,000 rpm and analysed for adsorption efficiency. The residual lead ion concentration (C_e) in the supernatant is determined by ICP-OES. The amount of Pb²⁺ adsorbed by the LDH adsorbent (q_e, mg/g) is calculated using the following formula:

$$q_e = \frac{(C_0 - C_e) \times V}{m}$$

where C₀ is initial lead ion concentration, C_e is equilibrium concentration, V is volume of lead ion solution, and m is quantity of adsorbent. Concentration of adsorbed Pb²⁺ (q_e) was plotted versus residual concentration (C_e) to get the adsorption isotherms.

IV. 4.3.2 Models of adsorption isotherm

The isotherms are fitted with the commonly used Langmuir (eq. 1) and Freundlich (eq. 2) models using respectively the following equations [350]:

$$\frac{C_e}{q_e} = \frac{1}{K_L q_m} + \frac{C_e}{q_m} \quad (\text{eq. 1})$$

where q_m = maximum amount of adsorbed species (mg/g) and K_L is the Langmuir constant (L/mg) and R_L = $\frac{1}{1+K_L C_0}$ = separation factor or equilibrium factor. When R_L < 1 adsorption is favourable, when R_L = 0 adsorption is irreversible, when R_L = 1 adsorption is linear, when R_L > 1 adsorption is unfavourable.

$$(\text{eq. 2}) \quad \ln q_e = \ln K_F + \frac{1}{n} \ln C_e$$

where K_F = adsorption capacity (L/mg) and $1/n$ = adsorption intensity or surface heterogeneity. When $0 < 1/n < 1$ adsorption is favourable; when $1/n > 1$ adsorption is unfavourable, when $1/n = 1$ adsorption is irreversible.

IV. 4.3.3 Results of isotherms of Pb^{2+} adsorption by LDH- PO_4

The adsorption properties of the LDH adsorbents are evaluated by fitting the adsorption isotherms (Fig. IV-11) with the commonly used Langmuir and Freundlich models (Fig. IV-12 and Table. IV-6.). The Langmuir model is based on the assumption of monolayer adsorption, assuming a homogeneous surface and equal affinity of the active sites for the adsorbent molecules [351]. On the other hand, the Freundlich isotherm equation is an empirical equation that describes adsorption on heterogeneous surfaces [352]. It is evident that, for the adsorption of Pb^{2+} on the five adsorbents, the Langmuir model is more suitable for the than the Freundlich model. This suggests that the LDH- PO_4 surface displays independent and strongly reactive adsorption sites.

Table. IV-6 Parameters of Pb^{2+} adsorption isotherms obtained from Langmuir and Freundlich linear regression fitting.

LDH- PO_4	Langmuir Model			Freundlich Model		
	K_L (L/mg)	q_m (mg/g)	R^2	K_F (L/mg)	n	R^2
$Ni_2FeLDH/COP-PO_4$	0.049	71.0	0.992	8.15	2.62	0.958
$Ni_3FeLDH/COP-PO_4$	0.044	68.8	0.990	9.11	2.79	0.913
$Ni_3FeLDH/88A-PO_4$	0.103	537.6	0.999	284.0	8.90	0.752
$Ni_5FeLDH/88A-PO_4$	0.022	183.5	0.998	21.56	2.73	0.918
$Ni_3FeLDH/88A$	0.018	56.8	0.985	7.51	3.04	0.860

The maximum adsorption capacity according to Langmuir fitting, 537.6 mg/g for $Ni_3FeLDH/88A-PO_4$ is similar to the value obtained by the PSO kinetic fitting (495 mg/g). $Ni_3FeLDH/88A-PO_4$ and $Ni_5FeLDH/88A-PO_4$ exhibit much higher Pb^{2+} adsorption capacities (538 and 184 mg/g respectively) than $Ni_2FeLDH/COP-P$ and $Ni_3FeLDH/COP-P$ (71 mg/g and 69 mg/g respectively), more than 7 times higher. The

phosphate-free material (Ni₃FeLDH/88A) has the lowest adsorption efficiency (57 mg/g), indicating that the adsorption capacity is significantly enhanced after phosphate modification. The stronger adsorption capacity of Ni₃FeLDH/88A-PO₄ compared to Ni₅FeLDH/88A-PO₄ is related to its higher surface area combined with higher P content. From Table. IV-7, which reports the adsorption capacities of Pb²⁺ by various LDH-based materials and phosphorus-containing adsorbents, it is evident that the LDHs synthesized in this work display the best adsorption capacity ever obtained.

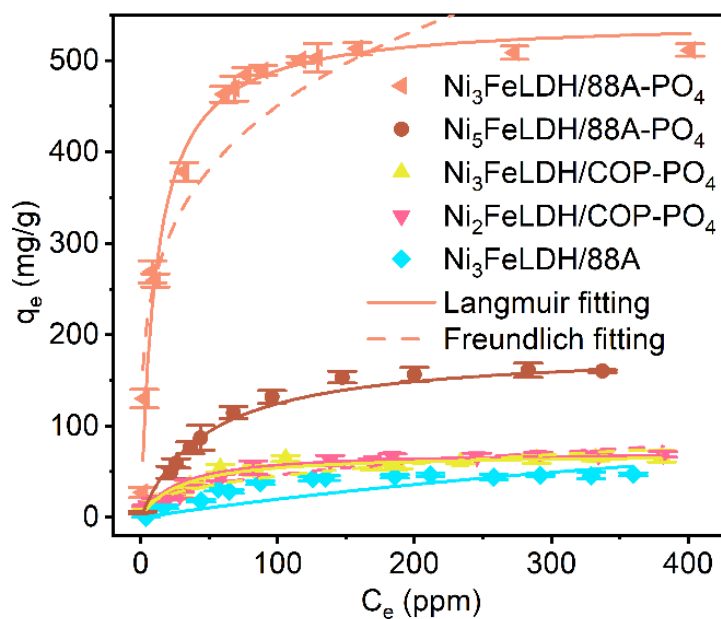


Fig. IV-11 Pb²⁺ adsorption isotherms of LDH adsorbents with non-linear Langmuir and Freundlich fits.

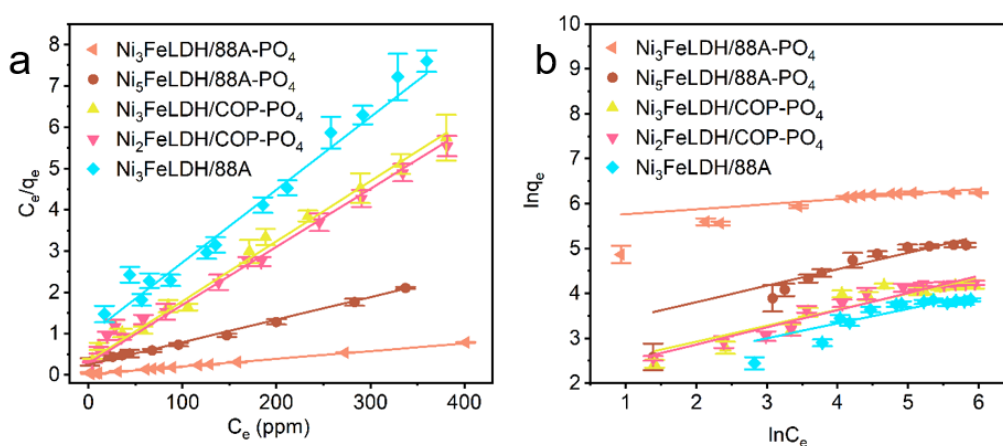


Fig. IV-12 (a) Langmuir fitting and (b) Freundlich fitting of Pb²⁺ adsorption isotherms of LDH adsorbents.

Table. IV-7 Pb²⁺ adsorption by various materials.

No.	Adsorbent	Adsorption capacity (mg/g)	Ref.
1	Co-Al-LDH@Fe ₂ O ₃ /3DPCNF	426.76	[353]
2	NiFe-MoS ₄ ²⁻ -LDH/CF	299.00	[317]
3	MnFe-LDH/MnFe ₂ O ₃ @3DNF	468.48	[354]
4	Mg ₂ Al LDH	66.16	[355]
6	SA-LDH	243.67	[356]
7	BC-LDH	294.00	[357]
8	MgAl@AC	94.57	[358]
9	Amorphous Tin(VI) Hydrogen Phosphate (ATHP)	372.99	[359]
10	P-FH@BC	321.52	[360]
11	Potato Starch Phosphate (PSP)	105.62	[361]
12	Phosphorylated Magnetic Chitosan Composite (P-MCS)	151.06	[362]
13	Hydroxyapatite Coated Activated Carbon (C-HAP)	401.58	[363]
14	Ni ₃ FeLDH/88A-PO ₄	537.6	This work
15	Ni ₅ FeLDH/88A-PO ₄	183.5	This work

IV. 4.4 Selectivity towards Pb²⁺/Ni²⁺/Cd²⁺ adsorption

IV. 4.4.1 Effect of M²⁺ competition

The adsorption of mixture of Pb²⁺, Cd²⁺, Ni²⁺ was carried out in a 50 mL centrifuge tube in batch mode. 10 mg of adsorbent was suspended in 40 mL aqueous solution containing 200 ppm of each M²⁺ ions and stirred with a thermostatic oscillator at room temperature, and the pH value was adjusted to 7. After 2 h contact time, the solution was centrifuged and, the concentrations of Pb²⁺, Cd²⁺, Ni²⁺ ions in supernatants were

analysed by ICP-OES.

IV. 4.4.2 Selectivity towards $\text{Pb}^{2+}/\text{Ni}^{2+}/\text{Cd}^{2+}$ adsorption

One of the key characteristics of adsorption processes and adsorbents is their selectivity toward sorbates. Selectivity can be a property that may be sought or avoided depending on the targeted wastewater treatments. In the case of adsorption of highly toxic metals such as Pb^{2+} , selectivity is an important criterion that determines the choice of the adsorbent. The adsorption selectivity of LDH- PO_4 for Pb^{2+} was evaluated in competition with Ni^{2+} and Cd^{2+} cations (Fig. IV-13). For LDH- PO_4 adsorbents the affinity for heavy metals decreases as follows: $\text{Pb}^{2+} > \text{Ni}^{2+} > \text{Cd}^{2+}$. Both $\text{Ni}_3\text{FeLDH}/88\text{A-PO}_4$, $\text{Ni}_5\text{FeLDH}/88\text{A-PO}_4$ display the same relative adsorption selectivity toward the mixture of Pb^{2+} , Cd^{2+} , Ni^{2+} , except that $\text{Ni}_3\text{FeLDH}/88\text{A-PO}_4$ adsorbs more Pb^{2+} , Ni^{2+} and Cd^{2+} (1.5-1.7 time more) [364]. $\text{Ni}_3\text{FeLDH}/88\text{A-PO}_4$ demonstrates very high selectivity, its capability to remove 100% of Pb^{2+} of a 200 ppm solution is not even altered by the competition of equimolar quantities of Cd^{2+} and Ni^{2+} .

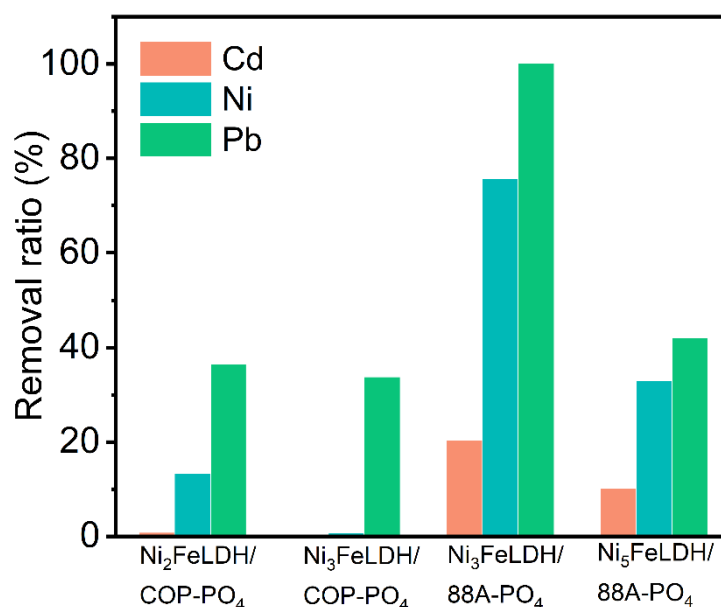


Fig. IV-13 Selective adsorption of $\text{Ni}_3\text{FeLDH}/88\text{A-PO}_4$, $\text{Ni}_5\text{FeLDH}/88\text{A-PO}_4$, $\text{Ni}_2\text{FeLDH}/\text{COP-PO}_4$ and $\text{Ni}_3\text{FeLDH}/\text{COP-PO}_4$ towards mixture of Pb^{2+} , Cd^{2+} , Ni^{2+} .

From Table. IV-8, it can be observed that the adsorption capacity of Ni₃FeLDH/88A-PO₄ for a mixture of HM or for a single HM is nearly the same (q_e (Cd²⁺+ Ni²⁺+ Pb²⁺) = 505 mg/g and q_e (Pb²⁺) = 525 mg/g. The adsorption efficiencies of Ni₂FeLDH/COP-PO₄ and Ni₃FeLDH/COP-PO₄ are much lower. Ni₃FeLDH/88A and Ni₃FeLDH/88A-PO₄ also show a certain extent adsorption capacity for nickel ions, which indicates that LDH does not release nickel ions during adsorption thereby further polluting the water [365].

Table. IV-8. Removal% of competing Pb²⁺/Ni²⁺/Cd²⁺ cations for LDH-PO₄ adsorption and relative q_e values.

LDH-PO ₄	Cd%	Ni%	Pb%	q_e (Cd) (mg/g)	q_e (Ni) (mg/g)	q_e (Pb) (mg/g)	q_e (Ni+Cd+Pb) (mg/g)	q_e (Pb) mg/g
Ni ₂ FeLDH/COP-PO ₄	0.84	13.32	46.45	2.4	16.4	90.0	108.9	72.4
Ni ₃ FeLDH/COP-PO ₄	0.00	0.69	33.77	0.0	1.9	83.9	85.8	69.7
Ni ₃ FeLDH/88A-PO ₄	30.19	62.93	100	87.3	169.1	248.5	504.9	525.3
Ni ₅ FeLDH/88A-PO ₄	20.34	45.78	62.21	58.9	103.7	148.5	311.0	170.6

IV. 4.5 Insight in the Pb²⁺ adsorption mechanism

The reactivity of LDH-PO₄ synthesized via co-precipitation and MIL-88A conversion methods differs significantly (Fig. IV-14). While the LDH structure remains intact in all XRD patterns, indicating that the LDH lattice is structurally unaffected by Pb²⁺ adsorption, Ni_xFeLDH/88A-PO₄ (x=3,5) demonstrates strong interaction with Pb²⁺, leading to the formation of additional crystallized phases. These phases can be identified as a mixture of Pb₃(PO₄)₂ (JCPDS 13-0278) and Pb(OH)₂ (JCPDS 75-1177). Pb(OH)₂ is the major phase that precipitates from Pb²⁺/Ni_xFeLDH/COP-PO₄ (x=2,3), even though these adsorbents contain more PO₄³⁻ anions (Table. IV-1). Phosphate species are less accessible to Pb²⁺ in these cases, as they are embedded in strongly aggregated LDH platelets.

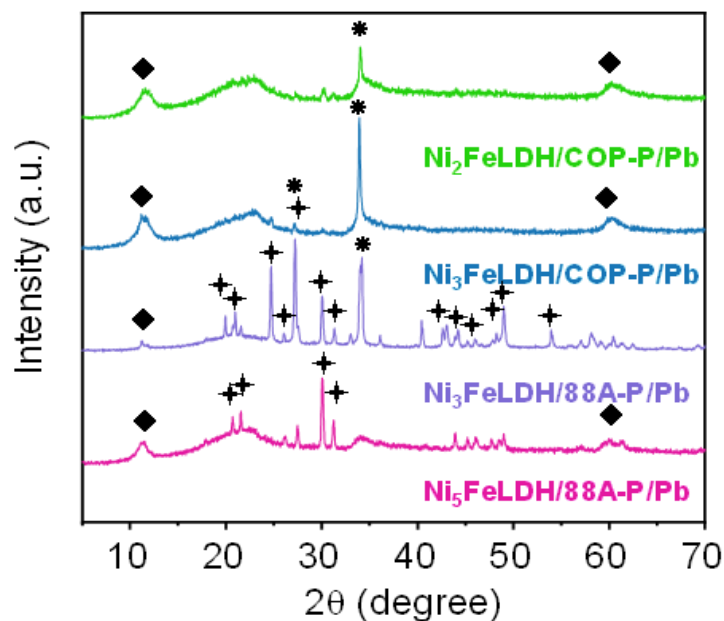


Fig. IV-14 XRD of residues after Pb^{2+} adsorption
 (◆), $\text{Pb}_3(\text{PO}_4)_2$ (✦), $\text{Pb}(\text{OH})_2$ (★) phases.

In contrast, the 3D nanostructured platelet rod-like architecture of LDH- PO_4 derived from MIL-88A offers a porous morphology where PO_4^{3-} anions are easily accessible for $\text{Pb}_3(\text{PO}_4)_2$ formation [366]. The presence of a broad vibration band at 1400 cm^{-1} in the FTIR spectrum (Fig. IV-15) of $\text{Ni}_3\text{FeLDH}/88\text{A-PO}_4/\text{Pb}^{2+}$ residue suggests the presence of the carbonate pyromorphite phase ($\text{Pb}_5(\text{PO}_4, \text{CO}_3)_3(\text{OH}, \text{CO}_3)$) as a minor phase, whose diffraction lines superimpose on those of $\text{Pb}_3(\text{PO}_4)_2$ [367]. All adsorbents after adsorption of lead contain asymmetric stretching vibrations attributed to the P-O bond located at 1045 cm^{-1} , which is not much different from that before the reaction [368]. The above phosphate bands of $\text{Ni}_3\text{FeLDH}/88\text{A-PO}_4$ and $\text{Ni}_5\text{FeLDH}/88\text{A-PO}_4$ were significantly shifted to a lower frequency of 988 cm^{-1} after exposure to lead solutions [369]. This transition is typical of coordination complexation of phosphate groups with metal ions [370]. For $\text{Ni}_3\text{FeLDH}/88\text{A-PO}_4$, a peak of Pb was observed at 539 cm^{-1} , which unfortunately did not occur for the other three adsorbents.

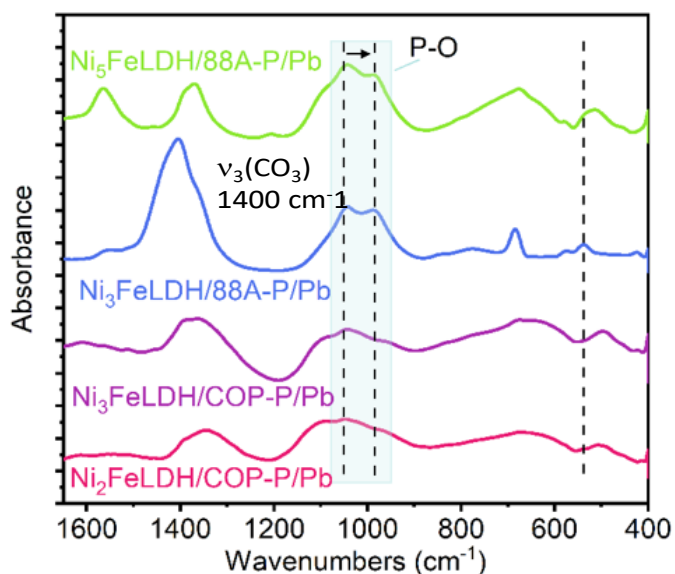


Fig. IV-15 FTIR spectra of $\text{Ni}_3\text{FeLDH}/88\text{A-P}$, $\text{Ni}_5\text{FeLDH}/88\text{A-P}$, $\text{Ni}_2\text{FeLDH}/\text{COP-P}$ and $\text{Ni}_3\text{FeLDH}/\text{COP-P}$ residues after Pb^{2+} adsorption.

The coexistence of multiple crystalline phases in $\text{Ni}_3\text{FeLDH}/88\text{A-PO}_4$ and other residues of adsorption is consistent with the SEM (Fig. IV-16) and EDS (Fig. IV-17) results. In the case of the most reactive adsorbent, $\text{Ni}_3\text{FeLDH}/88\text{A-PO}_4$, two new structures appear with lamellar hexagonal and needle-like morphologies and upon magnification, uniform semi-spherical bumps are observed distributed on the surface of the rod structure [371].

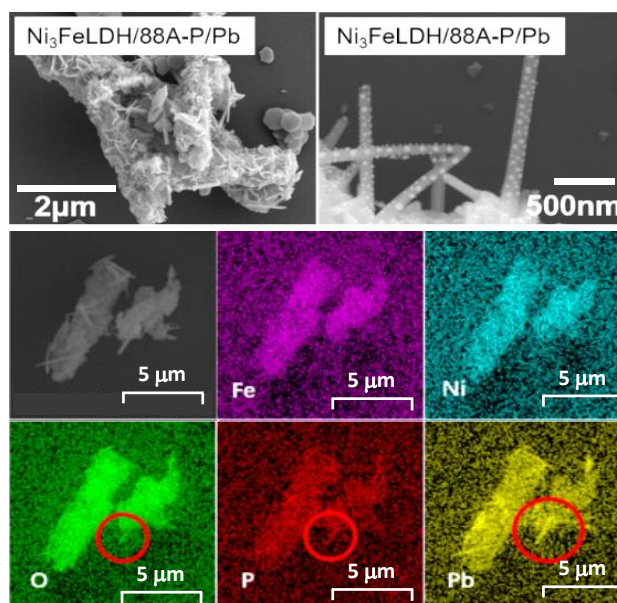


Fig. IV-16 SEM images and elemental mapping of $\text{Ni}_3\text{FeLDH}/88\text{A-PO}_4$ results after Pb^{2+} adsorption.

The low content of Fe-Ni elements in the needles confirms the formation of Pb and P rich phases. Lead EDS signal is detected on the surfaces of the four adsorbents, although, its content varied significantly. In the residues of Ni₂FeLDH/COP-PO₄ and Ni₃FeLDH/COP-PO₄, there is no significant change in its nickel-iron ratio after Pb²⁺ adsorption, with Pb content on the surface being 1.69% and 3.99%, respectively. This suggests that Pb²⁺ is adsorbed mainly on the surface of the LDH platelets, predominantly as Pb(OH)₂ as shown by XRD (Fig. IV-14). However, for Ni₃FeLDH/88A-PO₄, the different structures are examined separately due to their distinct structural alterations. Regardless of the structure, the lead content is found to be extremely high, especially in the rod and flake structures, where the lead content exceeds 40%. Even on the surface of the rod structure, the lead content is 20.8%, significantly higher than the 0.78% lead content on the surface of Ni₅FeLDH/88A-PO₄. Additionally, the content of iron and nickel in different positions varies greatly, indicating not only adsorption but also co-reaction between Pb²⁺ and Ni₃FeLDH/88A-PO₄.

The mapping results indicate that Pb²⁺ is not uniformly distributed on the adsorbent surface, with varying content observed on the different adsorbent surfaces (Fig. IV-17c). Specifically, lead content is highest on the Ni₃FeLDH/88A-PO₄ surface and lowest on the Ni₅FeLDH/88A-PO₄ surface, which aligns with the EDS results. In the rod structure of Ni₃FeLDH/88A-PO₄, there are no signals for iron and nickel but strong signals for oxygen, phosphorus, and lead, particularly lead (highlighted in the circled portion of Fig. IV-16). This suggests the presence of a lead phosphoric acid compound. Comparatively, the phosphorus and lead contents in Ni₃FeLDH/88A-PO₄ are significantly higher than those in the other three adsorbents, consistent with its high adsorption capacity. Following the adsorption process, there is a notable increase in phosphorus and lead content, accompanied by a corresponding decrease in oxygen content in Ni₃FeLDH/88A-PO₄. This indicates the accumulation of Pb-PO₄ species on the surface of the original adsorbent, contributing to the observed changes in elemental composition.

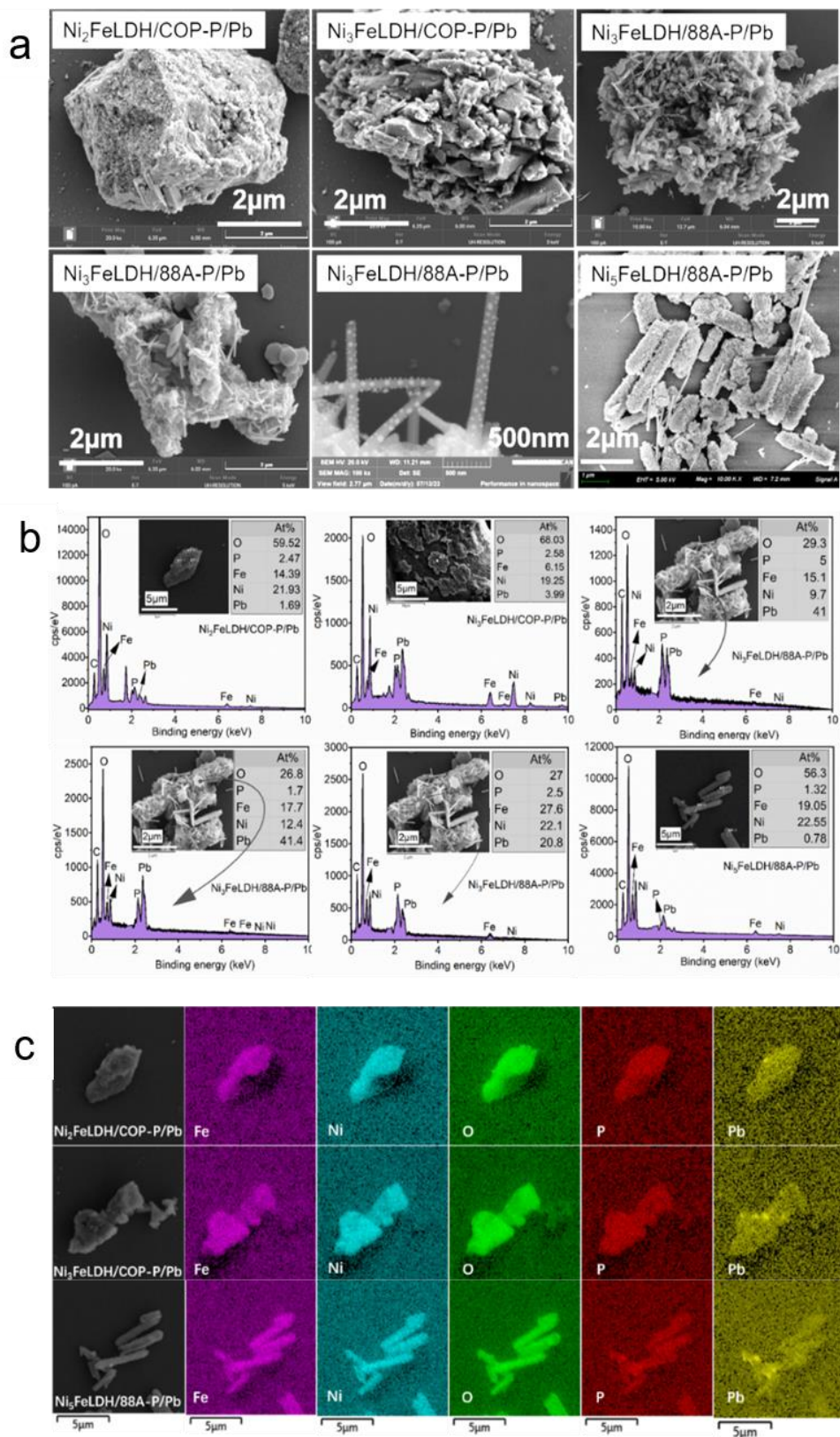


Fig. IV-17 (a) SEM, (b) EDS spectra and (c) elemental mapping of Ni₃FeLDH/88A-PO₄, Ni₅FeLDH/88A-PO₄, Ni₂FeLDH/COP-PO₄ and Ni₃FeLDH/COP-PO₄ after Pb²⁺ adsorption.

The XPS analysis of phosphorus (P) and lead (Pb) was conducted on the residues to investigate the energy changes of the bonds involving both elements (Fig. IV-18 and Fig. IV-19). After Pb^{2+} adsorption, the P $2p_{1/2}$ and P $2p_{3/2}$ peaks shifted to lower energy for all four adsorbents compared to the pristine sorbents, suggesting protonation of surface ligands as a result of lead adsorption [368]. The energy shifts observed in the P 2p peaks are even more pronounced for $\text{Ni}_3\text{FeLDH}/88\text{A-PO}_4$ and $\text{Ni}_5\text{FeLDH}/88\text{A-PO}_4$ ($\Delta\text{P}2p_{1/2} = 0.47$ and 0.51 eV respectively), which can be attributed to the increased reactivity of phosphate with Pb^{2+} . Regarding the Pb 4f spectrum, it exhibits a spin-orbit splitting into Pb $4f_{7/2}$ and Pb $4f_{5/2}$ components. The peak observed at 137.86 eV is indicative of the bonding of lead to oxygen [372]. The significant differences observed in the energy bonding of Pb $4f_{5/2}$ and Pb $4f_{7/2}$ between residues derived from coprecipitation and MIL-88A conversion suggest that Pb^{2+} is engaged with different components in both series. Specifically, in the coprecipitation-derived residues, Pb^{2+} appears to be mainly associated with $\text{Pb}(\text{OH})_2$, whereas in the MIL-88A conversion-derived residues, it is primarily linked with $\text{Pb}_3(\text{PO}_4)_2$, or potentially even $\text{Pb}_5(\text{PO}_4, \text{CO}_3)_3(\text{OH}, \text{CO}_3)$.

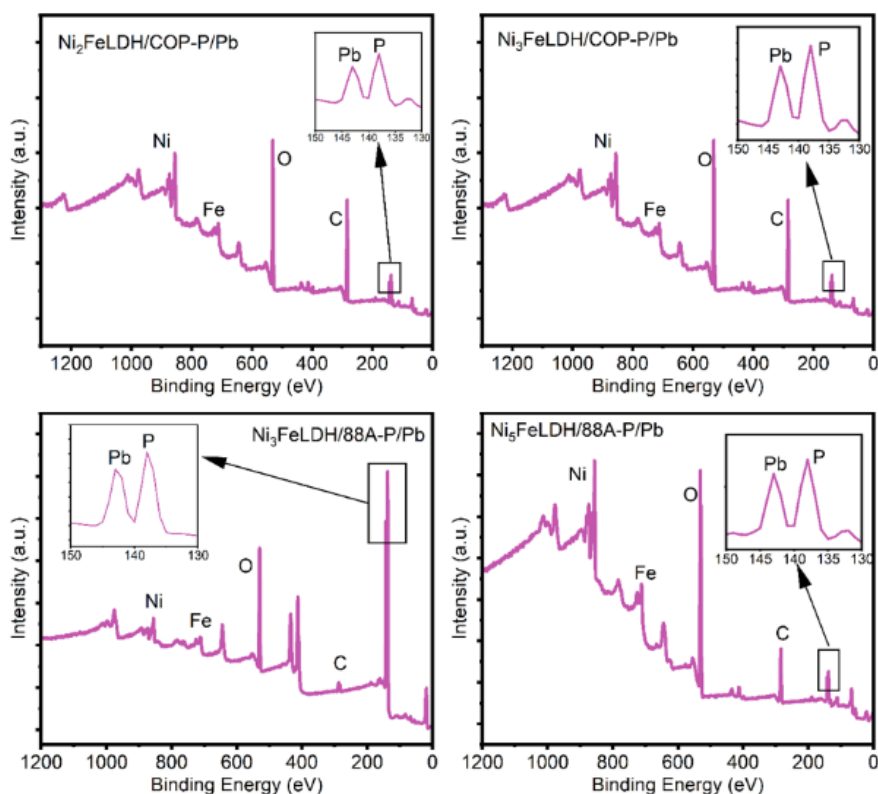


Fig. IV-18 XPS of $\text{Ni}_3\text{FeLDH}/88\text{A-PO}_4$, $\text{Ni}_5\text{FeLDH}/88\text{A-PO}_4$, $\text{Ni}_2\text{FeLDH}/\text{COP-PO}_4$ and $\text{Ni}_3\text{FeLDH}/\text{COP-PO}_4$ after the reaction.

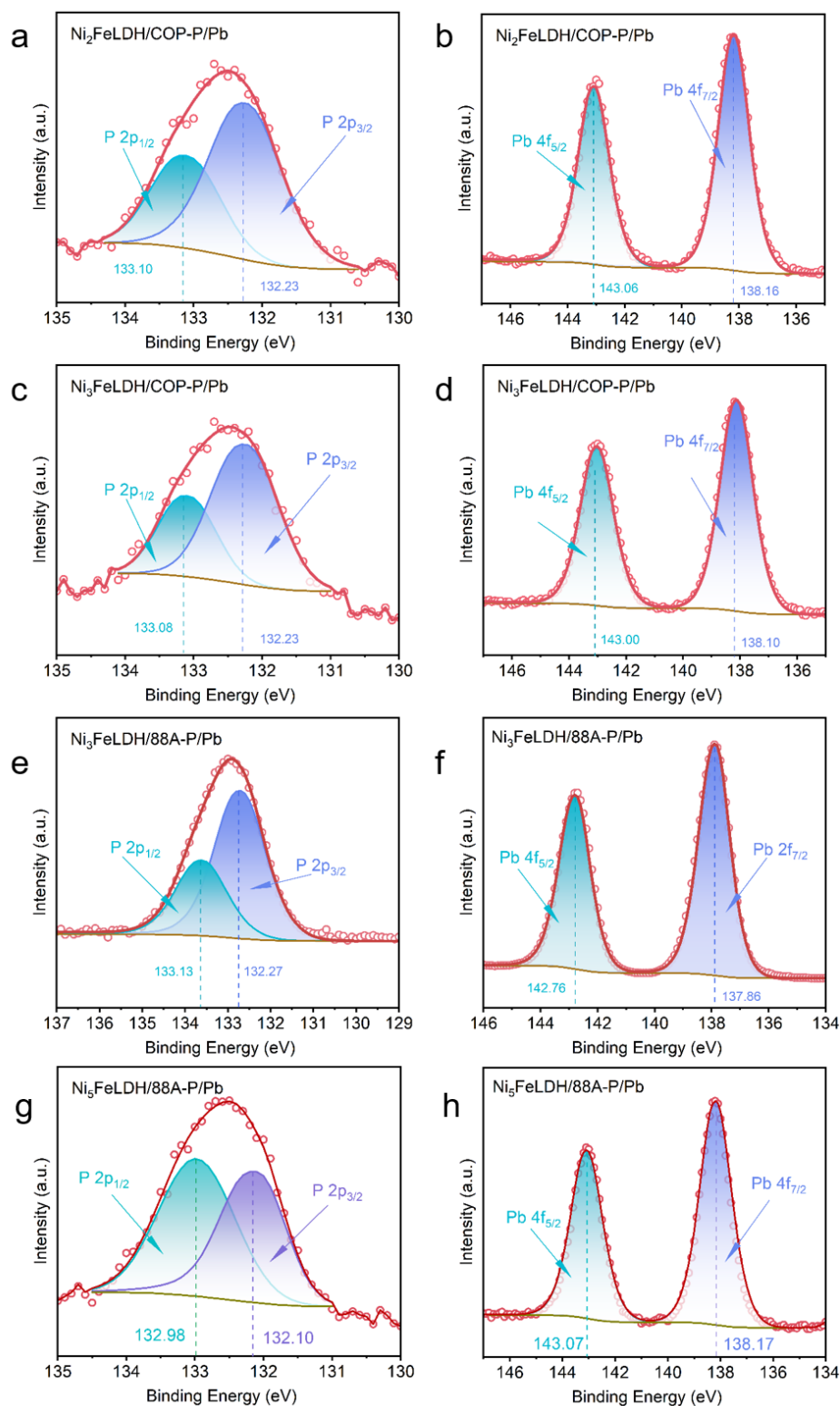


Fig. IV-19 (a) (c) (e) (g) P 2p and (b) (d) (f) and (h) Pb 4f of XPS signals for $\text{Ni}_3\text{FeLDH/88A-PO}_4$, $\text{Ni}_5\text{FeLDH/88A-PO}_4$, $\text{Ni}_2\text{FeLDH/COP-PO}_4$ and $\text{Ni}_3\text{FeLDH/COP-PO}_4$ after Pb^{2+} adsorption.

The adsorption mechanism diagram (Fig. IV-20) synthesized from the analysis illustrates several processes integral to the overall purification of lead ion solutions. Chief among these processes is the adsorption of phosphate ions, which emerges as the most crucial mechanism. Phosphates act by trapping lead ions through chelation, significantly contributing to their removal from solution. Additionally, surface adsorption and co-precipitation mechanisms also play essential roles in immobilizing lead ions, further enhancing the purification process.

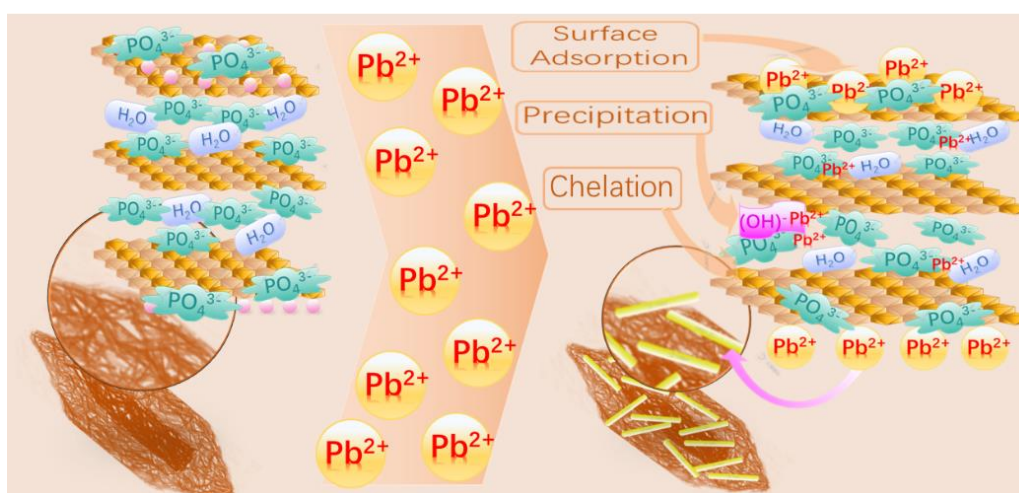


Fig. IV-20 Adsorption mechanism of Pb^{2+} by $Ni_3FeLDH/88A-PO_4$.

IV.5 Conclusion

The study presents the successful synthesis of 3D nanostructured Ni_xFe LDH ($x=3$ and 5) materials loaded with PO_4^{3-} anions ($Ni_xFeLDH/88A-P$ ($x=3,5$)) through a multi-step synthesis process involving MIL-88A (Fe) conversion into Ni_xFe -LDH followed by ion exchange with phosphate anions. These materials exhibit a rod-like morphology characterized by uniformly distributed LDH nanoflakes, high surface area, and high porous volumes. In comparison to LDH- PO_4 materials prepared via conventional coprecipitation ($Ni_xFeLDH/COP-PO_4$ ($x=3,5$)), the newly synthesized LDH-based materials demonstrate significantly enhanced adsorption properties towards highly toxic Pb^{2+} ions. Particularly, $Ni_3FeLDH/88A-PO_4$ exhibits superior Pb^{2+} removal performance ($538\text{ mg }Pb^{2+}/g\text{ LDH-}PO_4$) compared to other reported adsorbents in the literature. The removal of Pb^{2+} is attributed to phosphate chelation with Pb^{2+} and precipitation of $Pb-PO_4$ and $Pb(OH)_2$ phases. Consequently, 3-D Ni_3FeLDH derived

from MOF MIL88A loaded with PO_4 emerges as a promising adsorbent for the removal of Pb^{2+} and other heavy metals from water, including Cd^{2+} and Ni^{2+} . This study underscores the potential of LDH loaded with reactive anions for heavy metal removal applications.

Chapter V

Catalytic reactivity of LDH-88A and LDO-88A for the degradation of organic pollutants

V.1 Introduction

Recently, due to increased urbanization and industrialization to meet human needs, a massive quantity of toxic wastes has been released into the environment [373]. As a result, water pollution is prioritized over other concerns worldwide due to the constant discharge of industrial wastes containing different organic dyes, agrochemicals, personal care products, pharmaceuticals and aromatic compounds into water bodies [210]. Among water pollutants, organic contaminants such as industrial dyes and pharmaceutical products in drinking water systems already pose a potential threat to human health due to their toxicity and non-biodegradability [374, 375]. Typical organic pollutants, such as bisphenol A (2,2-bis (4-hydroxyphenyl) propane, BPA) (Fig.V-1), is chemical raw material that are widely made into polycarbonate [376], polyphenoxy, epoxy resins [377], and used in household plastic products [378]. It is also used as a coating on metal surfaces to make canned foods [379] less susceptible to deterioration and spoilage. However, it is also a secretor of disruptors and environmental hormones that can cause endocrine disruption [380] in animals and humans, threatening the health [381] of fetuses and children [382], and can also lead to cancer or metabolic disruption leading to obesity in humans. For instance, there is evidence that prenatal exposure of the BPA could lead to the neurodevelopment disorders such as autism [383]. On the other end, the use of polymeric baby bottles has been proven to place infants at slight risk of the BPA exposure [384]. In addition to the humans, the BPA exposure has harmful effects on aquatic organisms such as fish. For instance, the short-term exposure of the BPA at 100 mM has induced oxidative stress in the Atlantic salmon fish kidney cell line [385]. Therefore, it is becoming increasingly urgent to develop effective technologies to reduce organic pollution of water [386].

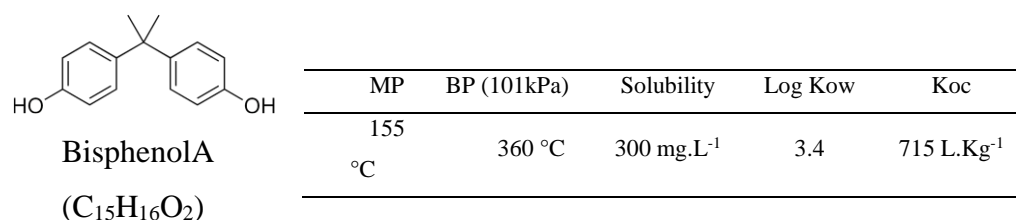


Fig.V-1. Structural and physico-chemical data of bisphenol A.

Advanced oxidation processes (AOPs) are capable of destroying a wide range of

organic matter in water, even at low concentrations. The AOP process produces highly reactive chemical species hydroxyl and/or sulphate radicals (HO^\bullet and $\text{SO}_4^{\bullet-}$) - that can break down even the most bio-chelating molecules into benign biodegradable products. Persulfates (PS) are important catalysts through the generation of highly reactive radical species such as $\text{SO}_4^{\bullet-}$ radical point ($E_0 = 2.5\text{-}3.1\text{ V}$) and hydroxyl radical HO^\bullet radical point ($E_0 = 1.89\text{-}2.72\text{ V}$) [16]. A large number of activation methods (e.g. transition metal, heat, ultraviolet light, ultrasonic irradiation, semiconductor, carbon-based catalysts and electrochemical activation) have been developed and can be used for PS activation [387-391]. Among these systems, non-homogeneous catalysts have been commonly used due to their advantages of energy efficiency, low hazard, and easy recovery from the aquatic environment [392].

Among the several heterogeneous catalysts used for catalytic degradation of organic pollutants, Layered Double Hydroxides (LDH), particularly LDH containing multivalent transition metal cations (Cr, Mn, Fe, Co, Ni, Cu) and their calcined derivatives (Layered Double Oxides, LDO, which has the advantages of simple preparation, good catalytic performance, low metal solubility, and wide pH range [393].) have received increasing attention. Indeed, LDH and LDO have demonstrated efficient catalytic properties in various oxidation processes such as fenton and fenton-like processes [394, 395], photocatalytic and photo-fenton processes, sulfate radical or non-radical activation processes. Yan et al. synthesised CuMgFe-LDH as an efficient activated PS catalyst for the removal of ethylbenzene [396]. Yan et al. synthesised CuMgFe-LDH as an efficient activated PS catalyst for the removal of ethylbenzene [397] (Table.V-1). This is due to their easily adjustable atomic compositions, morphology, atomic vacancies, crystal facets, and surface stress, factors that greatly determine their electronic properties and consequently their catalytic properties, thanks to a great choice of synthesis methods (see chapter 1).

However, their high surface charge properties, compare to other materials, favor strong platelet aggregation and make it difficult to prepare LDH with porous morphology and surface accessibility. The recent preparation of three-dimensional (3D) LDH hollow structures has open the field to the synthesis of LDH with expected enhanced catalytic properties. Huo et al. [160] constructed a multistage LDH/MOF electrocatalyst using in situ pseudocrystalline conversion, during which ultrathin Fe-Ni

LDH nanosheets were generated in the middle of heterometallic MOF. The ultrathin LDH arrays contain abundant metal sites and extended electron transport channels, which enable the multistage FeNi-LDH/MOFs to exhibit remarkable electrochemical activities in the oxygen evolution reaction (OER).

Table.V-1 Catalytic degradation of organic pollutants in water by Fe-based LDH and LDO.

Catalysts	Reaction conditions	Reaction time and maximum removal	Ref.
Fe ₂ Co ₁ -LDH	[BPA] = 30.00 mg/L, [PS] = 4 mM, [catalyst] = 0.3 g/L, T = 25 °C.	Reaction = 60 min, removal rate = 99.38%	[398]
Mg-Fe-LDH@biochar	[DOX] = 35.00 mg/L, [PMS] = 7.5 g/L, [catalyst] = 0.75 g/L, [LMF] = 5.00 mg/L,	Reaction = 120 min, removal rate = 88.76%	[399]
AC@CoFe-LDH	[PS] = 1 g/L, [catalyst] = 0.2 g/L, T = 25 °C	Reaction = 60 min, removal rate = 93.20%	[400]
FeCo-LDH	[RhB] = 20 mg/L, [PMS] = 0.15 g/L, [catalyst] = 0.2 g/L, T = 25 °C	Reaction = 10 min, removal rate = 99%	[401]
CuFe-LDH	[MV] = 20 mg/L, [PS] = 0.2 g/L, [catalyst] = 0.2 g/L, T = 25 °C	Reaction = 18 min, removal rate = 99%	[402]
Ni-Fe-Zn LDH	[OFL] = 20 mg/L, [PS] = 6 mM, [catalyst] = 0.4 g/L, T = 25 °C	Reaction = 100 min, removal rate = 93.11%	[403]
Fe ₂ O ₃ @NiFe LDH@biotemplate	[RhB] = 40 mg/L, [PS] = 5 mM, [catalyst] = 0.1 g/L, T = 25 °C	Reaction = 50 min, removal rate = 100%	[404]

	[ethylbenzene] = 0.08 mM,		
CuMgFe-LDH	[PS] = 4 mM, [catalyst] = 0.3 g/L, T = 20 °C	Reaction = 24 h, removal rate = 95.5%	[396]
Cu/ZnO/CoFe-CLDH	[BPA] = 10 mg/L, [PS] = 40 mM, [catalyst] = 0.5 g/L, T = 25 °C	Reaction = 5 h, removal rate = 99%	[405]
Bi ₂ O ₃ /CuNiFe-LDH	[LOM] = 15 g/L, [PS] = 0.74 mM, [catalyst] = 0.4 g/L, T = 25 °C	Reaction = 40 min, removal rate = 84.6%	[406]
Fe ₃ O ₄ @CuFe-LDH	[Qu] = 40 mg/L, [PS] = 0.45 g/L, [catalyst] = 35 mg/L, T = 25 °C	Reaction = 30 min, removal rate = 92.1%	[407]
CuMgFe/-LDO	[Phenol] = 0.1 mM, [PS] = 0.5 mM, [catalyst] = 0.5 mM, T = 25 °C	Reaction = 30 min, removal rate = 95.3%	[408]
CuMgAl-LDO	[SMD] = 5 mM, [PS] = 0.7 mM, [catalyst] = 0.3 g/L, T = 25 °C	Reaction = 40 min, removal rate = 100%	[409]

where BPA is bisphenol A, DOX is doxycycline, LMF, LOM is lomefloxacin, RhB is Rhoadmine B, MV is methyl violetazo dye, OFL is ofloxacin, Qu is quinoline, TMP is trimethoprim, SMD is sulfameter

Nevertheless, the choice of template remains limited by the composition or shape of the template. That is, the right template is the key to making 3D hollow structures with complex structures [214]. However, conventional hydrothermal methods for synthesizing MIL-88A typically require more than 10 hours of heating in a reactor [223, 224] or stirring the reaction at room temperature for 24 h [225, 226]. In contrast, microwave heating, a more powerful alternative technology, is characterized by non-contact, reduced reaction times and lower energy consumption [227]. Therefore, the

present study strictly follows the concept of "simple, convenient, efficient and environmentally friendly", and LDH converted from MOF, LDH/88A and its oxidation product, LDO/88A, which have been mentioned in previous chapters (Ni₃FeLDH/88A and Ni₃FeLDO/88A), are used to study the PS-catalyzed degradation of bisphenol A. In the present study, the LDH-88A and its LDO-88A, MIL-88A, were synthesized by microwave synthesis. The research work in this paper proves that the novel LDH and LDO with regular shapes have very promising prospects as novel catalysts and will play a more important role in this field in the future.

V.2. Application of LDH/MIL88A catalytic PS degradation of BPA

In order to gain a clear understanding of the catalytic performance of Ni₃FeLDH/88A, a series of conditional experiments were carried out to further elucidate the activation process.

V.2.1 Effects of light

As many papers reported, the photoactivity of LDH and LDO for degradation of organic molecules and BPA [24, 410, 411], we first investigated the effect of light in combination with LDH/MIL88A and calcined derivatives.

Irradiation experiments: Irradiation experiments were conducted in a 100 mL reactor placed in a rectangular box equipped with four UVA polychromatic fluorescence tubes (F15W/350BL, Sylvania blacklight, Germany), which were positioned above the solution (Fig.V-2). The polychromatic emission spectrum of the irradiation system reaching the solution was measured using an optical fiber with a charge coupled device (CCD) spectrophotometer (Ocean Optics USD 2000 + UV-vis), which was calibrated using a DH-2000-CAL deuterium tungsten halogen reference lamp. The total irradiance in the UV region of solar radiation (290-400 nm) reaching the solution was 1390 $\mu\text{W cm}^{-2}$.



Fig.V-2 Equipment for irradiation experiments.

Experimental conditions: The degradation experiments were carried out in the dark in 150 mL beakers. In a typical procedure, 0.2 g/L^{-1} $\text{Ni}_3\text{FeLDH}/88\text{A}$ was ultrasonically dispersed in 50 mL Milli-Q water for 30 min, and pH was definite value (7.1 ± 0.1) without the addition of acid and alkali. The prepared $\text{Ni}_3\text{FeLDH}/88\text{A}$ suspension was magnetically stirred at a room temperature ($20 \text{ }^\circ\text{C}$). The BPA and PDS stock solutions were then mixed with the suspension to start the reaction, with the desired initial concentrations, $20 \text{ } \mu\text{M}$ and 0.5 mM . Unless otherwise stated, all experiments were conducted at the initial pH of 7.1. During the reaction, 2 mL sample was regularly taken out and filtered with a $0.22 \text{ } \mu\text{m}$ PTFE filter.

The effect of light on the catalytic degradation of BPA by $\text{Ni}_3\text{FeLDH}/88\text{A}$ is shown in Fig.V-3. When using $\text{Ni}_3\text{FeLDH}/88\text{A}$ alone without any other activation, the BPA content remained at 100% after ten minutes with or without light, which indicates that there is neither photodegradation under light neither adsorption of BPA by the solid material. In order to explore the synergistic combination of $\text{Ni}_3\text{FeLDH}/88\text{A}$ with light and persulfate activation, experiments were also performed in the same condition with addition of ammonium peroxodisulfate ($(\text{NH}_4)_2\text{S}_2\text{O}_8$) (PS). First, effect of PS was tested without the presence of LDH. The degradation efficiency of PS for bisphenol A at ten minutes under dark conditions was 4.8%. Under the light condition, the degradation efficiency increases to 18.2%. This indicates that PS alone has little effect on the degradation of bisphenol A, even though PS is a strong oxidant with a high standard reduction potential. However, when both $\text{Ni}_3\text{FeLDH}/88\text{A}$ and PS are present in the

solution, BPA decreases by 81% in ten minutes, indicating that LDH can catalyze the degradation of BPA by PS. It is worth mentioning that the efficiency of catalytic degradation is almost the same under light and dark conditions, which indicates that light has no effect on the catalytic degradation process. Following these results, research focused on the joint action of PS and HDL on the catalytic degradation of BPA.

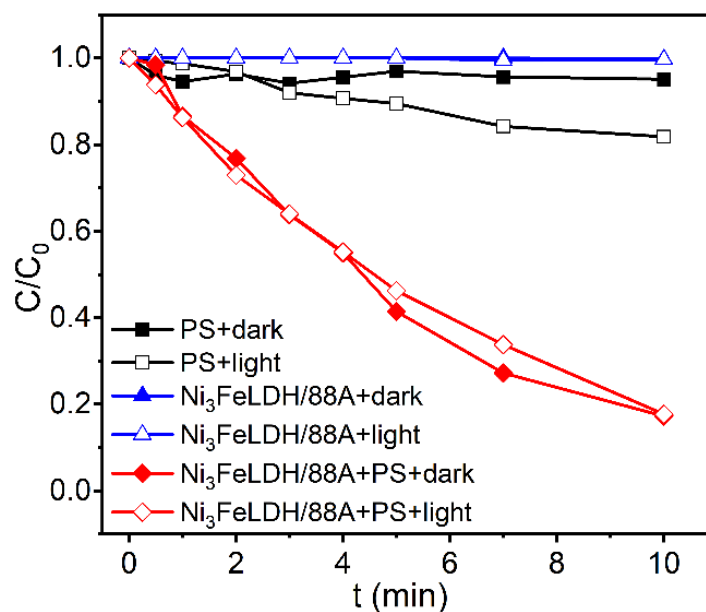


Fig.V-3. Kinetic of BPA degradation under catalytic activation of PS by Ni₃FeLDH/88A (20 μM BPA, 0.5 mM PS, 0.2g/L Ni₃FeLDH/88A, 50 mL H₂O).

V.2.2. Effect of persulfate S₂O₈²⁻ (PS) concentration

The persulfate species (PS), including peroxomonosulfate (HSO₅⁻, PMS), and persulfate (S₂O₈²⁻, PDS, referred to as PS in this study), have demonstrated remarkable efficacy as catalysts for oxidizing refractory organic molecules. When combined with certain transition metal ions, either in solution or solid phases, PS-based oxidation processes exhibit notable potential. These processes may manifest as advanced oxidation processes (AOPs) generating active radicals (such as SO₄^{•-}, SO₅^{•-}, S₂O₈^{•-}) or as non-radical processes. This study delves into the role of peroxydisulfate (S²O₈²⁻, PDS) in conjunction with Ni_xFe LDH and Ni_xFe LDO catalysts for the degradation of bisphenol A (BPA). Initially, we examined the impact of the initial concentration of PS on BPA degradation under conditions similar to those used in

experiments evaluating the effect of light. The concentrations of PS tested ranged from 0.05 to 0.5 mM in a 100 mL solution.

As depicted in Fig.V-4, a 44.7% degradation of BPA was achieved with 0.05 mM PS. Upon increasing the PS concentration to 0.1 mM, the degradation reached 71.7%, indicating that appropriate PS and catalyst interactions can yield more active species. However, there was no significant change in BPA degradation with further increases in PS concentration beyond 0.1 mM, up to 0.5 mM. Evidently, the LDH metal cations of Ni₃Fe/MIL88A play a pivotal role in activating persulfate.

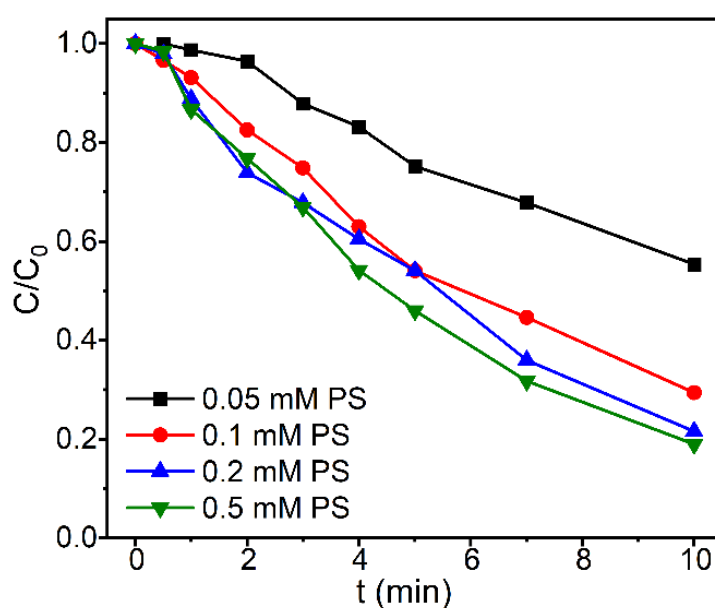


Fig.V-4 Effect of PS concentration on BPA degradation activated by Ni₃Fe/MIL88A (20 μM BPA, 0.2g/L LDH, 50 mL H₂O).

From a chemical composition standpoint, it is noteworthy that the atomic percentages of Ni²⁺ and Fe³⁺ in Ni₃Fe/MIL88A, as measured by ICP, are respectively Ni: 41.53% and Fe: 13.17%. Therefore, for 10 mg of Ni₃Fe/MIL88A, there are 0.0708 mmole Ni²⁺ and 0.0236 mmole Fe³⁺, accounting for both bulk and surface elements. Consequently, the PS/Ni and PS/Fe molar ratios are respectively 0.28 and 0.85 for 0.2 mM PS, the minimum values for maximum efficiency, and 0.68 and 2.12 for 0.5 mM PS, the saturated concentration of PS.

Although quantifying the number of accessible Ni²⁺ and Fe³⁺ surface sites is

challenging, the PS concentration used corresponds to a stoichiometric excess of PS compared to metal activators. The existence of a maximum PS/LDH ratio that limits efficiency may stem from a surface saturation effect, beyond which the accessibility of Ni/Fe sites to PS becomes limited.

Regarding the identification of the active species accountable for catalytic oxidation, Dongting Yue et al. reported that the transient species, $\cdot\text{SO}_4^-$ and $\text{HO}\cdot$, formed under activation of Ni_2Fe LDH are responsible for the BPA degradation [412]. The $\text{HO}\cdot$ species arise from the conversion of $\cdot\text{SO}_4^-$ ($\cdot\text{SO}_4^- + \text{H}_2\text{O} \rightarrow \text{SO}_4^{2-} + \text{H}^+ + \cdot\text{OH}$).

V.2.3. Effect of catalysis concentration

The concentration of catalyst plays a key role in both the efficiency of organic degradation and the kinetic model governing their breakdown. Therefore, we conducted investigations into the effect of catalyst concentration on the degradation of BPA. The experimental conditions for kinetic experiments, as used to study the effect of light, were upheld, with the sole variation being the concentration of catalyst ranging from 0, 40, 100, 200, to 400 mg/L.

Fig.V-5 investigates the impact of catalyst dosage on BPA removal, revealing that higher catalyst dosages correspond to more favorable BPA removal rates. Under identical PS dosage conditions, the degradation rate of BPA is growing rapidly with increasing catalyst dosage. For instance, with a catalyst dosage of 40 mg/L, approximately 39.5% of the BPA is removed within 10 minutes. However, when the catalyst dosage is increased to 100 mg/L of $\text{Ni}_3\text{FeLDH}/88\text{A}$, the remaining BPA is halved compared to the 40 mg/L dosage. Remarkably, with a catalyst loading of 400 mg/L, complete removal of BPA is achieved within a mere 7 min.

For the catalytic degradation effect of different doses of catalysts at seven minutes of reaction was analyzed (Fig.V-6), and it was found that the gap in catalytic degradation ability was greater from 0 to 40 to 100 mg/L than from 100 to 200 to 400 mg/L. These findings underscore that the addition of catalysts facilitates the creation of

additional active sites that react with PS, thereby accelerating the production of free radicals [413]. The increase in the number of surface sites available for PS activation, as the catalyst amount rises, exerts a profound influence on the kinetic degradation of BPA. Notably, with 400 mg/L of Ni₃Fe/MIL88A, only 7 minutes are required for total BPA degradation.

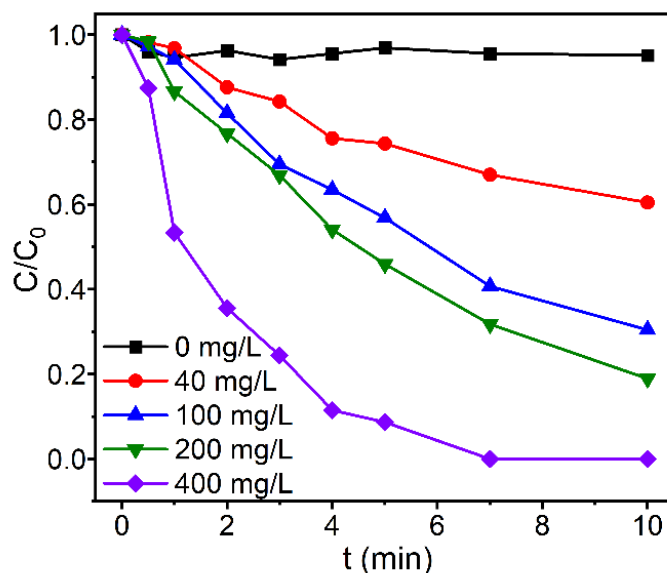


Fig.V-5 Effect of Ni₃Fe/MIL88A concentration on the degradation of BPA activated by PS (20 μM BPA, 0.5 mMPS, 50 mL H₂O).

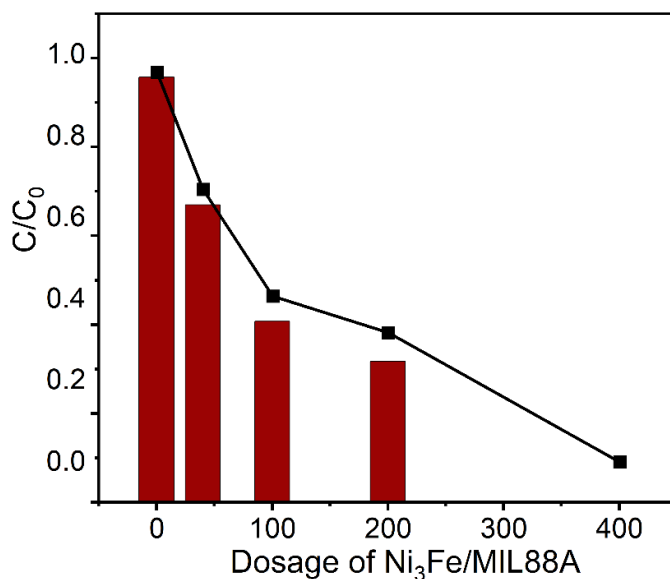


Fig.V-6 Catalytic degradation of different concentrations of catalysts at seven minutes of reaction.

V.2.4. Comparison with Ni₃FeLDH/COP and MIL-88A

The objective of our study was to enhance the catalytic reactivity of Ni_xFe LDH by controlling its morphology. To achieve this, we compared the catalytic degradation efficiency of 3D Ni₃FeLDH/88A with that of Ni₃FeLDH/COP synthesized by coprecipitation, as well as with its precursor MIL-88A. The catalytic degradation efficiencies were evaluated under both light and dark conditions, with all other experimental conditions kept constant (Fig.V-7).

Our results indicate that MIL-88A exhibited minimal catalytic ability, with its 21.8% degradation rate under light conditions primarily attributed to the degradation of bisphenol A by PS. In contrast, Ni₃FeLDH/COP catalysed the degradation of 53% of bisphenol A within ten minutes. Remarkably, Ni₃FeLDH/88A demonstrated even greater efficiency, with over 80% degradation of bisphenol A achieved within the same time frame. These findings conclusively demonstrate that the degradation efficiency decreases following: Ni₃FeLDH/88A > Ni₃FeLDH/COP > MIL-88A.

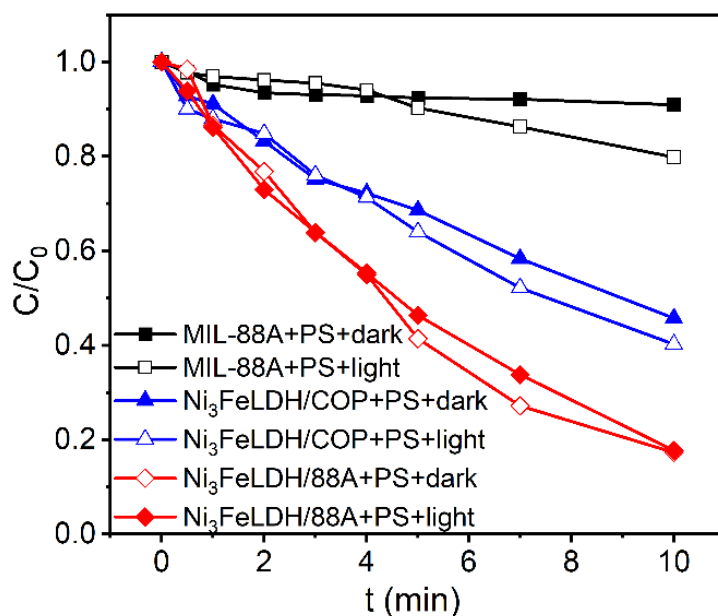


Fig.V-7 Catalytic degradation of BPA by PS activated by Ni₃FeLDH/88A, Ni₃FeLDH/COP and MIL-88A, under light/dark conditions (20 μM BPA, 0.5 mM PS, 0.2g/L Ni₃FeLDH/88A, 50 mL H₂O).

However, as already discussed previously, it is worth noting that for both

Ni₃FeLDH/88A and Ni₃FeLDH/COP, light does not appear to have any effect on their catalytic activity. The optical absorption characteristics of Ni₃FeLDH/88A and Ni₃FeLDH/COP were investigated using UV-Vis diffuse reflectance spectroscopy (UV-vis DRS) (Fig.V-8a) in order to evaluate the band gap of both Ni_xFe LDH. In the spectra of both Ni₃FeLDH/COP and Ni₃FeLDH/88A, the absorption band observed around 341 nm corresponds to the ligand metal charge transition spectra from the O2p to the 3d orbitals of Ni²⁺/Fe³⁺ in an octahedral environment. The bandgap energies (E_g) of LDH were calculated using the Tauc plot of the Kubelka-Munk function as follows:

$$K/S=F(R_{\infty})=(1- R_{\infty})^2/(2 R_{\infty}) \quad [414]$$

where R_{∞} is the Kubelka-Munk function, $R_{\infty} = R_{\text{sample}}/R_{\text{standard}}$, S is the scattering coefficient, and K is the absorption coefficient of the sample, $K/S = F(R_{\infty})$. When 'S' is a constant and the effective absorption coefficient $K = 2 \alpha$ (where α is the absorption coefficient).

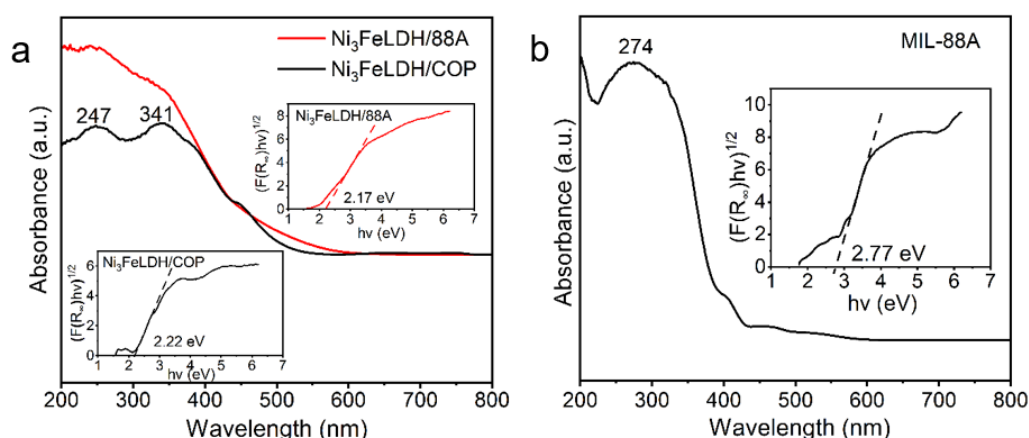


Fig.V-8 UV-vis of (a) Ni₃FeLDH/88A and Ni₃FeLDH/COP and (b) MIL-88A.

Thus, Tauc's equation is as follows:

$$(F(R_{\infty})hv)=A(hv-E_g)^n$$

where h and ν are the Planck's constant and the frequency of the photon with linear extrapolation respectively, and $n = 1/2$ when indirect band transition is allowed which is the case of most LDH semiconductors as reported by Si-Min Xu et al. [415]. The graph $[F(R)hv]^{1/2}$ vs. $h\nu$ in eV is shown in Fig.V-8 a. The E_g values of Ni₃FeLDH/88A and Ni₃FeLDH/COP were estimated as 2.17 eV and 2.22 eV, respectively, similar values than reported in the literature for Ni₂Fe-LDH structure [416]. The Valence Band Maximum (VBM) and the Conduction Band (CBM) of Ni₂FeCl-LDH consist of Ni-3d,

O-2p, and Fe-3d orbital energy, respectively. The lack of photocatalytic activity towards BPA observed in Ni₃FeLDH/88A and Ni₃FeLDH/COP semiconductors stems from rapid recombination or trapping of the electron-hole (e⁻/h⁺) species generated upon irradiation. This phenomenon is likely attributed to the presence of defects or impurities within the crystal lattice or on the surface of LDH platelets. Based on the observed outcomes, it is reasonable to conclude that the unique 3D mesoporous morphology of Ni₃FeLDH/88A does not facilitate light absorption and subsequent photocatalytic reactivity as effectively as the co-precipitated phase. This suggests that the specific structural characteristics of the Ni₃FeLDH/88A material may not be conducive to efficient utilization of light energy for catalytic processes when compared to the coprecipitated phase. For MIL-88A, which was also tested by UV, the results (Fig.V-8 b) showed that its E_g was larger than LDH, but it also had no absorption peaks in visible light, and therefore no photocatalytic ability.

V.2.5. Kinetic study

In the investigated cases, the degradation of BPA was fitted by the pseudo-first-order kinetics, which can be expressed by the equation:

$$\ln(C_t/C_0) = -kt$$

Here, C_t represents the pollutant concentration (mmol/L) at time t, C₀ is the initial concentration of the pollutant, k denotes the apparent rate constant (min⁻¹), and t signifies the reaction time (min). This equation illustrates the logarithmic relationship between the concentration of the pollutant at any given time and its initial concentration, with the rate constant determining the degradation rate over time [417]. Since there was no adsorption of BPA by the catalysts, the kinetics of adsorption were not considered, and the degradation kinetics solely relied on the catalytic oxidation reaction. Therefore, the observed degradation followed a pseudo-first-order reaction, indicating that the rate of degradation was primarily governed by the catalytic activity of the materials rather than any adsorption processes.

The kinetic results of BPA degradation catalysed by Ni₃FeLDH/88A, Ni₃FeLDH/COP, and MIL-88A are presented in Fig.V-9. The fitting results suggest that the kinetic data for all three substances align well with the pseudo-primary model.

The calculated k -values are 0.017 min^{-1} ($R^2 = 0.908$) for MIL-88A, 0.081 min^{-1} ($R^2 = 0.975$) for $\text{Ni}_3\text{FeLDH/COP}$, and 0.153 min^{-1} ($R^2 = 0.999$) for $\text{Ni}_3\text{FeLDH/88A}$, respectively. Notably, the reaction rate constant of $\text{Ni}_3\text{FeLDH/88A}$ significantly surpasses those of $\text{Ni}_3\text{FeLDH/COP}$ and MIL-88A, and even exceeds those of other LDHs utilized in the catalytic degradation of BPA. This underscores the superior catalytic performance of $\text{Ni}_3\text{FeLDH/88A}$ in promoting the degradation of BPA compared to the other tested materials [418-420].

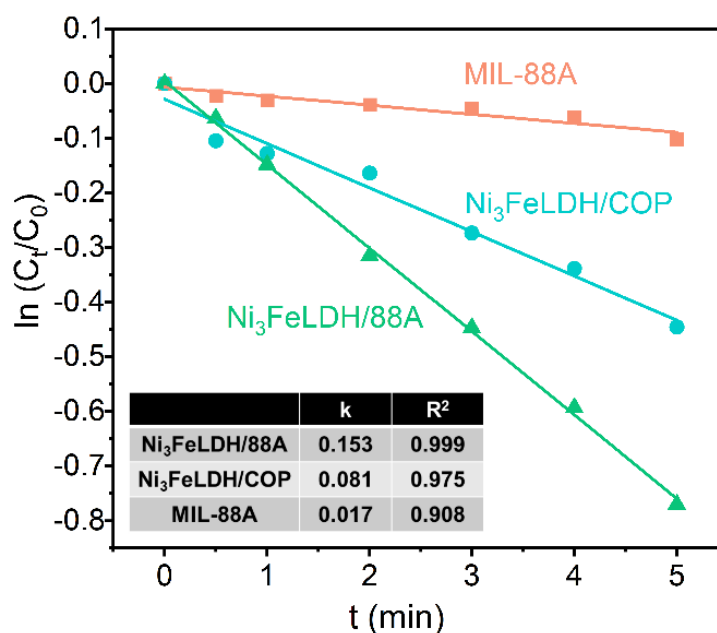


Fig.V-9 Kinetic results of catalytic degradation of BPA by $\text{Ni}_3\text{FeLDH/88A}$, $\text{Ni}_3\text{FeLDH/COP}$ and MIL-88A.

V.2.6. recycle experiment

The reusability and stability of catalysts are pivotal in their practical implementation within Advanced Oxidation Process (AOP) technology. Sequential experiments are conducted to evaluate the reusability and stability of $\text{Ni}_3\text{FeLDH/88A}$ for degrading BPA. After each reaction cycle, $\text{Ni}_3\text{FeLDH/88A}$ is recovered from the reaction solution via filtration and undergoes multiple washes with ultrapure water and ethanol to eliminate surface-bound contaminants. The experimental findings, illustrated in Fig.V-10, demonstrate promising results. Over three cycles, complete degradation of BPA was achieved. Notably, the first two cycles achieved complete degradation within

a brief 30 min, while the third cycle required 60 min, still maintaining 100% degradation efficiency. This phenomenon may be attributed to a decrease in the surface active metal site or a loss of solids during dispersion and recovery, factors that could be readily addressed in scale-up processes. These observations strongly advocate for the multiple recoveries of Ni₃FeLDH/88A, highlighting its potential for sustained performance within the process.

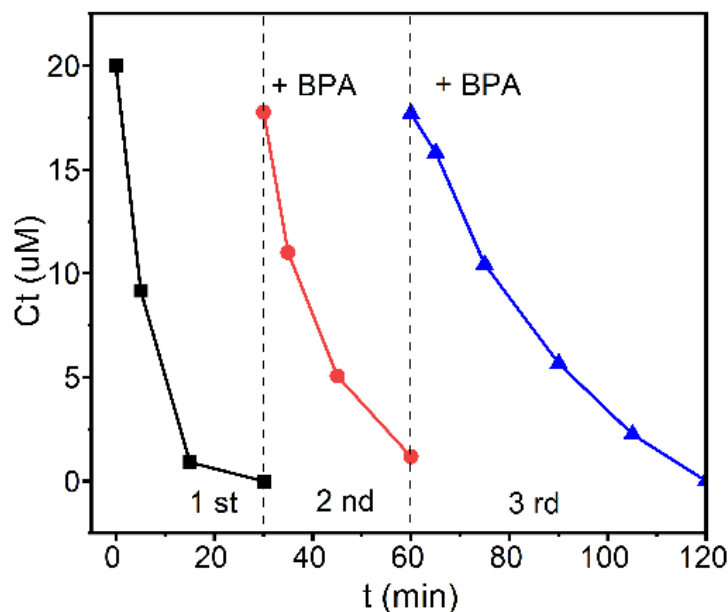


Fig.V-10 Ni₃FeLDH/88A degradation of BPA in cycling experiments (20 µM BPA, 0.5 mM PS, 0.2g/L Ni₃FeLDH/88A, 50 mL H₂O).

V.2.7. catalytic mechanism exploration

To examine the catalyst's behavior during the catalytic degradation of BPA, we compared the structural characteristics (XRD, FTIR, SEM) of LDH precursors and residues. The X-ray diffractograms of Ni₃FeLDH/88A before and after the catalytic reaction are depicted in Fig. V-11 a. The inter-reticular distances (d_{hkl}) and intensities of the (003), (006), (012), and (110) planes, characteristic of the LDH structure, showed minimal change after the catalytic reaction. This suggests an exceptionally high stability of the Ni₃FeLDH/88A catalyst during the reaction. This conclusion is further supported by the SEM image (Fig. V-11 b). The rod-like structure of the catalytically reacted Ni₃FeLDH/88A remained unchanged, as did the surface features of the lamellar

structure.

To go deeper into the behavior of Ni₃FeLDH/88A during catalytic degradation, we subjected Ni₃FeLDH/88A to reaction with peroxydisulfate anion (S₂O₈²⁻) to investigate if anion exchange of PS occurs during the catalytic reaction. Anion exchange was conducted in an aqueous solution with the same concentration and pH as the catalytic reaction, aiming to exclude the influence of BPA and its by-products on Ni₃FeLDH/88A. The reacted Ni₃FeLDH/88A was separated, washed with water-ethanol-water, and then dried overnight in an oven at 60 °C. From the XRD data (Fig. V-11 a), a shift of the d₀₀₃ towards lower 2θ values was observed, from 7.90 Å to 8.34 Å. This indicates a modification of the chemical composition of the interlayer. X. Huang et al. reported a similar interlayer distance (8.0 Å) for an Mg₃Al-S₂O₈²⁻ LDH phase obtained by anion exchange on the Mg₃Al-NO₃ precursor. However, considering the size of the anion, this interlayer gallery width appears rather low to accommodate such an anion.

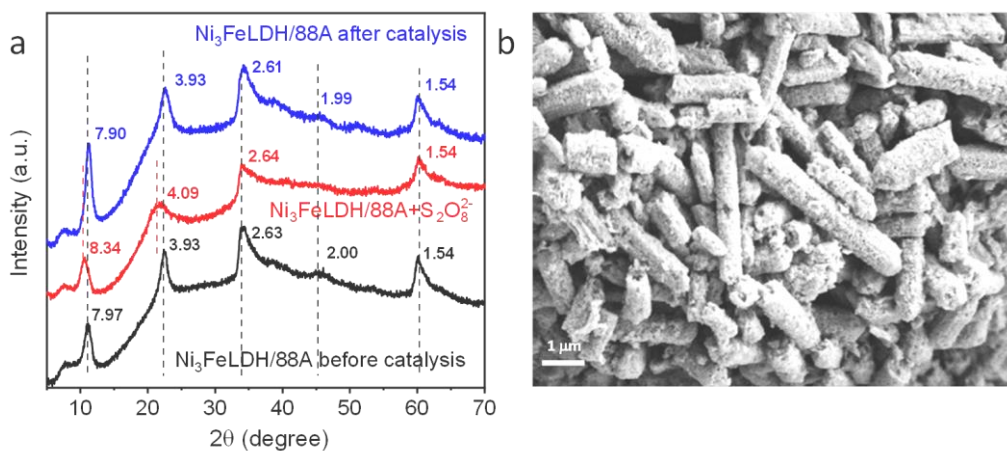


Fig.V-11 (a) XRD patterns of Ni₃FeLDH/88A before and after catalysis and after reaction with S₂O₈²⁻ anion; (b) SEM images of Ni₃FeLDH/88A after catalysis (1 cycle).

The FTIR spectra of Ni₃FeLDH/88A compounds before and after the catalytic reaction are depicted in Fig. V-12 a. Initially, it is observed that the characteristic vibration bands ($\nu_{\text{as}}(-\text{CO}_2^-)$ at 1566 cm⁻¹ and $\nu_{\text{s}}(-\text{CO}_2^-)$ at 1384 cm⁻¹) of the fumarate anion, which was intercalated in the Ni₃Fe-LDH during MIL88A conversion, decrease under catalytic reaction with persulfate. Furthermore, the spectrum after the reaction

exhibits three new distinct sharp peaks at 1117 cm^{-1} , 1036 cm^{-1} , and 619 cm^{-1} , characteristic of ν_3 , ν_1 , and ν_4 vibration bands of tetrahedral sulfate anions (Nakamoto, Infrared and Raman Spectra of Inorganic and Coordination Compounds). The spectra provide evidence for the absence of peroxodisulfate vibration bands ($\nu_{as}(-\text{SO}_2^-)$ at 1278 cm^{-1} and $\nu_s(-\text{SO}_2^-)$ at 1036 cm^{-1}) [421], as demonstrated by comparison with $\text{Na}_2\text{S}_2\text{O}_8$ infrared spectra (Fig. V-12 b). This suggests that $\text{S}_2\text{O}_8^{2-}$ decomposes during the reaction into SO_4^{2-} , which subsequently reacts with $\text{Ni}_3\text{FeLDH}/88\text{A}$. Surface adsorption and intercalation of SO_4^{2-} are then involved.

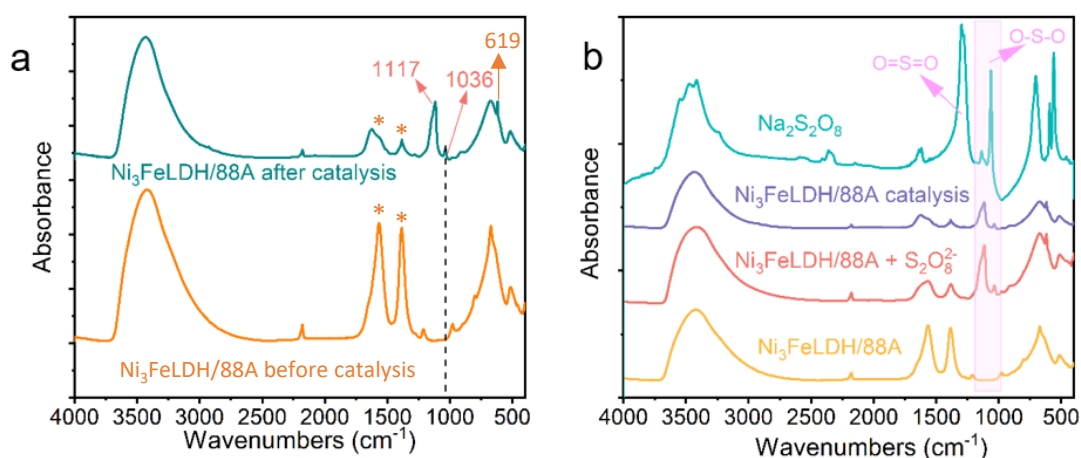


Fig.V-12 FTIR spectra of (a) $\text{Ni}_3\text{FeLDH}/88\text{A}$ before and after catalytic degradation of BPA and (b) before and after degradation of BPA by $\text{Ni}_3\text{FeLDH}/88\text{A}$ and $\text{Ni}_3\text{FeLDH}/88\text{A}$ after reaction with $\text{S}_2\text{O}_8^{2-}$.

V.3. Catalytic reactivity of $\text{Ni}_3\text{FeLDO}/88\text{A}$ for the degradation of BPA and structural characterizations of LDH catalysts.

V.3.1 Catalytic reactivity of $\text{Ni}_3\text{FeLDO}/88\text{A}$ for BPA degradation activated by PS

In our study, $\text{Ni}_3\text{FeLDO}/88\text{A}-300$ is obtained by calcining $\text{Ni}_3\text{FeLDH}/88\text{A}$ at $300\text{ }^\circ\text{C}$ in air for 2 h. For comparison, $\text{Ni}_3\text{FeLDH}/\text{COP}$ is also treated under the same conditions to obtain $\text{Ni}_3\text{FeLDO}/\text{COP}-300$ (details in Chapter II). All four compounds

were utilized to catalyze the degradation of bisphenol A by PS (Fig.V-13). The results indicate that the degradation efficiencies of the calcined materials surpass those of the uncalcined LDHs. The time required for complete catalytic degradation of BPA by Ni₃FeLDO/COP-300 was only half of that by Ni₃FeLDH/COP. Additionally, Ni₃FeLDH/88A-300 reduces the time for fully catalyzed degradation to one-third. Even when compared to Ni₃FeLDO/COP-300, Ni₃FeLDH/88A-300 catalyzed the degradation of 90% of BPA in half the time, showcasing superior catalytic ability. Clearly, calcination of the LDH increases the number of surface active sites and enhances catalytic reactivity towards PS. It's worth noting that calcination above 200 °C leads to partial dihydroxylation of the structure, as well as the formation of amorphous oxide (NiO) and mixed oxide (NiFe₂O₄, pre-spinel phase), that enhance the catalytic reactivity compare to pristine LDH.

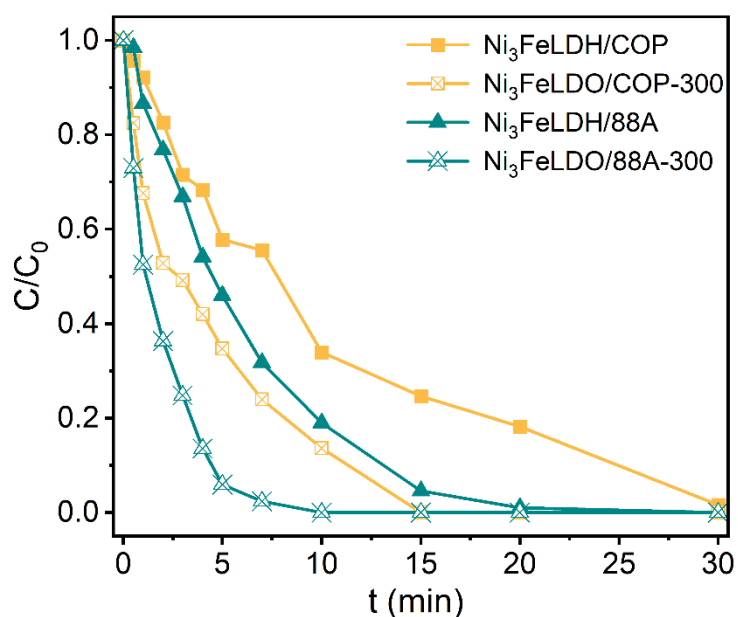


Fig.V-13 Catalytic degradation of BPA by PS-activated Ni₃FeLDH/88A, Ni₃FeLDH/88A-300, Ni₃FeLDH/COP and Ni₃FeLDH/COP-300 (20 μM BPA, 0.5 mM PS, 0.2g/L catalysts, 50 mL H₂O).

To evaluate the reusability and stability of Ni₃FeLDO/88A-300 for the degradation of bisphenol A, replicate experiments were conducted. After each reaction, Ni₃FeLDO/88A-300 was recovered from the reaction solution using diafiltration and washed several times with ultrapure water and ethanol to remove surface-adsorbed contaminants. These results indicate that the rate of catalytic degradation of

Ni₃FeLDO/88A-300 decreases over time, which implies that the reactivity gradually decreases with repeated use (Fig. V-14). This phenomenon may be attributed to the reduction of active sites and the weakening of the interaction between Ni₃FeLDO/88A-300 and PS due to the adsorption of organic pollutants on the surface of Ni₃FeLDO/88A-300 and the covering of its active sites due to the adsorption of degradation by-products on the surface of Ni₃FeLDO/88A-300, respectively. After three cycles of reuse, the BPA removal rate was still 100%. Therefore, the good catalytic efficiency, long-term stability and convenient recycling of Ni₃FeLDO/88A-300 catalysts show great advantages.

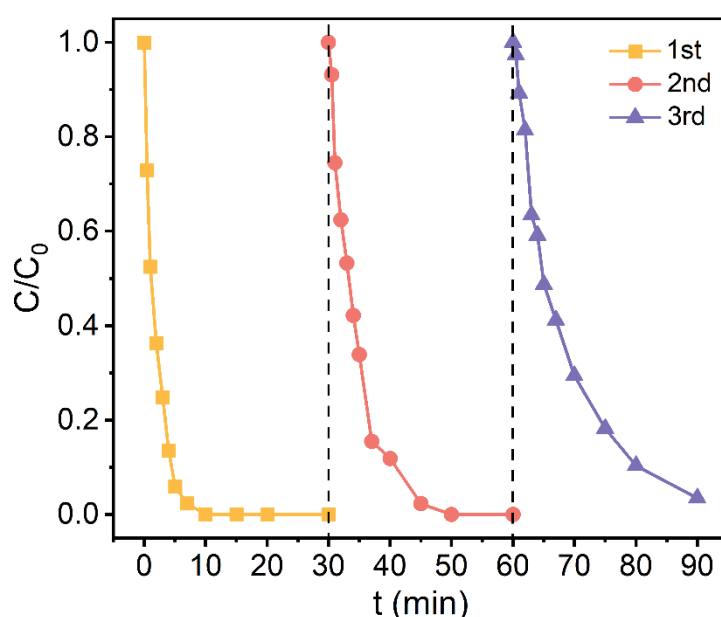


Fig.V-14 Ni₃FeLDO/88A-300 degradation of BPA in cycling experiments.

V.3.2 Characterization of Ni₃FeLDO/88A

The valence states of the reacted Ni₃FeLDO/88A were analysed using X-ray photoelectron spectroscopy (XPS) (Fig.V-15). The full-scan XPS spectra of Ni₃FeLDO/88A exhibits binding energies at 169, 284, 530, 712, and 855 eV, attributed to S 1s, C 1s, O 1s, Fe 2p, and Ni 2p, respectively [422]. The O 1s spectrum of Ni₃FeLDO/88A can be decomposed into three peaks at 529.93, 531.50, and 532.09 eV, corresponding to metal-oxygen bonding (Ni-O and Fe-O), oxygen vacancies (Ov), and water molecules adsorbed on the surface in metal oxides, respectively [423, 424]. The

peak in Ov is associated with a high degree of distortion caused by in situ partial reduction [425]. The Ni 2p spectrum was fitted to six peaks. The peaks at 854.70 and 872.05 eV are attributed to Ni²⁺, while the peaks at 856.24 and 873.31 eV should be attributed to Ni³⁺. Additionally, there are two oscillating satellite peaks (denoted as sat.) at 861.73 and 879.86 eV. Compared with the material before catalysis, the proportion of Ni³⁺ increased to 24.22%, indicating that some of the divalent iron was oxidized after degradation. This is consistent with the reduction, i.e., the presence of Fe²⁺. The high-resolution XPS spectra of Fe 2p show two peaks at 710.13 and 723.66 eV for Fe²⁺ and two peaks at 711.79 and 725.25 eV for Fe³⁺. The content of Fe in the different valence states mentioned above was 48.50% for Fe²⁺ and 39.02% for Fe³⁺, respectively [426, 427]. This indirectly suggests that nickel may play a major role in the Ni₃FeLDO/88A catalytic process.

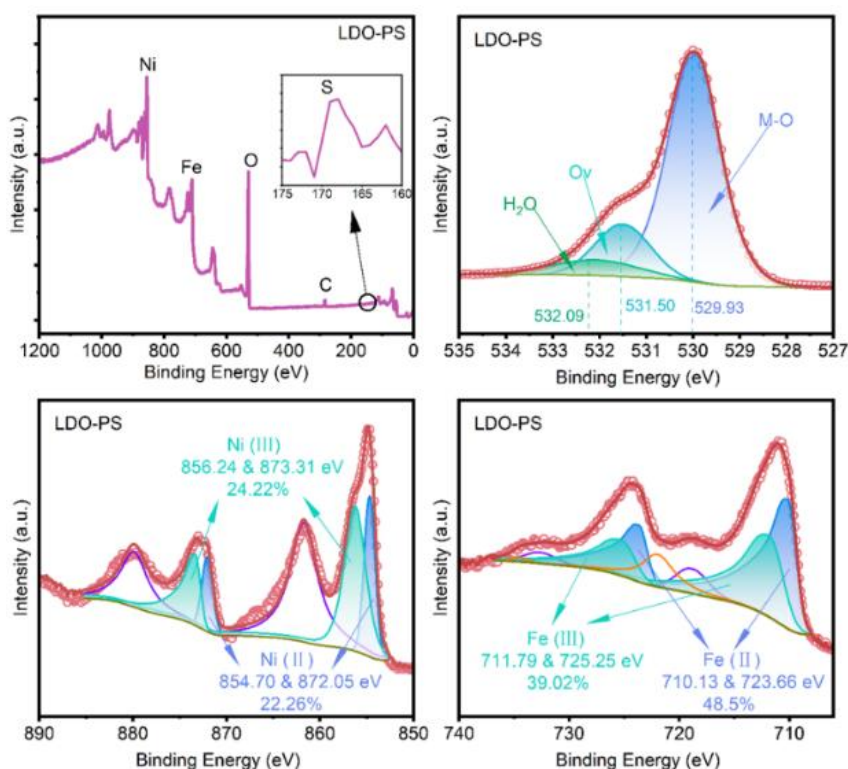


Fig.V-15 XPS of Ni₃FeLDO/88A after catalytic degradation of BPA

During the catalytic decomposition of PS, the sample surface was characterized in by FTIR (Fig.V-16). The peak observed at 1650 cm⁻¹ is attributed to the bending vibrations of the interlayer water molecules. The absorption peak at 1120 cm⁻¹ corresponds to the asymmetric stretching vibration of the ν₃(SO₄) bond of SO₄²⁻ anion

generated by the decomposition of PS [409]. The vibrational bands at 3390-3420 cm^{-1} are then attributed to the stretching vibrations of the hydrogen bonds in the surface -OH groups. The OH bond of $\text{Ni}_3\text{FeLDO}/88\text{A}$ shifts left from 3437 to 3426 and 3422 cm^{-1} after the reaction. This result, together with the S-O bond, suggests the interaction between PS and $\text{Ni}_3\text{FeLDO}/88\text{A}$ [428]. Furthermore, the FTIR spectra of $\text{Ni}_3\text{FeLDO}/88\text{A}$ residue after the catalytic reaction exhibit a series of sharp bands in the range of 1250-1700 cm^{-1} . Some of these bands correspond to the vibration bands of BPA [429]. However, kinetic experiments show no adsorption of BPA on $\text{Ni}_3\text{FeLDO}/88\text{A}$. Therefore, these bands are attributed to the adsorption of the oxidized form of BPA generated from the catalytic degradation reaction. Presence of bands pointed at 1691 cm^{-1} could be in agreement with the formation of benzoquinone, already suggested by Ullah Ramzan et al. [429] reported for the in situ study of photodegradation of BPA by TiO_2 .

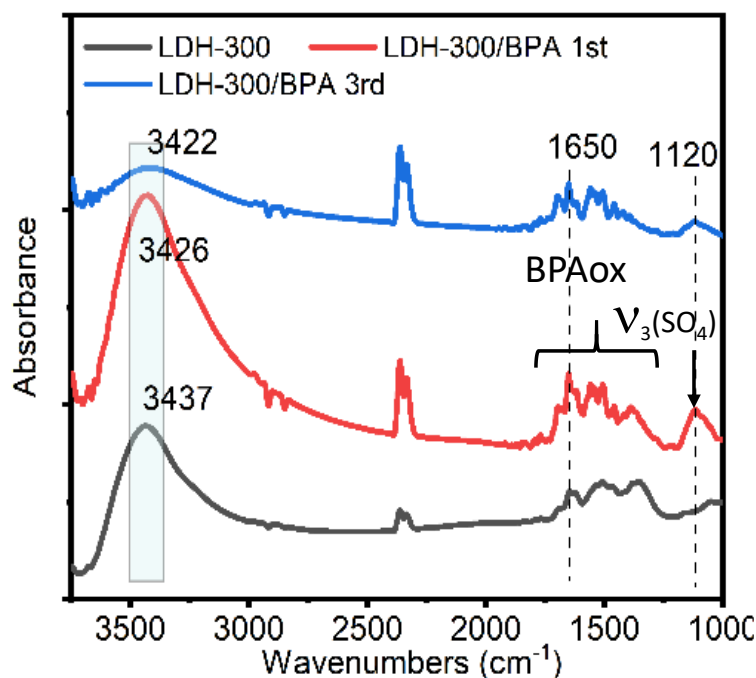


Fig.V-16 FTIR of $\text{Ni}_3\text{FeLDO}/88\text{A}$ after catalysis degradation of BPA.

The XRD results of LDO (Fig. V-17 a) after the reaction showed no significant changes compared to before the reaction, indicating that its crystalline structure remained unchanged after catalytic degradation. The pattern observed is consistent with a mixture of NiO and NiFe_2O_4 . The broad peak observed at 20-25° (2theta) is attributed

to the diffraction by amorphous nanoparticles of mixed oxides. This finding is also supported by the SEM results (Fig. V-17 b), which revealed that despite one and three rounds of catalytic degradation, there were no noticeable alterations in the structure of LDO. However, small particle aggregates were observed on the surface.

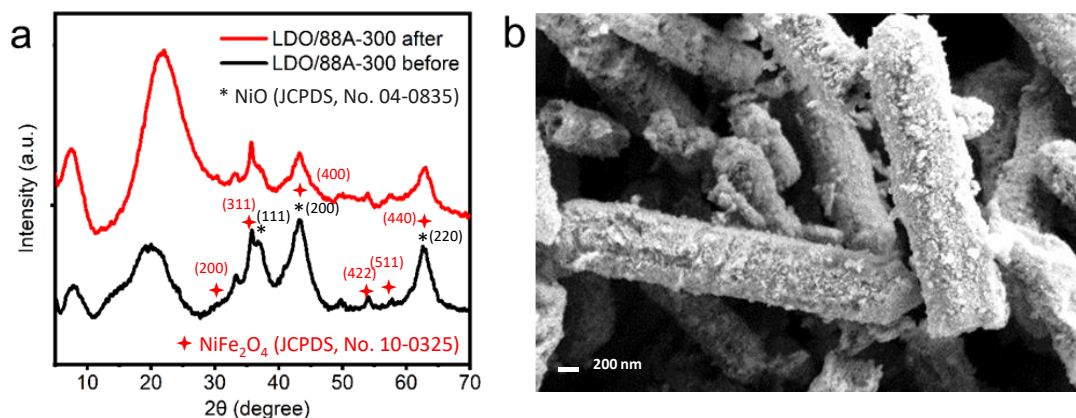


Fig.V-17 XRD and SEM of Ni₃FeLDO/88A after catalysis degradation of BPA.

V.4. Conclusion

In this chapter, we investigated the performance of catalyst-activated PS for the oxidative degradation of BPA. The catalysts, derived from Ni₃FeLDH/88A and Ni₃FeLDO/88A introduced in Chapter 2, were synthesized using MIL-88A as a precursor. Our focus was on exploring various factors influencing BPA degradation and understanding the activation mechanism of PS. Additionally, we compared the catalytic degradation efficiency of Ni₃FeLDH/88A with co-precipitated Ni₃FeLDH/COP.

Our conclusions are as follows:

1. The catalytic degradation efficiency of Ni₃FeLDH/88A is positively correlated with its concentration: higher concentrations lead to faster degradation rates. The addition of PS also influences catalytic efficiency. Initially, catalytic efficiency increases with PS addition, but then reaches a plateau. This behaviour is attributed to the competition between PS and bisphenol A in the consumption of SO₄^{•-}.
2. Ni₃FeLDH/88A exhibits significantly enhanced catalytic activity compared to its precursor MIL-88A, which has no catalytic degradation ability. Moreover,

Ni₃FeLDH/88A outperforms conventional co-precipitated Ni₃FeLDH/COP. BPA degradation by PS catalyzed by these substances follows a pseudo-first-order kinetic model. Notably, the rate constant of Ni₃FeLDH/88A (0.153 min⁻¹) exceeds that of the other substances. Light does not influence the catalytic process.

3. Recycling and regeneration experiments with Ni₃FeLDH/88A demonstrate its recyclability. However, the catalytic degradation time increases due to the accumulation of by-products covering the material's active sites during BPA degradation.

4. Calcined Ni₃FeLDH/88A-300 exhibits superior catalytic degradation efficiency for BPA compared to Ni₃FeLDH/88A and Ni₃FeLDH/COP-300 obtained via co-precipitation calcination. It also demonstrates recycling properties. Notably, the structure of Ni₃FeLDH/88A-300 remains unchanged before and after catalytic BPA degradation, indicating stability.

VI. Conclusion and perspectives

The primary objective of this study is to prepare layered double hydroxides derived from metal-organic frameworks. Specifically, the focus is on the Ni_xFe/88A materials obtained through the transformation of MIL-88A (iron) via urea hydrolysis with Ni²⁺ ionization in controlled alkaline conditions. The aim is to explore the transformation mechanism and the potential application of these materials in removing organic and inorganic pollutants from water. To achieve this objective, several approaches were employed, including microwave synthesis of various MOFs and their conversion to LDHs, investigation of LDH-catalyzed degradation of BPA, and synthesis and application of LDH-based heavy metal adsorbents.

MIL-88A is synthesized using a novel method to improve efficiency. Traditional hydrothermal synthesis typically demands over 6 hours of reaction time. In contrast, microwave-assisted precipitation offers a more efficient alternative for MIL-88A synthesis. The study investigates optimal synthesis conditions for this approach. Results indicate that MIL-88A synthesized via the microwave method exhibits a more homogeneous microstructure and enhanced crystalline stability compared to conventionally synthesized counterparts.

A novel method has been developed for the conversion of Metal-Organic Frameworks (MOFs) into new 3D Layered Double Hydroxide (LDH) structures. Mesoporous Ni_xFe LDHs are prepared by converting MIL-88A(Fe), serving as a sacrificial "template" structure. This conversion involves reacting nickel nitrate in a basic medium, with pH controlled by urea decomposition. The hydrolysis/nucleation/growth steps occur predominantly on the surface of the MOF, leading to the intergrowth of Ni_xFe LDH nanoplates (LDH/88A) while retaining the initial 3D rod-like structure of MIL-88A. The reaction is conducted in a microwave reactor, and its optimal conditions are investigated.

Additionally, other MOF/LDH conversion reactions have been explored to create new mesoporous 3D LDH structures with diverse compositions and morphologies. The effects of various ligands and metal cations on these reactions have been studied. Microwave syntheses of MOFs such as MIL-101(Fe) and MIL-88(Al), which are

analogous to MIL-88A(Fe) with modifications in ligands, have been optimized. Furthermore, conditions for their conversion into NiFe-LDH and NiAl-LDHs have been investigated.

Moreover, the reactivity of MIL-88A (Fe) with Co (II), Al (III), and Mg (II) salts has been examined, revealing conversion results highly sensitive to the nature of the metal and the medium conditions, particularly pH.

To enhance heavy metal adsorption capabilities, the new 3D LDH structures have been modified by incorporating phosphate anions, known for their reactivity towards heavy metals. The adsorption performance of heavy metals (Pb (II), Cd (II), Ni (II)) by $\text{Ni}_x\text{FeLDH}/88\text{A-PO}_4$ ($x=3,5$) is investigated and compared with precursors $\text{Ni}_x\text{FeLDH}/88\text{A-Cl}$ ($x=3,5$), coprecipitated phases $\text{Ni}_x\text{FeLDH}/\text{COP-PO}_4$ ($x=2,3$), and MIL-88A (Fe).

The results demonstrate that the $\text{Ni}_3\text{Fe}/88\text{A-PO}_4$ compound exhibits one of the highest Pb (II) adsorption capacities (538 mg/g) reported in the literature, surpassing those of coprecipitated phases. The adsorption process aligns with the pseudo-second-order kinetic model and the Langmuir adsorption thermodynamic model. Structural analysis of residues post-adsorption (via XRD, FTIR, XPS) reveals the nucleation and precipitation of $\text{Pb}(\text{OH})_2$ and $\text{Pb}_3(\text{PO}_4)_2$ phases on the LDH rod surface.

$\text{Ni}_x\text{Fe}/88\text{A}$ and their calcined derivatives have demonstrated strong catalytic reactivity for the degradation of organic pollutants, particularly bisphenol A (BPA) activated by peroxydisulfate. Experimental conditions have been optimized to achieve the best efficiency. The mesoporous $\text{Ni}_x\text{FeLDH}/88\text{A-S}_2\text{O}_8^{2-}$ coupling promotes very rapid BPA degradation kinetics (a few minutes), more effective than coprecipitated analogues. These new catalysts are stable and recyclable.

LDHs derived from MOFs with three-dimensional structures give them more attractive properties than LDHs prepared by conventional methods: (i) LDHs grown on porous templates can expose more active sites; (ii) dispersed and homogeneous growth avoids stacking and aggregation problems of layered LDHs; and (iii) LDHs with a core-shell or hollow structure have a greater mass-transfer advantage. These unique features open new doors for the development of novel materials in the energy and environmental

fields. Therefore, by combining the advantages of LDHs, the development of MOF-derived LDHs for applications in water decomposition, supercapacitors, environmental remediation, sensors, and other fields can be continued.

This initial exploratory study of the conversion of MOF structures into LDHs needs further investigation to gain a deeper understanding of the role played by the nature of the MOF (Metal-Ligand) systems and reactive metal cations (M^{2+} , M^{3+}) in the formation mechanisms of new 3D nanostructured LDH phases. More comprehensive characterization of surface properties will enable us to evaluate the nature of reactive sites in terms of both adsorption properties and the catalytic degradation properties of organic pollutants. The promising results achieved for the adsorption of Pb^{2+} by LDH phases derived from MIL-88A should be reproducible for other heavy metal pollutants as well.

Annexes

A.1. Experimental section

A.1.1. Chemicals

Chapter II:

Ferric nitrate nonahydrate ($\text{Fe}(\text{NO}_3)_3 \cdot 9 \text{H}_2\text{O}$), nickel nitrate hexahydrate ($\text{Ni}(\text{NO}_3)_2 \cdot 6 \text{H}_2\text{O}$), urea ($\text{CO}(\text{NH}_2)_2$), fumaric acid ($\text{HOOC}-\text{CH}=\text{CH}-\text{COOH}$), sodium hydroxide (NaOH) all from Aladdin Scientific.

Chapter III:

Ferric chloride hexahydrate ($\text{FeCl}_3 \cdot 6 \text{H}_2\text{O}$), aluminum sulfate dodecahydrate ($\text{Al}(\text{SO}_4)_3 \cdot 12 \text{H}_2\text{O}$), magnesium nitrate ($\text{Mg}(\text{NO}_3)_2$), terephthalic acid (H_2BDC), Cobalt nitrate hexahydrate ($\text{Co}(\text{NO}_3)_2 \cdot 6 \text{H}_2\text{O}$) all from Aladdin Scientific.

Chapter IV:

Sodium hydroxide (NaOH), nitric acid (HNO_3), sodium chloride (NaCl), dipotassium hydrogen phosphate (K_2HPO_4) all from Aladdin Scientific.

Chapter V:

Bisphenol A (BPA), $\geq 99\%$, Sigma-Aldrich, Chloroform, For HPLC, Carlo Erba. sodium persulfate (PS) from Aladdin Scientific.

A1.2. Synthesis

Chapter II:

Synthesis of MIL-88A by microwave: 0.195 mmol $\text{Fe}(\text{NO}_3)_3 \cdot 9 \text{H}_2\text{O}$ and 0.06 mmol fumaric acid are ultrasonically dissolved in 2 mL and 13 mL of ultrapure water, respectively. After mixing the above two solutions with stirring, the resulting solution is transferred to a microwave reactor heated 30 min at 110 °C. After centrifugation and separation, the precipitate is washed three times each with water and ethanol and transferred to an oven at 60 °C to dry overnight to obtain MIL-88A.

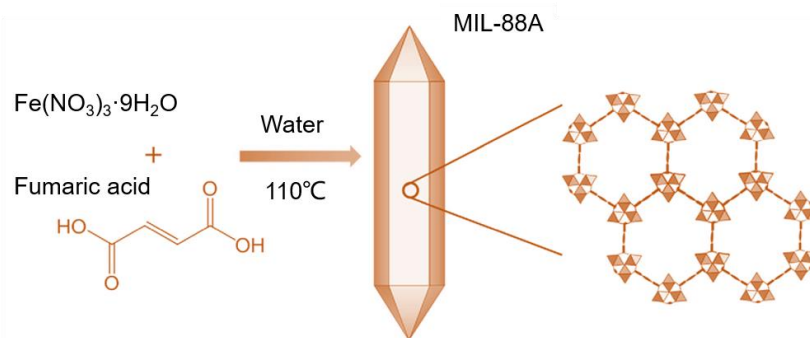


Fig.A-1 Schematic illustration of synthesis of MIL-88A [232].

Synthesis of MIL-88A by hydrothermal method: 69.6 mg (0.6 mmol) fumaric acid ultrasonic is dissolved in 13mL deionized water and 262.6 mg (0.65 mmol) $\text{Fe}(\text{NO}_3)_3 \cdot 6\text{H}_2\text{O}$ is dissolved 2mL of deionized water by stirring at room temperature. Then mix them to form a clear yellow solution, the mixed solution was transferred into Teflon stainless steel reactor. [229]. The product is separated by centrifugation and washed three times with ultrapure water and ethanol, respectively, before being dried in an oven at 60 °C overnight.

Synthesis of NiFe-LDH/88A. Then, 50 mg of MIL-88A is dispersed in 4 mL of ethanol (solution A). 150 mg of $\text{Ni}(\text{NO}_3)_3 \cdot 6\text{H}_2\text{O}$ and 100 mg of urea are dissolved in 6 ml of deionized water (solution B). Then, solutions A and B are mixed and stirred at room temperature (solution C). Finally, solution C is placed in a microwave reactor and heated at 110 °C for 1 h. The product is washed three times with deionized water and ethanol by centrifugation and then dried at 60 °C overnight to obtain $\text{Ni}_3\text{FeLDH}/88\text{A}-\text{NO}_3$ [168].

Synthesis $\text{Ni}_3\text{FeLDH}/\text{COP}$ by coprecipitation method: 0.1 M ferric nitrate and 0.3 M nickel nitrate are dissolved in 100 mL of water (solution A), 1 M sodium hydroxide and 0.05 M sodium hydroxide are dissolved in 50 mL of water (solution B), solution A and solution B are mixed slowly under nitrogen atmosphere with continuous stirring with a magnetic stirrer and maintaining a pH of 10. Stirring is continued overnight after consumption of the salt solution. The resulting sample is centrifuged and washed with ultrapure water until the pH is unchanged and transferred to an oven at 40 °C for one day.

Chapter III:

Convert MIL-88A to MgFe-LDH: Similar to the conversion to NiFe-LDH/88A, nickel was replaced with magnesium under the same conditions, specifically: 50 mg MIL-88A was dispersed in 4 mL of ethanol (solution A), 0.6 mmol (132 mg) of $\text{Mg}(\text{NO}_3)_2 \cdot 6 \text{H}_2\text{O}$ and 100 mg of urea were dissolved in 6 mL of deionized water (solution B). Then, solution A and solution B were mixed via stirring at room temperature (solution C). At last, the solution C was heated at different temperature for different time by microwave without stirring [164].

Convert MIL-88A to CoNiFeLDH: 50 mg MIL-88A was dispersed in 4 mL of ethanol (solution A). Different ratio of $\text{Co}(\text{NO}_3)_2 \cdot 6 \text{H}_2\text{O}$ and $\text{Ni}(\text{NO}_3)_2 \cdot 6 \text{H}_2\text{O}$ and 100 mg of urea were dissolved in 6 mL of deionized water (solution B). The total molar amount of cobalt and nickel to the molar ratio of iron is 3. Solution A and solution B were mixed via stirring at room temperature (solution C). At last, the solution C was heated at 100 °C for 60 min by microwave without stirring [164].

Convert MIL-88A to NiAlFe-LDH: 50 mg MIL-88A(Fe) dispersed in 4 mL EtOH (solution A), and 100 mg urea and different ratio of Ni/Al dissolved in 6 mL H_2O (solution B), the ratio of total amount of Ni/Al and Fe is 3. Solution A and B are mixed and heated 110 °C for 60 min.

Synthesis of Al-FA: 3.71 g $\text{Al}_2(\text{SO}_4)_3 \cdot 18\text{H}_2\text{O}$ was added to 15.9 mL of water and heated to 60 °C for 5 min by microwave (solution A). 0.95 g NaOH and 1.29 g fumaric acid are dissolved in 19.1 mL water (solution B). Solution A is added into solution B and the mixture is heated in microwave at 60 °C for 10 min by stirring [287]. The product is collected by centrifuge and washed by water for 3 times.

Convert Al-Fu to NiAlLDH/FA. The conversion was first explored as follows: 50 mg Al-FA was dispersed in 4 mL of H_2O (solution A). 0.06 mmol (150 mg) $\text{Ni}(\text{NO}_3)_2 \cdot 6\text{H}_2\text{O}$ and 100 mg of urea were dissolved in 6 mL of ethanol (solution B). Then, solution A and solution B were mixed via stirring at room temperature (solution C). At last, the solution C was heated at different 60 °C, 80 °C, 110 °C, 130 °C and 150 °C for 30 min by microwave without stirring.

Synthesis of Al-Fu-comp: 50 mg Al-Fu-comp was dispersed in 4 mL of H₂O (solution A). 0.06 mmol (150mg) Ni(NO₃)₂·6H₂O and 100 mg of urea were dissolved in 6 mL of ethanol (solution B). Then, solution A and solution B were mixed via stirring at room temperature and then heated at 150 °C for 30 min by microwave without stirring.

Synthesis of MIL-101 by hydrothermal method: 2.48 mmol FeCl₃·6H₂O and 1.24 mmol H₂BDC were added to 20 mL DMF and mixture was stirred by magnetic stirrer. Then the homogenous dissolved solution was heated 110 °C for 20 h in a Teflon reactor. Then the first product was purified by washing hot DMF (70 °C, 15 min) several times. The purified light orange product was dried in a vacuum oven at 60 °C overnight [293].

Synthesis of MIL-101 by Microwave method: 4.96 mmol (1.3406 g) FeCl₃·6H₂O and 2.48 mmol (0.412 g) H₂BDC dissolve in 40 ml DMF, Stir until completely dissolved, resulting in a bright yellow transparent solution. Microwave the solution to 110 °C for 30 min. Wash twice with DMF and twice with ethanol and place overnight in a 60 °C oven.

Synthesis of Al-BDC: 3.1 mmol AlCl₃·6H₂O dissolved in 5ml H₂O (solution A), and 3.1 mmol H₂BDC dissolved in 5ml DMF (solution B), respectively. Solutions A and B were thoroughly mixed and then placed in microwave heated at 150 °C for 60 min. The white solid was collected by centrifugation, washed three times with deionized water and ethanol, respectively, and baked in an oven at 60 °C [306].

Chapter IV:

Synthesis of Ni_xFeLDH/COP-Cl (x = 2, 3) and Ni_xFeLDH/88A-Cl (x = 3, 5): 2.0 g of LDH (Ni₃FeLDH/88A-NO₃, Ni₅FeLDH/88A-NO₃, Ni₂FeLDH/COP-NO₃ and Ni₃FeLDH/COP-NO₃) are homogeneously dispersed in 100 mL of 0.05 M NaCl solution, at a pH adjusted to 7.0, stirred overnight in nitrogen atmosphere, centrifuged and separated, then washed with ultrapure water until the pH was unchanged, and dried into an oven at 60 °C for 24 h, leading to the as-prepared LDH-Cl.

Synthesis of Ni_xFeLDH/88A-PO₄ (x =3, 5) and Ni_xFeLDH/COP-PO₄ (x = 2, 3): 1.7 g LDH-Cl (Ni₃FeLDH/88A-Cl, Ni₅FeLDH/88A-Cl, Ni₂FeLDH/COP-Cl,

Ni₃FeLDH/COP-Cl) are homogeneously dispersed in 100 mL of 0.095 M of potassium dihydrogen phosphate (K₂HPO₄) solution, at a pH adjusted to 7.0, stirred overnight in a nitrogen atmosphere. The Ni₃FeLDH/88A-PO₄, Ni₅FeLDH/88A-PO₄, Ni₂FeLDH/COP-PO₄, Ni₃FeLDH/COP-PO₄ materials were recovered after centrifugation and separation, washing with deionized water until the pH is unchanged, and dried in an oven at 40 °C for 24 h. These phosphates loaded LDH sorbents will be abbreviated as LDH-PO₄ for simplifying.

A1.3. Instrumentation

Powder X-ray diffraction patterns were recorded with a Philips X'Pert automated X-ray diffractometer using CuK α radiation ($\lambda = 0.154051$ nm), over the 2-70° (2 θ).

FTIR spectra were recorded with a Nicolet 5700 spectrometer from Thermo Electron Corporation using the KBr pellet technique.

The metallic composition of LDH was determined using inductively coupled plasma-atomic emission spectroscopy (ICP-AES Agilent 5800). Priori analysis, the samples were mineralized by dispersion in 6 mL of HNO₃ (69%) and 2 mL of HCl (37%) and heating at 230 °C for 1 h using microwave irradiation (Anton-Paar Multiwave 5000). CHNS contents in the hybrid materials were measured using a Thermo Scientific CHNS/O FlashSmart.

The morphologies of the powders mounted on conductive carbon adhesive tabs and the films deposited on GCE or CPE were investigated by scanning electron microscopy (SEM) using a Zeiss Supra 55 FEG-VP Field-Emission Scanning Electron Microscope operating at 3 kV. Transmission electron microscopy (TEM) images were taken using a microscope JEOL 2100 operating at an acceleration voltage of 200 kV. A suspension of 5 mg/mL was prepared and stirred overnight, followed by a deposition of a droplet on copper grid and left to dry at room temperature.

FeTSPP in solution and intercalated in the LDH were characterized by UV-Vis using Shimadzu v-2400 spectrophotometer. Thin films of ZnCr-FeTSPP and Zn-FeTSPP, prepared on ITO glass plates following the same procedure as used to prepare

thin films on GCE and CPE, were analysed by transmittance under dried conditions and in the presence of electrolyte solutions.

X-ray photoelectron spectroscopy (XPS) measurements were performed in an ultrahigh vacuum photoelectron spectrometer equipped with an Omicron DAR 400 X-ray source and an Omicron EA 125 hemispherical analyzer. The Mg K α source (1253.6 eV) running at 300 W is separated from the analyzer by an angle of 55°. A medium magnification mode and constant pass energy of the analyzer equal to 20 eV were used for analysis. Photoelectron data were recorded at a take-off angle of 90° (normal detection).

A.1.4 Pb²⁺ adsorption experiments

A.1.4-1 Models for kinetic experiments.

Adsorption kinetic curves were fitted using the various mathematical models available, the pseudo-first-order model [344] (eq. 1), the pseudo-second-order model [345] (eq. 2), and the intraparticle diffusion model [346] (eq. 3) expressed as follows:

Pseudo-first-order model	Pseudo-second-order model	Intraparticle diffusion model
$\ln(q_e - q_t) = \ln q_e - k_1 t$ (eq. 1)	$\frac{t}{q_t} = \frac{1}{k_2 q_e^2} + \frac{t}{q_e}$ (eq. 2)	$q_t = k_i t^{0.5} + C$ (eq. 3)

where q_e (mg·g⁻¹) and q_t (mg/g) are the amounts of Pb²⁺ at equilibrium and at time t (h), respectively, and k_1 (h⁻¹) and k_2 (g mg⁻¹ h⁻¹) and are the rate constants of the pseudo-first-order and pseudo-second-order adsorption models, and k_i (mg g⁻¹ h^{0.5}) is the rate constant for intra-particle diffusion and C (mg/g) reflects the thickness of the boundary layer, respectively.

A.1.4-2 Models for adsorption isotherm experiments.

The isotherms are fitted with the commonly used Langmuir (eq. 1) and Freundlich (eq. 2) models using respectively the following equations (Kalam et al., 2021):

$$\frac{C_e}{q_e} = \frac{1}{K_L q_m} + \frac{C_e}{q_m} \quad (\text{eq. 1})$$

where q_m = maximum amount of adsorbed species (mg/g) and K_L is the Langmuir constant (L/mg) and $R_L = \frac{1}{1 + K_L C_0}$ = separation factor or equilibrium factor. When $R_L <$

1 adsorption is favourable, when $R_L = 0$ adsorption is irreversible, when $R_L = 1$ adsorption is linear, when $R_L > 1$ adsorption is unfavourable.

$$\ln q_e = \ln K_F + \frac{1}{n} \ln C_e \quad (\text{eq. 2})$$

where K_F = adsorption capacity (L/mg) and $1/n$ = adsorption intensity or surface heterogeneity. When $0 < 1/n < 1$ adsorption is favourable; when $1/n > 1$ adsorption is unfavourable, when $1/n = 1$ adsorption is irreversible.

Abstract

New mesoporous Layered Double Hydroxide materials with 3D assemblies and morphologies have been prepared through microwave-assisted topotactic conversion of "Metal Organic Frameworks" (MOFs) structures (MIL-88A, MIL-101). Syntheses have been optimized. The study focused on the Ni_xFe/88A material obtained from the conversion of MIL-88A(Fe) by reaction of Ni²⁺ ions in a controlled basic medium using urea decomposition. The obtained morphologies are mesoporous 3D rod-like structures formed by the intergrowth of Ni_xFe/88A-X (X = NO⁻, Cl⁻, PO₄³⁻) LDH nanoplates. A comprehensive study on heavy metal adsorption properties showed that nanostructured Ni_xFe/88A-PO₄ materials exhibit excellent adsorption capacities for Pb(II) (Cd(II), and Ni(II)), by surface nucleation/precipitation of Pb(OH)₂ and Pb₃(PO₄)₂. In parallel, these new Ni_xFe/88A-X materials and their calcined derivatives have been studied for their catalytic properties in activating peroxydisulfate for the degradation of organic pollutants, particularly bisphenol A.

Résumé

De nouveaux matériaux Hydroxides Doubles Lamellaires mésoporeux présentant des assemblages 3D à morphologies 3D ont été préparés par conversion topotactique, assistée par micro-ondes, de structures de type « Metal Organic Frameworks », MOFs (MIL-88A, MIL-101). Les synthèses ont été optimisées. L'étude s'est focalisée sur le matériau Ni_xFe/88A provenant de la conversion du MIL-88A(Fe) par réaction des ions Ni²⁺ en milieu basique contrôlé par décomposition de l'urée. Les morphologies obtenues sont 3D mésoporeuses, sous forme de bâtonnet, formées par l'intercroissance de nanoplaquettes d'HDL Ni_xFe/88A-X (X = NO₃⁻, Cl⁻, PO₄³⁻). Une étude approfondie sur les propriétés d'adsorption de métaux lourds a montré que les matériaux nanostructurés Ni_xFe/88A-PO₄ présentent d'excellentes capacités d'adsorption de Pb(II) (Cd(II) et Ni(II)), par nucléation/précipitation en surface de Pb(OH)₂ et Pb₃(PO₄)₂. En parallèle, ces nouveaux matériaux Ni_xFe/88A-X et leurs dérivés calcinés ont été étudiés pour leur propriétés catalytiques d'activation de peroxydisulfate pour le dégradation de polluants organiques et du bisphénol A en particulier.

La fabrication de matériaux fonctionnels est depuis longtemps reconnue comme un sujet central dans les domaines de l'énergie et de l'environnement. La composition, la morphologie et la structure des matériaux leur confèrent un large éventail de propriétés pour répondre aux besoins des applications visées. En particulier, les structures métallo-organiques (MOF), qui ont un réseau périodique avec des groupes organiques et des centres métalliques comme noeuds, deviennent une alternative aux matériaux conventionnels en raison de leur supériorité polyvalente. Fondamentalement, la grande surface et la structure complexe des pores favorisent le contact des MOF avec les substances dans la plupart des systèmes. La spécificité des tâches peut être obtenue grâce à leur structure facilement ajustable. La conversion sacrificielle en nouveaux matériaux est envisager pour conserver les propriétés morphologiques des précurseurs MOFs, tandis que les traitements chimiques/thermiques leur confèrent des propriétés plus variées. Beaucoup d'efforts ont été investis dans la construction d'oxydes et de carbures métalliques ou de leurs composites par traitement thermique de MOF. En fin de compte, le réseau organique fragile est transformé en une matrice de carbone plus robuste, plus résistante aux produits chimiques, aux courants, aux acides et aux bases. En tant que catalyseurs pour les applications énergétiques et environnementales, ils offrent de grandes possibilités et de nombreuses percées. Cependant, certaines propriétés morphologiques et structurelles sont perdues lorsque la structure se rétrécit au cours de la conversion thermique. En outre, il existe un risque d'agrégation des noeuds métalliques dispersés périodiquement, ce qui entrave la fabrication de catalyseurs métalliques dispersés de manière atomique. Il a été constaté que les hydroxydes métalliques cultivés à partir de modèles de MOFs peuvent être régulés chimiquement afin d'éviter les dommages similaires à ceux de la pyrolyse. Des hydroxydes dérivés de MOFs bien définis peuvent être générés à partir de noeuds métalliques convertis in situ en choisissant judicieusement la température de réaction, le temps et les conditions de synthèse.

Les hydroxydes doubles lamellaires (HDL) sont composés de couches d'hydroxydes métalliques divalents et trivalents ainsi que d'anions dans les domaines inter-couches/inter-lamellaires, représentés par $[M^{2+}_{1-x}M^{3+}_x(OH)_2][(A^{n-})_{x/n}.mH_2O]$. Les HDL sont également considérés comme un matériau optionnel dans de nombreux domaines en raison de ses propriétés de composition hautement réglables et de sa

structure stratifiée facile à appliquer. La grande surface spécifique, les sites métalliques hautement exposés et les groupes fonctionnels de surface permettent aux HDL d'exceller dans la catalyse et l'adsorption. La cavité intérieure du matériau double hydroxyde en couche creuse dérivé du MOF augmente non seulement la capacité de chargement du matériau actif et désobstrue la voie de diffusion, mais fournit également un espace tampon pour l'expansion du volume du matériau actif, ce qui est propice à l'utilisation durable du matériau actif, améliorant ainsi efficacement la stabilité globale du matériau actif.

D'autre part, avec les progrès continus de l'industrialisation, une grande quantité d'eaux usées industrielles contenant une variété de composés inorganiques et organiques a été générée, ce qui a entraîné une pollution de plus en plus grave des eaux de surface et des eaux souterraines, donnant lieu à de graves problèmes environnementaux et à une inquiétude généralisée. Bien que la plupart de ces polluants soient présents en faibles concentrations dans les eaux usées, ils constituent une menace pour les organismes aquatiques et donc pour la santé humaine en raison de leur importante bioaccumulation, de leurs propriétés environnementales très persistantes, de leur toxicité potentielle pour l'homme et de leur innocuité écologique. Par exemple, le bisphénol A (BPA), qui est utilisé dans la fabrication de résines époxy et de plastiques, est soupçonné d'être un perturbateur endocrinien qui affecte négativement le système immunitaire humain et les glandes mammaires à des concentrations inférieures aux niveaux critiques de toxicité. De même, divers métaux lourds tels que Ba (II), Zn (II), Hg (II), Co (II), Cr (III), Pb (II), Fe (III) et Cd (II) sont généralement toxiques, non dégradables et ne peuvent pas se polymériser efficacement en unités macromoléculaires, ce qui exacerbe le problème de l'élimination. Parmi ces métaux lourds toxiques, les déchets de plomb (Pb (II)) sont les plus préoccupants. Le Pb (II) est une neurotoxine chronique très toxique, non biodégradable, persistante dans l'environnement et associée à de nombreux problèmes cardiovasculaires et rénaux, qui pénètre dans les systèmes d'eau à partir de différentes activités industrielles. Il est donc urgent de s'attaquer aux polluants susmentionnés.

L'objectif principal de ce travail est la préparation d'hydroxydes doubles lamellaires dérivés de structures MOFs. L'étude se concentre sur les matériaux Ni_xFe_{88A} obtenus en transformant MIL-88A (fer) par hydrolyse de l'urée avec

ionisation Ni^{2+} dans des milieux alcalins contrôlés, en explorant le mécanisme de transformation et leur application dans l'élimination des polluants organiques/inorganiques de l'eau. Pour atteindre cet objectif, les approches suivantes ont été utilisées : synthèse par micro-ondes d'une variété de MOF et leur conversion en LDH, étude de la dégradation du BPA catalysée par la LDH, et synthèse et application d'adsorbants de métaux lourds à base de LDH.

Le MOF MIL-88A est synthétisé à l'aide d'une nouvelle méthode. Comme la synthèse hydrothermale du MIL-88A nécessite plus de 6 heures de réaction, la précipitation assistée par micro-ondes, plus efficace, est choisie pour synthétiser le MIL-88A, et les conditions optimales de synthèse sont étudiées. Les résultats montrent que la microstructure du MIL-88A synthétisé par la méthode des micro-ondes est plus homogène et que la forme cristalline est plus stable.

Une nouvelle méthode est développée pour la conversion de MOF en tant que précurseur de nouvelles structures LDH 3D. Les LDH mésoporeux Ni_xFe sont préparés en convertissant le MIL-88A (Fe), utilisé ici comme structure "modèle" sacrificielle, en faisant réagir le nitrate de nickel dans un milieu basique, dont le pH est contrôlé par la décomposition de l'urée. Les étapes d'hydrolyse/nucléation/croissance sont localisées à la surface du MOF et conduisent à l'intercroissance de nanoplaquettes Ni_xFe LDH (LDH/88A), en conservant la structure initiale 3D en forme de tige du MIL-88A. La réaction est réalisée dans un réacteur à micro-ondes et ses conditions optimales sont étudiées.

D'autres réactions de conversion MOF/LDH ont été explorées pour préparer de nouvelles structures LDH 3D mésoporeuses avec des compositions et des morphologies variées. Les effets des ligands et des cations métalliques ont été étudiés. Les synthèses par micro-ondes des MOF MIL-101(Fe), analogue au MIL-88A (Fe) (ligand fumarate remplacé par un benzenedicarboxylate), et MIL-88 (Al), analogue au MIL-88 (Fe), ont été optimisées, et les conditions de leur conversion en LDH NiFe et NiAl ont été étudiées. La réactivité de MIL-88A (Fe) avec les sels de Co (II), Al (III), et Mg (II) a été testée avec des résultats de conversion très sensibles à la nature du métal et aux conditions du milieu (pH).

Afin de développer de nouveaux matériaux plus efficaces pour l'adsorption des métaux lourds, les nouvelles structures 3D LDH ont été modifiées en insérant des anions phosphates, qui sont réactifs vis-à-vis des métaux lourds. L'adsorption de métaux lourds (Pb (II), Cd (II), Ni (II)) par $\text{Ni}_x/88\text{A-PO}_4$ ($x=3,5$) est étudiée et comparée aux précurseurs $\text{Ni}_x\text{Fe}/88\text{A-Cl}$ ($x=3,5$), aux phases coprécipitées $\text{Ni}_x\text{Fe}/\text{COP-PO}_4$ ($x=2,3$) et MIL-88A (Fe). Les résultats montrent que le composé $\text{Ni}_3\text{Fe}/88\text{A-PO}_4$ présente l'une des capacités d'adsorption de Pb (II) les plus élevées (538 mg/g) jamais rapportées dans la littérature, supérieure à celle des phases coprécipitées. L'adsorption est compatible avec le modèle cinétique du pseudo-second ordre et le modèle thermodynamique d'adsorption de Langmuir. L'analyse structurale des résidus après adsorption (XRD, FTIR, XPS) a révélé la nucléation et la précipitation des phases $\text{Pb}(\text{OH})_2$ et $\text{Pb}_3(\text{PO}_4)_2$ à la surface du barreau de LDH.

Le $\text{Ni}_x\text{Fe}/88\text{A}$ et ses dérivés calcinés ont démontré une forte réactivité catalytique pour la dégradation des polluants organiques, en particulier le bisphénol A (BPA) activé par le peroxydisulfate. Les conditions expérimentales ont été optimisées pour obtenir la meilleure efficacité. Le couplage HDL mésoporeux $\text{Ni}_x\text{Fe}/88\text{A-S}_2\text{O}_8^{2-}$ favorise une cinétique de dégradation du BPA très rapide (quelques minutes), plus efficace que les analogues coprécipités. Ces nouveaux catalyseurs sont stables et recyclables.

Les HDL dérivés de MOF à structure tridimensionnelle leur confèrent des propriétés plus intéressantes que les LDH préparés par des méthodes conventionnelles : (i) les LDH cultivés sur des modèles poreux peuvent exposer davantage de sites actifs ; (ii) la croissance dispersée et homogène évite les problèmes d'empilement et d'agrégation des HDL en couches ; et (iii) les HDL avec une structure cœur-coquille ou creuse présentent un plus grand avantage en termes de transfert de masse. Ces caractéristiques uniques ouvrent de nouvelles portes pour le développement de nouveaux matériaux dans les domaines de l'énergie et de l'environnement. Par conséquent, en combinant les avantages des HDL, le développement de HDL dérivés de MOF pour des applications dans la décomposition de l'eau, les supercondensateurs, l'assainissement de l'environnement, les capteurs et d'autres domaines peut être poursuivi.

References

- [1] Z. Jiang, X. Xu, Y. Ma, H. S. Cho, D. Ding, C. Wang, J. Wu, P. Oleynikov, M. Jia, J. Cheng, Y. Zhou, O. Terasaki, T. Peng, L. Zan, H. Deng, Filling metal-organic framework mesopores with TiO₂ for CO₂ photoreduction, *Nature* 586(7830) (2020) 549-554.
- [2] L. Liu, Q. Xu, Q. L. Zhu, Electrically conductive Metal-Organic Frameworks for electrocatalytic applications, *Advanced Energy and Sustainability Research* 2(11) (2021) 2100100.
- [3] H. F. Wang, L. Chen, H. Pang, S. Kaskel, Q. Xu, MOF-derived electrocatalysts for oxygen reduction, oxygen evolution and hydrogen evolution reactions, *Chemical Society Reviews* 49(5) (2020) 1414-1448.
- [4] L. Li, Y. Liu, Y. Han, X. Qi, X. Li, H. Fan, L. Meng, Metal-organic framework-derived carbon coated copper sulfide nanocomposites as a battery-type electrode for electrochemical capacitors, *Materials Letters* 236 (2019) 131-134.
- [5] P. He, X. Y. Yu, X. W. Lou, Carbon-incorporated nickel-cobalt mixed metal phosphide nanoboxes with enhanced electrocatalytic activity for oxygen evolution, *Angewandte Chemie International Edition* 56(14) (2017) 3897-3900.
- [6] C. Forano, U. Costantino, V. Prévot, C.T. Gueho, Chapter 14.1-Layered Double Hydroxides (LDH), in: F. Bergaya, G. Lagaly (Eds.), *Developments in Clay Science*, Elsevier 2013, pp. 745-782.
- [7] Y. Y. Dong, D. D. Ma, X. T. Wu, Q. L. Zhu, Electron-withdrawing anion intercalation and surface sulfurization of NiFe-layered double hydroxide nanoflowers enabling superior oxygen evolution performance, *Inorganic Chemistry Frontiers* 7(1) (2020) 270-276.
- [8] M. Zubair, I. Ihsanullah, H. Abdul Aziz, M. Azmier Ahmad, M. A. Al-Harhi, Sustainable wastewater treatment by biochar/layered double hydroxide composites: Progress, challenges, and outlook, *Bioresource Technology* 319 (2021) 124128.
- [9] K. Shen, X.D. Chen, J.Y. Chen, Y.W. Li, Development of MOF-derived carbon-based nanomaterials for efficient catalysis, *ACS Catalysis* 6(9) (2016) 5887-5903.
- [10] Z. Jiang, J. Li, D. Jiang, Y. Gao, Y. Chen, W. Wang, B. Cao, Y. Tao, L. Wang, Y. Zhang, Removal of atrazine by biochar-supported zero-valent iron catalyzed persulfate oxidation: reactivity, radical production and transformation pathway, *Environmental Research* 184 (2020) 109260.
- [11] R. P. Schwarzenbach, B. I. Escher, K. Fenner, T. B. Hofstetter, C.A. Johnson, U. von Gunten, B. Wehrli, The challenge of micropollutants in aquatic systems, *Science* 313(5790) (2006) 1072-1077.
- [12] M. Usman, A. Ahmed, B. Yu, Q. Peng, Y. Shen, H. Cong, A review of different synthetic

- approaches of amorphous intrinsic microporous polymers and their potential applications in membrane-based gases separation, *European Polymer Journal* 120 (2019) 109262.
- [13] M. Usman, L. He, Y. F. Wang, B. Yu, H. L. Cong, Magnetic poly (PMMA-EGDMA) nanospheres prepared by miniemulsion polymerization, *Ferroelectrics* 529(1) (2018) 168-173.
- [14] X. Zheng, X. Huo, Y. Zhang, Q. Wang, Y. Zhang, X. Xu, Cardiovascular endothelial inflammation by chronic coexposure to lead (Pb) and polycyclic aromatic hydrocarbons from preschool children in an e-waste recycling area, *Environmental Pollution* 246 (2019) 587-596.
- [15] Q. Wang, D. O'Hare, Recent Advances in the Synthesis and application of layered double hydroxide (LDH) nanosheets, *Chemical Reviews* 112(7) (2012) 4124-4155.
- [16] F. Cavani, F. Trifiró, T. Vaccari, Hydrotalcite-type anionic clays: Preparation, properties and applications, 11 (1991) 173-301.
- [17] A. C. Bouali, M. Serdechnova, C. Blawert, J. Tedim, M. G. S. Ferreira, M. L. Zheludkevich, Layered double hydroxides (LDHs) as functional materials for the corrosion protection of aluminum alloys: A review, *Applied Materials Today* 21 (2020) 100857.
- [18] K. Fan, P. Xu, Z. Li, M. Shao, X. Duan, Layered double hydroxides: next promising materials for energy storage and conversion, *Next Materials* 1(4) (2023) 100040.
- [19] R. Allmann, The crystal structure of pyroaurite, *Acta Crystallographica Section B* 24(7) (1968) 972-977.
- [20] H.F.W. Taylor, Crystal structures of some double hydroxide minerals, *Mineralogical Magazine* 39(304) (1973) 377-389.
- [21] Y. Chen, S. Zhang, X. Han, X. Zhang, M. Yi, S. Yang, D. Yu, W. Liu, Catalytic dechlorination and charring reaction of polyvinyl chloride by CuAl layered double hydroxide, *Energy & Fuels* 32(2) (2018) 2407-2413.
- [22] A. Tyagi, M.C. Joshi, A. Shah, V.K. Thakur, R.K. Gupta, Hydrothermally tailored three-Dimensional Ni-V layered double hydroxide nanosheets as high-performance hybrid supercapacitor applications, *ACS Omega* 4(2) (2019) 3257-3267.
- [23] C. Li, M. Wei, D.G. Evans, X. Duan, Layered double hydroxide-based nanomaterials as highly efficient catalysts and adsorbents, *Small* 10(22) (2014) 4469-4486.
- [24] G. Zhang, X. Zhang, Y. Meng, G. Pan, Z. Ni, S. Xia, Layered double hydroxides-based photocatalysts and visible-light driven photodegradation of organic pollutants: A review, *Chemical Engineering Journal* 392 (2020) 123684.
- [25] A. Malak-Polaczyk, C. Vix-Guterl, E. Frackowiak, Carbon/layered double hydroxide (LDH) composites for supercapacitor application, *Energy & Fuels* 24(6) (2010) 3346-3351.

- [26] M. Daud, A. Hai, F. Banat, M.B. Wazir, M. Habib, G. Bharath, M.A. Al-Harhi, A review on the recent advances, challenges and future aspect of layered double hydroxides (LDH) - containing hybrids as promising adsorbents for dyes removal, *Journal of Molecular Liquids* 288 (2019) 110989.
- [27] V.K. Ameena Shirin, R. Sankar, A.P. Johnson, H.V. Gangadharappa, K. Pramod, Advanced drug delivery applications of layered double hydroxide, *Journal of Controlled Release* 330 (2021) 398-426.
- [28] Y. Gao, J. Wu, Q. Wang, C.A. Wilkie, D. O'Hare, Flame retardant polymer/layered double hydroxide nanocomposites, *Journal of Materials Chemistry A* 2(29) (2014) 10996-11016.
- [29] G. Fan, F. Li, D.G. Evans, X. Duan, Catalytic applications of layered double hydroxides: recent advances and perspectives, *Chemical Society Reviews* 43(20) (2014) 7040-7066.
- [30] P.J. Sideris, U.G. Nielsen, Z. Gan, C.P. Grey, Mg/Al ordering in layered double hydroxides revealed by multinuclear NMR spectroscopy, *Science* 321(5885) (2008) 113-117.
- [31] G.R. Williams, A.I. Khan, D. O'Hare, Mechanistic and kinetic studies of guest ion intercalation into layered double hydroxides using time-resolved, in-situ X-ray powder diffraction, in: X. Duan, D.G. Evans (Eds.), *layered double hydroxides*, Springer Berlin Heidelberg, Berlin, Heidelberg, 2006, pp. 161-192.
- [32] V. Prévot, C. Forano, J.P. Besse, Hybrid derivatives of layered double hydroxides, *Applied Clay Science* 18(1) (2001) 3-15.
- [33] S. Zhao, J. Xu, M. Wei, Y. F. Song, Synergistic catalysis by polyoxometalate-intercalated layered double hydroxides: oximation of aromatic aldehydes with large enhancement of selectivity, *Green Chemistry* 13(2) (2011) 384-389.
- [34] T. Li, H. N. Miras, Y. F. Song, Polyoxometalate (POM)-layered double hydroxides (LDH) composite materials: design and catalytic applications, *Catalysts*, 2017.
- [35] Z. P. Xu, P.S. Braterman, Synthesis, structure and morphology of organic layered double hydroxide (LDH) hybrids: comparison between aliphatic anions and their oxygenated analogs, *Applied Clay Science* 48(1) (2010) 235-242.
- [36] H. Yan, X.-J. Zhao, Y. Q. Zhu, M. Wei, D.G. Evans, X. Duan, The periodic table as a guide to the construction and properties of layered double hydroxides, in: D.M.P. Mingos (Ed.), *the periodic table II: catalytic, materials, biological and medical applications*, Springer International Publishing, Cham, 2019, pp. 89-120.
- [37] M. Oliver-Tolentino, J. Vazquez-Samperio, M. Tufiño-Velázquez, J. Flores-Moreno, L. Lartundo-Rojas, R. de G. Gonzalez-Huerta, Bifunctional electrocatalysts for oxygen reduction/evolution reactions derived from NiCoFe LDH materials, *Journal of Applied Electrochemistry* 48(8) (2018) 947-957.
- [38] M. Zhang, Y. Liu, B. Liu, Z. Chen, H. Xu, K. Yan, Trimetallic NiCoFe-layered double hydroxides nanosheets efficient for oxygen evolution and highly selective oxidation of

- biomass-derived 5-hydroxymethylfurfural, *ACS Catalysis* 10(9) (2020) 5179-5189.
- [39] J. Liang, Y. Wei, Y. Yao, X. Zheng, J. Shen, G. He, H. Chen, Constructing high-efficiency photocatalyst for degrading ciprofloxacin: three-dimensional visible light driven graphene based NiAlFe LDH, *Journal of Colloid and Interface Science* 540 (2019) 237-246.
- [40] S. Abelló, S. Mitchell, M. Santiago, G. Stoica, J. Pérez-Ramírez, Perturbing the properties of layered double hydroxides by continuous coprecipitation with short residence time, *Journal of Materials Chemistry* 20(28) (2010) 5878-5887.
- [41] K. Rozoy, U. Berner, C. Taviot-Gueho, F. Leroux, G. Renaudin, D. Kulik, L.W. Diamond, synthesis and characterization of the LDH hydrotalcite-pyroaurite solid-solution series, *Cement and Concrete Research* 40(8) (2010) 1248-1254.
- [42] J.T. Klopogge, L. Hickey, R.L. Frost, The effects of synthesis pH and hydrothermal treatment on the formation of zinc aluminum hydrotalcites, *Journal of Solid State Chemistry* 177(11) (2004) 4047-4057.
- [43] M.J. Williams, E. Sánchez, E.R. Aluri, F.J. Douglas, D.A. MacLaren, O.M. Collins, E.J. Cussen, J.D. Budge, L.C. Sanders, M. Michaelis, C.M. Smales, J. Cinatl, S. Lorrio, D. Krueger, R.T.M. de Rosales, S.A. Corr, Microwave-assisted synthesis of highly crystalline, multifunctional iron oxide nanocomposites for imaging applications, *RSC Advances* 6(87) (2016) 83520-83528.
- [44] G. Fetter, G. Heredia, A.M. Maubert, P. Bosch, Synthesis of Al-intercalated montmorillonites using microwave irradiation, *Journal of Materials Chemistry* 6(11) (1996) 1857-1858.
- [45] H.S. Ku, E. Siores, A. Taube, J.A.R. Ball, Productivity improvement through the use of industrial microwave technologies, *Computers & Industrial Engineering* 42(2) (2002) 281-290.
- [46] S. Kannan, R. Vir Jasra, Microwave assisted rapid crystallization of Mg–M(III) hydrotalcite where M(III) = Al, Fe or Cr, *Journal of Materials Chemistry* 10(10) (2000) 2311-2314.
- [47] M. Pokhriyal, D.K. Yadav, S. Pal, S. Uma, R. Nagarajan, Rapid and one-step transformation of LiAlH₄ to inorganic and organic anion intercalated Li-Al layered double hydroxides, *European Journal of Inorganic Chemistry* 2019(19) (2019) 2412-2418.
- [48] D.K. Yadav, S. Uma, R. Nagarajan, Microwave-assisted synthesis of ternary Li-M-Al LDHs (M = Mg, Co, Ni, Cu, Zn, and Cd) and examining their use in phenol oxidation, *Applied Clay Science* 228 (2022) 106655.
- [49] Y. Zhou, J. Li, Y. Yang, B. Luo, X. Zhang, E. Fong, W. Chu, K. Huang, Unique 3D flower-on-sheet nanostructure of NiCo LDHs: Controllable microwave-assisted synthesis and its application for advanced supercapacitors, *Journal of Alloys and Compounds* 788 (2019) 1029-1036.

- [50] P. Yang, J. Yu, Z. Wang, Q. Liu, T. Wu, Urea method for the synthesis of hydrotalcites, *Reaction Kinetics and Catalysis Letters* 83(2) (2004) 275-282.
- [51] S. Park, D. Kwon, J.Y. Kang, J.C. Jung, Influence of the preparation method on the catalytic activity of MgAl hydrotalcites as solid base catalysts, *Green Energy & Environment* 4(3) (2019) 287-292.
- [52] N. Thomas, Mechanochemical synthesis of layered hydroxy salts, *Materials Research Bulletin* 47(11) (2012) 3568-3572.
- [53] A. Inayat, M. Klumpp, W. Schwieger, The urea method for the direct synthesis of ZnAl layered double hydroxides with nitrate as the interlayer anion, *Applied Clay Science* 51(4) (2011) 452-459.
- [54] L. Bian, W. Wang, R. Xia, Z. Li, Ni-based catalyst derived from Ni/Al hydrotalcite-like compounds by the urea hydrolysis method for CO methanation, *RSC Advances* 6(1) (2016) 677-686.
- [55] S. Naseem, B. Gevers, R. Boldt, F.J.W.J. Labuschagné, A. Leuteritz, Comparison of transition metal (Fe, Co, Ni, Cu, and Zn) containing tri-metal layered double hydroxides (LDHs) prepared by urea hydrolysis, *RSC Advances* 9(6) (2019) 3030-3040.
- [56] P. Benito, M. Herrero, C. Barriga, F.M. Labajos, V. Rives, Microwave-assisted homogeneous precipitation of hydrotalcites by urea hydrolysis, *Inorganic Chemistry* 47(12) (2008) 5453-5463.
- [57] S.K. Sharma, P.K. Kushwaha, V.K. Srivastava, S.D. Bhatt, R.V. Jasra, Effect of hydrothermal conditions on structural and textural properties of synthetic hydrotalcites of varying Mg/Al ratio, *Industrial & Engineering Chemistry Research* 46(14) (2007) 4856-4865.
- [58] H.J. Jang, C.H. Lee, S. Kim, S.H. Kim, K.B. Lee, Hydrothermal synthesis of K₂CO₃-promoted hydrotalcite from hydroxide-form precursors for novel high-temperature CO₂ sorbent, *ACS Applied Materials & Interfaces* 6(9) (2014) 6914-6919.
- [59] H. Yi, S. Liu, C. Lai, G. Zeng, M. Li, X. Liu, B. Li, X. Huo, L. Qin, L. Li, M. Zhang, Y. Fu, Z. An, L. Chen, Recent advance of transition-metal-based layered double hydroxide nanosheets: synthesis, properties, modification, and electrocatalytic applications, *Advanced Energy Materials* 11(14) (2021) 2002863.
- [60] Y. You, G.F. Vance, H. Zhao, Selenium adsorption on Mg-Al and Zn-Al layered double hydroxides, *Applied Clay Science* 20(1) (2001) 13-25.
- [61] H.-M. Liu, X.-J. Zhao, Y.-Q. Zhu, H. Yan, DFT study on MgAl-layered double hydroxides with different interlayer anions: structure, anion exchange, host-guest interaction and basic sites, *Physical Chemistry Chemical Physics* 22(4) (2020) 2521-2529.
- [62] Q. Pan, F. Zheng, D. Deng, B. Chen, Y. Wang, Interlayer spacing regulation of NiCo-LDH nanosheets with ultrahigh specific capacity for battery-type supercapacitors, *ACS Applied*

- Materials & Interfaces 13(47) (2021) 56692-56703.
- [63] S. Han, W. Hou, C. Zhaag, D. Sun, X. Huang, C. Wang, Structure and the point of zero charge of magnesium aluminum hydroxide, *Journal of the Chemical Society - Faraday Transactions* 94(7) (1998) 915-918.
- [64] M. Laipan, Q. Chen, Z. Wang, M. Zhang, M. Yuan, R. Zhu, L. Sun, Interlayer anions of layered double hydroxides as mobile active sites to improve the adsorptive performance toward Cd²⁺, *Inorganic Chemistry* 62(34) (2023) 13857-13866.
- [65] J. Ding, L. Li, Y. Wang, H. Li, M. Yang, G. Li, Topological transformation of LDH nanosheets to highly dispersed PtNiFe nanoalloys enhancing CO oxidation performance, *Nanoscale* 12(27) (2020) 14882-14894.
- [66] W. Lv, Q. Mei, M. Du, J. Xiao, W. Ye, Q. Zheng, Interaction between poly (vinyl alcohol) and layered double hydroxide (LDH) particles with different topological shape and their application in electrospinning, *The Journal of Physical Chemistry C* 120(26) (2016) 14435-14443.
- [67] Z. Gao, K. Sasaki, X. Qiu, Structural memory effect of Mg-Al and Zn-Al layered double hydroxides in the presence of different natural humic acids: process and mechanism, *Langmuir* 34(19) (2018) 5386-5395.
- [68] S.R. Batten, N.R. Champness, X.-M. Chen, J. Garcia-Martinez, S. Kitagawa, L. Öhrström, M. O'Keeffe, M. Paik Suh, J. Reedijk, Terminology of metal-organic frameworks and coordination polymers (IUPAC Recommendations 2013), 85(8) (2013) 1715-1724.
- [69] H. Furukawa, K.E. Cordova, M. O'Keeffe, O.M. Yaghi, The chemistry and applications of Metal-Organic Frameworks, *Science* 341(6149) (2013) 1230444.
- [70] O.M. Yaghi, M. O'Keeffe, N.W. Ockwig, H.K. Chae, M. Eddaoudi, J. Kim, Reticular synthesis and the design of new materials, *Nature* 423(6941) (2003) 705-714.
- [71] S. Kitagawa, R. Kitaura, S.-i. Noro, Functional porous coordination polymers, *Angewandte Chemie International Edition* 43(18) (2004) 2334-2375.
- [72] Z. Wang, S.M. Cohen, Postsynthetic modification of metal-organic frameworks, *Chemical Society Reviews* 38(5) (2009) 1315-1329.
- [73] B.F. Hoskins, R. Robson, Design and construction of a new class of scaffolding-like materials comprising infinite polymeric frameworks of 3D-linked molecular rods. A reappraisal of the zinc cyanide and cadmium cyanide structures and the synthesis and structure of the diamond-related frameworks [N(CH₃)₄] [CuIZnII(CN)₄] and CuI [4,4',4'',4'''-tetracyanotetraphenylmethane] BF₄ · x C₆H₅NO₂, *Journal of the American Chemical Society* 112(4) (1990) 1546-1554.
- [74] G.B. Gardner, D. Venkataraman, J.S. Moore, S. Lee, Spontaneous assembly of a hinged coordination network, *Nature* 374(6525) (1995) 792-795.
- [75] O.M. Yaghi, H. Li, Hydrothermal synthesis of a Metal-Organic Framework containing

- large rectangular channels, *Journal of the American Chemical Society* 117(41) (1995) 10401-10402.
- [76] Megumu, Munakata, Takayoshi, Kuroda-Sowa, Masahiko, Maekawa, Akihiro, Hirota, Susumu, K. J. I. Chemistry, Building of 2D sheet of tetrakis (methylthio) tetrathiafulvalenes coordinating to copper (I) halides with Zigzag and helical frames and the 3D network through the S.cntdot. .cntdot. .cntdot.S Contacts, (10) (1995) 34.
- [77] D. Riou, O. Roubeau, G. Férey, Composite microporous compounds. Part I: Synthesis and structure determination of two new vanadium alkylidiphosphonates (MIL-2 and MIL-3) with three-dimensional open frameworks, *Microporous and Mesoporous Materials* 23(1) (1998) 23-31.
- [78] S.R. Batten, N.R. Champness, X.-M. Chen, J. Garcia-Martinez, S. Kitagawa, L. Öhrström, M. O'Keeffe, M.P. Suh, J. Reedijk, Coordination polymers, metal-organic frameworks and the need for terminology guidelines, *CrystEngComm* 14(9) (2012) 3001-3004.
- [79] M. Kondo, T. Yoshitomi, H. Matsuzaka, S. Kitagawa, K. Seki, Three-dimensional framework with channeling cavities for small molecules: $\{[M_2(4, 4'\text{-bpy})_3(\text{NO}_3)_4] \cdot x\text{H}_2\text{O}\}_n$ (M = Co, Ni, Zn), *Angewandte Chemie International Edition in English* 36(16) (1997) 1725-1727.
- [80] H. Li, M. Eddaoudi, M. O'Keeffe, O.M. Yaghi, Design and synthesis of an exceptionally stable and highly porous metal-organic framework, *Nature* 402(6759) (1999) 276-279.
- [81] P. Tong, J. Liang, X. Jiang, J. Li, Research progress on metal-organic framework composites in chemical sensors, *Critical Reviews in Analytical Chemistry* 50(4) (2020) 376-392.
- [82] V.F. Yusuf, N.I. Malek, S.K. Kailasa, Review on metal-organic framework classification, synthetic approaches, and influencing factors: applications in energy, drug delivery, and wastewater treatment, *ACS Omega* 7(49) (2022) 44507-44531.
- [83] R. Haldar, T.K. Maji, Metal-organic frameworks (MOFs) based on mixed linker systems: structural diversities towards functional materials, *CrystEngComm* 15(45) (2013) 9276-9295.
- [84] S. Kitagawa, K. Uemura, Dynamic porous properties of coordination polymers inspired by hydrogen bonds, *Chemical Society Reviews* 34(2) (2005) 109-119.
- [85] H. Kanoh, A. Kondo, H. Noguchi, H. Kajiro, A. Tohdoh, Y. Hattori, W. C. Xu, M. Inoue, T. Sugiura, K. Morita, H. Tanaka, T. Ohba, K. Kaneko, Elastic layer-structured metal organic frameworks (ELMs), *Journal of Colloid and Interface Science* 334(1) (2009) 1-7.
- [86] S. Vagin, A.K. Ott, B. Rieger, Paddle-wheel zinc carboxylate clusters as building units for metal-organic frameworks, *Chemie Ingenieur Technik* 79(6) (2007) 767-780.
- [87] G. Férey, Metal-organic frameworks: the young child of the porous solids family, *Studies in Surface Science and Catalysis*, 170(8) (2007), 66-84.

- [88] W. Lu, Z. Wei, Z.-Y. Gu, T.-F. Liu, J. Park, J. Park, J. Tian, M. Zhang, Q. Zhang, T. Gentle iiii, M. Bosch, H.-C. Zhou, Tuning the structure and function of metal-organic frameworks via linker design, *Chemical Society Reviews* 43(16) (2014) 5561-5593.
- [89] H. Deng, S. Grunder, K.E. Cordova, C. Valente, H. Furukawa, M. Hmadeh, F. Gándara, A.C. Whalley, Z. Liu, S. Asahina, H. Kazumori, M. O’Keeffe, O. Terasaki, J.F. Stoddart, O.M. Yaghi, Large-pore apertures in a series of metal-organic frameworks, *Science* 336(6084) (2012) 1018-1023.
- [90] T. Tsuruoka, S. Furukawa, Y. Takashima, K. Yoshida, S. Isoda, S. Kitagawa, Nanoporous nanorods fabricated by coordination modulation and oriented attachment growth, *Angewandte Chemie International Edition* 48(26) (2009) 4739-4743.
- [91] H. Guo, Y. Zhu, S. Qiu, J.A. Lercher, H. Zhang, Coordination modulation induced synthesis of nanoscale Eu^{1-x}Tbx-Metal-Organic Frameworks for luminescent thin films, *Advanced Materials* 22(37) (2010) 4190-4192.
- [92] J. Łuczak, M. Kroczevska, M. Baluk, J. Sowik, P. Mazierski, A. Zaleska-Medynska, Morphology control through the synthesis of metal-organic frameworks, *Advances in Colloid and Interface Science* 314 (2023) 102864.
- [93] F. Wang, H. Guo, Y. Chai, Y. Li, C. Liu, The controlled regulation of morphology and size of HKUST-1 by “coordination modulation method”, *Microporous and Mesoporous Materials* 173 (2013) 181-188.
- [94] G.-P. Yang, L. Hou, L. F. Ma, Y. Y. Wang, Investigation on the prime factors influencing the formation of entangled metal-organic frameworks, *CrystEngComm* 15(14) (2013) 2561-2578.
- [95] K. Shen, M. Zhang, H. Zheng, Critical factors influencing the structures and properties of metal-organic frameworks, *CrystEngComm* 17(5) (2015) 981-991.
- [96] Z. Pan, H. Zheng, T. Wang, Y. Song, Y. Li, Z. Guo, S.R. Batten, Hydrothermal synthesis, structures, and physical properties of four new flexible multicarboxylate ligands-based compounds, *Inorganic Chemistry* 47(20) (2008) 9528-9536.
- [97] C. Zhang, M. Zhang, L. Qin, H. Zheng, Crystal structures and spectroscopic properties of metal-organic frameworks based on rigid ligands with flexible functional groups, *Crystal Growth & Design* 14(2) (2014) 491-499.
- [98] M. Schlesinger, S. Schulze, M. Hietschold, M. Mehring, Evaluation of synthetic methods for microporous metal-organic frameworks exemplified by the competitive formation of [Cu₂(btc)₃(H₂O)₃] and [Cu₂(btc)(OH)(H₂O)], *Microporous and Mesoporous Materials* 132(1) (2010) 121-127.
- [99] P. P. Liu, A. L. Cheng, Q. Yue, N. Liu, W. W. Sun, E. Q. Gao, Cobalt (II) coordination networks dependent upon the spacer length of flexible bis(tetrazole) ligands, *Crystal Growth & Design* 8(5) (2008) 1668-1674.

- [100] R. Seetharaj, P.V. Vandana, P. Arya, S. Mathew, Dependence of solvents, pH, molar ratio and temperature in tuning metal organic framework architecture, *Arabian Journal of Chemistry* 12(3) (2019) 295-315.
- [101] C. Volkringer, T. Loiseau, N. Guillou, G. Férey, M. Haouas, F. Taulelle, E. Elkaim, N. Stock, High-throughput aided synthesis of the porous metal-organic framework-type aluminum pyromellitate, MIL-121, with extra carboxylic acid functionalization, *Inorganic Chemistry* 49(21) (2010) 9852-9862.
- [102] F. Yuan, J. Xie, H. M. Hu, C. M. Yuan, B. Xu, M. L. Yang, F.-X. Dong, G. L. Xue, Effect of pH/metal ion on the structure of metal-organic frameworks based on novel bifunctionalized ligand 4'-carboxy-4, 2':6',4''-terpyridine, *CrystEngComm* 15(7) (2013) 1460-1467.
- [103] K. Akhbari, A. Morsali, Effect of the guest solvent molecules on preparation of different morphologies of ZnO nanomaterials from the $[Zn_2(1,4\text{-bdc})_2(\text{dabco})]$ metal-organic framework, *Journal of Coordination Chemistry* 64(20) 3521-3530.
- [104] S. Soni, P.K. Bajpai, C.J.C. Arora, A.o. Nanomaterials, A review on metal-organic framework: synthesis, properties and application, 2(2) (2018).
- [105] D. Banerjee, J. Finkelstein, A. Smirnov, P.M. Forster, L.A. Borkowski, S.J. Teat, J.B. Parise, Synthesis and structural characterization of magnesium based coordination networks in different solvents, *Crystal Growth & Design* 11(6) (2011) 2572-2579.
- [106] C. C. Wang, H. P. Jing, P. Wang, S. J. Gao, Series metal-organic frameworks constructed from 1, 10-phenanthroline and 3, 3', 4, 4'-biphenyltetracarboxylic acid: Hydrothermal synthesis, luminescence and photocatalytic properties, *Journal of Molecular Structure* 1080 (2015) 44-51.
- [107] M.C. Bernini, E.V. Brusau, G.E. Narda, G.E. Echeverria, C.G. Pozzi, G. Punte, C.W. Lehmann, The effect of hydrothermal and non-hydrothermal synthesis on the formation of holmium (III) succinate hydrate frameworks, *European Journal of Inorganic Chemistry* 2007(5) (2007) 684-693.
- [108] A.T. Çolak, G. Pamuk, O.Z. Yeşilel, F. Yüksel, Hydrothermal synthesis and structural characterization of Zn (II) and Cd (II)-pyridine-2, 3-dicarboxylate 2D coordination polymers, $\{(NH_4)_2[M(\mu\text{-pydc})_2]\cdot 2H_2O\}_n$, *Solid State Sciences* 13(12) (2011) 2100-2104.
- [109] F.A. Almeida Paz, J. Klinowski, Hydrothermal synthesis and structural characterization of a novel cadmium-organic framework, *Journal of Solid State Chemistry* 177(10) (2004) 3423-3432.
- [110] S. Natarajan, S. Manual, P. Mahata, V.K. Rao, P. Ramaswamy, A. Banerjee, A.K. Paul, K.V. Ramya, The use of hydrothermal methods in the synthesis of novel open-framework materials, *Journal of Chemical Sciences* 118(6) (2006) 525-536.
- [111] G. Férey, C. Mellot-Draznieks, C. Serre, F. Millange, J. Dutour, S. Surblé, I. Margiolaki,

- A chromium terephthalate-based solid with unusually large pore volumes and surface area, *Science* 309(5743) (2005) 2040-2042.
- [112] Y. Pan, D. Heryadi, F. Zhou, L. Zhao, G. Lestari, H. Su, Z. Lai, Tuning the crystal morphology and size of zeolitic imidazolate framework-8 in aqueous solution by surfactants, *CrystEngComm* 13(23) (2011) 6937-6940.
- [113] P. Horcajada, T. Chalati, C. Serre, B. Gillet, C. Sebrie, T. Baati, J.F. Eubank, D. Heurtaux, P. Clayette, C. Kreuz, J.-S. Chang, Y.K. Hwang, V. Marsaud, P.-N. Bories, L. Cynober, S. Gil, G. Férey, P. Couvreur, R. Gref, Porous metal-organic-framework nanoscale carriers as a potential platform for drug delivery and imaging, *Nature Materials* 9(2) (2010) 172-178.
- [114] Sung, Hwa, Jhung, Jin-Ho, Lee, Jong-San, C.J.B.o.t.K.C. Society, Microwave synthesis of a nanoporous hybrid material, Chromium Trimesate, (2005).
- [115] T. Chalati, P. Horcajada, R. Gref, P. Couvreur, C.J.J.o.M.C. Serre, Optimisation of the synthesis of MOF nanoparticles made of flexible porous iron fumarate MIL-88A, 21 (2011).
- [116] E. Haque, N.A. Khan, J.H. Park, S.H.J.C.-A.E.J. Jhung, Synthesis of a metal-organic framework material, iron terephthalate, by ultrasound, microwave, and conventional electric heating: a kinetic study, 16 (2010).
- [117] T. Ahnfeldt, J. Moellmer, V. Guillerm, R. Staudt, C. Serre, N. Stock, High-throughput and time-resolved energy-dispersive X-ray diffraction (EDXRD) study of the formation of CAU-1-(OH)₂: microwave and conventional heating, *Chemistry-A European Journal* 17(23) (2011) 6462-6468.
- [118] X.U. Li-Hong, Z. Dong-Yu, L.I. Yang, G.J.A.P.-C.S. Lin, Improvement of the electro-optical properties of nematic liquid crystals by doping with ZIF-8 Materials, *Acta Physico-Chimica Sinica* 32(9) (2016) 2377-2382.
- [119] H. Bux, F. Liang, Y. Li, J. Cravillon, M. Wiebcke, J. Caro, Zeolitic imidazolate framework membrane with molecular sieving properties by microwave-assisted solvothermal synthesis, *Journal of the American Chemical Society* 131(44) (2009) 16000-16001.
- [120] N. Stock, S. Biswas, Synthesis of Metal-Organic Frameworks (MOFs): routes to various MOF topologies, morphologies, and composites, *Chemical Reviews* 112(2) (2012) 933-969.
- [121] M.K. Beyer, H. Clausen-Schaumann, Mechanochemistry: The mechanical activation of covalent bonds, *Chemical Reviews* 105(8) (2005) 2921-2948.
- [122] J.H. Bang, K.S. Suslick, Applications of ultrasound to the synthesis of nanostructured materials, *Advanced Materials* 22(10) (2010) 1039-1059.
- [123] M. Eddaoudi, J. Kim, N. Rosi, D. Vodak, J. Wachter, M. O'Keeffe, O.M. Yaghi,

- Systematic design of pore size and functionality in isorecticular MOFs and their application in methane storage, *Science* 295(5554) (2002) 469-472.
- [124] H.R. Abid, H. Tian, H.-M. Ang, M.O. Tade, C.E. Buckley, S. Wang, Nanosize Zr-metal organic framework (UiO-66) for hydrogen and carbon dioxide storage, *Chemical Engineering Journal* 187 (2012) 415-420.
- [125] A.R. Millward, O.M. Yaghi, Metal-Organic frameworks with exceptionally high capacity for storage of carbon dioxide at room temperature, *Journal of the American Chemical Society* 127(51) (2005) 17998-17999.
- [126] J. Kim, W.Y. Kim, W.-S. Ahn, Amine-functionalized MIL-53 (Al) for CO₂/N₂ separation: effect of textural properties, *Fuel* 102 (2012) 574-579.
- [127] S.S.Y. Chui, S.M.F. Lo, J.P.H. Charmant, A.G. Orpen, I.D. Williams, A chemically functionalizable nanoporous material [Cu₃(TMA)₂(H₂O)₃]_n, *Science* 283(5405) (1999) 1148-1150.
- [128] P. Horcajada, S. Surblé, C. Serre, D.-Y. Hong, Y.-K. Seo, J.-S. Chang, J.-M. Grenèche, I. Margiolaki, G. Férey, Synthesis and catalytic properties of MIL-100 (Fe), an iron (III) carboxylate with large pores, *Chemical Communications* (27) (2007) 2820-2822.
- [129] R. Banerjee, A. Phan, B. Wang, C. Knobler, H. Furukawa, M. O'Keeffe, O.M. Yaghi, High-throughput synthesis of zeolitic imidazolate frameworks and application to CO₂ capture, *Science* 319(5865) (2008) 939-943.
- [130] J.-S. Choi, W.-J. Son, J. Kim, W.-S. Ahn, Metal-organic framework MOF-5 prepared by microwave heating: Factors to be considered, *Microporous and Mesoporous Materials* 116(1) (2008) 727-731.
- [131] S.H. Jung, J.H. Lee, J.W. Yoon, C. Serre, G. Férey, J.S. Chang, Microwave synthesis of chromium terephthalate MIL-101 and its benzene sorption ability, *Advanced Materials* 19(1) (2007) 121-124.
- [132] P. Horcajada, C. Serre, M. Vallet-Regí, M. Sebban, F. Taulelle, G. Férey, Metal-Organic frameworks as efficient materials for drug delivery, *Angewandte Chemie International Edition* 45(36) (2006) 5974-5978.
- [133] K. M. L. Taylor Pashow, J. Della Rocca, Z. Xie, S. Tran, W. Lin, Postsynthetic modifications of iron-carboxylate nanoscale metal-organic frameworks for imaging and drug delivery, *Journal of the American Chemical Society* 131(40) (2009) 14261-14263.
- [134] Z. Ni, R. I. Masel, Rapid production of metal-organic frameworks via microwave-assisted solvothermal synthesis, *Journal of the American Chemical Society* 128(38) (2006) 12394-12395.
- [135] H. Y. Cho, D. A. Yang, J. Kim, S. Y. Jeong, W. S. Ahn, CO₂ adsorption and catalytic application of Co-MOF-74 synthesized by microwave heating, *Catalysis Today* 185(1) (2012) 35-40.

- [136] Y. K. Seo, G. Hundal, I. T. Jang, Y. K. Hwang, C. H. Jun, J. S. Chang, Microwave synthesis of hybrid inorganic-organic materials including porous $\text{Cu}_3(\text{BTC})_2$ from Cu (II)-trimesate mixture, *Microporous and Mesoporous Materials* 119(1) (2009) 331-337.
- [137] Z. Lai, Development of ZIF-8 membranes: opportunities and challenges for commercial applications, *Current Opinion in Chemical Engineering* 20 (2018) 78-85.
- [138] W. J. Son, J. Kim, J. Kim, W.-S. Ahn, Sonochemical synthesis of MOF-5, *Chemical Communications* (47) (2008) 6336-6338.
- [139] D. A. Yang, H. Y. Cho, J. Kim, S. T. Yang, W. S. Ahn, CO_2 capture and conversion using Mg-MOF-74 prepared by a sonochemical method, *Energy & Environmental Science* 5(4) (2012) 6465-6473.
- [140] Z. Q. Li, L. G. Qiu, T. Xu, Y. Wu, W. Wang, Z. Y. Wu, X. Jiang, Ultrasonic synthesis of the microporous metal-organic framework $\text{Cu}_3(\text{BTC})_2$ at ambient temperature and pressure: An efficient and environmentally friendly method, *Materials Letters* 63(1) (2009) 78-80.
- [141] J. Kim, S. T. Yang, S. B. Choi, J. Sim, J. Kim, W. S. Ahn, Control of catenation in CuTATB-n metal-organic frameworks by sonochemical synthesis and its effect on CO_2 adsorption, *Journal of Materials Chemistry* 21(9) (2011) 3070-3076.
- [142] H. Y. Cho, J. Kim, S. N. Kim, W. S. Ahn, High yield 1 L scale synthesis of ZIF-8 via a sonochemical route, *Microporous and Mesoporous Materials* 169 (2013) 180-184.
- [143] A. Martinez Joaristi, J. Juan-Alcañiz, P. Serra-Crespo, F. Kapteijn, J. Gascon, Electrochemical synthesis of some archetypical Zn^{2+} , Cu^{2+} , and Al^{3+} metal organic frameworks, *Crystal Growth & Design* 12(7) (2012) 3489-3498.
- [144] U. Mueller, M. Schubert, F. Teich, H. Puetter, K. Schierle-Arndt, J. Pastré, Metal-organic frameworks prospective industrial applications, *Journal of Materials Chemistry* 16(7) (2006) 626-636.
- [145] A. Pichon, S.L. James, An array-based study of reactivity under solvent-free mechanochemical conditions insights and trends, *CrystEngComm* 10(12) (2008) 1839-1847.
- [146] P. J. Beldon, D. L. Fábíán, R.S. Stein, A. Thirumurugan, A. K. Cheetham, Rapid room-temperature synthesis of zeolitic imidazolate frameworks by using mechanochemistry, *Portal Komunikacji Naukowej* 49(50) (2010) 9640-9643.
- [147] K.S. Park, Z. Ni, A.P. Côté, J.Y. Choi, R. Huang, F.J. Uribe-Romo, H.K. Chae, M. O'Keeffe, O.M. Yaghi, Exceptional chemical and thermal stability of zeolitic imidazolate frameworks, *Proceedings of the National Academy of Sciences of the United States of America* 103(27) (2006) 10186-10191.
- [148] J.H. Cavka, S. Jakobsen, U. Olsbye, N. Guillou, C. Lamberti, S. Bordiga, K.P. Lillerud, A new zirconium inorganic building brick forming metal organic frameworks with

- exceptional stability, *Journal of the American Chemical Society* 130(42) (2008) 13850-13851.
- [149] T. Loiseau, C. Serre, C. Huguenard, G. Fink, F. Taulelle, M. Henry, T. Bataille, G. Férey, A rationale for the large breathing of the porous aluminum terephthalate (MIL-53) upon hydration, *Chemistry - A European Journal* 10(6) (2004) 1373-1382.
- [150] V. Colombo, S. Galli, H.J. Choi, G.D. Han, A. Maspero, G. Palmisano, N. Masciocchi, J.R. Long, High thermal and chemical stability in pyrazolate-bridged metal-organic frameworks with exposed metal sites, *Chemical Science* 2(7) (2011) 1311-1319.
- [151] W. Zhang, Y. Hu, J. Ge, H.-L. Jiang, S.-H. Yu, A facile and general coating approach to moisture/water-resistant metal-organic frameworks with intact porosity, *Journal of the American Chemical Society* 136(49) (2014) 16978-16981.
- [152] X. W. Zhu, X.-P. Zhou, D. Li, Exceptionally water stable heterometallic gyroidal MOFs: tuning the porosity and hydrophobicity by doping metal ions, *Chemical Communications* 52(39) (2016) 6513-6516.
- [153] R.G. Pearson, Hard and soft acids and bases, *Journal of the American Chemical Society* 85(22) (1963) 3533-3539.
- [154] Y. Bai, Y. Dou, L. H. Xie, W. Rutledge, J. R. Li, H. C. Zhou, Zr-based metal-organic frameworks: design, synthesis, structure, and applications, *Chemical Society Reviews* 45(8) (2016) 2327-2367.
- [155] D. Feng, Z. Y. Gu, J. R. Li, H. L. Jiang, Z. Wei, H. C. Zhou, Zirconium-metalloporphyrin PCN-222: mesoporous metal-organic frameworks with ultrahigh stability as biomimetic catalysts, *Angewandte Chemie International Edition* 51(41) (2012) 10307-10310.
- [156] K. Shen, L. Zhang, X. Chen, L. Liu, D. Zhang, Y. Han, J. Chen, J. Long, R. Luque, Y. Li, B. Chen, Ordered macro-microporous metal-organic framework single crystals, *Science* 359(6372) (2018) 206-210.
- [157] Y. Liu, Z. Liu, D. Huang, M. Cheng, G. Zeng, C. Lai, C. Zhang, C. Zhou, W. Wang, D. Jiang, H. Wang, B. Shao, Metal or metal-containing nanoparticle@MOF nanocomposites as a promising type of photocatalyst, *Coordination Chemistry Reviews* 388 (2019) 63-78.
- [158] H. J. Yang, Z. Chang, Y. Qiao, H. Deng, X.W. Mu, P. He, H.S. Zhou, constructing a super-saturated electrolyte front surface for stable rechargeable aqueous zinc batteries, *Angewandte Chemie International Edition* 59(24) (2020) 9377-9381.
- [159] Y. Haldorai, S.R. Choe, Y.S. Huh, Y.-K. Han, Metal-organic framework derived nanoporous carbon/Co₃O₄ composite electrode as a sensing platform for the determination of glucose and high-performance supercapacitor, *Carbon* 127 (2018) 366-373.
- [160] J. Huo, Y. Wang, L. Yan, Y. Xue, S. Li, M. Hu, Y. Jiang, Q.-G. Zhai, In situ semi-transformation from heterometallic MOFs to Fe-Ni LDH/MOF hierarchical architectures for boosted oxygen evolution reaction, *Nanoscale* 12(27) (2020) 14514-14523.

- [161] D. Taherinia, M. Hajilo, F. Mirzaee Valadi, MIL-88A derived CoFe-layered double hydroxides with optimized composition for the enhanced electrocatalytic oxygen evolution reaction, *New Journal of Chemistry* 47(11) (2023) 5555-5563.
- [162] W. Zhang, M. Ding, X. Zhang, H. Shang, Biosynthesis-mediated Ni-Fe-Cu LDH to sulfides transformation enabling sensitive detection of endogenous hydrogen sulfide with dual-readout signals, *Analytica Chimica Acta* 1229 (2022) 340390.
- [163] J. Zhang, Z. Li, Y. Chen, S. Gao, X.W.D.J.A.C. Lou, Nickel-iron layered double hydroxide hollow polyhedrons as a superior sulfur host for Lithium-sulfur batteries, *57 34* (2018) 10944-10948.
- [164] X. Qian, W. Chen, J. Yang, S. Chen, G. Guan, MOFs-derived bifunctional Ni-Fe-Mo sulfide electrode catalysts with hollow bipyramidal structures for efficient photovoltaics and hydrogen generation, *Electrochimica Acta* 437 (2023) 141524.
- [165] H. Wei, Q. Li, B. Jin, H. Liu, Ce-doped three-dimensional Ni/Fe LDH composite as a sulfur host for Lithium & dash; Sulfur Batteries, *Nanomaterials*, 2023.
- [166] W. Shao, Q. Wang, C. Huang, D. Zhang, High valence state metal-ion doped Fe-Ni layered double hydroxides for oxygen evolution electrocatalysts and asymmetric supercapacitors, *Materials Advances* 3(3) (2022) 1816-1824.
- [167] M. Simi, B. Rezaei, S. Saeidi, K. Zarean Mousaabadi, A.A. Ensafi, Binary spindle-like cobalt-iron layered-double hydroxide as an efficient electrocatalyst for oxygen evaluation reaction, *International Journal of Hydrogen Energy* 47(50) (2022) 21344-21351.
- [168] H. Xu, C. Shan, X. Wu, M. Sun, B. Huang, Y. Tang, C.-H. Yan, Fabrication of layered double hydroxide microcapsules mediated by cerium doping in metal-organic frameworks for boosting water splitting, *Energy & Environmental Science* 13(9) (2020) 2949-2956.
- [169] D. Han, L. Hao, M. Chang, J. Dong, Y. Gao, Y. Zhang, Facile synthesis of Co-Ni layered double hydroxides nanosheets wrapped on a prism-like metal-organic framework for efficient oxygen evolution reaction, *Journal of Colloid and Interface Science* 634 (2023) 14-21.
- [170] S. Jiang, S. Li, Z. Liu, Y. Xu, Y. Zhang, L. Zhang, Y. Xu, S. Li, Y. Jiao, J. Chen, In situ hollow nanoarchitectonics of MIL-88A@Co(OH)₂ composites for supercapacitors and oxygen evolution reactions, *New Journal of Chemistry* 47(9) (2023) 4355-4363.
- [171] D. Chanda, H. Kwon, M.M. Meshesha, J.S. Gwon, M. Ju, K. Kim, B.L. Yang, Modulating interfacial electronic coupling of copper-mediated NiFe layered double hydroxide nanoprisms via structural engineering for efficient OER in wireless photovoltaic-coupled and anion exchange membrane water electrolysis, *Applied Catalysis B: Environmental* 340 (2024) 123187.
- [172] L. Zhang, B. Zhu, D. Xu, Z. Qian, P. Xie, T. Liu, J. Yu, Yolk-shell FeSe₂@CoSe₂/FeSe₂ heterojunction as anode materials for sodium-ion batteries with high rate capability and

- stability, *Journal of Materials Science & Technology* 172 (2024) 185-195.
- [173] M. Xiao, C. Zhang, P. Wang, W. Zeng, J. Zhu, Y. Li, W. Peng, Q. Liu, H. Xu, Y. Zhao, H. Li, L. Chen, J. Yu, S. Mu, Polymetallic phosphides evolved from MOF and LDH dual-precursors for robust oxygen evolution reaction in alkaline and seawater media, *Materials Today Physics* 24 (2022) 100684.
- [174] H. Wei, J. Liu, Y. Liu, L. Wang, L. Li, F. Wang, X. Ren, F. Ren, Hollow Co-Fe LDH as an effective adsorption/catalytic bifunctional sulfur host for high-performance Lithium-sulfur batteries, *Composites Communications* 28 (2021) 100973.
- [175] Q. Niu, M. Yang, D. Luan, N.W. Li, L. Yu, X.W. Lou, Construction of Ni-Co-Fe hydr(oxy)oxide@Ni-Co layered double hydroxide yolk-shelled microrods for enhanced oxygen evolution, *Angewandte Chemie International Edition* 61(49) (2022) e202213049.
- [176] Y. Li, J. H. Shi, T. Huang, G. F. Huang, W. Q. Huang, Carboxylate-mediated proton transfer promotes water oxidation on spindle-like Ce-doped FeCo hydroxide, *Applied Physics Letters* 121(17) (2022) 173901.
- [177] Z. Qian, K. Wang, K. Shi, Z. Fu, Z. Mai, X. Wang, Z. Tang, Y. Tian, Interfacial electron transfer of heterostructured MIL-88A/Ni(OH)₂ enhances the oxygen evolution reaction in alkaline solutions, *Journal of Materials Chemistry A* 8(6) (2020) 3311-3321.
- [178] S. Huang, S. Fan, L. Xie, Q. Wu, D. Kong, Y. Wang, Y.V. Lim, M. Ding, Y. Shang, S. Chen, H.Y. Yang, Promoting highly reversible sodium storage of iron sulfide hollow polyhedrons via cobalt incorporation and graphene wrapping, *Advanced Energy Materials* 9(33) (2019) 1901584.
- [179] G. Wang, D. Huang, M. Cheng, S. Chen, G. Zhang, L. Lei, Y. Chen, L. Du, R. Li, Y. Liu, Metal-organic frameworks template-directed growth of layered double hydroxides: A fantastic conversion of functional materials, *Coordination Chemistry Reviews* 460 (2022) 214467.
- [180] Z. Xiao, Y. Mei, S. Yuan, H. Mei, B. Xu, Y. Bao, L. Fan, W. Kang, F. Dai, R. Wang, L. Wang, S. Hu, D. Sun, H. C. Zhou, Controlled hydrolysis of metal-organic frameworks: hierarchical Ni/Co-layered double hydroxide microspheres for high-performance supercapacitors, *ACS Nano* 13(6) (2019) 7024-7030.
- [181] X. Yu, J. Sun, W. Zhao, S. Zhao, H. Chen, K. Tao, Y. Hu, L. Han, MOF-derived Bi₂O₃@C microrods as negative electrodes for advanced asymmetric supercapacitors, *RSC Advances* 10(24) (2020) 14107-14112.
- [182] D. Chen, X. Chen, Z. Cui, G. Li, B. Han, Q. Zhang, J. Sui, H. Dong, J. Yu, L. Yu, L. Dong, Dual-active-site hierarchical architecture containing NiFe-LDH and ZIF-derived carbon-based framework composite as efficient bifunctional oxygen electrocatalysts for durable rechargeable Zn-air batteries, *Chemical Engineering Journal* 399 (2020) 125718.
- [183] K. Ao, Q. Wei, W.A. Daoud, MOF-derived sulfide-based electrocatalyst and scaffold for

- boosted hydrogen production, *ACS Applied Materials & Interfaces* 12(30) (2020) 33595-33602.
- [184] H. Zhang, J. Xu, Y. Jin, Y. Tong, Q. Lu, F.J.C.A.E.J. Gao, Quantum effects allow the construction of two-dimensional Co_3O_4 -embedded nitrogen-doped porous carbon nanosheet arrays from bimetallic MOFs as bifunctional oxygen Electrocatalysts, *Chemistry - A European Journal* 24 (2018) 14552-14530.
- [185] Z. Xiao, Y. Bao, Z. Li, X. Huai, M. Wang, P. Liu, L. Wang, Construction of hollow cobalt-nickel phosphate nanocages through a controllable etching strategy for high supercapacitor performances, *ACS Applied Energy Materials* 2(2) (2019) 1086-1092.
- [186] Y. Feng, Q. Chen, M. Jiang, J. Yao, Tailoring the properties of UiO-66 through defect engineering: A review, *Industrial & Engineering Chemistry Research* 58(38) (2019) 17646-17659.
- [187] Z. Jiang, Z. Li, Z. Qin, H. Sun, X. Jiao, D. Chen, LDH nanocages synthesized with MOF templates and their high performance as supercapacitors, *Nanoscale* 5(23) (2013) 11770-11775.
- [188] L. Ye, J. Wang, Y. Zhang, M. Zhang, X. Jing, Y. Gong, A self-supporting electrode with in-situ partial transformation of Fe-MOF into amorphous NiFe-LDH for efficient oxygen evolution reaction, *Applied Surface Science* 556 (2021) 149781.
- [189] Q. Dong, C. Shuai, Z. Mo, R. Guo, N. Liu, G. Liu, J. Wang, W. Liu, Y. Chen, J. Liu, Y. Jiang, Q. Gao, The in situ derivation of a NiFe-LDH ultra-thin layer on Ni-BDC nanosheets as a boosted electrocatalyst for the oxygen evolution reaction, *CrystEngComm* 23(5) (2021) 1172-1180.
- [190] Y. Bao, Y. Deng, M. Wang, Z. Xiao, M. Wang, Y. Fu, Z. Guo, Y. Yang, L. Wang, A controllable top-down etching and in-situ oxidizing strategy: metal-organic frameworks derived $\alpha\text{-Co/Ni(OH)}_2\text{@Co}_3\text{O}_4$ hollow nanocages for enhanced supercapacitor performance, *Applied Surface Science* 504 (2020) 144395.
- [191] H. Hu, B. Guan, B. Xia, X.W. Lou, Designed Formation of $\text{Co}_3\text{O}_4/\text{NiCo}_2\text{O}_4$ double-shelled nanocages with enhanced pseudocapacitive and electrocatalytic properties, *Journal of the American Chemical Society* 137(16) (2015) 5590-5595.
- [192] W. Wang, H. Yan, U. Anand, U. Mirsaidov, Visualizing the conversion of metal-organic framework nanoparticles into hollow layered double hydroxide nanocages, *Journal of the American Chemical Society* 143(4) (2021) 1854-1862.
- [193] G. Lee, W. Na, J. Kim, S. Lee, J. Jang, Improved electrochemical performances of MOF-derived Ni-Co layered double hydroxide complexes using distinctive hollow-in-hollow structures, *Journal of Materials Chemistry A* 7(29) (2019) 17637-17647.
- [194] J. Cao, S. Sun, X. Li, Z. Yang, W. Xiong, Y. Wu, M. Jia, Y. Zhou, C. Zhou, Y. Zhang, Efficient charge transfer in aluminum-cobalt layered double hydroxide derived from Co-

- ZIF for enhanced catalytic degradation of tetracycline through peroxymonosulfate activation, *Chemical Engineering Journal* 382 (2020) 122802.
- [195] Y.-T. Pan, J. Wan, X. Zhao, C. Li, D.-Y. Wang, Interfacial growth of MOF-derived layered double hydroxide nanosheets on graphene slab towards fabrication of multifunctional epoxy nanocomposites, *Chemical Engineering Journal* 330 (2017) 1222-1231.
- [196] Y. Hou, S. Qiu, Y. Hu, C.K. Kundu, Z. Gui, W. Hu, Construction of bimetallic ZIF-derived Co-Ni LDHs on the surfaces of GO or CNTs with a recyclable method: toward reduced toxicity of gaseous thermal decomposition products of unsaturated polyester resin, *ACS Applied Materials & Interfaces* 10(21) (2018) 18359-18371.
- [197] J. Tang, Y. Shen, X. Miao, H. Qin, D. Song, Y. Li, Y. Qu, Z. Yin, J. Ren, L. Wang, B. Wang, Template-directed growth of hierarchically structured MOF-derived LDH cage hybrid arrays for supercapacitor electrode, *Journal of Electroanalytical Chemistry* 840 (2019) 174-181.
- [198] P. Wang, Y. Li, S. Li, X. Liao, S. Sun, Water-promoted zeolitic imidazolate framework-67 transformation to Ni-Co layered double hydroxide hollow microsphere for supercapacitor electrode material, *Journal of Materials Science: Materials in Electronics* 28(13) (2017) 9221-9227.
- [199] M. Lyu, C. Chen, J.-C. Buffet, D. O'Hare, A facile synthesis of layered double hydroxide based core@shell hybrid materials, *New Journal of Chemistry* 44(24) (2020) 10095-10101.
- [200] D. Song, L. Wang, Y. Qu, B. Wang, Y. Li, X. Miao, Y. Yang, C. Duan, A high-performance three-dimensional hierarchical structure MOF-derived NiCo LDH nanosheets for non-enzymatic glucose detection, *Journal of The Electrochemical Society* 166(16) (2019) B1681.
- [201] Y. Li, B. Liu, H. Wang, X. Su, L. Gao, F. Zhou, G. Duan, Co₃O₄ nanosheet-built hollow dodecahedrons via a two-step self-templated method and their multifunctional applications, *Science China Materials* 61 (2018) 1-12.
- [202] D.K. Yadav, V. Ganesan, R. Gupta, M. Yadav, P.K. Sonkar, P.K. Rastogi, Copper oxide immobilized clay nano architectures as an efficient electrochemical sensing platform for hydrogen peroxide, *Journal of Chemical Sciences* 132(1) (2020) 68.
- [203] S. Saghir, Z. Xiao, Hierarchical mesoporous ZIF-67@LDH for efficient adsorption of aqueous methyl orange and alizarine Red S, *Powder Technology* 377 (2021) 453-463.
- [204] R. Deng, D. Huang, W. Xue, L. Lei, S. Chen, C. Zhou, X. Liu, X. Wen, B. Li, Eco-friendly remediation for lead-contaminated riverine sediment by sodium lignin sulfonate stabilized nano-chlorapatite, *Chemical Engineering Journal* 397 (2020) 125396.
- [205] H. Wang, B. Chen, D.J. Liu, X. Xu, L. Osmieri, Y. Yamauchi, Nanoarchitectonics of

- metal-organic frameworks for capacitive deionization via controlled pyrolyzed Approaches, *Small* 18(2) (2022).
- [206] J. Zhang, J. Fang, J. Han, T. Yan, L. Shi, D. Zhang, N. P, S co-doped hollow carbon polyhedra derived from MOF-based core-shell nanocomposites for capacitive deionization, *Journal of Materials Chemistry A* 6(31) (2018) 15245-15252.
- [207] W. Tang, J. Liang, D. He, J. Gong, L. Tang, Z. Liu, D. Wang, G. Zeng, Various cell architectures of capacitive deionization: Recent advances and future trends, *Water Research* 150 (2019) 225-251.
- [208] C. X. Yu, F. L. Hu, J. G. Song, J. L. Zhang, S. S. Liu, B. X. Wang, H. Meng, L. L. Liu, L. F. Ma, Ultrathin two-dimensional metal-organic framework nanosheets decorated with tetra-pyridyl calix [4] arene: Design, synthesis and application in pesticide detection, *Sensors and Actuators B: Chemical* 310 (2020) 127819.
- [209] V. Prevot, Y. Tokudome, 3D hierarchical and porous layered double hydroxide structures: an overview of synthesis methods and applications, *Journal of Materials Science* 52(19) (2017) 11229-11250.
- [210] E.M. Abd El-Monaem, H.M. Elshishini, S.S. Bakr, H.G. El-Aqapa, M. Hosny, G. Andaluri, G.M. El-Subruiti, A.M. Omer, A.S. Eltaweil, A comprehensive review on LDH-based catalysts to activate persulfates for the degradation of organic pollutants, *npj Clean Water* 6(1) (2023) 34.
- [211] L. Wu, Z. Sun, Y. Zhen, S. Zhu, C. Yang, J. Lu, Y. Tian, D. Zhong, J. Ma, Oxygen vacancy-induced nonradical degradation of organics: critical trigger of oxygen (O₂) in the Fe-Co LDH/peroxymonosulfate system, *Environmental Science. Technology*. 55(22) (2021) 15400-15411.
- [212] R. Ramachandran, S. Thangavel, L. Minzhang, S. Haiquan, X. Zong-Xiang, F. Wang, Efficient degradation of organic dye using Ni-MOF derived NiCo-LDH as peroxymonosulfate activator, *Chemosphere* 271 (2021) 128509.
- [213] Z. Liu, L. Teng, L. Ma, Y. Liu, X. Zhang, J. Xue, M. Ikram, M. Ullah, L. Li, K. Shi, Porous 3D flower-like CoAl-LDH nanocomposite with excellent performance for NO₂ detection at room temperature, *RSC Advances* 9(38) (2019) 21911-21921.
- [214] Z. Jiang, Z. Li, Z. Qin, H. Sun, X. Jiao, D. Chen, LDH nanocages synthesized with MOF templates and their high performance as supercapacitors, *Nanoscale* 5 (2013).
- [215] B. Gole, A.K. Bar, P.S. Mukherjee, Fluorescent metal-organic framework for selective sensing of nitroaromatic explosives, *Chemical Communications* 47(44) (2011) 12137-12139.
- [216] S. Ma, H. C. Zhou, Gas storage in porous metal-organic frameworks for clean energy applications, *Chemical Communications* 46(1) (2010) 44-53.
- [217] S. Qiu, M. Xue, G. Zhu, Metal-organic framework membranes: from synthesis to

- separation application, *Chemical Society Reviews* 43(16) (2014) 6116-6140.
- [218] A. Bavykina, N. Kolobov, I.S. Khan, J.A. Bau, A. Ramirez, J. Gascon, Metal-organic frameworks in heterogeneous catalysis: recent progress, new trends, and future perspectives, *Chemical Reviews* 120(16) (2020) 8468-8535.
- [219] Liu, Ning, Huang, Wenyuan, Zhang, Xiaodong, Tang, Liang, Wang, Ultrathin graphene oxide encapsulated in uniform MIL-88A(Fe) for enhanced visible light-driven photodegradation of RhB, *Applied Catalysis B: Environmental* 221(119) (2018) 0926-3373.
- [220] S. Sundriyal, H. Kaur, S.K. Bhardwaj, S. Mishra, K.-H. Kim, A. Deep, Metal-organic frameworks and their composites as efficient electrodes for supercapacitor applications, *Coordination Chemistry Reviews* 369 (2018) 15-38.
- [221] H. Hu, L. Han, M. Yu, Z. Wang, X.W. Lou, Metal-organic-framework-engaged formation of Co nanoparticle-embedded carbon@Co₉S₈ double-shelled nanocages for efficient oxygen reduction, *Energy & Environmental Science* 9(1) (2016) 107-111.
- [222] K.G.M. Laurier, F. Vermoortele, R. Ameloot, D.E. De Vos, J. Hofkens, M.B.J. Roeffaers, Iron (III)-based metal-organic frameworks as visible light photocatalysts, *Journal of the American Chemical Society* 135(39) (2013) 14488-14491.
- [223] T. Chalati, P. Horcajada, R. Gref, P. Couvreur, C. Serre, Optimisation of the synthesis of MOF nanoparticles made of flexible porous iron fumarate MIL-88A, *Journal of Materials Chemistry* 21(7) (2011) 2220-2227.
- [224] F. Wang, S. S. Liu, Z. Feng, H. Fu, M. Wang, P. Wang, W. Liu, C. C. Wang, High efficient peroxymonosulfate activation for rapid atrazine degradation by FeS_x@MoS₂ derived from MIL-88A (Fe), *Journal of Hazardous Materials* 440 (2022) 129723.
- [225] X. W. Zhang, F. Wang, C. C. Wang, P. Wang, H. Fu, C. Zhao, Photocatalysis activation of peroxodisulfate over the supported Fe₃O₄ catalyst derived from MIL-88A (Fe) for efficient tetracycline hydrochloride degradation, *Chemical Engineering Journal* 426 (2021) 131927.
- [226] H. Fu, X. X. Song, L. Wu, C. Zhao, P. Wang, C. C. Wang, Room-temperature preparation of MIL-88A as a heterogeneous photo-Fenton catalyst for degradation of rhodamine B and bisphenol a under visible light, *Materials Research Bulletin* 125 (2020) 110806.
- [227] A. Zielińska, P. Oleszczuk, B. Charmas, J. Skubiszewska-Zięba, S. Pasieczna-Patkowska, Effect of sewage sludge properties on the biochar characteristic, *Journal of Analytical and Applied Pyrolysis* 112 (2015) 201-213.
- [228] J. B. Huo, G. Yu, Layered double hydroxides derived from MIL-88A (Fe) as an efficient adsorbent for enhanced removal of lead (II) from water, *International Journal of Molecular Sciences*, 2022.
- [229] Z. Y. Liu, Q. Y. Wang, J. M. Hu, Introducing carbon dots to NiFe LDH via a mild

- coprecipitation-aging method to construct a heterojunction for effective oxygen evolution, *Catalysis Science & Technology* 14(1) (2024) 110-118.
- [230] B. Chameh, M. Moradi, S. Hajati, F.A. Hessari, M.A. Kiani, Morphology control of Ni doped rod like MIL-88A derived FeS₂ embedded in nitrogen-rich carbon as an efficient electrocatalyst for the oxygen reduction reaction, *Journal of Molecular Structure* 1237 (2021) 130329.
- [231] C. Serre, F. Millange, S. Surblé, G. Férey, A Route to the synthesis of trivalent transition-metal porous carboxylates with trimeric secondary building units, *Angewandte Chemie International Edition* 43(46) (2004) 6285-6289.
- [232] N.T. Xuan Huynh, V. Chihaiia, D.N. Son, Hydrogen storage in MIL-88 series, *Journal of Materials Science* 54(5) (2019) 3994-4010.
- [233] W. Jiumei, J. Wan, Y. Ma, Y. Wang, M. Pu, Z.J.R.A. Guan, Metal-organic frameworks MIL-88A with suitable synthesis conditions and optimal dosage for effective catalytic degradation of Orange G through persulfate activation, 6 (2016) 112502-112511.
- [234] Z. Zango, K. Jumbri, N. Sambudi, N.H.H. Abu Bakar, N.A.F. Abdullah, C. Basheer, B. Saad, Removal of anthracene in water by MIL-88 (Fe), NH₂-MIL-88 (Fe), and mixed-MIL-88 (Fe) metal-organic frameworks, *RSC Advances* 9 (2019) 41490-41501.
- [235] J. Amaro-Gahete, R. Klee, D. Esquivel, J.R. Ruiz, C. Jiménez-Sanchidrián, F.J. Romero-Salguero, Fast ultrasound-assisted synthesis of highly crystalline MIL-88A particles and their application as ethylene adsorbents, *Ultrasonics Sonochemistry* 50 (2019) 59-66.
- [236] S. E. Park, J. S. Chang, Y.K. Hwang, D.S. Kim, S.H. Jhung, J.S. Hwang, Supramolecular interactions and morphology control in microwave synthesis of nanoporous materials, *Catalysis Surveys from Asia* 8(2) (2004) 91-110.
- [237] E. Bagherzadeh, S.M. Zebarjad, H.R. Madaah Hosseini, A. Khodaei, Interplay between morphology and band gap energy in Fe-MIL-88A prepared via a high temperature surfactant-assisted solvothermal method, *Materials Chemistry and Physics* 277 (2022) 125536.
- [238] V.P. Viswanathan, S.V. Mathew, D.P. Dubal, N.N. Adarsh, S. Mathew, Exploring the effect of morphologies of Fe (III) metal-organic framework MIL-88A (Fe) on the photocatalytic degradation of rhodamine B, *ChemistrySelect* 5(25) (2020) 7534-7542.
- [239] Y. Zhang, J. Zhou, X. Chen, L. Wang, W. Cai, Coupling of heterogeneous advanced oxidation processes and photocatalysis in efficient degradation of tetracycline hydrochloride by Fe-based MOFs: Synergistic effect and degradation pathway, *Chemical Engineering Journal* 369 (2019) 745-757.
- [240] K.-Y. Lin, H.-A. Chang, C.-J. Hsu, Iron-based metal organic framework, MIL-88A, as a heterogeneous persulfate catalyst for decolorization of rhodamine B in water, *RSC Advances*. 5 (2015).

- [241] H. Liu, G. Wang, J. Park, J. Wang, H. Liu, C. Zhang, Electrochemical performance of α - Fe_2O_3 nanorods as anode material for lithium-ion cells, *Electrochimica Acta* 54(6) (2009) 1733-1736.
- [242] C. Natalia, G. Vasyi, S. Małgorzata, Y. Ganna, Effect of Fe oxidation state (+2 versus +3) in precursor on the structure of Fe oxides/carbonates-based composites examined by XPS, FTIR and EXAFS, *Solid State Sciences* 121 (2021) 106752.
- [243] A. Benítez, J. Amaro-Gahete, D. Esquivel, F.J. Romero-Salguero, J. Morales, Á. Caballero, MIL-88A metal-organic framework as a stable sulfur-host cathode for long-cycle Li-S batteries, *Nanomaterials*, 2020.
- [244] S. Zhao, Y. Li, M. Wang, B. Chen, Y. Zhang, Y. Sun, K. Chen, Q. Du, Z. Jing, Y. Jin, Preparation of MIL-88A micro/nanocrystals with different morphologies in different solvents for efficient removal of Congo red from water: Synthesis, characterization, and adsorption mechanisms, *Microporous and Mesoporous Materials* 345 (2022) 112241.
- [245] J. Zhang, L. Yu, Y. Chen, X.F. Lu, S. Gao, X.W. Lou, Designed formation of double-shelled Ni-Fe layered-double-hydroxide nanocages for efficient oxygen evolution reaction, *Advanced Materials* 32(16) (2020) 1906432.
- [246] V. Prevot, C. Forano, J. Pierre Besse, Reactivity of oxalate with ZnAl layered double hydroxides through new materials, *Journal of Materials Chemistry* 9(1) (1999) 155-160.
- [247] H. Roussel, V. Briois, E. Elkaim, A. de Roy, J.P. Besse, Cationic order and structure of [Zn-Cr-Cl] and [Cu-Cr-Cl] layered double hydroxides: A XRD and EXAFS study, *The Journal of Physical Chemistry B* 104(25) (2000) 5915-5923.
- [248] A. Lesbani, T. Taher, N.R. Palapa, R. Mohadi, A. Yuliana, Mardiyanto, Methyl orange dye removal using Ni/Fe- NO_3 and Ni/Fe- $[\alpha\text{-SiW}_{12}\text{O}_{40}]$ layered double hydroxides, *IOP Conference Series: Materials Science and Engineering* 902(1) (2020) 012042.
- [249] A.H. Iglesias, O.P. Ferreira, D.X. Gouveia, A.G. Souza Filho, J.A.C. de Paiva, J. Mendes Filho, O.L. Alves, Structural and thermal properties of Co-Cu-Fe hydrotalcite-like compounds, *Journal of Solid State Chemistry* 178(1) (2005) 142-152.
- [250] B. Wang, Q. Liu, Z. Qian, X. Zhang, J. Wang, Z. Li, H. Yan, Z. Gao, F. Zhao, L. Liu, Two steps in situ structure fabrication of Ni-Al layered double hydroxide on Ni foam and its electrochemical performance for supercapacitors, *Journal of Power Sources* 246 (2014) 747-753.
- [251] Y. Zou, X. Wang, Y. Ai, Y. Liu, J. Li, Y. Ji, X. Wang, Coagulation behavior of graphene oxide on nanocrystalline Mg/Al layered double hydroxides: batch experimental and theoretical calculation study, *Environmental Science & Technology* 50(7) (2016) 3658-3667.
- [252] M. Thommes, K. Kaneko, A.V. Neimark, J.P. Olivier, F. Rodriguez-Reinoso, J. Rouquerol, K.S.W. Sing, Physisorption of gases, with special reference to the evaluation

- of surface area and pore size distribution (IUPAC Technical Report), 87(9-10) (2015) 1051-1069.
- [253] Y. Luo, A. Zheng, M. Xue, Y. Xie, S. Yu, Z. Yin, C. Xie, Z. Hong, W. Tan, W. Zou, L. Dong, B. Gao, Ball-milled Bi₂MoO₆/biochar composites for synergistic adsorption and photodegradation of methylene blue: kinetics and mechanisms, *Industrial Crops and Products* 186 (2022).
- [254] H. Li, J. Liu, W. Hou, N. Du, R. Zhang, X. Tao, Synthesis and characterization of g-C₃N₄/Bi₂MoO₆ heterojunctions with enhanced visible light photocatalytic activity, *Applied Catalysis B: Environmental* 160-161(1) (2014) 89-97.
- [255] V.P. Viswanathan, K.S. Divya, D.P. Dubal, N.N. Adarsh, S. Mathew, Ag/AgCl@MIL-88A (Fe) heterojunction ternary composites: towards the photocatalytic degradation of organic pollutants, *Dalton Transactions* 50(8) (2021) 2891-2902.
- [256] H. Y. Zhu, R. Jiang, Y. Q. Fu, R. R. Li, J. Yao, S. T. Jiang, Novel multifunctional NiFe₂O₄/ZnO hybrids for dye removal by adsorption, photocatalysis and magnetic separation, *Applied Surface Science* 369 (2016) 1-10.
- [257] Y. Shen, P. Zhao, Q. Shao, F. Takahashi, K. Yoshikawa, In situ catalytic conversion of tar using rice husk char/ash supported nickel-iron catalysts for biomass pyrolytic gasification combined with the mixing-simulation in fluidized-bed gasifier, *Applied Energy* 160 (2015) 808-819.
- [258] F.S. Yen, W.C. Chen, J.M. Yang, C.T. Hong, Crystallite size variations of nanosized Fe₂O₃ powders during γ - to α -phase transformation, *Nano Letters* 2(3) (2002) 245-252.
- [259] R.-r. Shan, L.-g. Yan, Y.-m. Yang, K. Yang, S.-j. Yu, H.-q. Yu, B.-c. Zhu, B. Du, Highly efficient removal of three red dyes by adsorption onto Mg-Al-layered double hydroxide, *Journal of Industrial and Engineering Chemistry* 21 (2015) 561-568.
- [260] M. Hmoudah, A. El Qanni, R. Tesser, R. Esposito, A. Petrone, O. S. Jung, T. Salmi, V. Russo, M. Di Serio, Assessment of the robustness of MIL-88A in an aqueous solution: Experimental and DFT investigations, *Materials Science and Engineering: B* 288 (2023) 116179.
- [261] J. Yu, Y. Lu, C. Yuan, J. Zhao, M. Wang, R. Liu, Carbon supported polyindole-5-carboxylic acid covalently bonded with pyridine-2,4-diamine copper complex as a non-precious oxygen reduction catalyst, *Electrochimica Acta* 143 (2014) 1-9.
- [262] A. Mohammadi, M. Barikani, M.M. Lakouraj, Biocompatible polyurethane / thiocalix [4] arenes functionalized Fe₃O₄ magnetic nanocomposites: Synthesis and properties, *Materials Science and Engineering: C* 66 (2016) 106-118.
- [263] K. Kaviyarasu, E. Manikandan, J. Kennedy, M. Jayachandran, De Gomes, M. Maaza, Synthesis and characterization studies of NiO nanorods for enhancing solar cell efficiency using photon upconversion materials, *Ceramics International* 42(7) (2016) 8385-8394.

- [264] C. Sangwichien, G.L. Aranovich, M.D.J.C. Donohue, S.A. Physicochemical, aspects, density functional theory predictions of adsorption isotherms with hysteresis loops, 206 (2002) 313-320.
- [265] Z. Wu, Z. Zou, J. Huang, F. Gao, NiFe₂O₄ Nanoparticles/NiFe layered double-hydroxide nanosheet heterostructure array for efficient overall water splitting at large current densities, ACS Applied Materials & Interfaces 10(31) (2018) 26283-26292.
- [266] H. Yang, Y. Liu, S. Luo, Z. Zhao, X. Wang, Y. Luo, Z. Wang, J. Jin, J. Ma, Lateral-size-mediated efficient oxygen evolution reaction: insights into the atomically thin quantum dot structure of NiFe₂O₄, ACS Catalysis 7(8) (2017) 5557-5567.
- [267] M. Gong, Y. Li, H. Wang, Y. Liang, J.Z. Wu, J. Zhou, J. Wang, T. Regier, F. Wei, H. Dai, An advanced Ni-Fe layered double hydroxide electrocatalyst for water oxidation, Journal of the American Chemical Society 135(23) (2013) 8452-8455.
- [268] J. Wang, G. Yang, L. Wang, W. Yan, Synthesis of one-dimensional NiFe₂O₄ nanostructures: tunable morphology and high-performance anode materials for Li ion batteries, Journal of Materials Chemistry A 4(22) (2016) 8620-8629.
- [269] G. Dong, M. Fang, J. Zhang, R. Wei, L. Shu, X. Liang, S. Yip, F. Wang, L. Guan, Z. Zheng, J.C. Ho, In situ formation of highly active Ni-Fe based oxygen-evolving electrocatalysts via simple reactive dip-coating, Journal of Materials Chemistry A 5(22) (2017) 11009-11015.
- [270] R. Ramachandran, C. Zhao, M. Rajkumar, K. Rajavel, P. Zhu, W. Xuan, Z.-X. Xu, F. Wang, Porous nickel oxide microsphere and Ti₃C₂T_x hybrid derived from metal-organic framework for battery-type supercapacitor electrode and non-enzymatic H₂O₂ sensor, Electrochimica Acta 322 (2019) 134771.
- [271] C. Wang, J. Kim, V. Malgras, J. Na, J. Lin, J. You, M. Zhang, J. Li, Y. Yamauchi, Metal-Organic frameworks and their derived materials: emerging catalysts for a sulfate radicals-based advanced oxidation process in water purification, Small 15(16) (2019).
- [272] M.U. Tahir, H. Arshad, W. Xie, X. Wang, M. Nawaz, C. Yang, X. Su, Synthesis of morphology controlled NiCo-LDH microflowers derived from ZIF-67 using binary additives and their excellent asymmetric supercapacitor properties, Applied Surface Science 529 (2020) 147073.
- [273] G. Zhao, C. Li, X. Wu, J. Yu, X. Jiang, W. Hu, F. Jiao, Reduced graphene oxide modified NiFe-calcinated layered double hydroxides for enhanced photocatalytic removal of methylene blue, Applied Surface Science 434 (2018) 251-259.
- [274] L. Niu, X. Liu, X. Liu, Z. Lv, C. Zhang, X. Wen, Y. Yang, Y. Li, J. Xu, In situ XRD study on promotional effect of potassium on carburization of spray-dried precipitated Fe₂O₃ catalysts, ChemCatChem 9(9) (2017) 1691-1700.
- [275] M.M. Rao, B.R. Reddy, M. Jayalakshmi, V.S. Jaya, B. Sridhar, Hydrothermal synthesis

- of Mg-Al hydrotalcites by urea hydrolysis, *Materials Research Bulletin* 40(2) (2005) 347-359.
- [276] X. Li, X. Hao, Z. Wang, A. Abudula, G. Guan, In-situ intercalation of NiFe LDH materials: An efficient approach to improve electrocatalytic activity and stability for water splitting, *Journal of Power Sources* 347 (2017) 193-200.
- [277] J. Wang, J. Wan, Y. Ma, Y. Wang, M. Pu, Z. Guan, Metal-organic frameworks MIL-88A with suitable synthesis conditions and optimal dosage for effective catalytic degradation of Orange G through persulfate activation, *RSC Advances* 6(113) (2016) 112502-112511.
- [278] Y. Zhang, H. Hu, Z. Wang, B. Luo, W. Xing, L. Li, Z. Yan, L. Wang, Boosting the performance of hybrid supercapacitors through redox electrolyte-mediated capacity balancing, *Nano Energy* 68 (2020).
- [279] A.A. Lobinsky, V.P. Tolstoy, Synthesis of 2D Zn-Co LDH nanosheets by a successive ionic layer deposition method as a material for electrodes of high-performance alkaline battery-supercapacitor hybrid devices, *RSC Advances* 8(52) (2018) 29607-29612.
- [280] Y. Sun, J. Zhou, W. Cai, R. Zhao, J. Yuan, Hierarchically porous NiAl-LDH nanoparticles as highly efficient adsorbent for p-nitrophenol from water, *Applied Surface Science* 349 (2015) 897-903.
- [281] K. Bhuvaneshwari, G. Palanisamy, K. Sivashanmugan, T. Pazhanivel, T. Maiyalagan, ZnO nanoparticles decorated multiwall carbon nanotube assisted ZnMgAl layered triple hydroxide hybrid photocatalyst for visible light-driven organic pollutants removal, *Journal of Environmental Chemical Engineering* 9(1) (2021) 104909.
- [282] C. Dong, X. Yuan, X. Wang, X. Liu, W. Dong, R. Wang, Y. Duan, F. Huang, Rational design of cobalt-chromium layered double hydroxide as a highly efficient electrocatalyst for water oxidation, *Journal of Materials Chemistry A* 4(29) (2016) 11292-11298.
- [283] M.F. Chowdhury, C.-M. Kim, A. Jang, High-efficient and rapid removal of anionic and cationic dyes using a facile synthesized sole adsorbent NiAlFe-layered triple hydroxide (LTH), *Chemosphere* 332 (2023) 138878.
- [284] X.F. Lu, B.Y. Xia, S.-Q. Zang, X.W. Lou, Metal-organic frameworks based electrocatalysts for the oxygen reduction reaction, *Angewandte Chemie International Edition* 59(12) (2020) 4634-4650.
- [285] D.J. Tranchemontagne, J.R. Hunt, O.M. Yaghi, Room temperature synthesis of metal-organic frameworks: MOF-5, MOF-74, MOF-177, MOF-199, and IRMOF-0, *Tetrahedron* 64(36) (2008) 8553-8557.
- [286] E. Alvarez, N. Guillou, C. Martineau, B. Bueken, B. Van de Voorde, C. Le Guillouzer, P. Fabry, F. Nouar, F. Taulelle, D. de Vos, J.-S. Chang, K.H. Cho, N. Ramsahye, T. Devic, M. Daturi, G. Maurin, C. Serre, The structure of the aluminum fumarate metal-organic framework A520, *Angewandte Chemie International Edition* 54(12) (2015) 3664-3668.

- [287] S. Abdi, M. Nasiri, Enhanced hydrophilicity and water flux of poly (ether sulfone) membranes in the presence of aluminum fumarate metal-organic framework nanoparticles: preparation and characterization, *ACS Applied Materials & Interfaces* 11(16) (2019) 15060-15070.
- [288] T.J. Matemb Ma Ntep, H. Reinsch, P.P.C. Hügenell, S.-J. Ernst, E. Hastürk, C. Janiak, Designing a new aluminium muconate metal-organic framework (MIL-53-muc) as a methanol adsorbent for sub-zero temperature heat transformation applications, *Journal of Materials Chemistry A* 7(43) (2019) 24973-24981.
- [289] S. karmakar, J. Dechnik, C. Janiak, S. De, Aluminium fumarate metal-organic framework: A super adsorbent for fluoride from water, *Journal of Hazardous Materials* 303 (2016) 10-20.
- [290] C. Jing, Y. Chen, X. Zhang, X. Guo, X. Liu, B. Dong, F. Dong, X. Zhang, Y. Liu, S. Li, Y. Zhang, Low carbonate contaminative and ultrasmall NiAl LDH prepared by acid salt treatment with high adsorption capacity of methyl orange, *Industrial & Engineering Chemistry Research* 58(27) (2019) 11985-11998.
- [291] P. Arulmurugan, N.A. Manikandan, G. Pugazhenthii, Synthesis and characterization of polystyrene (PS) / modified Ni-Al LDH nanocomposite: role of composition, modifier and synthesis route of layered double hydroxides (LDH), *Macromolecular Symposia* 382(1) (2018) 1800078.
- [292] L. Zhang, M. Ou, H. Yao, Z. Li, D. Qu, F. Liu, J. Wang, J. Wang, Z. Li, Enhanced supercapacitive performance of graphite-like C₃N₄ assembled with NiAl-layered double hydroxide, *Electrochimica Acta* 186 (2015) 292-301.
- [293] A.D.S. Barbosa, D. Julião, D.M. Fernandes, A.F. Peixoto, C. Freire, B. de Castro, C.M. Granadeiro, S.S. Balula, L. Cunha-Silva, Catalytic performance and electrochemical behaviour of Metal-organic frameworks: MIL-101 (Fe) versus NH₂-MIL-101 (Fe), *Polyhedron* 127 (2017) 464-470.
- [294] S. Bauer, C. Serre, T. Devic, P. Horcajada, J. Marrot, G. Férey, N. Stock, High-throughput assisted rationalization of the formation of metal organic frameworks in the Iron (III) aminoterephthalate solvothermal system, *Inorganic Chemistry* 47(17) (2008) 7568-7576.
- [295] J. Tang, M. Yang, M. Yang, J. Wang, W. Dong, G. Wang, Heterogeneous Fe-MIL-101 catalysts for efficient one-pot four-component coupling synthesis of highly substituted pyrroles, *New Journal of Chemistry* 39(6) (2015) 4919-4923.
- [296] H. Hu, H. Zhang, Y. Chen, Y. Chen, L. Zhuang, H. Ou, Enhanced photocatalysis degradation of organophosphorus flame retardant using MIL-101(Fe)/persulfate: Effect of irradiation wavelength and real water matrixes, *Chemical Engineering Journal* 368 (2019) 273-284.
- [297] D. Wang, F. Jia, H. Wang, F. Chen, Y. Fang, W. Dong, G. Zeng, X. Li, Q. Yang, X.

- Yuan, Simultaneously efficient adsorption and photocatalytic degradation of tetracycline by Fe-based MOFs, *Journal of Colloid and Interface Science* 519 (2018) 273-284.
- [298] Z. Li, X. Liu, W. Jin, Q. Hu, Y. Zhao, Adsorption behavior of arsenicals on MIL-101(Fe): The role of arsenic chemical structures, *Journal of Colloid and Interface Science* 554 (2019) 692-704.
- [299] J. Shin, M. Kim, J. Cirera, S. Chen, G. Halder, T. Yersak, F. Paesani, S. Cohen, Y. Meng, MIL-101(Fe) as a lithium-ion battery electrode material: A relaxation and intercalation mechanism during lithium insertion, *Journal of Materials Chemistry A* (2015).
- [300] Q. Xie, Y. Li, Z. Lv, H. Zhou, Y. Xiangjun, J. Chen, H. Guo, Effective adsorption and removal of phosphate from aqueous solutions and eutrophic water by Fe-based MOFs of MIL-101, *Scientific Reports* 7 (2017).
- [301] E.P. Barrett, L.G. Joyner, P.P. Halenda, The determination of pore volume and area distributions in porous substances. I. computations from nitrogen isotherms, *Journal of the American Chemical Society* 73(1) (1951) 373-380.
- [302] S. Brunauer, P.H. Emmett, E. Teller, Adsorption of gases in multimolecular layers, *Journal of the American Chemical Society* 60(2) (1938) 309-319.
- [303] M. Hartmann, M. Fischer, Amino-functionalized basic catalysts with MIL-101 structure, *Microporous and Mesoporous Materials* 164 (2012) 38-43.
- [304] M. Lu, L. Li, S. Shen, D. Chen, W. Han, Highly efficient removal of Pb²⁺ by a sandwich structure of metal-organic framework/GO composite with enhanced stability, *New Journal of Chemistry* 43(2) (2019) 1032-1037.
- [305] J. Liu, J. Song, H. Xiao, L. Zhang, Y. Qin, D. Liu, W. Hou, N. Du, Synthesis and thermal properties of ZnAl layered double hydroxide by urea hydrolysis, *Powder Technology* 253 (2014) 41-45.
- [306] D. Wang, R. Huang, W. Liu, D. Sun, Z. Li, Fe-based MOFs for photocatalytic CO₂ reduction: role of coordination unsaturated sites and dual excitation pathways, *ACS Catalysis* 4(12) (2014) 4254-4260.
- [307] T. Sun, X. Ren, J. Hu, S. Wang, Expanding pore size of Al-BDC Metal-Organic frameworks as a way to achieve high adsorption selectivity for CO₂/CH₄ separation, *The Journal of Physical Chemistry C* 118(29) (2014) 15630-15639.
- [308] M.A. Shannon, P.W. Bohn, M. Elimelech, J.G. Georgiadis, B.J. Mariñas, A.M. Mayes, Science and technology for water purification in the coming decades, *Nature* 452(7185) (2008) 301-310.
- [309] E.-J. Kim, C.-S. Lee, Y.-Y. Chang, Y.-S. Chang, Hierarchically structured manganese oxide-coated magnetic nanocomposites for the efficient removal of heavy metal ions from aqueous systems, *ACS Applied Materials & Interfaces* 5(19) (2013) 9628-9634.
- [310] H. Bessbousse, T. Rhlalou, J.F. Verchère, L. Lebrun, Removal of heavy metal ions from

- aqueous solutions by filtration with a novel complexing membrane containing poly (ethyleneimine) in a poly (vinyl alcohol) matrix, *Journal of Membrane Science* 307(2) (2008) 249-259.
- [311] N. Meunier, P. Drogui, C. Montané, R. Hausler, G. Mercier, J.-F. Blais, Comparison between electrocoagulation and chemical precipitation for metals removal from acidic soil leachate, *Journal of hazardous materials* 137(1) (2006) 581-590.
- [312] E. Dialynas, E. Diamadopoulos, Integration of a membrane bioreactor coupled with reverse osmosis for advanced treatment of municipal wastewater, *Desalination* 238(1) (2009) 302-311.
- [313] W. Tang, D. He, C. Zhang, P. Kovalsky, T.D. Waite, Comparison of faradaic reactions in capacitive deionization (CDI) and membrane capacitive deionization (MCDI) water treatment processes, *Water Research* 120 (2017) 229-237.
- [314] K.G. Bhattacharyya, S.S. Gupta, Adsorption of a few heavy metals on natural and modified kaolinite and montmorillonite: A review, *Advances in Colloid and Interface Science* 140(2) (2008) 114-131.
- [315] F. Fu, L.P. Xie, B. Tang, Q. Wang, S.J.C.E.J. Jiang, Application of a novel strategy-Advanced Fenton-chemical precipitation to the treatment of strong stability chelated heavy metal containing wastewater, 189 (2012) 283-287.
- [316] N. Abdullah, N. Yusof, W.J. Lau, J. Jaafar, A.F.J.J.o.I. Ismail, E. Chemistry, recent trends of heavy metal removal from water/wastewater by membrane technologies, (2019).
- [317] Y. Wang, Y. Gu, D. Xie, W. Qin, H. Zhang, G. Wang, Y. Zhang, H. Zhao, A hierarchical hybrid monolith: MoS₄²⁻-intercalated NiFe layered double hydroxide nanosheet arrays assembled on carbon foam for highly efficient heavy metal removal, *Journal of Materials Chemistry A* 7(20) (2019) 12869-12881.
- [318] S. Iftekhhar, G. Heidari, N. Amanat, E.N. Zare, M.B. Asif, M. Hassanpour, V.P. Lehto, M. Sillanpaa, Porous materials for the recovery of rare earth elements, platinum group metals, and other valuable metals: a review, *Environmental Chemistry Letters* 20(6) (2022) 3697-3746.
- [319] X. Feng, R. Long, L. Wang, C. Liu, Z. Bai, X. Liu, A review on heavy metal ions adsorption from water by layered double hydroxide and its composites, *Separation and Purification Technology* 284 (2022) 120099.
- [320] N. Kano, S. Zhang, Adsorption of heavy metals on layered double hydroxides (LDHs) intercalated with chelating agents, *Advanced Sorption Process Applications* (2018).
- [321] Y. Dong, X. Kong, X. Luo, H. Wang, Adsorptive removal of heavy metal anions from water by layered double hydroxide: A review, *Chemosphere* 303 (2022) 134685.
- [322] K. Zheng, L. Liao, Y. Zhang, H. Tan, J. Liu, C. Li, D. Jia, Hierarchical NiCo-LDH core/shell homostructural electrodes with MOF-derived shell for electrochemical energy

- storage, *Journal of Colloid and Interface Science* 619 (2022) 75-83.
- [323] F. Cao, M. Gan, L. Ma, X. Li, F. Yan, M. Ye, Y. Zhai, Y. Zhou, Hierarchical sheet-like Ni-Co layered double hydroxide derived from a MOF template for high-performance supercapacitors, *Synthetic Metals* 234 (2017) 154-160.
- [324] W. Ma, Y. Chen, J. Qin, G. Hu, C. Xu, Synthesis of stable flowerlike MgAl-LDH@MIL-88A and its adsorption performance for fluoride, *Journal of Chemical Research* 46(6) (2022) 17475198221106680.
- [325] Y. Cao, A. Khan, T.A. Kurniawan, R. Soltani, A.B. Albadarin, Synthesis of hierarchical micro-mesoporous LDH/MOF nanocomposite with in situ growth of UiO-66-(NH₂)₂ MOF on the functionalized NiCo-LDH ultrathin sheets and its application for thallium (I) removal, *Journal of Molecular Liquids* 336 (2021) 116189.
- [326] X. Guan, X. Yuan, Y. Zhao, H. Wang, H. Wang, J. Bai, Y. Li, Application of functionalized layered double hydroxides for heavy metal removal: A review, *Science of The Total Environment* 838 (2022) 155693.
- [327] X. Tao, D. Liu, J. Song, Q. Ye, D. Xu, Plasma modification of ZnMgAl-LDHs for adsorption property improvement, *Journal of the Taiwan Institute of Chemical Engineers* 74 (2017) 281-288.
- [328] W. Song, X. Zhang, L. Zhang, Z. Yu, X. Li, Y. Li, Y. Cui, Y. Zhao, L. Yan, Removal of various aqueous heavy metals by polyethylene glycol modified MgAl-LDH: Adsorption mechanisms and vital role of precipitation, *Journal of Molecular Liquids* 375 (2023) 121386.
- [329] M. Qu, Y. Jiang, M. Yang, S. Liu, Q. Guo, W. Shen, M. Li, R. He, Regulating electron density of NiFe-P nanosheets electrocatalysts by a trifle of Ru for high-efficient overall water splitting, *Applied Catalysis B: Environmental* 263 (2020) 118324.
- [330] D. Sokol, D.E.L. Vieira, A. Zarkov, M.G.S. Ferreira, A. Beganskiene, V.V. Rubanik, A.D. Shilin, A. Kareiva, A.N. Salak, Sonication accelerated formation of Mg-Al-phosphate layered double hydroxide via sol-gel prepared mixed metal oxides, *Scientific Reports* 9(1) (2019) 10419.
- [331] J. Yu, A. Wang, J. Tan, X. Li, J.A. van Bokhoven, Y. Hu, Synthesis of novel nanotubular mesoporous nickel phosphates with high performance in epoxidation, *Journal of Materials Chemistry* 18(30) (2008) 3601-3607.
- [332] Y. Zheng, B. Cheng, W. You, J. Yu, W. Ho, 3D hierarchical graphene oxide-NiFe LDH composite with enhanced adsorption affinity to Congo red, methyl orange and Cr(VI) ions, *Journal of Hazardous Materials* 369 (2019) 214-225.
- [333] M. Zhang, B. Gao, Y. Yao, M. Inyang, Phosphate removal ability of biochar/MgAl-LDH ultra-fine composites prepared by liquid-phase deposition, *Chemosphere* 92(8) (2013) 1042-1047.

- [334] H. Li, H. Cui, L. Li, Y. Zhang, Q. Wang, N. Wei, X. Song, S. Shao, N. Mao, Incorporation of Nanometer-Sized Layered Double Hydroxide with Anions that Improve the Corrosion Resistance of Epoxy Polymer, *ACS Applied Nano Materials* 6(21) (2023) 20419-20430.
- [335] T.-H. Kim, L. Lundehøj, U.G. Nielsen, An investigation of the phosphate removal mechanism by MgFe layered double hydroxides, *Applied Clay Science* 189 (2020) 105521.
- [336] M. Anggraini, A. Kurniawan, L.K. Ong, M.A. Martin, J.-C. Liu, F.E. Soetaredjo, N. Indraswati, S. Ismadji, Antibiotic detoxification from synthetic and real effluents using a novel MTAB surfactant-montmorillonite (organoclay) sorbent, *RSC Advances* 4(31) (2014) 16298-16311.
- [337] K. Fan, Y. Ji, H. Zou, J. Zhang, B. Zhu, H. Chen, Q. Daniel, Y. Luo, J. Yu, L. Sun, Hollow iron–vanadium composite spheres: A highly efficient iron-based water oxidation electrocatalyst without the need for nickel or cobalt, *Angewandte Chemie International Edition* 56(12) (2017) 3289-3293.
- [338] L. Yu, H. Zhou, J. Sun, F. Qin, F. Yu, J. Bao, Y. Yu, S. Chen, Z. Ren, Cu nanowires shelled with NiFe layered double hydroxide nanosheets as bifunctional electrocatalysts for overall water splitting, *Energy & Environmental Science* 10(8) (2017) 1820-1827.
- [339] W.-D. Zhang, Q.-T. Hu, L.-L. Wang, J. Gao, H.-Y. Zhu, X. Yan, Z.-G. Gu, In-situ generated Ni-MOF/LDH heterostructures with abundant phase interfaces for enhanced oxygen evolution reaction, *Applied Catalysis B: Environmental* 286 (2021) 119906.
- [340] J. Jiang, F. Sun, S. Zhou, W. Hu, H. Zhang, J. Dong, Z. Jiang, J. Zhao, J. Li, W. Yan, M. Wang, Atomic-level insight into super-efficient electrocatalytic oxygen evolution on iron and vanadium co-doped nickel (oxy)hydroxide, *Nature Communications* 9(1) (2018) 2885.
- [341] C. Sotelo-Vazquez, N. Noor, A. Kafizas, R. Quesada-Cabrera, D.O. Scanlon, A. Taylor, J.R. Durrant, I.P. Parkin, Multifunctional P-doped TiO₂ films: A new approach to self-cleaning, transparent conducting oxide materials, *Chemistry of Materials* 27(9) (2015) 3234-3242.
- [342] K. Yang, L.-g. Yan, Y.-m. Yang, S.-j. Yu, R.-r. Shan, H.-q. Yu, B.-c. Zhu, B. Du, Adsorptive removal of phosphate by Mg–Al and Zn–Al layered double hydroxides: Kinetics, isotherms and mechanisms, *Separation and Purification Technology* 124 (2014) 36-42.
- [343] L. Song, J. Huo, X. Wang, F. Yang, J. He, C. Li, Phosphate adsorption by a Cu (II)-loaded polyethersulfone-type metal affinity membrane with the presence of coexistent ions, *Chemical Engineering Journal* 284 (2016) 182-193.
- [344] E.D. Revellame, D.L. Fortela, W. Sharp, R. Hernandez, M.E. Zappi, Adsorption kinetic modeling using pseudo-first order and pseudo-second order rate laws: A review, *Cleaner*

- Engineering and Technology 1 (2020) 100032.
- [345] L. Largette, R. Pasquier, A review of the kinetics adsorption models and their application to the adsorption of lead by an activated carbon, *Chemical Engineering Research and Design* 109 (2016) 495-504.
- [346] Y.S. Ho, G. McKay, Pseudo-second order model for sorption processes, *Process Biochemistry* 34(5) (1999) 451-465.
- [347] M.N. Afridi, W.-H. Lee, J.-O. Kim, Effect of phosphate concentration, anions, heavy metals, and organic matter on phosphate adsorption from wastewater using anodized iron oxide nanoflakes, *Environmental Research* 171 (2019) 428-436.
- [348] Y. Wang, X. Xie, X. Chen, C. Huang, S. Yang, Biochar-loaded Ce^{3+} -enriched ultra-fine ceria nanoparticles for phosphate adsorption, *Journal of Hazardous Materials* 396 (2020) 122626.
- [349] W.-Y. Huang, D. Li, Z.-Q. Liu, Q. Tao, Y. Zhu, J. Yang, Y.-M. Zhang, Kinetics, isotherm, thermodynamic, and adsorption mechanism studies of $La(OH)_3$ -modified exfoliated vermiculites as highly efficient phosphate adsorbents, *Chemical Engineering Journal* 236 (2014) 191-201.
- [350] S. Kalam, S.A. Abu-Khamsin, M.S. Kamal, S. Patil, Surfactant adsorption isotherms: A review, *ACS Omega* 6(48) (2021) 32342-32348.
- [351] K. Naseem, R. Begum, W. Wu, M. Usman, A. Irfan, A.G. Al-Sehemi, Z.H. Farooqi, Adsorptive removal of heavy metal ions using polystyrene-poly(N-isopropylmethacrylamide-acrylic acid) core/shell gel particles: Adsorption isotherms and kinetic study, *Journal of Molecular Liquids* 277 (2019) 522-531.
- [352] M.F. Abou Taleb, G.A. Mahmoud, S.M. Elsigeny, E.-S.A. Hegazy, Adsorption and desorption of phosphate and nitrate ions using quaternary (polypropylene-g-N,N-dimethylamino ethylmethacrylate) graft copolymer, *Journal of Hazardous Materials* 159(2) (2008) 372-379.
- [353] M.B. Poudel, G.P. Awasthi, H.J. Kim, Novel insight into the adsorption of Cr(VI) and Pb(II) ions by MOF derived Co-Al layered double hydroxide@hematite nanorods on 3D porous carbon nanofiber network, *Chemical Engineering Journal* 417 (2021) 129312.
- [354] M. Babu Poudel, M. Shin, H. Joo Kim, Interface engineering of MIL-88 derived MnFe-LDH and $MnFe_2O_3$ on three-dimensional carbon nanofibers for the efficient adsorption of Cr (VI), Pb (II), and As (III) ions, *Separation and Purification Technology* 287 (2022) 120463.
- [355] D. Zhao, G. Sheng, J. Hu, C. Chen, X. Wang, The adsorption of Pb (II) on Mg_2Al layered double hydroxide, *Chemical Engineering Journal* 171(1) (2011) 167-174.
- [356] X. Zhang, R. Shan, X. Li, L. Yan, Z. Ma, R. Jia, S. Sun, Effective removal of Cu (II), Pb (II) and Cd (II) by sodium alginate intercalated $MgAl$ -layered double hydroxide:

- adsorption properties and mechanistic studies, *Water Science and Technology* 83(4) (2021) 975-984.
- [357] X. Su, Y. Chen, Y. Li, J. Li, W. Song, X. Li, L. Yan, Enhanced adsorption of aqueous Pb (II) and Cu (II) by biochar loaded with layered double hydroxide: Crucial role of mineral precipitation, *Journal of Molecular Liquids* 357 (2022) 119083.
- [358] A.K.A. Khalil, I.W. Almanassra, A. Chatla, I. Ihsanullah, T. Laoui, M. Ali Atieh, Insights into the adsorption of lead ions by Mg-Al LDH doped activated carbon composites: Implications for fixed bed column and batch applications, *Chemical Engineering Science* 281 (2023) 119192.
- [359] C. Zhu, X. Dong, Z. Chen, R. Naidu, Adsorption of aqueous Pb (II), Cu (II), Zn (II) ions by amorphous tin (VI) hydrogen phosphate: an excellent inorganic adsorbent, *International Journal of Environmental Science and Technology* 13(5) (2016) 1257-1268.
- [360] H. Li, Q. Jiang, J. Zhang, Y. Wang, Y. Zhang, Synchronization adsorption of Pb (II) and Ce (III) by biochar supported phosphate-doped ferrihydrite in aqueous solution: Adsorption efficiency and mechanisms, *Colloids and Surfaces A: Physicochemical and Engineering Aspects* 648 (2022) 129230.
- [361] A. Bashir, T. Manzoor, L.A. Malik, A. Qureshi, A.H. Pandith, Enhanced and selective adsorption of Zn (II), Pb (II), Cd (II), and Hg(II) ions by a dumbbell- and flower-shaped potato starch phosphate polymer: A combined experimental and DFT calculation study, *ACS Omega* 5(10) (2020) 4853-4867.
- [362] D. Wu, Y. Wang, Y. Li, Q. Wei, L. Hu, T. Yan, R. Feng, L. Yan, B. Du, Phosphorylated chitosan/CoFe₂O₄ composite for the efficient removal of Pb (II) and Cd (II) from aqueous solution: Adsorption performance and mechanism studies, *Journal of Molecular Liquids* 277 (2019) 181-188.
- [363] Y. Long, J. Jiang, J. Hu, X. Hu, Q. Yang, S. Zhou, Removal of Pb (II) from aqueous solution by hydroxyapatite/carbon composite: Preparation and adsorption behavior, *Colloids and Surfaces A: Physicochemical and Engineering Aspects* 577 (2019) 471-479.
- [364] X. Liang, Y. Zang, Y. Xu, X. Tan, W. Hou, L. Wang, Y. Sun, Sorption of metal cations on layered double hydroxides, *Colloids and Surfaces A: Physicochemical and Engineering Aspects* 433 (2013) 122-131.
- [365] N. S. Kwak, H.-M. Park, T.S. Hwang, Preparation of ion-exchangeable nanobeads using suspension polymerization and their sorption properties for indium in aqueous solution, *Chemical Engineering Journal* 191 (2012) 579-587.
- [366] C Jin, Z. X Ping, S. W. Li, Shape-controlled synthesis and related growth mechanism of Pb (OH)₂ nanorods by solution-phase reaction, *Chin. Phys. Lett.* 27(5) (2010) .
- [367] M. Kwaśniak-Kominek, M. Manecki, J. Matusik, M. Lempart, Carbonate substitution in lead hydroxyapatite Pb₅(PO₄)₃OH, *Journal of Molecular Structure* 1147 (2017) 594-602.

- [368] L. Zhang, Y. Liu, Y. Wang, X. Li, Y. Wang, Investigation of phosphate removal mechanisms by a lanthanum hydroxide adsorbent using p-XRD, FTIR and XPS, *Applied Surface Science* 557 (2021) 149838.
- [369] R. Nadeem, T.M. Ansari, A.M. Khalid, Fourier transform infrared spectroscopic characterization and optimization of Pb (II) biosorption by fish (*Labeo rohita*) scales, *Journal of Hazardous Materials* 156(1) (2008) 64-73.
- [370] R. Aravindhan, B. Madhan, J.R. Rao, B.U. Nair, Recovery and reuse of chromium from tannery wastewaters using *Turbinaria ornata* seaweed, *Journal of Chemical Technology and Biotechnology* 79(11) (2004) 1251-1258.
- [371] W. Chu, Z. Lu, R. Tan, S. Tang, W. Xu, W. Song, J. Zhao, Comparative study on Pb²⁺ removal using hydrothermal synthesized β -SrHPO₄, Sr₃(PO₄)₂, and Sr₅(PO₄)₃(OH) powders, *Powder Technology* 329 (2018) 420-425.
- [372] J. Bi, X. Huang, J. Wang, T. Wang, H. Wu, J. Yang, H. Lu, H. Hao, Oil-phase cyclic magnetic adsorption to synthesize Fe₃O₄@C@TiO₂-nanotube composites for simultaneous removal of Pb (II) and Rhodamine B, *Chemical Engineering Journal* 366 (2019) 50-61.
- [373] E.M. Abd El-Monaem, A.S. Eltaweil, H.M. Elshishini, M. Hosny, M.M. Abou Alsoaud, N.F. Attia, G.M. El-Subruiti, A.M. Omer, Sustainable adsorptive removal of antibiotic residues by chitosan composites: An insight into current developments and future recommendations, *Arabian Journal of Chemistry* 15(5) (2022) 103743.
- [374] B.S. Rathi, P.S. Kumar, P. L. Show, A review on effective removal of emerging contaminants from aquatic systems: Current trends and scope for further research, *Journal of Hazardous Materials* 409 (2021) 124413.
- [375] C. Wang, J. Kim, V. Malgras, J. Na, J. Lin, J. You, M. Zhang, J. Li, Y. Yamauchi, Metal-organic frameworks and their derived materials: emerging catalysts for a sulfate radicals-based advanced oxidation process in Water Purification, *Small* 15(16) (2019) 1900744.
- [376] P.V.L. Reddy, K.-H. Kim, B. Kavitha, V. Kumar, N. Raza, S. Kalagara, Photocatalytic degradation of bisphenol A in aqueous media: A review, *Journal of Environmental Management* 213 (2018) 189-205.
- [377] J. Muncke, Exposure to endocrine disrupting compounds via the food chain: Is packaging a relevant source?, *Science of The Total Environment* 407(16) (2009) 4549-4559.
- [378] Y.Q. Huang, C.K.C. Wong, J.S. Zheng, H. Bouwman, R. Barra, B. Wahlström, L. Neretin, M.H. Wong, Bisphenol A (BPA) in China: A review of sources, environmental levels, and potential human health impacts, *Environment International* 42 (2012) 91-99.
- [379] C.A. Staples, P.B. Dome, G.M. Klecka, S.T. Oblock, L.R. Harris, A review of the environmental fate, effects, and exposures of bisphenol A, *Chemosphere* 36(10) (1998) 2149-2173.

- [380] B.S. Rubin, Bisphenol A: An endocrine disruptor with widespread exposure and multiple effects, *The Journal of Steroid Biochemistry and Molecular Biology* 127(1) (2011) 27-34.
- [381] L.N. Vandenberg, R. Hauser, M. Marcus, N. Olea, W.V. Welshons, Human exposure to bisphenol A (BPA), *Reproductive Toxicology* 24(2) (2007) 139-177.
- [382] S. vom Saal Frederick, C. Hughes, An extensive new literature concerning low-dose effects of bisphenol A shows the need for a new risk assessment, *Environmental Health Perspectives* 113(8) (2005) 926-933.
- [383] Z. Nor, S. Yusof, H. Ghazi, Z. md isa, Does Bisphenol A contribute to autism spectrum disorder?, *Current Topics in Toxicology* 10 (2014) 63-70.
- [384] Z.A. Moghadam, M. Mirlohi, H. Pourzamani, A. Malekpour, Z. Amininoor, M.R. Merasi, Exposure assessment of Bisphenol A intake from polymeric baby bottles in formula-fed infants aged less than one year, *Toxicology Reports* 2 (2015) 1273-1280.
- [385] M. Yazdani, A.M. Andresen, T. Gjøen, Short-term effect of bisphenol-a on oxidative stress responses in Atlantic salmon kidney cell line: a transcriptional study, *Toxicol Mech Methods* 26(4) (2016) 295-300.
- [386] J.M. Lee, Y. Na, H. Han, S. Chang, Cooperative multi-catalyst systems for one-pot organic transformations, *Chemical Society Reviews* 33(5) (2004) 302-312.
- [387] R. Guan, X. Yuan, Z. Wu, L. Jiang, J. Zhang, Y. Li, G. Zeng, D. Mo, Efficient degradation of tetracycline by heterogeneous cobalt oxide/cerium oxide composites mediated with persulfate, *Separation and Purification Technology* 212 (2019) 223-232.
- [388] J. Ma, H. Li, L. Chi, H. Chen, C. Chen, Changes in activation energy and kinetics of heat-activated persulfate oxidation of phenol in response to changes in pH and temperature, *Chemosphere* 189 (2017) 86-93.
- [389] R. Khaghani, B. Kakavandi, K. Ghadirinejad, E. Dehghani Fard, A. Asadi, Preparation, characterization and catalytic potential of γ -Fe₂O₃@AC mesoporous heterojunction for activation of peroxymonosulfate into degradation of cyfluthrin insecticide, *Microporous and Mesoporous Materials* 284 (2019) 111-121.
- [390] S.S. Rezaei, E. Dehghanifard, M. Noorisepehr, K. Ghadirinejad, B. Kakavandi, A.R. Esfahani, Efficient clean-up of waters contaminated with diazinon pesticide using photodecomposition of peroxymonosulfate by ZnO decorated on a magnetic core/shell structure, *Journal of Environmental Management* 250 (2019) 109472.
- [391] M. Kermani, F. Mohammadi, B. Kakavandi, A. Esrafili, Z. Rostamifasih, Simultaneous catalytic degradation of 2,4-D and MCPA herbicides using sulfate radical-based heterogeneous oxidation over persulfate activated by natural hematite (α -Fe₂O₃/PS), *Journal of Physics and Chemistry of Solids* 117 (2018) 49-59.
- [392] G. Xian, G. Zhang, H. Chang, Y. Zhang, Z. Zou, X. Li, Heterogeneous activation of persulfate by Co₃O₄-CeO₂ catalyst for diclofenac removal, *Journal of Environmental*

Management 234 (2019) 265-272.

- [393] G.Q. Fan, Y.J. Bai, Y.L. Gao, W. Zhang, S. Zhang, Y. Shen, K. Liu, J. Yu, Investigation and analysis on potato viral disease in China, *J Northeast Agr Univ* 44 (2014) 74-79.
- [394] Z. H. Xie, C. S. He, H. Y. Zhou, L. L. Li, Y. Liu, Y. Du, W. Liu, Y. Mu, B. Lai, Effects of molecular structure on organic contaminants' degradation efficiency and dominant ROS in the advanced oxidation process with multiple ROS, *Environmental science & technology* 56(12) (2022) 8784-8795.
- [395] Y. Hong, H. Zhou, Z. Xiong, Y. Liu, G. Yao, B. Lai, Heterogeneous activation of peroxymonosulfate by CoMgFe-LDO for degradation of carbamazepine: Efficiency, mechanism and degradation pathways, *Chemical Engineering Journal* 391 (2020) 123604.
- [396] J. Yan, Y. Chen, L. Qian, W. Gao, D. Ouyang, M. Chen, Heterogeneously catalyzed persulfate with a CuMgFe layered double hydroxide for the degradation of ethylbenzene, *Journal of Hazardous Materials* 338 (2017) 372-380.
- [397] A. Jawad, J. Lang, Z. Liao, A. Khan, J. Ifthikar, Z. Lv, S. Long, Z. Chen, Z. Chen, Activation of persulfate by CuOx@Co-LDH: A novel heterogeneous system for contaminant degradation with broad pH window and controlled leaching, *Chemical Engineering Journal* 335 (2018) 548-559.
- [398] L. Wu, J. Hong, Q. Zhang, B.-Y. Chen, J. Wang, Z. Dong, Deciphering highly resistant characteristics to different pHs of oxygen vacancy-rich Fe₂Co₁-LDH/PS system for bisphenol A degradation, *Chemical Engineering Journal* 385 (2020) 123620.
- [399] R. Ma, X. Yan, X. Mi, Y. Wu, J. Qian, Q. Zhang, G.-H. Chen, Enhanced catalytic degradation of aqueous doxycycline (DOX) in Mg-Fe-LDH@biochar composite-activated peroxymonosulfate system: Performances, degradation pathways, mechanisms and environmental implications, *Chemical Engineering Journal* 425 (2021) 131457.
- [400] Q. Ma, L.-c. Nengzi, B. Li, Z. Wang, L. Liu, X. Cheng, Heterogeneously catalyzed persulfate with activated carbon coated with CoFe layered double hydroxide (AC@CoFe-LDH) for the degradation of lomefloxacin, *Separation and Purification Technology* 235 (2020) 116204.
- [401] C. Gong, F. Chen, Q. Yang, K. Luo, F. Yao, S. Wang, X. Wang, J. Wu, X. Li, D. Wang, G. Zeng, Heterogeneous activation of peroxymonosulfate by Fe-Co layered double hydroxide for efficient catalytic degradation of Rhodamine B, *Chemical Engineering Journal* 321 (2017) 222-232.
- [402] Y. Ma, F. Chen, Q. Yang, Y. Zhong, X. Shu, F. Yao, T. Xie, X. Li, D. Wang, G. Zeng, Sulfate radical induced degradation of methyl violet azo dye with CuFe layered double hydroxide as heterogeneous photoactivator of persulfate, *Journal of Environmental Management* 227 (2018) 406-414.
- [403] V. Gadore, S. Ranjan Mishra, M. Ahmaruzzaman, SnS₂ modified carbonate-intercalated

- Ni-Zn-Fe trimetallic LDH as a novel photocatalyst for persulfate activation: Influence of operational parameters, co-existing ions and organic compounds, *Chemical Engineering Journal* 475 (2023) 146157.
- [404] X. Dai, D. Gu, Q. Zhou, X. Zhang, C. Zhang, T. Sun, X. Liu, D. Song, L. Gao, J. Zheng, J. Rao, Y. Zhang, Interfacial heterojunction-engineered magnetic α - Fe_2O_3 @NiFeLDH@biotemplate catalyst for heterogeneous photocatalytic activated persulfate removal of organic pollutants, *Colloids and Surfaces A: Physicochemical and Engineering Aspects* 679 (2023) 132534.
- [405] J. Shen, A. Shi, J. Lu, X. Lu, H. Zhang, Z. Jiang, Optimized fabrication of Cu-doped ZnO/calcined CoFe-LDH composite for efficient degradation of bisphenol a through synergistic visible-light photocatalysis and persulfate activation: Performance and mechanisms, *Environmental Pollution* 323 (2023) 121186.
- [406] H. Zhang, L.-c. Nengzi, Z. Wang, X. Zhang, B. Li, X. Cheng, Construction of Bi_2O_3 /CuNiFe LDHs composite and its enhanced photocatalytic degradation of lomefloxacin with persulfate under simulated sunlight, *Journal of Hazardous Materials* 383 (2020) 121236.
- [407] J. Saien, M.F. Nasri, S. Pourehie, Enhanced activation of persulfate by magnetic CuFe-layered double hydroxide nanocomposites under visible light irradiation for degradation of quinoline, 19 (2021) 1515-1526.
- [408] Y. Chen, J. Yan, D. Ouyang, L. Qian, L. Han, M. Chen, Heterogeneously catalyzed persulfate by CuMgFe layered double oxide for the degradation of phenol, *Applied Catalysis A: General* 538 (2017) 19-26.
- [409] H. Zhang, Q. Jia, F. Yan, Q. Wang, Heterogeneous activation of persulfate by CuMgAl layered double oxide for catalytic degradation of sulfameter, *Green Energy & Environment* 7(1) (2022) 105-115.
- [410] W. Chen, W. Mao, Z. Liu, W. Hou, N. Kumar, J. Sun, X. Cai, C. Huang, W. Shen, F. Yang, Y. Cui, H.K. Lee, S. Tang, Photocatalytic degradation of bisphenol A by temperature-sensitive magnetic hydrogel with enhanced service life, *Journal of Hazardous Materials* 459 (2023) 132188.
- [411] M. Chen, P. Wu, Q. Wei, Y. Zhu, S. Yang, L. Ju, N. Zhu, Z. Lin, The role of oxygen vacancy over ZnCr-layered double oxide in enhancing solar light-driven photocatalytic degradation of bisphenol A, *Environmental Chemistry* 15(4) (2018) 226-235.
- [412] D. Yue, X. Yan, C. Guo, X. Qian, Y. Zhao, NiFe layered double hydroxide (LDH) nanosheet catalysts with Fe as electron transfer mediator for enhanced persulfate activation, *The journal of physical chemistry letters* 11(3) (2020) 968-973.
- [413] M. Abdul Nasir Khan, P. Kwame Klu, C. Wang, W. Zhang, R. Luo, M. Zhang, J. Qi, X. Sun, L. Wang, J. Li, Metal-organic framework-derived hollow Co_3O_4 /carbon as efficient

- catalyst for peroxymonosulfate activation, *Chemical Engineering Journal* 363 (2019) 234-246.
- [414] L. Mohapatra, Y.F. Tsang, X. Dou, K. Baek, MnFe-layered double hydroxides grown on spherical SiO₂ to construct core-shell heterostructures for enhanced simultaneous photocatalytic redox Reactions of Cr (VI) and As (III), *Journal of Water Process Engineering* 50 (2022) 103236.
- [415] S.-M. Xu, H. Yan, M. Wei, Band structure engineering of transition-metal-based layered double hydroxides toward photocatalytic oxygen evolution from water: A theoretical–experimental combination study, *The Journal of Physical Chemistry C* 121(5) (2017) 2683-2695.
- [416] S. Nayak, K.M. Parida, Dynamics of charge-transfer behavior in a plasmon-induced Quasi-Type-II p–n/n–n dual heterojunction in Ag@Ag₃PO₄/g-C₃N₄/NiFe LDH nanocomposites for photocatalytic Cr (VI) reduction and phenol oxidation, *ACS Omega* 3(7) (2018) 7324-7343.
- [417] R. Huang, Z. Fang, X. Yan, W. Cheng, Heterogeneous sono-Fenton catalytic degradation of bisphenol A by Fe₃O₄ magnetic nanoparticles under neutral condition, *Chemical Engineering Journal* 197 (2012) 242-249.
- [418] Q. Ye, J. Wu, P. Wu, J. Wang, W. Niu, S. Yang, M. Chen, S. Rehman, N. Zhu, Enhancing peroxymonosulfate activation of Fe-Al layered double hydroxide by dissolved organic matter: Performance and mechanism, *Water Research* 185 (2020) 116246.
- [419] A. Shahzad, J. Ali, J. Ifthikar, G.G. Aregay, J. Zhu, Z. Chen, Z. Chen, Non-radical PMS activation by the nanohybrid material with periodic confinement of reduced graphene oxide (rGO) and Cu hydroxides, *Journal of Hazardous Materials* 392 (2020) 122316.
- [420] X. Huang, X. Zhou, Q. Su, J. Zhou, G. Qian, N. Gao, J. Liu, Synergic thermal activation of peroxydisulfate intercalated Mg/Al layered double hydroxide at a low temperature, *Chemical Engineering Journal* 363 (2019) 133-140.
- [421] F. Babou, G. Coudurier, J.C. Vedrine, Acidic properties of sulfated zirconia: An infrared spectroscopic study, *Journal of Catalysis* 152(2) (1995) 341-349.
- [422] X. Zhang, X. Zhang, X.-G. Wang, Z. Xie, Z. Zhou, NiFe₂O₄-CNT composite: an efficient electrocatalyst for oxygen evolution reactions in Li-O₂ batteries guided by computations, *Journal of Materials Chemistry A* 4(24) (2016) 9390-9393.
- [423] M.C. Biesinger, B.P. Payne, A.P. Grosvenor, L.W.M. Lau, A.R. Gerson, R.S.C. Smart, Resolving surface chemical states in XPS analysis of first row transition metals, oxides and hydroxides: Cr, Mn, Fe, Co and Ni, *Applied Surface Science* 257(7) (2011) 2717-2730.
- [424] M.B. Nguyen, G.H. Le, T.D. Nguyen, Q.K. Nguyen, T.T.T. Pham, T. Lee, T.A. Vu, Bimetallic Ag-Zn-BTC/GO composite as highly efficient photocatalyst in the

- photocatalytic degradation of reactive yellow 145 dye in water, *Journal of Hazardous Materials* 420 (2021) 126560.
- [425] R. Xiang, Y. Duan, L. Peng, Y. Wang, C. Tong, L. Zhang, Z. Wei, Three-dimensional Core@Shell Co@CoMoO₄ nanowire arrays as efficient alkaline hydrogen evolution electro-catalysts, *Applied Catalysis B: Environmental* 246 (2019) 41-49.
- [426] H. Lv, H. Zhao, T. Cao, L. Qian, Y. Wang, G. Zhao, Efficient degradation of high concentration azo-dye wastewater by heterogeneous Fenton process with iron-based metal-organic framework, *Journal of Molecular Catalysis A: Chemical* 400 (2015) 81-89.
- [427] A.P. Grosvenor, B.A. Kobe, M.C. Biesinger, N.S.J.S. McIntyre, I. Analysis, Investigation of multiplet splitting of Fe 2p XPS spectra and bonding in iron compounds, 36 (2004).
- [428] L. Li, Q. Zhang, Y. She, Y. Yu, J. Hong, High-efficiency degradation of bisphenol A by heterogeneous Mn-Fe layered double oxides through peroxymonosulfate activation: Performance and synergetic mechanism, *Separation and Purification Technology* 270 (2021) 118770.
- [429] R. Ullah, I. Ahmad, Y. Zheng, Fourier transform infrared spectroscopy of "Bisphenol A", *Journal of Spectroscopy* 2016 (2016) 2073613.